Università degli Studi di Padova

DIPARTIMENTO DI FISICA E ASTRONOMIA "GALILEO GALILEI"
Corso di Laurea Magistrale in Astronomia

Tesi di laurea magistrale

Ensemble Asteroseismology with the TRILEGAL and the PARAM codes

An estimate of the systematic errors introduced by stellar models

Candidato:
Piero Dal Tio
Matricola 1130885

Relatore:
Prof.ssa Paola Marigo

Correlatori:
Dott. Léo Girardi
Dott.ssa Thaíse da Silva Rodrigues
Dott.ssa Josefa Montalbán Iglesias

Anno Accademico 2016-2017

ACKNOWLEDGMENTS

Ringrazio molto Paola Marigo, Léo Girardi, Josefina Montalbán e Thaíse Rodrigues per essere stati tutti ugualmente così disponibili nell'aiutarmi nello svolgimento e nella stesura di questo lavoro. Ringrazio anche Diego Bossini e Andrea Miglio per il loro supporto e la loro collaborazione. Infine, ringrazio la mia famiglia, i miei amici, i miei compagni di corso e Erica, che mi hanno sostenuto in questi anni di Università.

CONTENTS

LIST OF FIGURES

LIST OF TABLES

INTRODUCTION

Uncertainties in stellar physics have direct consequences in several fields of Astrophysics, ranging from investigations on exoplanet properties to stellar populations or galaxy evolution studies. For this reason, it is extremely important to achieve estimates of stellar parameters (mass, radius and age in particular) as precise as possible. Science has made great strides in this direction thanks to Asteroseismology, the study of stars by observations of their natural, resonant oscillations. The CNES CoRoT (**Co**nvection, **Ro**tation et **T**ransits planétaires, Baglin & Fridlund 2006) satellite and the NASA *Kepler* mission (Borucki et al. 2009) have been decisive in providing the necessary observations. Oscillation frequencies depend indeed on the internal structure of stars and this fact makes possible precision levels in stellar parameter estimations which have never been obtained before. In the next future, other missions like TESS (**T**ransiting **E**xoplanet **S**urvey **S**atellite, Ricker et al. 2009) and PLATO (**PLA**netary **T**ransits and **O**scillations of stars, Rauer et al. 2014) will extend the observations to a wider set of targets. These missions are of fundamental importance for the development of Ensemble Asteroseismology, the application of Asteroseismology to the study of stellar populations. The so-called solar-like oscillators, such as main-sequence and especially RGB stars, play a key role in Ensemble Asteroseismology. Some asteroseismic parameters which describes the oscillation spectrum of these stars are currently widely used to derive their mass, radius and age. The derivation method can be based on simple scaling relations (*direct method*) or on a bayesian approach (*grid-based* or *Bayesian methods*). Bayesian methods can provide more precise estimates than the direct method, but are they also accurate? The problem of accuracy comes from the model dependence of Bayesian methods, i.e. their results are affected by a systematic error component introduced by the choice of the evolutionary grid used to derive stellar parameters and their credible intervals. Our aim is to quantify systematic errors when the Bayesian method implemented in the PARAM code (Rodrigues et al. 2017) is applied on varying the input grid of evolutionary tracks. The evolutionary tracks considered correspond to models with different overshooting parameters during the hydrogen-core-burning phase. We apply the PARAM code to artificial stars generated with the stellar population synthesis code TRILEGAL (Girardi et al. 2005). The mass, radius and age which PARAM recovers for each star by using asteroseismic parameters, metallicity and effective temperature are compared to the original ones providing an estimate of systematic errors. We did TRILEGAL simulations of some open clusters observed by the Kepler/K2 Mission and of a sky region representative of a Kepler field. All artificial stars generated in these simulations are low-mass stars. The results of our work show not negligible systematic errors, especially for RGB stars ages. A lot of work should be done in order to investigate deeper the behaviours of systematic errors. Other evolutionary grids and other mass ranges and compositions should be considered. Moreover, looking at the incoming measurements of parallaxes from Gaia satellite (Lindegren et al. 2016), the entire analysis should be repeated by adding the absolute magnitude as known input information for PARAM.

In Chapter 1 we summarize the main concepts of Stellar Evolution Theory. In Chapter 2 we introduce Asteroseismology and the asteroseismic parameters $\Delta\nu$, $\nu_{\max}$ and $\Delta\Pi$ used for our analysis. In Chapter 2 can be found also an overview of the most important Space Missions for Asteroseismology and of Ensemble Asteroseismology. In Chapter 3 we provide a general description of the TRILEGAL and the PARAM codes and we show in detail simulations, evolutionary grids and physical inputs used in our analysis. Finally, in Chapter 4, we analyze PARAM results for masses, radii and ages by comparing them with the original values from TRILEGAL. In

such a way, we quantify systematic errors and we understand if they are negligible or not with respect to the error contribution coming from the width and shape of posterior probability density functions outgoing from PARAM. We conclude with a short discussion about future perspectives.

1 THE STELLAR EVOLUTION THEORY IN BRIEF

Treatments of this Chapter mainly follow Hansen et al. (2004), Kippenhahn & Weigert (1990) and Salaris & Cassisi (2005). Physical principles of mass and momentum conservation can be considered the starting point for the development of Stellar Evolution Theory. In fact, they are used to derive two fundamental stellar structure equations: the equation that relates the mass distribution to the local density and the hydrostatic equilibrium condition.

1.1 THE HYDROSTATIC EQUILIBRIUM

Let us derive these two equations. Firstly, we assume spherical symmetry, which implies that all quantities depend only on a radial coordinate in the stellar interior and also on time in an evolving star. We can adopt the radius ($r \in [0,\ R]$) of a spherical shell as radial Eulerian coordinate. The application of mass conservation to a spherical shell of mass $\mathrm{d}m$, thickness $\mathrm{d}r$, mean radius r and radial velocity v, gives

$$\mathrm{d}m(r,t) = 4\pi r^2 \rho \mathrm{d}r - 4\pi r^2 \rho v \mathrm{d}t \tag{1}$$

In a static situation (i.e. $v = 0$; almost always a good approximation), we obtain

$$\frac{\mathrm{d}m}{\mathrm{d}r} = 4\pi r^2 \rho \tag{2}$$

We can define the Lagrangian *mass coordinate*:

$$m(r) := m_r = \int_0^r 4\pi r'^2 \rho \mathrm{d}r' \qquad m \in [0,\ M]$$

and use it instead of the radius, so that Equation 2 becomes

$$\frac{\mathrm{d}r}{\mathrm{d}m} = \frac{1}{4\pi r^2 \rho} \tag{3}$$

or with a partial derivative in a non-static situation. Equation 3 is the first fundamental equation.
Let's consider now the equation of motion of a gas element. Gravity and pressure gradient are the two forces acting, against one another, on the gas element. Hence, the equation of motion for a cylindrical gas element with the axis along the radial direction can be easily derived. One obtains

$$\frac{\partial^2 r}{\partial t^2} = -\frac{Gm}{r^2} - \frac{1}{\rho}\frac{\partial P}{\partial r} \tag{4}$$

and, thanks to Equation 3, in terms of the mass coordinate becomes

$$\frac{\partial^2 r}{\partial t^2} = -\frac{Gm}{r^2} - 4\pi r^2 \frac{\partial P}{\partial m} \tag{5}$$

The majority of stars does not show strong structural changes so there must be not a significant acceleration ($\ddot{r} \simeq 0$). This means that stars are usually in hydrostatic

equilibrium. Therefore, the condition that holds in hydrostatic equilibrium is (from Equation 5 in a static situation)

$$\frac{\mathrm{d}P}{\mathrm{d}m} = -\frac{Gm}{4\pi r^4} \tag{6}$$

Equations 3 and 6 determine the mechanical behaviour of an isolated, spherically symmetric star. However, there are three unknown functions of m (i.e. r, P and ρ), so we need a third equation, the *equation of state*, which relates the pressure and density functions. The equation of state depends in general on temperature. Consequently, mechanical properties depend in general on thermal ones. Only in the special cases of *polytropes* (e.g. White Dwarfs can be approximately described with a polytropic model), the equation of state is independent of temperature.

1.2 THE THERMAL EQUILIBRIUM

Starting from the condition for hydrostatic equilibrium, we multiply by the volume $V = 4\pi r^3/3$ enclosed within the shell and then we integrate over m:

$$\int_0^M \frac{4}{3}\pi r^3 \frac{\mathrm{d}P}{\mathrm{d}m}\,\mathrm{d}m = -\frac{1}{3}\int_0^M \frac{Gm}{r}\,\mathrm{d}m \tag{7}$$

Note that

$$E_{\mathrm{gr}} := -\int_0^M \frac{Gm}{r}\,\mathrm{d}m$$

is the gravitational potential energy and

$$\int_0^M \frac{4}{3}\pi r^3 \frac{\mathrm{d}P}{\mathrm{d}m}\mathrm{d}m = \int_{P_{center}}^{P_{surf}} V\mathrm{d}P = V\,P\Big|_{P_{center}}^{P_{surf}} - \int_0^{V_{surf}} P\mathrm{d}V = \frac{4}{3}\pi R^3 P(R) - \int_0^{V_{surf}} P\mathrm{d}V$$

where the subscript *surf* indicates values at the surface of the volume V. If we integrate over the whole star, then $P(R) \simeq 0$, so

$$-\int_0^{V_{surf}} P\,\mathrm{d}V = \frac{1}{3}E_{\mathrm{gr}} \qquad \text{or} \qquad -\int_0^M \frac{P}{\rho}\,\mathrm{d}m = \frac{1}{3}E_{\mathrm{gr}} \tag{8}$$

Equation 8 is the general form of the Virial Theorem. The meaning of this theorem will be more clear if we apply it to an ideal gas for which the internal energy per unit mass is

$$u = \frac{3}{2}\frac{N k_B T}{M} = \frac{3}{2}\frac{P V}{M} = \frac{3}{2}\frac{P}{\rho}$$

Hence the Virial Theorem becomes

$$-\int_0^M \frac{2}{3}u\,\mathrm{d}m = \frac{1}{3}E_{\mathrm{gr}} \quad \longrightarrow \quad E_{\mathrm{int}} = -\frac{1}{2}E_{\mathrm{gr}}$$

where $E_{\mathrm{int}} := \int u\mathrm{d}m$ is the total internal energy of the star. Therefore the gravitational potential energy and the internal energy of a star in hydrostatic equilibrium are strictly connected through the virial theorem: a more tightly bound star must be hotter. A star in hydrostatic equilibrium is bound only if its total energy, $E_{\mathrm{tot}} = E_{\mathrm{int}} + E_{\mathrm{gr}}$, is negative. Thanks to the Virial Theorem we can immediately say that a star made of ideal gas might exist: $E_{\mathrm{tot}} = E_{\mathrm{gr}}/2 < 0$.

We said that gravitationally bound gas spheres must be hot, but a hot gas radiates and loses energy. The rate of energy loss is the luminosity of stars: $L = -\mathrm{d}E_{\mathrm{tot}}/\mathrm{d}t > 0$. Therefore the consequences of losing energy are

$$E_{\mathrm{tot}} = \frac{E_{\mathrm{gr}}}{2} \quad \longrightarrow \quad \begin{cases} \dot{E}_{\mathrm{gr}} = -2L < 0 & \text{the star contracts} \\ \dot{E}_{\mathrm{int}} = L > 0 & \text{the star gets hotter} \end{cases}$$

Roughly speaking, an half of the gravitational energy is lost and an half is used to heat the star. Anyway, nuclear reactions have not been taken into account yet. If the rate of nuclear energy production, L_{nuc}, is equal to the luminosity, then nuclear burning can compensate the energy loss and the star must conserve both $\dot{E}_{\text{gr}}$ and $\dot{E}_{\text{int}}$. We call this situation *thermal equilibrium*: the star neither expands nor contracts and its internal temperature is constant in time. Main-sequence stars are in thermal equilibrium for example. The thermal equilibrium is broken when the nuclear burning can't provide enough energy anymore (fuel exhaustion).

1.3 THE TIMESCALES OF STELLAR EVOLUTION

The *dynamical timescale*, τ_{dyn} is the time a star takes to react to a perturbation of the hydrostatic equilibrium. A possible estimate of this timescale is the free-fall timescale:

$$\tau_{\text{dyn}} \approx \sqrt{\frac{R^3}{GM}} \approx \frac{1}{2}\left(G\bar{\rho}\right)^{-1/2}$$

τ_{dyn} is usually of the order of hours, hence stars must be very close to hydrostatic equilibrium.
The *thermal timescale*, τ_{th} is the time a star takes to react to a perturbation of the thermal equilibrium. A possible estimate of this timescale is the Kelvin-Helmholtz timescale, i.e. the time to radiate away all the internal energy without burning energy and at constant luminosity:

$$\tau_{\text{th}} = \frac{E_{\text{int}}}{L} \approx \frac{|E_{\text{gr}}|}{2L} \approx \frac{GM^2}{2RL}$$

It turns out that the reactions are very slow ($\tau_{\text{th}} \simeq 1.5 \cdot 10^7$ yr for the Sun), so we have not direct observations that test the condition of thermal equilibrium in stars. We know that the Sun is in thermal equilibrium because we have and estimate of the Earth's age that puts constraints to the energy production mechanisms in the Sun. Finally, the *nuclear timescale* is the time a star takes to radiate all its nuclear energy supply (assuming L constant):

$$\tau_{\text{nuc}} = \frac{E_{\text{nuc}}}{L}$$

The nuclear timescale is two or three orders of magnitude higher than the thermal timescale, so stars can reach a state of thermal equilibrium. In conclusion, stars can be considered to be in both hydrostatic and thermal equilibrium during most of their lives.

1.4 THE EQUATION OF STATE IN REAL STARS

Real stars are not completely made of ideal gas. There are other sources of pressure like radiation and gas degeneracy (electron degeneracy in particular). We can distinguish different regimes where a pressure source dominates among the others. Different regimes correspond to different equations of state. These regimes are put in evidence in Figure 1 in the $\log T - \log \rho$ plane together with some models of zero-age main-sequence stars. See the caption for further information.

1.4.1 Specific heats and adiabatic derivatives

It is useful to write the equation of state $P = P(\rho, T, X_i)$ in differential form:

$$\frac{\mathrm{d}P}{P} = \chi_T \frac{\mathrm{d}T}{T} + \chi_\rho \frac{\mathrm{d}\rho}{\rho}$$

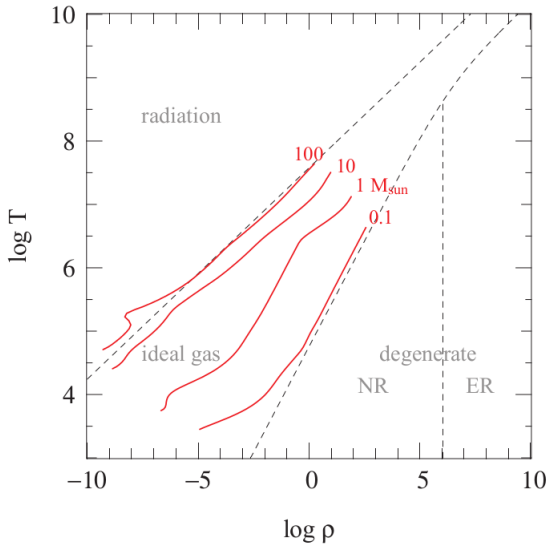

Figure 1.: *The equation of state for a gas of free particles in the* $\log T - \log \rho$ *plane. Dashed lines separate the regions where radiation pressure, ideal gas pressure, non-relativistic electron degeneracy and extremely relativistic electron degeneracy dominate for homogeneous solar composition* ($X = 0.7$, $Z = 0.02$)*. Red lines represent models of zero-age (so homogeneous) main-sequence stars with mass ranging from* $0.1\,M_\odot$ *to* $100\,M_\odot$*. The star center is located at the upper extremity and the surface at the lower one. We can see that radiation pressure dominates at higher masses and electron degeneracy pressure at very low masses. For a* $1\,M_\odot$ *star, instead, the major contribution comes from ideal gas pressure. Courtesy of O. Polls (Lecture Notes).*

where

$$\chi_T := \left(\frac{\partial \log P}{\partial \log T}\right)_{\rho, X_i} = \frac{T}{P}\left(\frac{\partial P}{\partial T}\right)_{\rho, X_i} \qquad \chi_\rho := \left(\frac{\partial \log P}{\partial \log \rho}\right)_{T, X_i} = \frac{\rho}{P}\left(\frac{\partial P}{\partial \rho}\right)_{T, X_i}$$

The subscript X_i means constant composition. In general χ_T and χ_ρ are functions of T and ρ, but in the case of weak dependence it results the following equation of state.

$$P = P_0\, \rho^{\chi_\rho}\, T^{\chi_T}$$

With $\chi_T = \chi_\rho = 1$ we obtain the equation of state of an ideal gas, instead $\chi_T = 4$ and $\chi_\rho = 0$ for a radiation dominated gas.
The definitions of specific heats follow from the first and the second laws of thermodynamics. For a unit mass element we have

$$\mathrm{d}q = T\,\mathrm{d}s = \mathrm{d}u + P\,\mathrm{d}v = \mathrm{d}u - \frac{P}{\rho^2}\,\mathrm{d}\rho \qquad \text{with} \quad v = 1/\rho$$

Now we can define the specific heats and the ratio $\gamma := c_P/c_V$:

$$c_V := \left(\frac{\mathrm{d}q}{\mathrm{d}T}\right)_v = \left(\frac{\partial u}{\partial T}\right)_v \qquad c_P := \left(\frac{\mathrm{d}q}{\mathrm{d}T}\right)_P = \left(\frac{\partial u}{\partial T}\right)_P - \frac{P}{\rho^2}\left(\frac{\partial \rho}{\partial T}\right)_P \tag{9}$$

$$\gamma = c_P/c_V = \frac{P}{\rho\, T}\,\frac{\chi_T^2}{\chi_\rho} \qquad \gamma = 5/3 \text{ for an ideal gas} \tag{10}$$

Let's introduce now other two important quantities, called *adiabatic derivatives*, which allow us to describe the thermodynamic response of a system to adiabatic changes. The *adiabatic exponent*, γ_{ad}, and the *adiabatic temperature gradient*, ∇_{ad}, measure the

response of the pressure and of the temperature respectively to adiabatic compression or expansion (i.e. to a change in density). They are defined as follows:

$$\gamma_{\text{ad}} = \left(\frac{\partial \log P}{\partial \log \rho}\right)_{\text{ad}} \qquad \nabla_{\text{ad}} = \left(\frac{\partial \log T}{\partial \log P}\right)_{\text{ad}}$$

γ_{ad} and ∇_{ad} are fundamental quantities because the former is related to the dynamical stability of stars and the latter to the stability against convection. For both quantities there are two limiting cases. It can be shown that $\gamma_{\text{ad}} = 5/3$ for non-relativistic particles (also degenerate particles) and $\gamma_{\text{ad}} = 4/3$ for extremely relativistic particles. On the other hand, ∇_{ad} ranges from 0.4 for an ideal gas without radiation to 0.25 for a radiation-dominated gas. The adiabatic derivatives are related to the other quantities introduced before through the equation of state.

1.4.2 Ionization

Complete ionization can be assumed in regions where $T > 10^6\,\text{K}$. In this case the relations we have derived hold. However, in cooler outer layers of stars it is necessary to consider the state of partial ionization of the gas. In these layers changes in density or temperature cause changes in the degree of ionization and have strong effects on thermodynamic properties and so on adiabatic derivatives.
Stars are not isolated systems, so they are not globally in thermodynamic equilibrium, but the local thermodynamic equilibrium is achieved. Therefore, the Saha's equation holds. In particular for hydrogen we have

$$\frac{x^2}{1-x^2} = \frac{(2\pi m_e)^{3/2}}{h^3}\,\frac{(kT)^{5/2}}{P_{\text{gas}}}\,e^{-\chi_H/k_B T}$$

where x is the *degree of ionization* (i.e. the ratio between the number density of ionized hydrogen atoms and the total number density of hydrogen atoms) and $\chi_H = 13.6\,\text{eV}$ is the ionization energy.
Moreover, in case of partial ionization, the energy of recombination is an additional source for the internal energy that has to be taken into account, thus

$$u = \frac{3}{2}\,\frac{P_{\text{gas}}}{\rho} + x\,\frac{\chi_H}{m_u} = \frac{3}{2}(1+x)\mathcal{R}T + x\,\frac{\chi_H}{m_u}$$

From the last two equations we see that x increases with T and decreases with P_{gas}. Moreover a small increase in T, and so in x, causes a large increase in u. Therefore, in a condition of partial ionization, a compression of the gas leads to an increase of u and T does not raise so much with P. This means that $\nabla_{\text{ad}} < 0.4$: it presents a minimum in partial ionization zones and low values of ∇_{ad}, as we will see, can induce convection. Consequently, the outer layers of stars might be convective. Finally, it can be demonstrated that also γ_{ad} decreases in partial ionization zones and this makes the dynamical stability of the outer layers weaker.

1.5 ENERGY TRANSPORT IN STELLAR INTERIORS

In stellar interiors energy can be transported outward in two ways: heat diffusion and convection. However, in order to understand the energy transport in stars, we firstly have to apply the conservation of energy on a local scale (applied to the whole star it gives the virial theorem). Let us consider a spherical shell of unit mass. The first law of thermodynamics states that

$$\mathrm{d}u = \mathrm{d}q + \frac{P}{\rho^2}\,\mathrm{d}\rho$$

and we can say that heat absorbed or released by the shell is

$$\mathrm{d}q = \left(\epsilon_{\mathrm{nuc}} - \epsilon_\nu - \frac{\partial l}{\partial m}\right)\mathrm{d}t \tag{11}$$

where ϵ_{nuc} is the rate of nuclear energy production per unit mass, ϵ_ν is the rate energy loss per unit mass due to neutrino production, l is the rate at which heat flows outward the shell. Combining these two relations we obtain another fundamental equation for stellar evolution:

$$\frac{\partial l}{\partial m} = \epsilon_{\mathrm{nuc}} - \epsilon_\nu - \frac{\partial u}{\partial t} + \frac{P}{\rho^2}\frac{\partial \rho}{\partial t} = \epsilon_{\mathrm{nuc}} - \epsilon_\nu + \epsilon_{\mathrm{gr}} \tag{12}$$

where ϵ_{gr} gathers the terms with time derivatives. In thermal equilibrium the stationary state implies $\epsilon_{\mathrm{gr}} = 0$.

1.5.1 Heat diffusion

In stellar interiors photons interact very frequently with matter and transport energy outward very slowly with random motions. This mechanism is called *radiative diffusion*. This flow of energy derives from a gradient in energy density which is associated with a temperature gradient. The energy flux can be written as follows:

$$\mathbf{F}_{\mathrm{rad}} = -\frac{1}{3}c\ell\nabla U = -\frac{1}{3}c\ell\left(\frac{\partial U}{\partial T}\right)_V \nabla T = -K\nabla T$$

where c is the speed of light, ℓ is the mean free path of photons and $K = \frac{1}{3}c\ell\left(\frac{\partial U}{\partial T}\right)_V$ is called *conductivity*. For photons $U = aT^4$, $a = 7.56 \cdot 10^{-15}\,\mathrm{erg\,cm^{-3}\,K^{-4}}$ and $\ell = 1/\kappa\rho$ (κ is an average over frequencies of the absorption coefficient, for example the Rosseland mean opacity), so

$$\mathbf{F}_{\mathrm{rad}} = -K\nabla T = -\frac{4}{3}\frac{acT^3}{\kappa\rho}\nabla T$$

In spherical symmetry $F = l/4\pi r^2$ and we find

$$\frac{\partial T}{\partial r} = -\frac{3\kappa\rho l}{16\pi acT^3 r^2} \qquad \text{or} \qquad \frac{\partial T}{\partial m} = -\frac{3\kappa l}{64\pi^2 acT^3 r^4} \tag{13}$$

that is the temperature gradient required to carry the entire luminosity only by radiation. This is another important equation for stellar structure in case of *radiative equilibrium*, i.e. in case of pure radiative diffusion as energy transport mechanism. In conditions of hydrostatic equilibrium we can use Equation 6:

$$\frac{\mathrm{d}T}{\mathrm{d}m} = \frac{\mathrm{d}P}{\mathrm{d}m}\frac{\mathrm{d}T}{\mathrm{d}P} = -\frac{Gm}{4\pi r^4}\frac{T}{P}\frac{\mathrm{d}\log T}{\mathrm{d}\log P}$$

and we can define the *radiative temperature gradient*

$$\nabla_{\mathrm{rad}} = \left(\frac{\mathrm{d}\log T}{\mathrm{d}\log P}\right)_{\mathrm{rad}} = \frac{3\kappa l P}{16\pi acGmT^4}$$

The energy flux due to *heat conduction*, the transport of heat through collisions between gas particles like ions and electrons, has the same expression with a different conductivity:

$$\mathbf{F}_{\mathrm{cd}} = -K_{\mathrm{cd}}\nabla T$$

However, heat conduction becomes important only for stars in late stages of evolution with dense degenerate cores and for white dwarfs.

1.5.2 Opacity

The relation between the energy flux of radiative diffusion and the temperature gradient depends on the opacity, κ. Therefore the opacity has a primary role in determining the stellar structure. The main sources of opacity are:

- Electron Scattering. $\kappa_{\rm es} = \sigma_e/(\rho/n_e)$ where $\sigma_e = 6.652 \cdot 10^{-25}\,{\rm cm}^2$ is the Thomson cross-section of electrons and n_e the number density of electrons. This opacity source is important in ionized regions not too dense (high n_e, but not too high density).

- Free-free absorption. It is the inverse process of *bremsstrahlung*. It can be shown that $\kappa_{\rm ff} \propto \rho T^{-7/2}$. An opacity law of this form is called *Kramers opacity*.

- Bound-free absorption. Again we have a Kramers opacity. This process is important in a temperature range where photons are energetic enough to ionize atoms but not to keep the gas fully ionized.

- Bound-bound absorption. This source is mainly important for temperatures lower than 10^6 K.

- Negative hydrogen ion. It is important in the photosphere of cool stars ($T < 10^4$ K). It determines the steepness of the Hayashi line.

1.5.3 Convection - criteria for stability

We have seen that radiative diffusion needs a temperature gradient and that a larger luminosity corresponds to a larger temperature gradient. However, when ∇T reaches a certain limit then gas becomes unstable to convection. Let us derive a criterion for stability against convection. We firstly consider a gas element which is perturbed and displaced outward. The element expands adiabatically in order to be always in pressure equilibrium with the surroundings. If its density is larger than that of the ambient, then it will fall inward, otherwise buoyancy forces will accelerate it outward and convection occurs. The element expands adiabatically, so

$$\frac{\delta P_e}{P_e} = \gamma_{\rm ad}\frac{\delta \rho_e}{\rho_e}$$

and the criterion for stability can be expressed as

$$\delta\rho_e > \frac{{\rm d}\rho}{{\rm d}r}\delta r \qquad \longrightarrow \qquad \frac{\rho_e}{\gamma_{\rm ad}}\frac{\delta P_e}{P_e} > \frac{{\rm d}\rho}{{\rm d}r}\delta r$$

Moreover, since the element is always in pressure equilibrium with the ambient, $\delta P_e = \frac{{\rm d}P}{{\rm d}r}\delta r$, so

$$\frac{1}{\rho}\frac{{\rm d}\rho}{{\rm d}r} < \frac{1}{P}\frac{{\rm d}P}{{\rm d}r}\frac{1}{\gamma_{\rm ad}} \qquad \longrightarrow \qquad \frac{{\rm d}\log\rho}{{\rm d}\log P} > \frac{1}{\gamma_{\rm ad}} \tag{14}$$

If this condition is violated then convection takes place and the hottest and innermost elements start to move upward transporting their energy. Condition 14 can be rewritten in a more practical way by using the differential form of the equation of state $P = P(\rho, T, \mu)$:

$$\frac{{\rm d}P}{P} = \chi_T\frac{{\rm d}T}{T} + \chi_\rho\frac{{\rm d}\rho}{\rho} + \chi_\mu\frac{{\rm d}\mu}{\mu} \quad \text{or} \quad {\rm d}\log P = \chi_T{\rm d}\log T + \chi_\rho{\rm d}\log\rho + \chi_\mu{\rm d}\log\mu$$

This time we consider also a possible change in the mean molecular weight, μ, i.e. in composition. χ_μ is defined as

$$\chi_\mu := \left(\frac{\partial \log P}{\partial \log \mu}\right)_{\rho,T} \qquad \chi_\mu = -1 \text{ for an ideal gas}$$

Now, we can easily derive the following relation.

$$\frac{\mathrm{d}\log\rho}{\mathrm{d}\log P} = \frac{1}{\chi_\rho}\left(1 - \chi_T \frac{\mathrm{d}\log T}{\mathrm{d}\log P} - \chi_\mu \frac{\mathrm{d}\log\mu}{\mathrm{d}\log P}\right) = \frac{1}{\chi_\rho}\left(1 - \chi_T\nabla - \chi_\mu\nabla_\mu\right)$$

where $\nabla := \mathrm{d}\log T/\mathrm{d}\log P$ and $\nabla_\mu := \mathrm{d}\log\mu/\mathrm{d}\log P$. Moreover, the adiabatic derivatives are related to each other and it can be shown that

$$\frac{1}{\gamma_{\mathrm{ad}}} = \frac{1}{\chi_\rho}\left(1 - \chi_T\nabla_{\mathrm{ad}}\right)$$

In conclusion, the criterion 14 becomes

$$\nabla < \nabla_{\mathrm{ad}} - \frac{\chi_\mu}{\chi_T}\nabla_\mu \tag{15}$$

In the case radiation provides the entire transport of energy then $\nabla = \nabla_{\mathrm{rad}}$ and we obtain the *Ledoux criterion*:

$$\nabla_{\mathrm{rad}} < \nabla_{\mathrm{ad}} - \frac{\chi_\mu}{\chi_T}\nabla_\mu \tag{16}$$

The *Schwarzshild criterion* descends from the Ledoux criterion and holds only in chemically homogeneous layers ($\nabla_\mu = 0$):

$$\nabla_{\mathrm{rad}} < \nabla_{\mathrm{ad}} \tag{17}$$

Therefore we expect instability to convection where

$$\nabla_{\mathrm{rad}} = \frac{3P\kappa l}{16\pi acGT^4 m} > \nabla_{\mathrm{ad}}$$

This might happen for many reasons:

- The opacity κ is high: like in the outer envelope of cool stars, the Sun included.
- The energy flux and so l/m is high: like near the star center where $l/m \simeq \epsilon_{\mathrm{nuc}}$ and in case of strong and peaked nuclear energy production there might be a convective core.
- The adiabatic temperature gradient is small: like in partial ionization zones at low temperature, i.e. in shallow surface layers.

1.5.4 Convection - the mixing length theory (MLT)

The *mixing length theory* approximately describes the convective motions by means of gas blobs that move up or down radially over a distance, ℓ_m, called *mixing length*. At the end of their travel blobs dissolve and achieve the thermal equilibrium with the ambient. ℓ_m is an unknown parameter and it is of the order of the local pressure scale height $H_P = |\mathrm{d}r/\mathrm{d}\ln P| = P/\rho g$. The MLT allows us to estimate the convective

energy flux. The temperature difference between the blob and its surroundings just before its dissolution is

$$\Delta T = T_{\text{blob}} - T_{\text{surr}} = \left[\left(\frac{\mathrm{d}T}{\mathrm{d}r} \right)_{\text{blob}} - \frac{\mathrm{d}T}{\mathrm{d}r} \right] \ell_m =$$
$$= \left[\left(-\frac{T}{H_P} \nabla_{\text{ad}} \right) - \left(-\frac{T}{H_P} \nabla \right) \right] \ell_m = T \frac{\ell_m}{H_P} (\nabla - \nabla_{\text{ad}})$$

and the energy flux carried by the blob is

$$F_{\text{conv}} = \overline{v}_{\text{blob}} \, \rho \Delta u = \overline{v}_{\text{blob}} \, \rho c_P \Delta T$$

where $\overline{v}_{\text{blob}}$ is the average velocity of blobs and $\Delta u = c_P \Delta T$ the excess of internal energy of a blob with respect to the ambient. If we assume that blobs move with a constant acceleration a along the distance ℓ_m, provided by the buoyancy force, then we can compute an estimate for $\overline{v}_{\text{blob}}$. In fact

$$\ell_m = \frac{1}{2} a t^2 = \frac{1}{2} \left(-g \frac{\Delta \rho}{\rho} \right) t^2 \simeq \frac{1}{2} \left(g \frac{\Delta T}{T} \right) t^2$$

hence

$$\overline{v}_{\text{blob}} \simeq \ell_m / t \simeq \sqrt{\frac{1}{2} \ell_m g \frac{\Delta T}{T}} \simeq \sqrt{\frac{\ell_m^2 g}{2 H_P} (\nabla - \nabla_{\text{ad}})}$$

and

$$F_{\text{conv}} = \rho c_P T \left(\frac{\ell_m}{H_P} \right)^2 \sqrt{\frac{1}{2} g H_P} \, (\nabla - \nabla_{\text{ad}})^{3/2}$$

where the quantity $\nabla - \nabla_{\text{ad}}$ is called *superadiabacity*. Convection is and extremely efficient mechanism of energy transport: it turns out that a small superadiabacity of the order of $10^{-5} \div 10^{-7}$ is sufficient to carry the whole energy flux of the Sun by convection in the deep stellar interior. Consequently, in analogy with what we have done for the radiative diffusion, we can write

$$\frac{\mathrm{d}T}{\mathrm{d}m} = -\frac{Gm}{4\pi r^4} \frac{T}{P} \nabla \quad \text{with} \quad \nabla = \nabla_{\text{ad}}$$

On the contrary, in the outermost layers superadiabacity is high, but the convective flux is small because density and temperature are lower than their mean values. At a certain point, near the surface, radiative diffusion is more efficient even if convection occurs.
The convective mixing has important consequences in stellar evolution that we can summarize in two points:

- A star with a convective core has a larger fuel supply (and so e larger lifetime) because convection brings the products of nuclear burning outward and the hydrogen of the envelope inward.
- During some events called *dredge ups*, the convective envelope of a star penetrates deep in the interior and brings up to the surface the nuclear burning products revealing the nuclear processes that have taken place.

Figure 2 summarizes many concepts we have seen about convection for a $1\,M_\odot$ star.

1.5.5 Convective overshooting

The classical theory of convection, according with the Schwarzschild criterion, sets the boundary of a convective zone at the surface where $\nabla_{\text{ad}} = \nabla_{\text{rad}}$. On this surface the acceleration of blobs is null because the buoyancy force vanishes, but blobs still

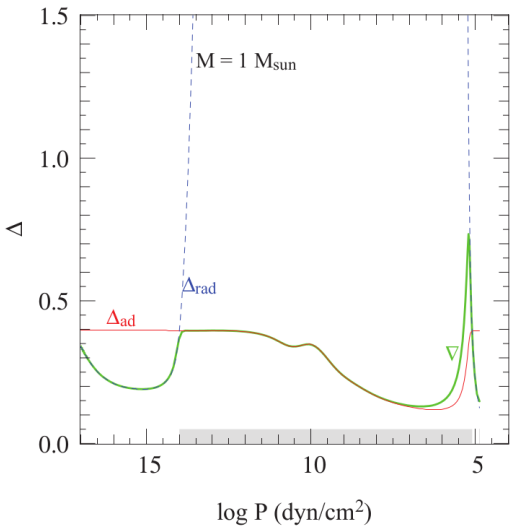

Figure 2.: *The quantities ∇_{ad}, ∇_{rad} and ∇ in a $1\,M_\odot$ stellar model plotted against* $\log P$. *If we apply the Schwarzshild criterion then we immediately realize that the core is radiative and the envelope convective (the gray bar indicates convective regions). We can also identify the positions of partial ionization zones looking at the depressions in ∇_{ad}. Note that convection is efficient only in the deep layers of the envelope where $\nabla_{ad} \simeq \nabla$. It becomes less efficient in the hydrogen partial ionization zone where $\nabla_{ad} < \nabla$ and it is totally inefficient very near to the surface. Courtesy of O. Polls (Lecture Notes).*

have a non-zero velocity so they penetrate a little into the radiative zone before being stopped. This phenomenon is called *convective overshooting*. It has the effect to continuously transport new fuel from a radiative envelope to a convective core with important consequences on the star evolution. Therefore overshooting affects the evolution of stars with a convective core during the main sequence, i.e. stars with $M \gtrsim 1.1\,M_\odot$. One can try to take overshooting into account in the framework of the MLT by introducing an estimate of the distance, d_{ov}, covered by blobs beyond the Schwarzschild surface. Usually the unknown overshooting parameter, α_{ov}, is defined so that $d_{ov} = \alpha_{ov} H_P$ and it must be calibrated from observations. We are going to turn back to this topic in the next sections and in Chapter 3.

1.6 NUCLEAR PROCESSES IN STARS

In this section we rapidly talk about the possible nuclear reactions that take place in stellar interiors. Let us consider a general reaction of the form $X + a \to Y + b$. Its cross-section is defined as

$$\sigma\,[\mathrm{cm}^2] = \frac{\text{number of reactions per second}}{\text{flux of incident particles } a} \tag{18}$$

If v is the relative velocity between the X and the a particles and denoting by n_X and n_a their number densities, then the number of reactions per second and per unit volume is $R_{Xa} = n_X\, n_a\, v\sigma/(1+\delta_{Xa})$. $\delta_{Xa} = 1$ if particles X and a are identical and it is zero otherwise. However, the cross-section depends on v so it is better to use the average:

$$\langle \sigma\, v \rangle = \int_0^\infty \Phi(v)\sigma(v) v\, \mathrm{d}v = \sqrt{\frac{8}{\pi m\,(k_B T)^3}} \int_0^\infty \sigma(E) E \exp\left(-\frac{E}{k_B T}\right) \mathrm{d}E \tag{19}$$

where $\Phi(v)$ is the normalized Maxwellian velocity distribution[1], $m = \frac{m_X m_a}{m_X + m_a}$ is the reduced mass and $E = mv^2/2$. We note that $\langle \sigma v \rangle$ depends only on T, so this quantity determines the temperature dependence of nuclear reactions. The starting point for the computation of the cross-section is the geometrical cross-section $\sigma_g = \pi\lambda^2$ where $\lambda = \hbar/p$ is the de Broglie wavelength. The detailed calculation of σ for a nuclear reaction is complicated: the electromagnetic forces, the tunnel effect and possible resonances must be considered. For example, particles would not pass the Coulomb barrier at typical stellar temperatures if there was not the tunnel effect. It can be shown that the tunnel effect probability is approximately given by

$$P = P_0 \exp(-bE^{-1/2}) \qquad \text{with} \qquad b = 2\pi \frac{Q_X Q_a e^2 m^{1/2}}{\hbar\sqrt{2}}$$

where Q_X and Q_a are the charges of two nuclei in that case. In addition, if the energy of the incoming particle corresponds to a quasi-stationary (i.e. with positive energy) nuclear level then the reaction probability increases by several orders of magnitude. We expect from this considerations that the cross-section should be of the form

$$\sigma(E) \propto \pi\lambda^2 P(E)\xi(E)$$

Where $\xi(E)$ is a function with some peaks that represents the effect of resonances. Since $\lambda^2 \propto 1/E$ and $P(E) \propto \exp(-bE^{-1/2})$, we can write

$$\sigma(E) = S(E) \frac{\exp(-bE^{-1/2})}{E} \tag{20}$$

where the *astrophysical S-factor*, $S(E)$, gathers all the other effects. Therefore Equation 19 becomes

$$\langle \sigma v \rangle = \sqrt{\frac{8}{\pi m (k_B T)^3}} \int_0^\infty S(E) f(E)\, \mathrm{d}E \tag{21}$$

with

$$f(E) = \exp\left(-\frac{E}{k_B T} - \frac{b}{E^{1/2}} \right)$$

The function $f(E)$ has a significant value only around a certain energy where it presents a sharp peak called *Gamow peak*. Moreover, $f(E)$ and consequently the reaction rate increase very strongly with temperature, instead they decrease strongly with the charge of the nuclei because of the quantity b.

1.6.1 Nuclear burning cycles

The strong dependence of nuclear reaction rates on temperature implies that the nuclear fusion processes are well separated and the evolution of a star is divided in phases characterized by different nuclear burning cycles.

Let's start talking about hydrogen burning whose net result is the fusion of four ^{1}H nuclei into a single ^{4}He nucleus. However, the simultaneous reaction between four protons is extremely unlikely, indeed the hydrogen burning happens through a chain of reactions. There are two possibilities:

- p-p chain: the main nuclear fusion process in the Sun. As shown in the following scheme, this chain has three possible channels, with different energy release, whose relative frequency depends on temperature and chemical composition. The left-hand channel dominates at temperatures $T \lesssim 1.5 \cdot 10^7$ K like in the Sun. If Q_H is the total energy released by the chain and R_{ppc} its rate, then the energy generation rate per unit mass is $\epsilon_{\text{nuc}} = Q_H R_{ppc}/\rho$ except for

1 If the particles velocities follow a Maxwellian distribution (we assume that this is the case) then the relative velocities also follow a Maxwellian distribution.

the left channel that produces only one helium atom and so $\epsilon_{\text{nuc}} = Q_H R_{ppc}/2\rho$.

$$^1\text{H} + {}^1\text{H} \longrightarrow {}^2\text{H} + \text{e}^+ + \nu$$

$$^2\text{H} + {}^1\text{H} \longrightarrow {}^3\text{He} + \gamma$$

$$^3\text{He} + {}^3\text{He} \longrightarrow {}^4\text{He} + 2\,{}^1\text{H} \qquad {}^3\text{He} + {}^4\text{He} \longrightarrow {}^7\text{Be} + \gamma$$

$Q_H = 26.20$.

$$^7\text{Be} + \text{e}^- \longrightarrow {}^7\text{Li} + \nu \qquad {}^7\text{Be} + {}^1\text{H} \longrightarrow {}^8\text{B} + \gamma$$

$$^7\text{Li} + {}^1\text{H} \longrightarrow {}^4\text{He} + {}^4\text{He} \qquad {}^8\text{B} \longrightarrow {}^8\text{Be} + \text{e}^+ + \nu$$

$Q_H = 25.66\,\text{MeV}$ $\qquad$ $^8\text{Be} \longrightarrow {}^4\text{He} + {}^4\text{He}$

$Q_H = 19.76\,\text{MeV}$

- CNO cycle: it takes place if C, N and O are already present in the star and if the temperature is sufficiently high ($T \gtrsim 1.5 \cdot 10^7$ K). If the cycle is stable (i.e. the rate of production of each nucleus equals its rate of consumption) then $Q_H = 29.97\,\text{MeV}$. The sequence of the reactions is illustrated in the following scheme.

$$^{12}\text{C} + {}^1\text{H} \longrightarrow {}^{13}\text{N} + \gamma$$

$$^{13}\text{N} \longrightarrow {}^{13}\text{C} + \text{e}^+ + \nu$$

$$^{13}\text{C} + {}^1\text{H} \longrightarrow {}^{14}\text{N} + \gamma$$

$$^{14}\text{N} + {}^1\text{H} \longrightarrow {}^{15}\text{O} + \gamma$$

$$^{15}\text{O} \longrightarrow {}^{15}\text{N} + \text{e}^+ + \nu$$

$$^{15}\text{N} + {}^1\text{H} \longrightarrow {}^{12}\text{C} + {}^4\text{He}$$

$$\longrightarrow {}^{16}\text{O} + \gamma$$

$$^{16}\text{O} + {}^1\text{H} \longrightarrow {}^{17}\text{F} + \gamma$$

$$^{17}\text{F} \longrightarrow {}^{17}\text{O} + \text{e}^+ + \nu$$

$$^{17}\text{O} + {}^1\text{H} \longrightarrow {}^{14}\text{N} + {}^4\text{He}$$

At temperatures $T \gtrsim 10^8$ K the helium burning takes place. Helium is fused into carbon and oxygen. In reality helium burning occurs in two steps:

$$^4\text{He} + {}^4\text{He} \longleftrightarrow {}^8\text{Be}$$

$$^8\text{Be} + {}^4\text{He} \longrightarrow {}^{12}\text{C} + \gamma$$

and the net effect is the so-called $triple - \alpha$ reaction

$$3\,{}^4\text{He} \longrightarrow {}^{12}\text{C} + \gamma$$

whose amount of energy released is $Q = 7.275$ MeV. Moreover, when the concentration of carbon becomes high enough then the ^{12}C atoms can react with a further ^{4}He atom and produce oxygen:

$$^{12}\text{C} + {}^4\text{He} \longrightarrow {}^{16}\text{O} + \gamma$$

This reaction has $Q = 7.162$ MeV. Therefore the energy released per reaction of the helium burning is significantly lower than the hydrogen burning one.

In the following list we summarize the main properties of the subsequent burning processes.

- Carbon burning, $T \gtrsim 5 \cdot 10^8$ K. The most important channels are the following

$$\begin{aligned} {}^{12}\text{C} + {}^{12}\text{C} \longrightarrow {}^{24}\text{MG}^* &\longrightarrow {}^{20}\text{Ne} + \alpha \qquad Q = 4.616\,\text{MeV} \\ &\longrightarrow {}^{23}\text{Na} + \text{p} \qquad Q = 2.238\,\text{MeV} \end{aligned}$$

- Neon burning, $T \simeq 1.5 \cdot 10^9$ K. The following chain takes place

$$\begin{aligned} {}^{20}\text{Ne} + \gamma &\longleftrightarrow {}^{16}\text{O} + \alpha \qquad Q = -4.73\,\text{MeV} \\ {}^{20}\text{Ne} + \alpha &\longrightarrow {}^{24}\text{Mg} + \gamma \qquad Q = 9.31\,\text{MeV} \end{aligned}$$

- Oxygen burning, $T \simeq 2.0 \cdot 10^9$ K. The most important channels are the following

$$\begin{aligned} {}^{16}\text{O} + {}^{16}\text{O} \longrightarrow {}^{32}\text{S}^* &\longrightarrow {}^{28}\text{Si} + \alpha \qquad Q = 9.59\,\text{MeV} \\ &\longrightarrow {}^{31}\text{P} + \text{p} \qquad Q = 7.68\,\text{MeV} \end{aligned}$$

- Silicon burning, $T \gtrsim 3 \cdot 10^9$ K. It occurs by means of a sequence of photodisgregations (γ, α) and $\alpha-$captures (α, γ). A part of the silicon is transformed into lighter nuclei and a part into heavier nuclei:

$$^{28}\text{Si}(\gamma,\alpha)\,{}^{24}\text{Mg}(\gamma,\alpha)\,{}^{20}\text{Ne}(\gamma,\alpha)\,{}^{16}\text{O}(\gamma,\alpha)\,{}^{12}\text{C}(\gamma,\alpha)\,2\alpha$$

$$^{28}\text{Si}(\alpha,\gamma)\,{}^{32}\text{S}(\alpha,\gamma)\,{}^{36}\text{Ar}(\alpha,\gamma)\,{}^{40}\text{Ca}(\alpha,\gamma)\,{}^{44}\text{Ti}(\alpha,\gamma)\,{}^{48}\text{Cr}(\alpha,\gamma)\,{}^{52}\text{Fe}(\alpha,\gamma)\,{}^{56}\text{Ni}$$

  The final composition is dominated by ^{56}Fe because it is the nucleus with the lowest binding energy.

1.6.2 Neutrino emission

So far we have reported the energy released by the various reactions, but those values are not comprehensive of the energy lost by neutrino emission. The reason is that neutrinos cross-section for interaction with the other particles in stellar interiors is so small that they can travel freely trough the whole star. Hence the energy carried by neutrinos contributes directly to the energy loss of the star and must be treated separately. Usually this energy loss is taken into account by subtracting its rate to ϵ_{nuc}. Other reactions that can produce neutrinos are:

$$\gamma + \text{e}^- \longrightarrow \text{e}^- + \nu + \overline{\nu} \qquad \text{e}^+ + \text{e}^- \longrightarrow \nu + \overline{\nu}$$

1.6.3 Composition changes

The rate of nuclear reactions and the element concentrations affect each other. It is therefore important to find an equation which is able to describe the composition variations. Let's start from the variation of the number density of nuclei i which react with nuclei j:

$$\left(\frac{\mathrm{d}n_i}{\mathrm{d}t}\right)_j = -(1+\delta_{ij})\,R_{ij}$$

However, the nucleus i can react with many different kind of nuclei j and other reactions between other nuclei k and l can produce $i-$nuclei. Hence, more precisely:

$$\frac{\mathrm{d}n_i}{\mathrm{d}t} = -\sum_j (1+\delta_{ij})\,R_{ij} + \sum_{k,l} R_{kl}$$

In practice the mass fractions $X_i = n_i A_i m_u/\rho$ are used instead of the number densities, so it is more useful the following form:

$$\frac{\mathrm{d}X_i}{\mathrm{d}t} = A_i \frac{m_u}{\rho}\left(-\sum_j (1+\delta_{ij})\,R_{ij} + \sum_{k,l} R_{kl}\right) \tag{22}$$

where A_i is the mass number of nuclei i. If convection takes place then other "mixing terms" have to be added to the right-hand term.

1.7 THE STARTING POINT FOR STELLAR MODELS

We have derived the fundamental equations for stellar structure and evolution:

$$\frac{\partial r}{\partial m} = \frac{1}{4\pi r^2 \rho} \tag{23}$$

$$\frac{\partial P}{\partial m} = -\frac{Gm}{4\pi r^4} - \frac{1}{4\pi r^2}\frac{\partial^2 r}{\partial t^2} \tag{24}$$

$$\frac{\partial l}{\partial m} = \epsilon_{\mathrm{nuc}} - \epsilon_\nu + \epsilon_{\mathrm{gr}} \tag{25}$$

$$\frac{\partial T}{\partial m} = -\frac{Gm}{4\pi r^4}\frac{T}{P}\cdot\begin{cases}\nabla_{\mathrm{rad}} = \dfrac{3\kappa l P}{16\pi a c G m T^4} & \text{if} \quad \nabla_{\mathrm{rad}} \le \nabla_{\mathrm{ad}} \\ \nabla & \text{if} \quad \nabla_{\mathrm{rad}} > \nabla_{\mathrm{ad}}\end{cases} \tag{26}$$

$$\frac{\partial X_i}{\partial t} = A_i \frac{m_u}{\rho}\left(-\sum_j (1+\delta_{ij})\,R_{ij} + \sum_{k,l} R_{kl}\right) + \text{mixing terms} \tag{27}$$

These equations are highly non-linear and time-dependent so they have to be solved numerically. In order to do that, we need also to set initial and boundary conditions. Firstly, we typically assume hydrostatic equilibrium so $\ddot{r} = 0$. We remember that ϵ_{gr} is linked to thermal structure changes (positive in contraction and negative in expansion phase): if the lifetime of a star is much longer than the thermal timescale then $\epsilon_{\mathrm{gr}} \simeq 0$. Changes in composition of the most abundant elements are nearly constant during a nuclear timescale. In conclusion, if the star is both in hydrostatic and thermal equilibrium (e.g. for zero-age main sequence stars) then only the initial mass fractions are required to construct the stellar model. On the other hand, if there is only hydrostatic equilibrium then $\epsilon_{\mathrm{gr}} = -T(\partial s/\partial t)$ remains and the function, $s(m, t_0)$, of the specific entropy profile must be added to initial conditions.

For what concerns the boundary conditions at the center ($m = 0$) we simply impose $r = l = 0$ because both density and energy generation rate must not to diverge. The surface boundary conditions are more complicated. It is useful to identify the surface with the photosphere, i.e. the surface where the optical depth

$\tau_{\rm ph} = \int_{R_{\rm ph}}^{\infty} \kappa\rho {\rm d}r$ is equal to 2/3. With an appropriate mean value of the opacity, we can write $\tau_{\rm ph} = \kappa_{\rm ph} \int_{R_{\rm ph}}^{\infty} \rho {\rm d}r$. Since it must be

$$\left(\frac{{\rm d}P}{{\rm d}r}\right)_{\rm ph} = -\frac{Gm(R_{\rm ph})}{R_{\rm ph}^2}\,\rho$$

we obtain the following boundary conditions

$$m(R_{\rm ph}) \simeq M \qquad P(R_{\rm ph}) \simeq \frac{GM}{R_{\rm ph}^2} \int_{R_{\rm ph}}^{\infty} \rho {\rm d}r = \frac{2}{3}\,\frac{GM}{\kappa_{\rm ph} R_{\rm ph}^2}$$

$$T(R_{\rm ph}) \simeq T_{\rm eff} \qquad L = 4\pi R_{\rm ph}^2 \sigma T_{\rm eff}^4$$

1.7.1 Homology relations

Stellar structure equations can be solved numerically, but the solutions for different stars are often similar. We can take advantage of this similarity and use scaling relations called *homology relations* to obtain a rough estimate of some stellar parameters. That is, if we know the parameters of a star then homology relations allow us to obtain immediately information about the parameters of a second *homologous* star. Let's give the definition of homologous stars.

Definition (Homologous stellar models)**.** Let A and B be two stellar models (of masses M_A and M_B, radii R_A and R_B). Two mass shells are homologous if they have the same relative mass coordinate $x := m/M$. The two stellar models are homologous if the homologous mass shells are located at the same relative radii:

$$x = \frac{m_A}{M_A} = \frac{m_B}{M_B} \qquad \longrightarrow \qquad \frac{r_A(x)}{R_A} = \frac{r_B(x)}{R_B} \qquad \forall x$$

This implies that homologous stars must have the same relative mass distribution and therefore the same relative density distribution. With the definition and the stellar structure equations we can derive, for homologous models, homology relations for all variables. Homology relations are often applied to main-sequence stars.

1.8 STAR FORMATION AND PRE-MAIN SEQUENCE EVOLUTION

Since the solutions of the stellar structure equations are not analytic then we will describe them qualitatively, but firstly we spend some words to explain how stars arise from molecular clouds. The star formation process can be divided into six phases:

- Cloud collapse. At the beginning there is a molecular cloud with mass $\approx 10^5\,M_\odot$, diameter $\approx 10\,{\rm pc}$, temperature $10 \div 100\,{\rm K}$ and number density $n = 10 \div 300\,{\rm molecules/cm^3}$. The cloud is in hydrostatic equilibrium with the surroundings, but a perturbation can break the equilibrium and induce the cloud collapse. The perturbation may be caused, for example, by a nearby supernova explosion. The hydrostatic equilibrium is stable against pressure perturbation if the mass of the cloud is lower than the *Jeans mass*:

$$M_J \approx 4 \cdot 10^4\,M_\odot \left(\frac{T}{100\,{\rm K}}\right)^{3/2} \left(\frac{n}{{\rm cm^{-3}}}\right)^{-1/2}$$

  In molecular clouds $M_J = 10^3 \div 10^4\,M_\odot$ and there are fragments that exceeds this mass values undergoing free-fall collapse. However, the free-fall timescale is of the order of $10^6\,{\rm yr}$ because of the low density.

- Cloud fragmentation. During the collapse the density increases and consequently the Jeans mass decreases. This means that the dimensions of fragments in the cloud that can collapse decrease: the smallest fragments will be of less than $0.1\,M_\odot$.

- Formation of a protostellar core. The increasing density caused the gas to become opaque to infrared photons. For this reason, the temperature and the gas pressure also increase and the collapse slows down. At a certain point the hydrostatic equilibrium is achieved, the contraction of the cloud is quasi-static and we can say that a *protostar* is born.

- Accretion. The surrounding gas is attracted by the protostellar core and forms and accretion disk. The infalling gas increases its gravitational energy heating the core and radiating. The luminosity provided by the accretion disk is $L_{\rm acc} = GM\dot{M}/2R$ where all quantities refer to the protostellar core. This is also most of the protostar luminosity.

- Dissociation and ionization. At $T \approx 2000\,\mathrm{K}$ molecular hydrogen dissociates and temperature increases only a little with contraction. Therefore hydrostatic equilibrium is broken and a phase of dynamical collapse follows. The collapse stops and the equilibrium is restored when the molecular hydrogen has been completely dissociated. Then temperature rises again until, at $10^4\,\mathrm{K}$, ionization of hydrogen and then of helium lead to further phases of dynamical collapse.

- Pre-main sequence phase (PMS). When the accretion slows down or stops we can talk about a *pre-main-sequence star* whose luminosity is due to gravitational contraction. In absence of accretion the surface cools and a temperature gradient settles in the star.

Pre-main-sequence stars have low temperatures and so high opacity. Therefore radiative transport is inefficient and the whole star is convective. There are also other kinds of fully convective stars, but all evolve along an almost vertical line in the H-R diagram. This line is called *Hayashi line* and the stars in hydrostatic equilibrium, but not fully convective, are located to the left. The region to the right, instead, is forbidden for stars in hydrostatic equilibrium. The position of the Hayashi line in the H-R diagram depends on mass: increasing mass it moves to higher temperatures. It turns out that the shape of the Hayashi line is determined by the opacity in the photosphere. The photospheres of fully convective stars are very cool so the main source of opacity is the negative hydrogen ion H^-. This kind of opacity increases strongly with temperature and consequently the luminosity varies a lot with even little changes in temperature. This fact explains the steepness of the Hayashi line. During its evolution a pre-main-sequence star moves along the correspondent Hayashi line until the opacity remains high. The temperature slowly rises, but at a certain moment the central parts become radiative ($\nabla_{\rm rad} < \nabla_{\rm ad}$): a radiative core forms. Then the star moves to the left of the Hayashi line in the H-R diagram and the radiative core grows. Stars with higher mass depart from the Hayashi line at higher luminosities. When the temperature is high enough the contraction stops, hydrogen burning starts and the star settles on the *zero-age main sequence* (ZAMS). This happens only for masses greater than $0.08\,M_\odot$. However, several reactions can take place before the temperature required for hydrogen burning is reached, e.g. the $^{12}\mathrm{C}(\mathrm{p},\gamma)\,^{13}\mathrm{N}$ reaction is the origin of the particular shape of the evolutionary track just before the ZAMS. The Kelvin-Helmholtz timescale gives and estimate of the pre-main sequence lifetime: this is shorter for more massive stars. In Figure 3 are shown some evolutionary tracks of pre-main-sequence stars with masses ranging from 0.3 to $2.5\,M_\odot$.

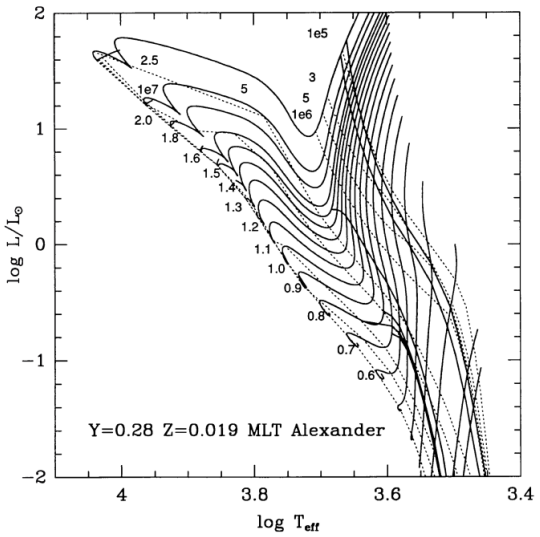

Figure 3.: *Pre-main sequence evolutionary tracks for $M = 0.3 \div 2.5\, M_\odot$ and the indicated initial composition from D'Antona & Mazzitelli (1994). The MLT with $\alpha_{ov} = 1.2$ is used. The dotted lines are called isochrones and connect points of different tracks corresponding to the same age. The first phase along the Hayashi line and the following evolution to the left are clearly visible. There are also solid lines which intersect the tracks. Two lines of those, near the $t = 10^5$ yr isochrone, indicate the region in the H-R diagram where the deuterium burning occurs. The other two lines indicate the region where lithium burning occurs. These burning processes are further examples of nuclear reactions that occur in the PMS phase.*

1.9 THE MAIN-SEQUENCE PHASE

1.9.1 The zero-age main sequence

ZAMS stars are in both hydrostatic and thermal equilibrium. Their composition is nearly homogeneous and so homology relations work rather well. The most common homology relations are the mass-luminosity and the mass-radius relations:

$$L \propto \mu^4 M^3 \qquad R \propto \mu^{\frac{\nu-4}{\nu+3}} M^{\frac{\nu-1}{\nu+3}}$$

with a value of ν appropriate to the hydrogen burning process that is taking place in the star ($\nu \simeq 4$ for pp-chain and $\nu \simeq 16$ for CNO cycle). In order to obtain a detailed ZAMS model we have to solve stellar structure equations numerically imposing hydrostatic and thermal equilibrium. Some examples of ZAMS models are shown in Figure 4. The central conditions of these models are also interesting (see Figure 4) because determine the main hydrogen burning process. See the caption of Figure 4 for further information and comments.

For what concerns the convective regions we can divide ZAMS stars into three groups (consequence of the Schwarzshild criterion for convection):

- fully convective: for $M < 0.35\, M_\odot$. The pp-chain dominates the energy production, but the low temperature maintains high the opacity in the whole star inducing convection.
- radiative core and convective envelope: for $0.35\, M_\odot < M < 1.2\, M_\odot$. The pp-chain dominates the energy production which takes place in a large area. The temperature in the envelope is still low and so the high opacity induces convection in the envelope.
- convective core and radiative envelope: for $M > 1.2\, M_\odot$. The CNO cycle dominates the energy production which is peaked near the center and induces convection in the core.

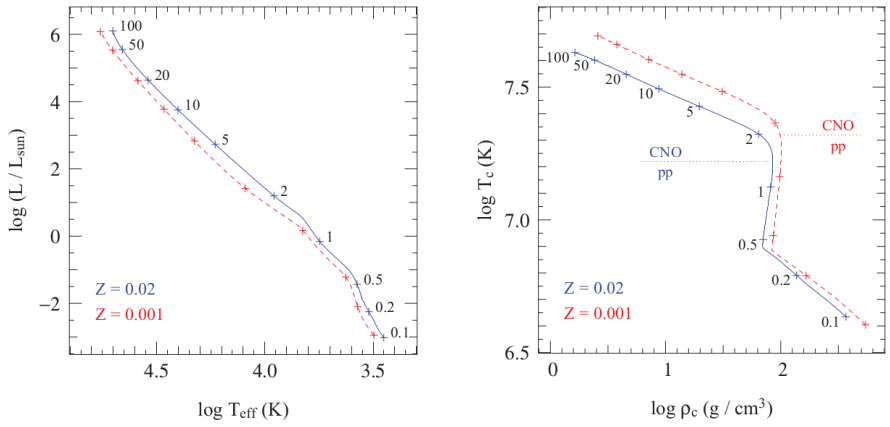

Figure 4.: *Left panel: ZAMS models in the H-R diagram. The masses go from* 0.1 *to* 100 $M_\odot$. *We can see that, for the same mass, metal-rich models are located at lower temperatures than metal-poor models. Right panel: the central temperature and density of the same models. The approximate boundaries of the regions where CNO cycle and pp-chain dominate are shown. The changes in central temperature and slope due to the different burning processes are clearly visible. Courtesy of O. Polls (Lecture Notes).*

1.9.2 The central hydrogen burning phase

During this phase, stars remain in hydrostatic equilibrium and the evolution is driven by the changes in composition. In fact the fusion of hydrogen into helium leads to an increase of μ and so also of the luminosity (remember the mass-luminosity relation). Since the hydrogen abundance decreases, the central temperature must increase to keep constant the energy production rate. However, approximately it is $\epsilon_{pp} \propto \rho T^4$ and $\epsilon_{CNO} \propto \rho T^{18}$ hence the central temperature does not increase so much. This means that $T_c/\mu \propto P_c/\rho_c$ decreases, i.e. P_c must decrease or ρ_c must increase. What happens depends again on the burning process:

- stars where the CNO cycle dominates: $\epsilon_{CNO} \propto \rho T^{18}$ so the density can't increase so much and P_c must decrease. Consequently, the pressure that the outer layers exert to the core must decrease too. If the pressure in the envelope decreases then it must expand to preserve hydrostatic equilibrium. This explains the decrease in T_{eff}. Moreover, we remember that the cores of these stars are convective and so they have a larger fuel supply and a larger main-sequence lifetime than the other main-sequence stars. When hydrogen is exhausted (red point of the evolutionary track, see Figure 5) the energy production stops. The star cools and contracts until, in a shell surrounding the helium core, the temperature reaches again the threshold for the CNO cycle and the *hydrogen-shell burning phase* begins. This is the blue final point of the evolutionary tracks.

- stars where the pp-chain dominates: $\epsilon_{pp} \propto \rho T^4$ so the central density increases more than in the previous case and the envelope needs to expand less. This explains why low-mass stars do not evolve a lot toward lower temperatures. The energy production in this case is not peaked near the center and hydrogen is burned more homogeneously in the core. This behaviour prevents the sudden contraction before the hydrogen-shell burning phase. For this reason the evolutionary tracks of low-mass stars have not an hook-like shape.

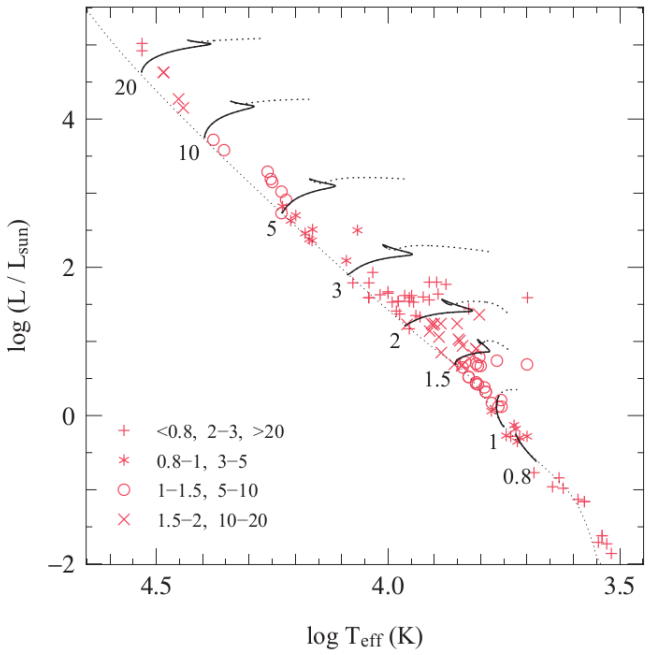

Figure 5.: *Evolutionary tracks in the H-R diagram during central hydrogen burning of stars with masses in the range* $0.8 \div 20\,M_\odot$ *and composition* $X = 0.7$, $Z = 0.02$. *Symbols show the locations of stars in binary systems with accurately measured M, L and* T_{eff}. *Different symbols correspond to different mass range as indicated. Courtesy of O. Polls (Lecture Notes).*

1.9.3 The main-sequence lifetime

Let's try to derive a relation between the main-sequence lifetime and the star mass. We have:

$$\frac{\mathrm{d}X}{\mathrm{d}t} = -\frac{\epsilon_{\mathrm{nuc}}}{q_H}$$

where $q_H = Q_H/4m_u$. We integrate now over all mass shells and we obtain:

$$\frac{\mathrm{d}M_H}{\mathrm{d}t} = -\frac{L}{q_H}$$

where M_H is the total mass of hydrogen. Finally, we integrate over the main-sequence lifetime:

$$\Delta M_H = \frac{1}{q_H}\int_0^{\tau_{\mathrm{MS}}} L\,\mathrm{d}t = \frac{\langle L\rangle \tau_{\mathrm{MS}}}{q_H}$$

so that

$$\tau_{\mathrm{MS}} = \frac{\Delta M_H q_H}{\langle L\rangle}$$

The total mass of hydrogen burned is roughly proportional to the total mass: $\tau_{\mathrm{MS}} \propto M$. Since the luminosity does not change a lot during the main-sequence phase, we can use the mass-luminosity relation for ZAMS models: $\langle L\rangle \propto M^\eta$. Therefore $\tau_{\mathrm{MS}} \propto M^{1-\eta}$ approximately. The value of η depends on mass, but in all cases τ_{MS} decreases strongly with mass. The effect of this high dependence is evident in the color-magnitude diagrams of star clusters: the main-sequence is interrupted at the *turn-off point*. The position and the corresponding mass of the turn-off point are important information in order to estimate the age of the star cluster. These aspects will be more clear by looking at the isochrone fitting method in Chapter 3.

1.10 THE HYDROGEN-SHELL BURNING PHASE

In order to describe the post-main sequence evolution it is useful to introduce the following classification of stars by mass:

- low-mass stars: $0.8\,M_\odot < M \lesssim M_{\rm HeF}$, $M_{\rm HeF} := 2\,M_\odot$. These stars burn hydrogen in a shell and develop a degenerate helium core. In the H-R diagram they trace a path called *red giant branch* (RGB). When the core reach the necessary mass, at the top of the RGB, helium ignites suddenly: this event is called *helium flash*.

- intermediate-mass stars: $M_{\rm HeF} \lesssim M \lesssim M_{\rm up}$, $M_{\rm up} := 8\,M_\odot$. During the hydrogen-shell burning the helium core remains non-degenerate and the ignition of helium is stable (there is not an helium flash). A degenerate carbon-oxygen core develops during the helium burning phase. At the end, both low-mass and intermediate-mass stars lose their envelopes and form a CO white dwarf.

- massive stars: $M \gtrsim M_{\rm up}$. They firstly ignite helium in a non-degenerate core and then they also ignite carbon in a non-degenerate core. Except for masses near to $M_{\rm up}$, these stars also ignite elements heavier than carbon.

1.10.1 The Schönberg-Chandrasekhar limit

After the main sequence there is not energy production in the core. Therefore either the energy flow in the core is zero or there is not thermal equilibrium. Null energy flow means isothermal core, but this condition can be satisfied only if the core mass is a small fraction of the total mass. The limit value for the ratio $M_{\rm core}/M$ is about 0.1 and it is called *Schönberg-Chandrasekhar limit*. If overshooting is taken into account then it turns out that intermediate and massive stars can't have a core in thermal equilibrium during the entire hydrogen-shell burning phase. Their cores contract and build up a temperature gradient in order to maintain hydrostatic equilibrium. Low-mass stars, instead, keep their cores isothermal in another way. Their cores are degenerate so the energy transport by electron conduction is very efficient and can keep the core isothermal.

1.10.2 The mirror principle

Let us consider a star with an active burning shell. We said that nuclear burning is very sensitive to temperature changes so the shell temperature must remain almost constant to preserve thermal equilibrium. Moreover, for the same reason, the shell can't contract or its temperature would increase. Consequently also the shell radius is nearly constant. Hence, if the core contracts then the shell density must decrease together with the pressure. If the pressure in the shell decreases then the pressure of the overlying layers must decrease too. These considerations can be summarized in the *mirror principle*:

> In a star with an active burning shell, the latter acts as a mirror between the core and the envelope. In other words, when the core contracts then the envelope expands and, on the contrary, when the core expands then the envelope contracts.

1.10.3 The hydrogen-shell burning phase of intermediate-mass and massive stars

We will follow the evolution of a $5\,M_\odot$ star with composition $X = 0.7$, $Z = 0.02$ as representative case of this mass range. In Figure 6 its evolutionary track in the H-R diagram is shown.

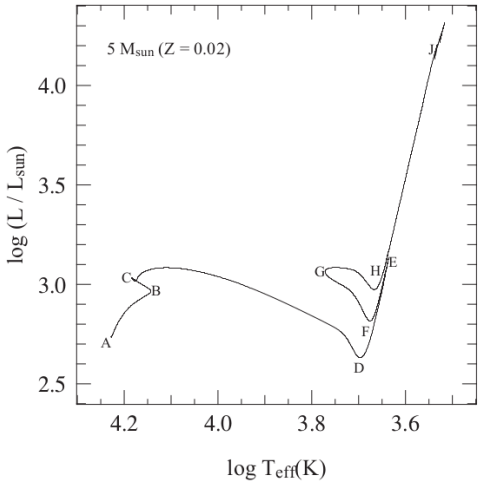

(a)

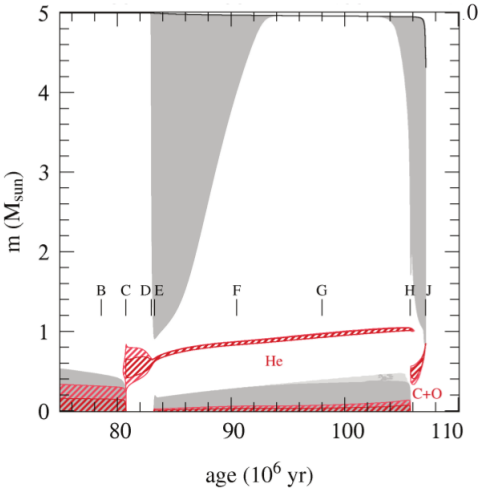

(b)

Figure 6.: *Panel 6a: evolutionary track of a* $5\,M_\odot$ *star with composition* $X = 0.7$, $Z = 0.02$ *starting from the ZAMS and ending at the top of the asymptotic giant branch (overshooting has not been taken into account). Panel 6b: the Kippenhan diagram of the same evolutionary track. This diagram shows the changes in the internal structure of the star with time. The gray areas are convective, light-gray areas are semi-convective (Ledoux criterion holds, but Schwarzshild criterion not). In red regions there is nuclear burning (dark red for* $\epsilon_{nuc} > 10L/M$ *and light red for* $\epsilon_{nuc} > 2L/M$*). Courtesy of O. Polls (Lecture Notes).*

Let's describe what happens in the various portions.

- A - C. This is the central hydrogen burning phase we have already discussed. At point C the hydrogen in the core is exhausted and core convection stops.
- C - D. The hydrogen burning shell is active. During this phase the core mass is below the Schönberg-Chandrasekhar limit so the core remains in thermal equilibrium and the star evolves slowly. There are not high differences in temperature and pressure between the core and the envelope so that the hydrogen shell is rather thick. The helium core grows until it reaches the Schönberg-Chandrasekhar limit when the contraction accelerates the evolution. Therefore near point D the envelope expands for the mirror principle and the temperature and density gradients between core and envelope increase and the hydrogen shell becomes thinner. The expanding envelope absorbs energy implying a decrease in luminosity. The evolution along the C-D portion is quick compared to the main sequence lifetimes: it lasts a few million years. As a consequence of this fact, it is very difficult to observe stars in this evolutionary state and this is the origin of the so-called *Hertzsprung gap* in the H-R diagram.
- D - E. Near point D the expanding envelope decreases its temperature, the opacity rises and it becomes convective. During the D-E portion the star is a red giant with a deep convective envelope. This explains why it is located so close to the Hayashi line. We remember that the temperature does not vary a lot along the Hayashi line and, in the meanwhile, the core contracts and the envelope expands so the luminosity increases. At point E the envelope is deep enough to reach the regions where hydrogen was burned during the phase A-C so that the nuclear reactions products are brought to the surface: this event is called *(first) dredge-up*. As we said before the helium core remains non-degenerate during the entire hydrogen-shell burning phase. At the end, at point E, these stars have developed a core with a mass greater than $0.3\,M_\odot$ (detailed calculations show that this is the lower limit to helium ignition) and the central temperature is 10^8 K, high enough to start burning helium. The helium burning stops the core contraction and so also the envelope expansion.

1.10.4 The hydrogen-shell burning phase of low-mass stars

We will follow the evolution of a $1\,M_\odot$ star with composition $X = 0.7$, $Z = 0.02$ as representative case of this mass range. In Figure 7 its evolutionary track in the H-R diagram is shown.

Let's describe what happens in the various portions.

- A - B. This is the central hydrogen burning phase we have already discussed.
- B - C. When the central hydrogen is exhausted the mass core is below the Schönberg-Chandrasekhar limit so the core remains in thermal equilibrium. Moreover, the helium core becomes degenerate before the SC-limit is reached so the thermal equilibrium is never broken thanks to electron conduction. Consequently the evolution in the B-C phase is much more slow (≈ 2 Gyr for our star) than that of more massive stars and there is not the Hertzsprung gap. Again hydrogen is burned in a thick shell, the core contracts and the envelope expands. At point C the helium core has become degenerate and the envelope has become convective: the star is close to the Hayashi line. The stars which are in this evolutionary stage form the *subgiant branch*, in the H-R diagram of old star clusters.
- C - F. This is the red giant branch. While hydrogen is burned in the shell, the helium core grows always in thermal equilibrium. The star evolves along the Hayashi line until, at point F, when $T_{\rm core} = 10^8$ K the helium flash occurs. Helium is ignited with an unstable process due to strong degeneracy.

- D. This is the point of deepest extension of the convective envelope: the first dredge-up occurs at this moment.
- E. After the dredge-up the hydrogen-burning shell moves to higher relative mass coordinate and finds a higher hydrogen abundance left by the convective envelope. The energy production therefore decreases somewhat together with the luminosity before continuing the evolution along the Hayashi line. This phenomenon leads to a larger number of stars in this region of the H-R diagram. We call this region *RGB-bump*.

Another important mechanism which affects the evolution during the RGB is mass loss by stellar wind. The envelope in this phase is indeed weakly bound. Our $1\,M_\odot$ star loses about $0.3\,M_\odot$ during this phase.

1.11 THE HELIUM BURNING PHASE

1.11.1 Helium burning in intermediate-mass stars

We proceed with the description of the evolutionary track of Figure 6 starting from the tip of the RGB (point E). During the entire helium burning phase hydrogen is burned in a shell. In the case of our $5\,M_\odot$ star, the helium burning phase lasts for about 22 Myr.

- E - F. At point E the core is non-degenerate and so helium is ignited in a stable way. Helium burning reactions are highly temperature-dependent so the energy production is peaked near the center leading to a convective core. Initially the 3α reaction dominates and then the reaction $^{12}\mathrm{C} + \alpha \longrightarrow {}^{16}\mathrm{O}$ also becomes important. In the E-F portion the star is almost convective, the envelope contracts and the radius decreases with luminosity. In the meanwhile the envelope becomes radiative and, at point F, the star can move away from the Hayashi line.
- F - H. The point F is the start of the *blue loop* (F-H). In the phase F-G the envelope continues contracting while temperature increases. Near point G the helium abundance has become rather low (≈ 0.3) and the envelope starts expanding until point H where the helium abundance is less than ten percent and the star has become again almost fully convective.

For what concerns the effect of overshooting, this makes larger the core mass at the end of the main sequence an so also the luminosity contribution of helium burning. This means that the helium burning phase becomes shorter in presence of overshooting. Also the temperature extension of the blue loops depend on overshooting providing useful observational tests.

1.11.2 Helium burning in low-mass stars

We refer to Figure 7. The important difference of low-mass stars and the other categories is that helium is ignited in a degenerate core leading to the helium flash. Moreover, all low-mass stars ignite helium at about the same core mass of $\approx 0.45\,M_\odot$. This means that the luminosity of helium burning low-mass stars is nearly independent of mass.

THE HELIUM FLASH The helium flash occurs at point F when $T_{\mathrm{core}} \approx 10^8\,\mathrm{K}$ and $\rho_{\mathrm{core}} \approx 10^6\,\mathrm{g/cm^3}$. The 3α reactions cause a temperature increase rather than a decrease. This happens because the degenerate pressure is almost independent of T and so it can't increase so much when the helium burning starts (no expansion and no work done). All the energy produced goes into raising the internal energy. When, like in this case, an increase in temperature causes a further increase in temperature we talk about *thermal runaway*. More precisely, the internal energy of

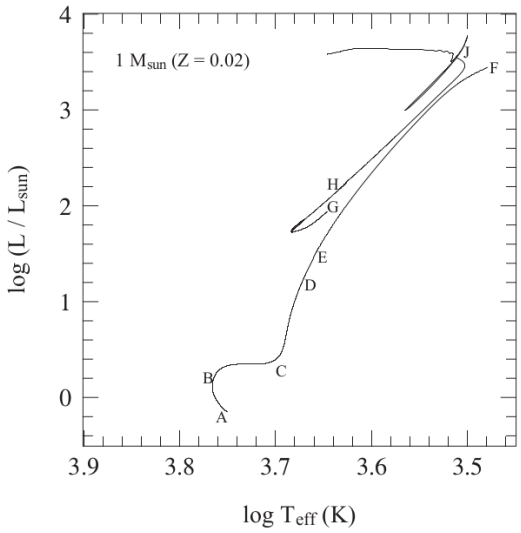

(a)

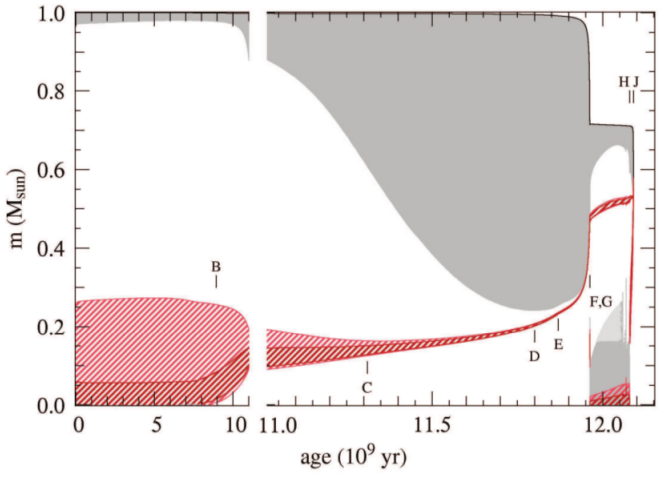

(b)

Figure 7.: *Panel 7a: evolutionary track of a* $1\,M_\odot$ *star with composition* $X = 0.7$, $Z = 0.02$ *starting from the ZAMS and ending at the top of the asymptotic giant branch (overshooting has not been taken into account). Panel 7b: the Kippenhahn diagram of the same evolutionary track. This diagram shows the changes in the internal structure of the star with time. The gray areas are convective, light-gray areas are semi-convective (Ledoux criterion holds, but Schwarzshild criterion not). In red regions there is nuclear burning (dark red for* $\epsilon_{nuc} > 5L/M$ *and light red for* $\epsilon_{nuc} > L/M$*). Courtesy of O. Polls (Lecture Notes).*

degenerate electrons does not increase (it depends on ρ): it is the internal energy of the non-degenerate ions that increases. The energy production during the helium flash is extremely high ($l \approx 10^{10}\, L_\odot$), but it lasts only for a few seconds. As a result, the star "jumps" from point F to point G in the H-R diagram. The degeneracy, eventually after some further smaller flashes, is broken and the core then expands, the envelope contracts for the mirror principle, the energy generation rate decreases. Thermal equilibrium is reached when the energy generation rate balances the energy loss rate. The following phase of helium burning (G-H) is stable and lasts for about 120 Myr.

THE HORIZONTAL BRANCH The position of the star in the H-R diagram during the phase G-H does not vary so much and, as we have just said, all low-mass stars have more or less the same luminosity in this phase. Also the temperature is similar so we see a star concentration in this region of the colour-magnitude diagram of old stellar populations. This star concentration is called *red clump*. However, the effective temperature after the helium flash in some cases depends rather strongly on the envelope mass (lower masses correspond to higher temperatures). Hence an *horizontal branch* (HB) can form in the colour-magnitude diagrams.

PULSATIONAL INSTABILITY Helium-burning stars are often radial pulsators. This is the case of Cepheids and RR-Lyrae stars. We defer the detailed description of these variable stars to Chapter 2.

1.11.3 Helium burning in massive stars

The evolution of massive stars during the helium burning phase differs from that of the low- and intermediate-mass stars in two main aspects:

- For stars with $M \gtrsim 15\, M_\odot$ the mass loss by stellar winds is very important. Stellar winds lead to the erosion of the outer layers and can be driven by radiation (i.e. by radiation pressure at the frequencies of absorption lines or on dust particles) or by stellar pulsations.

- When the helium burning phase ends, low- and intermediate-mass stars can't ignite carbon because they have developed a degenerate carbon-oxygen core and the temperature is not high enough. The cores of massive stars, instead, reach a temperature greater than $5 \cdot 10^8$ K and undergo non-degenerate carbon ignition.

Evolutionary tracks of massive stars in the range $12 \div 120\, M_\odot$ are shown in Figure 8. During the evolution, massive stars do not develop degenerate cores and they are nearly totally in radiative equilibrium. This explains why the evolution proceeds at almost constant luminosity.

RED SUPERGIANTS They are cool and luminous stars (see Figure 8) with a high mass loss by stellar wind up to $10^{-4}\, M_\odot/\text{yr}$. Massive stars with $M \lesssim 40\, M_\odot$ in the helium burning phase spend a lot of time as red supergiants. On the other hand, stars with $M \gtrsim 40\, M_\odot$ show sporadic outbursts with mass loss $\gtrsim 10^{-3}\, M_\odot$ so that they never become supergiants and they are destined to become Wolf-Rayet stars. Stars which show these outbursts are called *luminous blue variables*.

WOLF–RAYET STARS They are stars with both high temperature and luminosity (see Figure 8). They show strong emission lines which indicate high CNO abundances. For this reason they are supposed to be the exposed cores of massive stars in the helium burning phase.

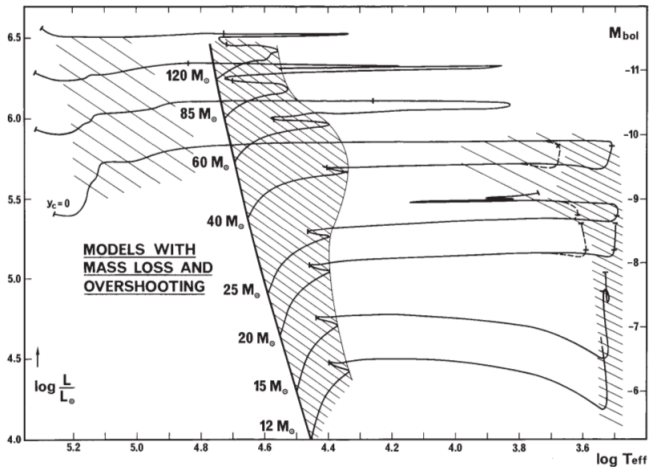

Figure 8.: *Evolutionary tracks of massive stars in the range* $12 \div 120\, M_{\odot}$. *Mass loss and overshooting* ($\alpha_{ov} = 0.25$) *are taken into account. The marked regions indicate long-lived evolution phases: the main sequence and the helium burning phase as red supergiants* ($\log T_{eff} < 4.0$) *or as Wolf-Rayet star* ($\log T_{eff} > 4.8$). *We can see the difference between the evolution of stars with mass greater and lower than* $40\, M_{\odot}$. *Figure taken from Maeder & Meynet (1987).*

1.12 LATE EVOLUTION

1.12.1 Late evolution of low- and intermediate-mass stars

At the end of the central helium burning phase, low- and intermediate-mass stars are not hot enough to ignite carbon. The stars are now located at point H in the H-R diagrams of Figures 6 and 7 and in the Kippenhahn diagram of Figure 9. Point H is the starting point of the *asymptotic giant branch* (AGB). The AGB phase can be divided into three periods:

- Early AGB phase. The carbon-oxygen core contracts and the helium burning process continues in a shell so that above layers expand. This expansion leads to a decrease in temperature of the shallower hydrogen-burning shell which can turn off after some time in stars with $M \gtrsim 4\, M_{\odot}$. The core grows and becomes degenerate.

- Second dredge-up. The envelope expands because of the mirror principle and, at point K of Figure 9 and for sufficiently high mass, it reaches the mass coordinate at which there was the hydrogen-burning shell. A dredge-up then occurs and the products of hydrogen burning (helium by the pp-chain and nitrogen by the CNO-cycle) are brought to the surface.

- The thermally pulsing AGB phase (TP-AGB). As the core grows the helium-burning shell approaches the region of the hydrogen-burning shell so that the helium-burning rate decreases and the above layers contract. This contraction causes a new ignition of the hydrogen (after point J in Figure 9). The two burning shells coexist for some time. However the two shells can't produce energy at the same rate and soon the helium-burning shell becomes thermally unstable. The latter shows periodic *thermal pulses* which induce the nucleosynthesis of carbon, nitrogen and also elements heavier than iron. Moreover, a strong mass loss driven by pulsations and radiation occurs during the TP-AGB phase.

The lifetime of the TP-AGB phase is of few million years depending on the mass loss rate. The mass loss prevents AGB stars to develop a carbon-oxygen core

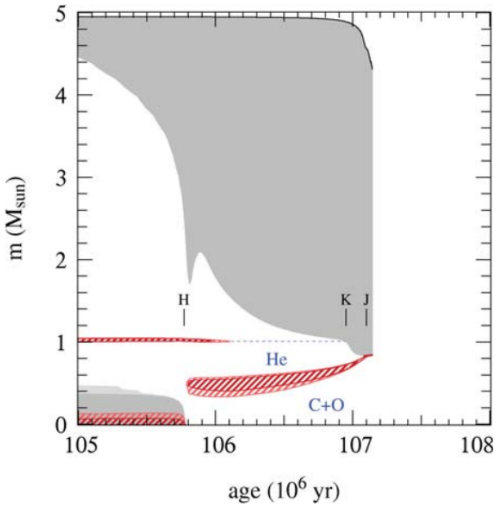

Figure 9.: *Kippenhahn diagram of the late evolution of a* $5\,M_\odot$ *star. We can see the point H where the hydrogen-burning shell extinguish, the point K of the second dredge-up and the point J where hydrogen is reignited. Courtesy of O. Polls (Lecture Notes).*

with mass greater than $M_{\text{Ch}} := 1.46\,M_\odot$, the *Chandrasekhar limit*. In fact the entire hydrogen-rich envelope is removed and carbon will be never ignited.

POST-AGB EVOLUTION After the AGB the H-rich envelope has been almost completely lost. The star evolves toward higher temperatures at almost constant luminosity. The hydrogen-burning shell has not been extinguished yet. At $T_{\text{eff}} > 3 \cdot 10^4\,\text{K}$ a strong UV flux destroys dust, molecules and ionizes the gas in the surrounding interstellar medium. The ionized gas (H II in particular) emits radiation and we talk about a *planetary nebula*. At $T_{\text{eff}} \approx 10^5\,\text{K}$ the hydrogen-burning shell extinguish definitively and the luminosity starts decreasing. The star finishes its evolution cooling as a *white dwarf* of degenerate carbon and oxygen. Nuclear fusion does not take place so white dwarfs radiates their thermal energy. White dwarfs' mass is usually around $0.6\,M_\odot$.

1.12.2 Late evolution of massive stars

Massive stars develop during the helium-burning phase a non-degenerate carbon-oxygen core with a mass high enough ($> 1.06\,M_\odot$) to ignite carbon. Then the evolution proceeds quickly through several nuclear burning phases and core contractions. A lot of heavy elements are produced up to iron and nickel (see Section 1.6). Neutrino energy losses are now important for the cooling process of the core and speed up its evolution. Only a few thousand years pass from the carbon ignition until the formation of an iron core. In the meanwhile the envelope is almost decoupled from the core because of the rapid evolution, so the star's position in the H-R diagram does not change a lot. At the end of this sequence of burning cycles the core has an iron nucleus surrounded by many shells made of increasingly lighter elements. No more energy can be produced by nuclear fusion and the inert core then collapses and finally explodes.

SUPERNOVAE The core collapse is arrested by nuclear forces when neutrons become degenerate. The collapse is not only stopped but also the material bounces back like a spring. The shock wave which originates in that way throws out the envelope. This event is called *supernova core-collapse*. If the initial mass of the star is below $25\,M_\odot$ then the remnant of this explosion is a neutron star supported by the degenerate pressure of neutrons, otherwise a black hole forms.

2 ASTEROSEISMOLOGY

2.1 INTRODUCTION

Uncertainties in stellar physics have direct consequences in several fields of Astrophysics; ranging from investigations on exoplanet properties to stellar populations or galaxy evolution studies. For this reason, it is extremely important to achieve estimates of stellar parameters (mass, radius and age in particular) as precise as possible. Science has made great strides in this direction thanks to Asteroseismology, the study of stars by observations of their natural, resonant oscillations. The CNES CoRoT (**Co**nvection, **Ro**tation et **T**ransits planétaires, Baglin & Fridlund 2006) satellite and the NASA Kepler mission (Borucki et al. 2009) have been decisive in providing the necessary observations. Oscillation frequencies depend indeed on the internal structure of stars and this fact makes possible precision levels in stellar parameter estimations which have never been obtained before. In the next future, other missions like TESS (**T**ransiting **E**xoplanet **S**urvey **S**atellite, Ricker et al. 2009) and PLATO (**PLA**netary **T**ransits and **O**scillations of stars, Rauer et al. 2014) will extend the observations to a wider set of targets. These missions are of fundamental importance for the development of Ensemble Asteroseismology, the application of Asteroseismology to the study of stellar populations. This involves studying similarities and differences in groups of stars by using asteroseismic diagrams, in which two properties of the oscillation spectra are plotted against one another. In order to understand Asteroseismology we start developing the Stellar Pulsation Theory. Derivations in this Chapter mainly follow the treatments of Cox (1980), Aerts et al. (2010) and Catelan & Smith (2015).

2.2 STELLAR PULSATION THEORY

We introduce the adiabatic exponents Γ_1, Γ_2 and Γ_3 which can be used instead of the adiabatic derivatives $\gamma_{\rm ad}$ and $\nabla_{\rm ad}$. They are defined as follows:

$$\Gamma_1 = \left(\frac{\partial \ln P}{\partial \ln \rho}\right)_{\rm ad} = \gamma_{\rm ad} \qquad \frac{\Gamma_2}{\Gamma_2 - 1} = \left(\frac{\partial \ln P}{\partial \ln T}\right)_{\rm ad} = \frac{1}{\nabla_{\rm ad}} \qquad \Gamma_3 = \left(\frac{\partial \ln T}{\partial \ln \rho}\right)_{\rm ad} + 1$$

and satisfy the relation

$$\frac{\Gamma_1}{\Gamma_3 - 1} = \frac{\Gamma_2}{\Gamma_2 - 1}$$

2.2.1 The period–mean density relation

Nowadays the existence of a connection between variability of single stars and stellar oscillations is clear. In this section we describe how a sound wave can travel through the stellar interior leading to mechanical oscillations. Let's start with the timescale of propagation. The sound speed is given by

$$c_s = \sqrt{\frac{\Gamma_1 P}{\rho}} \tag{28}$$

For an ideal gas we have $P/\rho = k_B T/\mu m_u$. Moreover, with $\mu \approx 0.6$ (solar-like abundances), $\Gamma_1 \approx \gamma = 5/3$ (monoatomic gas) and temperature 45 000 K (characteristic of the second ionization zones of helium), we obtain $c_s \approx 32.3\,\mathrm{km\,s^{-1}}$. Once we have

derived the radius of a star thanks to some measures, then we can approximate the propagation timescale as

$$\Pi \sim \frac{2R}{c_s}$$

With this rough formula we can only predict the order of magnitude of the period of some variable stars like Cepheids and RR Lyrae. A more precise estimate of the period is

$$\Pi = 2\int_0^R \mathrm{d}t(r) = 2\int_0^R \frac{\mathrm{d}r}{c_s(r)} = 2\int_0^R \frac{\mathrm{d}r}{\sqrt{\Gamma_1(r)P(r)/\rho(r)}} \tag{29}$$

but the functions at the denominator have in general a complex form. Hence we consider the homogeneous case ($\rho = \overline{\rho}$ and Γ_1 constants). In order to derive $P(r)$ in this case we integrate from r to R the hydrostatic equilibrium condition, Equation 6:

$$P(R) - P(r) = -\frac{2}{3}\pi\rho^2 G(r^2 - R^2)$$

but $P(R) \approx 0$, so

$$P(r) = -\frac{2}{3}\pi\rho^2 G(R^2 - r^2)$$

and Equation 29 becomes the *Ritter's period-mean density relation*:

$$\Pi\sqrt{\overline{\rho}} = \sqrt{\frac{3\pi}{2\Gamma_1 G}} := Q \tag{30}$$

where Q is called *pulsation constant*. The differences between observed and predicted periods are now certainly smaller than before. This agreement strongly suggests that stars for which this relation holds (Cepheids and RR Lyrae at least) radially pulsate. Let's investigate deeper radial pulsations.

2.2.2 Basic equations for the description of radial oscillations

The equations listed at the beginning of Section 1.7 have been derived assuming spherical symmetry so they are useful also for the radial pulsation theory. In this context, however, we can't do the same approximations we did in Section 1.7. The abundances can be kept constant, but the acceleration, $\ddot{r}$, is essential. Moreover, those equations describe a state of equilibrium if we neglect time derivatives. Pulsations, instead, are deviations from this state.

Firstly, we find another formulation for the energy conservation Equation 12. We want to relate $\mathrm{d}q/\mathrm{d}t = (\partial u/\partial t) + P(\partial\rho^{-1}/\partial t) = \epsilon_{\mathrm{gr}}$ with only two of the variables ρ, P and T. u is a state variable so it is possible to express u in terms of two of these three variables. For example, with $u = u(\rho, P)$, we find

$$\frac{\partial u}{\partial t} = \left(\frac{\partial u}{\partial P}\right)_\rho \frac{\partial P}{\partial t} + \left(\frac{\partial u}{\partial \rho}\right)_P \frac{\partial \rho}{\partial t}$$

so that

$$\begin{aligned}
\frac{\mathrm{d}q}{\mathrm{d}t} &= \left(\frac{\partial u}{\partial P}\right)_\rho \frac{\partial P}{\partial t} + \left(\frac{\partial u}{\partial \rho}\right)_P \frac{\partial \rho}{\partial t} - \frac{P}{\rho^2}\frac{\partial \rho}{\partial t} \\
&= P\left(\frac{\partial u}{\partial P}\right)_\rho \frac{\partial \ln P}{\partial t} + \rho\left(\frac{\partial u}{\partial \rho}\right)_P \frac{\partial \ln \rho}{\partial t} - \frac{P}{\rho}\frac{\partial \ln \rho}{\partial t} \\
&= P\left(\frac{\partial u}{\partial P}\right)_\rho \left[\frac{\partial \ln P}{\partial t} - \frac{P/\rho - \rho\,(\partial u/\partial \rho)_P}{P\,(\partial u/\partial P)_\rho}\frac{\partial \ln \rho}{\partial t}\right]
\end{aligned} \tag{31}$$

Similarly, in the case $u = u(P, T)$, it results

$$\frac{\mathrm{d}q}{\mathrm{d}t} = T\left(\frac{\partial u}{\partial P}\right)_\rho \left[\frac{\partial \ln T}{\partial t} - \frac{P/\rho - \rho\,(\partial u/\partial \rho)_T}{T\,(\partial u/\partial T)_\rho}\frac{\partial \ln \rho}{\partial t}\right] \tag{32}$$

and, in the adiabatic case,

$$\frac{\partial \ln T}{\partial t} = \left[\frac{P/\rho - \rho\,(\partial u/\partial \rho)_T}{T\,(\partial u/\partial T)_\rho}\right]\frac{\partial \ln \rho}{\partial t} \tag{33}$$

$$\Gamma_3 - 1 = \left(\frac{\partial \ln T}{\partial \ln \rho}\right)_{\mathrm{ad}} = \frac{P/\rho - \rho\,(\partial u/\partial \rho)_T}{T\,(\partial u/\partial T)_\rho} \tag{34}$$

Since $(\partial u/\partial T)_\rho = c_V$, we obtain

$$\frac{\mathrm{d}q}{\mathrm{d}t} = c_V T\left[\frac{\partial \ln T}{\partial t} - (\Gamma_3 - 1)\frac{\partial \ln \rho}{\partial t}\right]$$

At this point, Equation 25 can be rewritten as

$$\frac{\partial \ln T}{\partial t} = (\Gamma_3 - 1)\frac{\partial \ln \rho}{\partial t} + \frac{1}{c_V T}\left(\epsilon_{\mathrm{eff}} - \frac{\partial l}{\partial m}\right) \tag{35}$$

where $\epsilon_{\mathrm{eff}} := \epsilon_{\mathrm{nuc}} - \epsilon_\nu$ is the *effective generation rate*. Similarly, starting from Equation 31, we obtain

$$\frac{\partial \ln P}{\partial t} = \Gamma_1 \frac{\partial \ln \rho}{\partial t} + \frac{\rho}{P}(\Gamma_3 - 1)\left(\epsilon_{\mathrm{eff}} - \frac{\partial l}{\partial m}\right) \tag{36}$$

2.2.3 Perturbation Theory and Linearization

THE EULERIAN AND LAGRANGIAN DESCRIPTIONS As we have just said, the solutions of the stellar structure equations are nearly time-independent, so we can neglect time-derivatives and obtain static solutions. We will consider these solutions as reference and oscillations as perturbations from the equilibrium state. Let us formalize the concept of perturbation in the Eulerian and Lagrangian descriptions.

In the Eulerian description the reference frame is fixed, independent of the motion. All physical quantities depend on the position $\mathbf{r}$ in the reference frame and on time. Hence, for every position $\mathbf{r}$ we have $f = f(\mathbf{r}, t)$ for every physical quantity f like density, pressure, velocity etc.. As a consequence, time derivatives are partial derivatives. Let f be a physical quantity at a given coordinate $\mathbf{r}$ of the perturbed model and let f_0 be its value at the same coordinate, but in the unperturbed model. Then, we define the *Eulerian perturbation* f' as

$$f'(\mathbf{r}, t) := f(\mathbf{r}, t) - f_0(\mathbf{r}, t) \tag{37}$$

In the Lagrangian description the reference frame is integral with a mass element, so follows it during the motion. In this case the physical quantities are of the form $f_{\mathrm{el}}(t)$, where the subscript indicates that they refer to a specific mass element. As a consequence, time derivatives are total derivatives. Let f_{el} be a physical quantity corresponding to a given mass element of the perturbed model and let $f_{\mathrm{el},0}$ be its value for the same element, but in the unperturbed model. Then, we define the *Lagrangian perturbation* δf as

$$\delta f(t) := f_{\mathrm{el}}(t) - f_{\mathrm{el},0}(t) \tag{38}$$

There is a relation between δf and f' that can be easily derived:

$$\begin{aligned}\delta f(t) &= f_{\rm el}(t) - f_{\rm el,0}(t) \\ &= f(\mathbf{r}_{\rm el},\, t) - f_0(\mathbf{r}_{\rm el,0},\, t) \qquad \text{with } \mathbf{r}_{\rm el} = \mathbf{r}_{\rm el,0} + \delta\mathbf{r} \\ &= f(\mathbf{r}_{\rm el},\, t) - f_0(\mathbf{r}_{\rm el},\, t) + f_0(\mathbf{r}_{\rm el},\, t) - f_0(\mathbf{r}_{\rm el,0},\, t)\end{aligned}$$

which, expanding to the first order, becomes

$$\delta f = f' + \nabla f_0 \cdot \delta\mathbf{r} \tag{39}$$

In our stellar models the independent variable is the radius in the Eulerian description and the mass coordinate in the Lagrangian description. Hereafter we will use the Lagrangian description unless clear indications, so we suppress the subscript 'el'. The quantity f can be the radial coordinate r. In this case the *relative radial displacement* $\xi := \delta r / r_0$ is often used. If all the perturbations are small (i.e. $\delta f / f_0 \ll 1$ and consequently $\delta f / f_0 \simeq \delta f / f$) then we can neglect all non-linear terms. This is the fundamental hypothesis of the linear theory.

Now, in order to be able to describe in detail the oscillations, we linearize the perturbed stellar structure equations. In practice we replace all quantities f present in the original equations with $f_0 + \delta f$ (the mass coordinate m is the independent variable in the Lagrangian description so it has not to be perturbed).

LINEARIZATION OF THE PERTURBED CONTINUITY EQUATION Equation 23 is usually called Continuity Equation and its perturbed form is the following:

$$\frac{\partial}{\partial m}[r_0(1+\xi)] = \frac{1}{4\pi r_0^2 (1+\xi)^2 \rho_0 (1 + \delta\rho/\rho_0)} \tag{40}$$

Thanks to the binomial expansion, $(1+x)^n \simeq 1 + nx$ for $x \ll 1$, and neglecting non-linear terms we can easily obtain

$$4\pi r_0^2 \rho_0 \left[(1+\xi)\frac{\partial r_0}{\partial m} + r_0 \frac{\partial \xi}{\partial m}\right] = (1 - 2\xi) - \frac{\delta\rho}{\rho_0}$$

but Equation 23 gives directly $\partial r_0 / \partial m$ and after the substitution it results

$$\frac{\delta\rho}{\rho_0} = -3\xi - 4\pi r_0^3 \rho_0 \frac{\partial \xi}{\partial m} \tag{41}$$

This is the Linearized Continuity Equation. The subscripts '0' can be suppressed since $1 \gg \delta f / f_0 \simeq \delta f / f$.

LINEARIZATION OF THE PERTURBED MOMENTUM EQUATION The Momentum Equation 24 can be linearized in a similar way if we remember that we have assumed $\partial f_0 / \partial t = 0$ so that unperturbed quantities depend only on m. The perturbed form is

$$\frac{\partial^2}{\partial t^2}[r_0(1+\xi)] = -4\pi r_0^2 (1+\xi)^2 \frac{\partial}{\partial m}\left[P_0\left(1 + \frac{\delta P}{P_0}\right)\right] - \frac{Gm}{r_0^2(1+\xi)^2} \tag{42}$$

After some manipulations we obtain the linearized equation:

$$r_0 \frac{\partial^2 \xi}{\partial t^2} = -4\pi r_0^2 \left(4\xi + \frac{\delta P}{P_0}\right)\frac{\mathrm{d}P_0}{\mathrm{d}m} - 4\pi r_0^2 P_0 \frac{\partial}{\partial m}\left(\frac{\delta P}{P_0}\right) \tag{43}$$

LINEARIZATION OF THE PERTURBED ENERGY CONSERVATION EQUATION The perturbed form of Equation 36 is

$$\frac{1}{P_0(1+\delta P/P_0)}\frac{\partial \delta P}{\partial t} = \frac{\Gamma_{1,0}(1+\delta\Gamma_1/\Gamma_{1,0})}{\rho_0(1+\delta\rho/\rho_0)}\frac{\partial \delta\rho}{\partial t} + \frac{\rho_0(1+\delta\rho/\rho_0)}{P_0(1+\delta P/P_0)}\cdot \\ \cdot\left[\Gamma_{3,0}\left(1+\frac{\delta\Gamma_3}{\Gamma_{3,0}}\right)-1\right]\left[\left(\epsilon_{\text{eff}}-\frac{\partial l}{\partial m}\right)_0+\delta\left(\epsilon_{\text{eff}}-\frac{\partial l}{\partial m}\right)\right] \quad (44)$$

In the unperturbed solution $\mathrm{d}q/\mathrm{d}t = \epsilon_{\text{gr}} = 0$ therefore $(\mathrm{d}l/\mathrm{d}m)_0 = \epsilon_{\text{eff},0}$. After some manipulations we arrive to the linearized equation:

$$\frac{\partial}{\partial t}\left(\frac{\delta P}{P_0}\right) = \Gamma_{1,0}\frac{\partial}{\partial t}\left(\frac{\delta\rho}{\rho_0}\right) + \frac{\rho_0}{P_0}(\Gamma_{3,0}-1)\,\delta\left(\epsilon_{\text{eff}}-\frac{\partial l}{\partial m}\right) \quad (45)$$

If we start from Equation 35 we will get

$$\frac{\partial}{\partial t}\left(\frac{\delta T}{T_0}\right) = (\Gamma_{3,0}-1)\frac{\partial}{\partial t}\left(\frac{\delta\rho}{\rho_0}\right) + (c_{V,0}T)^{-1}\,\delta\left(\epsilon_{\text{eff}}-\frac{\partial l}{\partial m}\right) \quad (46)$$

LINEARIZATION OF THE PERTURBED ENERGY TRANSFER EQUATION Firstly we put Equation 26 in a more convenient form. We consider the radiative case for the moment, so

$$l = -\frac{64\pi^2 acr^4T^4}{3\kappa}\frac{\partial \ln T}{\partial m} \quad (47)$$

which can be easily linearized differentiating and dividing by itself:

$$\frac{\delta l}{l} = 4\xi + 4\left(\frac{\delta T}{T}\right) - \frac{\delta\kappa}{\kappa} + \left(\frac{\partial \ln T}{\partial m}\right)^{-1}\frac{\partial}{\partial m}\left(\frac{\delta T}{T}\right) \quad (48)$$

2.2.4 The Linear Adiabatic Wave Equation

If heat exchanges do not happen during the oscillation cycle then the process is adiabatic. This means that $\mathrm{d}q/\mathrm{d}t = 0$ also for the perturbed model and implies $\delta\epsilon_{\text{eff}} = \delta(\partial l/\partial m)$. The adiabatic approach is an approximation and it must be justified. In order to do that, we use the following relation which we do not demonstrate:

$$\frac{c_V}{\chi_T} = \frac{P}{\rho T}\left(\frac{1}{\Gamma_3-1}\right) \quad (49)$$

and we use it to rewrite Equation 45:

$$\frac{\partial}{\partial t}\left(\frac{\delta P}{P}\right) = \Gamma_1\frac{\partial}{\partial t}\left(\frac{\delta\rho}{\rho}\right) + \chi_T\frac{\delta(\epsilon_{\text{eff}}-\partial l/\partial m)}{c_V T} \quad (50)$$

Now we can notice that:

- Γ_1 and χ_T are of the order of unity for non-degenerate gases;
- $\delta(\epsilon_{\text{eff}} - \partial l/\partial m)$ is the rate of energy gain or loss;
- $c_V T$ is the heat content;
- the ratio $c_V T/\delta(\epsilon_{\text{eff}} - \partial l/\partial m)$ is the thermal timescale;
- $\partial(\delta\rho/\rho)/\partial t$ represents the pulsation timescale.

The ratio between τ_{th} and Π can be estimated as follows:

$$\frac{\Pi}{\tau_{\text{th}}} \sim \frac{1}{(G\bar{\rho})^{1/2}} \frac{RL}{GM^2} = 10^{-12} \frac{(R/R_\odot)^{5/2}(L/L_\odot)}{(M/M_\odot)^{5/2}} \tag{51}$$

In conclusion $\tau_{\text{th}} \gg \Pi$ for the majority of stars so the second term to the right in Equation 50 can be neglected. This is the only non-adiabatic term so we can say that we are working in adiabatic approximation. The same approximation can be applied to Equation 46. Summarizing, in adiabatic approximation we can write:

$$\frac{\delta P}{P_0} = \Gamma_{1,0} \frac{\delta \rho}{\rho_0} \tag{52}$$

$$\frac{\delta T}{T_0} = (\Gamma_{3,0} - 1) \frac{\delta \rho}{\rho_0} \tag{53}$$

We are searching for an equation which can predict the oscillation frequencies. This equation, the *Linear Adiabatic Wave Equation* (LAWE), can be derived combining the latter two equation with the linearized continuity and momentum equations. After some algebraic steps we obtain the following equation:

$$r_0 \frac{\partial^2 \xi}{\partial t^2} = 4\pi r_0^2 \xi \frac{\mathrm{d}}{\mathrm{d}m}[(3\Gamma_{1,0} - 4)P_0] + \frac{1}{r_0} \frac{\partial}{\partial m}\left[16\pi^2 \Gamma_{1,0} P_0 \rho_0 r_0^6 \frac{\partial \xi}{\partial m}\right] \tag{54}$$

We search solutions of the form $\xi(m, t) = \eta(m)\, e^{j\sigma t}$ (i.e. we separate the variables). j is the imaginary unit and σ will assume the role of angular frequency. At the end, suppressing subscripts, it results

$$-\frac{1}{r^2}\frac{\mathrm{d}}{\mathrm{d}m}\left(16\pi^2 \Gamma_1 P \rho r^6 \frac{\mathrm{d}\eta}{\mathrm{d}m}\right) - 4\pi r \left\{\frac{\mathrm{d}}{\mathrm{d}m}[(3\Gamma_1 - 4)P]\right\} \eta = \sigma^2 \eta \tag{55}$$

which is the LAWE. In the Eulerian description it becomes

$$-\frac{1}{\rho r^4}\frac{\mathrm{d}}{\mathrm{d}r}\left(\Gamma_1 P r^4 \frac{\mathrm{d}\eta}{\mathrm{d}r}\right) - \frac{1}{\rho r}\left\{\frac{\mathrm{d}}{\mathrm{d}r}[(3\Gamma_1 - 4)P]\right\} \eta = \sigma^2 \eta \tag{56}$$

BOUNDARY CONDITIONS We want solutions to represent standing waves so the following boundary conditions must be satisfied. It must be $\delta r = 0$ at $r = 0$, otherwise spherical symmetry will be violated. This condition can be translated into $\partial \xi / \partial r = \mathrm{d}\eta/\mathrm{d}r = 0$ at $r = 0$, otherwise $\mathrm{d}^2\eta/\mathrm{d}r^2$ and so ξ will diverge (if we expand the first term to the left of Equation 56 it will be clear). This central condition together with Equation 41 expressed in the Eulerian description lead to

$$3\xi + \frac{\delta \rho}{\rho} = 0 \qquad \text{at } r = 0 \tag{57}$$

We want the solutions to remain finite also at the surface. In order to formalize this condition we write Equation 43 in the Eulerian form and we separate the variables. After rearranging and combining with the hydrostatic equilibrium condition, we obtain

$$\frac{\partial}{\partial t}\left(\frac{\delta P}{P_0}\right) = -\frac{1}{P_0}\frac{\mathrm{d}P_0}{\mathrm{d}r}\left[\left(4 + \frac{\sigma^2 r_0^3}{G m_0}\right)\eta + \frac{\delta P}{P_0}\right] \tag{58}$$

where we can recognize the inverse of the pressure scale height $\lambda_P = (\mathrm{d}\ln P_0/\mathrm{d}r)^{-1}$. $\lim_{r\to R} \lambda_P = 0$ so $\partial(\delta P/P_0)/\partial r$ remains finite at the surface only if

$$\left(4 + \frac{\sigma^2 r_0^3}{G m_0}\right)\eta + \frac{\delta P}{P_0} = 0 \qquad \text{at } r = R \tag{59}$$

NORMALIZATION The LAWE's solutions are determined except for a normalization factor so that they are usually normalized imposing

$$\eta = \frac{\delta r}{r} = 1 \qquad \text{at } r = R \tag{60}$$

Now the solutions are completely determined in fact the integration of the LAWE gives $\eta(m)$ (or $\eta(r)$), then $\xi = \eta\, e^{j\sigma t}$. Moreover, Equation 41 gives the density perturbation that can be used to derive the pressure and temperature perturbations through Equations 52 and 53.

EIGENVALUES AND EIGENFUNCTIONS OF THE LAWE The LAWE with the boundary conditions discussed above is a *Sturm-Liouville* problem.

Definition (Sturm-Liouville problem)**.** A Sturm-Liouville equation is a second-order linear differential equation of the form:

$$\frac{1}{a(x)}\left(-\frac{\mathrm{d}}{\mathrm{d}x}\left[b(x)\frac{\mathrm{d}y}{\mathrm{d}x}\right] + c(x)\,y\right) = \lambda\, y \qquad \lambda \in \mathbb{C}$$

where $a(x)$ and $b(x)$ are positive functions and $c(x)$ is real. In our case these functions are defined in an interval with boundary conditions on y and on $\mathrm{d}y/\mathrm{d}t$. If boundary conditions are present then it is a Sturm-Liouville problem. This is an eigenvalue problem with operator

$$\mathcal{L}(\#) = \frac{1}{a(x)}\left(-\frac{\mathrm{d}}{\mathrm{d}x}\left[b(x)\frac{\mathrm{d}\#}{\mathrm{d}x}\right] + c(x)\cdot\#\right)$$

A solution exists only for certain values of λ, the *eigenvalues*. The solutions are called *eigenfunctions*.

In the specific case of the LAWE the eigenvalue problem is

$$\mathcal{L}(\eta) = \sigma^2\,\eta \tag{61}$$

with

$$\mathcal{L}(\#) := -\frac{1}{\rho r^4}\frac{\mathrm{d}}{\mathrm{d}r}\left(\Gamma_1 P r^4 \frac{\mathrm{d}\#}{\mathrm{d}r}\right) - \frac{1}{\rho r}\left\{\frac{\mathrm{d}}{\mathrm{d}r}[(3\Gamma_1 - 4)P]\right\}\# \tag{62}$$

Referring to the above definition we have $x = r$, $y = \eta$, $\lambda = \sigma^2$ and

$$a(r) = \rho r^4 \tag{63}$$

$$b(r) = -\Gamma_1 P \rho r^4 \tag{64}$$

$$c(r) = r^3\frac{\mathrm{d}}{\mathrm{d}r}[(3\Gamma_1 - 4)P] \tag{65}$$

The eigenvalues and the eigenfunctions of a Sturm-Liouville problem have several properties which also LAWE's solutions have:

- The eigenvalues σ^2 are infinite and a certain eigenfunction corresponds to each one.
- The eigenvalues of the LAWE are always real. Positive eigenvalues correspond to periodic solutions with period $2\pi/\sigma$. Instead, if $\sigma^2 < 0$ then σ is purely imaginary and the perturbation $\xi = \eta\, e^{j\sigma t}$ grows or is damped exponentially: it is unstable.
- We denote with n the radial order of the solutions. It results $\sigma_n < \sigma_{n+1}$ and the lowest angular frequency is σ_0 which corresponds to the fundamental mode.

The eigenfunctions of positive eigenvalues are standing waves and the radial order is the number of nodes in the interval $(0, R)$.

- The eigenfunctions $\eta_n(r)$ (and also $\xi_n(r, t)$) are orthogonal to each other with respect to $a(r)$:

$$\int_0^R \eta_h(r)\eta_k(r)a(r)\mathrm{d}r = \int_0^M \eta_h(m)\eta_k(m)\frac{r^2}{4\pi}\mathrm{d}m = \frac{J_h}{4\pi}\delta_{hk} \tag{66}$$

$$\int_0^R \xi_h^*(r, t)\xi_k(r, t)a(r)\mathrm{d}r = \int_0^M \xi_h^*(m, t)\xi_k(m, t)\frac{r^2}{4\pi}\mathrm{d}m = \frac{J_h}{4\pi}\delta_{hk} \tag{67}$$

where

$$J_n := \int_0^M |\xi_n|^2 r^2 \,\mathrm{d}m = \int_0^M |\xi_n|^2 \rho \,\mathrm{d}V \tag{68}$$

is the *oscillatory moment of inertia*. Therefore the general solution is a linear combination of the eigenfunctions.

- The operator $\mathcal{L}$ is hermitian:

$$\int_0^R \eta_h \mathcal{L}(\eta_k)\,\mathrm{d}r = \int_0^R \eta_k \mathcal{L}(\eta_h)\,\mathrm{d}r \qquad \int_0^R \xi_h^* \mathcal{L}(\xi_k)\,\mathrm{d}r = \int_0^R \xi_k \mathcal{L}(\xi_h)^*\,\mathrm{d}r$$

- The following relation between eigenvalues and eigenfunctions holds:

$$\sigma_n^2 = \frac{1}{J_n}\int_0^M \xi_n^*\,\mathcal{L}(\xi_n) r^2\,\mathrm{d}m \tag{69}$$

CONDITION FOR EXISTENCE OF OSCILLATORY SOLUTIONS We consider for simplicity only the case Γ_1 =const. Equation 56 becomes

$$\frac{\mathrm{d}}{\mathrm{d}r}\left(Pr^4\frac{\mathrm{d}\eta}{\mathrm{d}r}\right) + r^3\frac{3\Gamma_1 - 4}{\Gamma_1}\frac{\mathrm{d}P}{\mathrm{d}r}\eta + \frac{r^4\rho}{\Gamma_1}\sigma^2\eta = 0 \tag{70}$$

Now we integrate in $\mathrm{d}r$ over the whole star:

$$r^4 P\frac{\mathrm{d}\eta}{\mathrm{d}r}\bigg|_0^R + \frac{3\Gamma_1 - 4}{\Gamma_1}\int_0^R r^3\frac{\mathrm{d}P}{\mathrm{d}r}\eta\,\mathrm{d}r + \frac{\sigma^2}{\Gamma_1}\int_0^R r^4\rho\eta\,\mathrm{d}r \tag{71}$$

but assuming $P(R) = 0$ and using the hydrostatic equilibrium condition $\mathrm{d}P/\mathrm{d}r = -\rho Gm/r^2 = -\rho g$, it results

$$\sigma^2 = (3\Gamma_1 - 4)\frac{\int_0^R r^3\rho g\eta\,\mathrm{d}r}{\int_0^R r^4\rho\eta\,\mathrm{d}r} \tag{72}$$

If $\eta = \eta_0$ then it has constant sign in the star so $\operatorname{sgn}\sigma_0^2 = \operatorname{sgn}(3\Gamma_1 - 4)$. Moreover, since $\sigma_n \geq \sigma_0$, we have oscillatory solutions for all the eigenvalues only if $\Gamma_1 > 4/3$.

THE HOMOLOGOUS CASE η =const is a solution of the LAWE. η =const implies homologous motions. Assuming Γ_1 =const we find

$$-\frac{1}{r\rho}(3\Gamma_1 - 4)\frac{\mathrm{d}P}{\mathrm{d}r}\eta = \sigma^2\eta \tag{73}$$

If we consider an homogeneous model with constant mean density $\overline{\rho}$ then

$$-\frac{1}{\overline{\rho}r}\frac{\mathrm{d}P}{\mathrm{d}r} = \frac{Gm}{r^3} = \frac{G}{r^3}\left(\frac{4}{3}\pi r^3\overline{\rho}\right) = \frac{4\pi G\overline{\rho}}{3} \tag{74}$$

so Equation 73 leads to

$$\sigma^2 = (3\Gamma_1 - 4)\frac{4\pi G}{3}\bar{\rho} \tag{75}$$

Since η =const has not nodes then this eigenvalue must correspond to the fundamental mode whose period is

$$\Pi = \frac{2\pi}{\sigma} = \frac{2\pi}{[(3\Gamma_1 - 4)4\pi G\bar{\rho}/3]^{1/2}} \tag{76}$$

which confirms the period-mean density relation, $\Pi \propto (G\bar{\rho})^{-1/2}$. It is equal to Ritter's relation except for a different value of the pulsation constant.

THE POLYTROPIC CASE We remember that the equation of state of polytropes is of the form $P = K\rho^{\gamma} = K\rho^{1+1/n}$ with n named *polytropic index* and K =const. More centrally concentrated models correspond to higher values of n. For this reason $n = 3$ gives a first approximation for main sequence stars, but Cepheids and RR Lyrae require a polytropic index between 3 and 5, the latter corresponding to a model with infinite central density. We can combine the continuity equation, the hydrostatic equilibrium condition and the polytropic relation to obtain

$$\frac{1}{\rho r^2}\frac{\mathrm{d}}{\mathrm{d}r}\left[r^2\rho^{K-2}\frac{\mathrm{d}\rho}{\mathrm{d}r}\right] = -\frac{4\pi G}{K\gamma} \qquad \text{with } \rho(r=0) = \rho_c \text{ and } \left.\frac{\mathrm{d}\rho}{\mathrm{d}r}\right|_{r=0} = 0 \tag{77}$$

Now we define two new variables, z and θ, through the following relations:

$$r = \alpha z \qquad \text{with } \alpha = \left(\frac{n+1}{4\pi G}K\rho_c^{\frac{1}{n}-1}\right)^{\frac{1}{2}} \tag{78}$$

$$\rho = \rho_c\,\theta^n(z) \tag{79}$$

so that Equation 77 gives the *Lane-Emden equation*:

$$\frac{1}{z^2}\frac{\mathrm{d}}{\mathrm{d}z}\left(z^2\frac{\mathrm{d}\theta}{\mathrm{d}z}\right) + \theta^n = 0 \tag{80}$$

which has an analytic solution only for $n = 0$, 1, 5. The LAWE can be solved for polytropic models and it results that

$$\frac{\eta(R)}{\eta(0)} \sim \frac{\rho_c}{\bar{\rho}} = \frac{1}{3}\left(-\frac{z}{\theta_n'}\right)_{z=z_1} \tag{81}$$

where $\theta_n' = \mathrm{d}\theta/\mathrm{d}z$ and z_1 is the coordinate of the first zero of the function $\theta(z)$ which corresponds to the stellar surface. This ratio depends only on n and increases with n: more centrally concentrated the model is more shallow are the layers interested by oscillations. For practical reasons the *dimensionless frequency*, ω, is usually introduced in this context:

$$\omega^2 = \frac{R^3}{GM}\sigma^2 \tag{82}$$

ASYMPTOTIC ANALYSIS If Equation 56 is rewritten in terms of the variable $w(r) = r^2(\Gamma_1 P)^{1/2}\eta(r)$ then it becomes

$$\frac{\mathrm{d}^2 w}{\mathrm{d}r^2} + \left[\frac{\sigma^2}{c_s^s} - \Phi\right]w = 0 \tag{83}$$

where $c_s^2 = \Gamma_1 P/\rho$ and $\Phi(r)$ is a function of r. We search for solutions of the form $w(r) \propto e^{jk_r r}$ with k_r defined by the *dispersion relation*:

$$k_r^2 = \frac{\sigma^2}{c_s^2} - \Phi \tag{84}$$

Therefore we have oscillatory solutions for $\sigma^2 > c_s^2\Phi$. If $\sigma^2 \gg c_s^2\Phi$ and so $k_r r \gg 1$, then we are in *aymptotic regime*. In this regime the solutions are stationary waves with an integer or half-integer number of wavelength in the radial range $a \leq r \leq b$ where the regime applies. The number of wavelengths can be measured as follows.

$$\int_a^b k_r \, \mathrm{d}r = (n+1)\pi \tag{85}$$

where n is the number of nodes in (a, b). We can enter in asymptotic regime if $\Phi \ll 1$, in this case $k_r \simeq \sigma/c_s$ and

$$\int_a^b k_r \, \mathrm{d}r = \sigma \int_a^b \frac{\mathrm{d}r}{c_s} \qquad \longrightarrow \qquad \sigma = (n+1)\pi \left[\int_a^b \frac{\mathrm{d}r}{c_s} \right]^{-1} \tag{86}$$

We define $\sigma_{n=0} = \pi \left[\int_a^b \frac{\mathrm{d}r}{c_s} \right]^{-1}$, hence $\sigma_n = \sigma_0(n+1)$: in asymptotic regime the oscillation frequencies are equally spaced by σ_0. It is important to underline that the condition $k_r r \gg 1$ is satisfied only for high radial orders. Such a behaviour is observed for example in the Sun.

2.2.5 Non-adiabatic oscillations

The adiabatic approximation leads to good estimates of the oscillation frequencies, but we can't explain how the modes are excited yet. We have to investigate non-adiabatic effects.

We start multiplying Equation 24 by $\partial r/\partial t$ and after rearranging we obtain

$$\frac{1}{2}\frac{\partial (v^2)}{\partial t} = \left(-4\pi r^2 \frac{\partial P}{\partial m} - \frac{Gm}{r^2} \right) \frac{\partial r}{\partial t} \tag{87}$$

Then we integrate in $\mathrm{d}m$ over the whole star:

$$\int_0^M \frac{1}{2}\frac{\partial (v^2)}{\partial t} \, \mathrm{d}m = - \underbrace{\frac{\mathrm{d}}{\mathrm{d}t} \left(\int_0^M -\frac{Gm}{r} \, \mathrm{d}m \right)}_{=\mathrm{d}\Omega/\mathrm{d}t} - \underbrace{4\pi r^2 P \frac{\partial r}{\partial t} \Big|_0^M}_{\simeq 0} + \int_0^M P \frac{\partial}{\partial m} \left(4\pi r^2 \frac{\partial r}{\partial t} \right) \mathrm{d}m \tag{88}$$

$$\int_0^M \frac{1}{2}\frac{\partial (v^2)}{\partial t} \, \mathrm{d}m \simeq -\frac{\mathrm{d}\Omega}{\mathrm{d}t} + \int_0^M P \frac{\partial}{\partial t} \left(\frac{1}{\rho} \right) \mathrm{d}m \tag{89}$$

where Ω is the total gravitational potential energy. If we further integrate over a pulsation cycle it results

$$W = - \underbrace{\int_0^\Pi \frac{\mathrm{d}\Omega}{\mathrm{d}t} \, \mathrm{d}t}_{\simeq 0} + \int_0^\Pi \mathrm{d}t \int_0^M P \frac{\partial}{\partial t} \left(\frac{1}{\rho} \right) \mathrm{d}m \tag{90}$$

$$\left\langle \frac{\mathrm{d}W}{\mathrm{d}t} \right\rangle := \frac{W}{\Pi} = \frac{1}{\Pi} \int_0^\Pi \mathrm{d}t \int_0^M P \frac{\partial}{\partial t} \left(\frac{1}{\rho} \right) \mathrm{d}m \tag{91}$$

Where W is the total mechanical work done during a pulsation cycle that is transformed into kinetic energy and $\langle \mathrm{d}W/\mathrm{d}t \rangle$ is defined as above. Therefore oscillations

are driven if $\langle dW/dt \rangle > 0$ and are damped otherwise. In general in a star there are both *driving* and *damping layers*. Let's study the consequences of this condition for driving. For the first law of thermodynamics we have

$$\int_0^\Pi P \frac{\partial}{\partial t}\left(\frac{1}{\rho}\right) dt = \int_0^\Pi \frac{dq}{dt} dt + \int_0^\Pi \frac{\partial E}{\partial t} dt = \int_0^\Pi \frac{dq}{dt} dt \tag{92}$$

hence

$$\left\langle \frac{dW}{dt} \right\rangle = \frac{1}{\Pi} \int_0^\Pi dt \int_0^M \frac{dq}{dt} dm \tag{93}$$

Now, since $dq/dt = \epsilon_{\text{eff}} - \partial l/\partial m$, Equation 36 can be rewritten as

$$\frac{\partial \ln P}{\partial t} = \Gamma_1 \frac{\partial \ln \rho}{\partial t} + \frac{\rho}{P}(\Gamma_3 - 1)\frac{dq}{dt} \tag{94}$$

Therefore, at maximum compression, we have

$$\left(\frac{\partial \ln P}{\partial t}\right)_{\text{m.c.}} = \frac{\rho}{P}(\Gamma_3 - 1)\frac{dq}{dt} \tag{95}$$

Since $(\Gamma_3 - 1)\rho/P > 0$ then heat gain ($dq/dt > 0$) during compression means increase in pressure. So the pressure will be higher during expansion than during compression leading to positive net work W and driving of pulsations. In conclusion, in a driving region, heat is gained during compression and consequently oscillations can't be exited with pure adiabatic processes. Before exploring the mechanism which leads to pulsation driving, we look at how the LAWE can be modified in order to take into account non-adiabatic effects.

THE LINEAR NON-ADIABATIC WAVE EQUATION The derivation starts taking the time derivative of Equation 43 written with the Eulerian formalism; it results

$$\rho r \frac{\partial^3 \xi}{\partial t^3} = -4\frac{\partial \xi}{\partial t}\frac{\partial P}{\partial r} - \frac{\partial}{\partial r}\left(P \frac{\partial}{\partial t}\frac{\delta P}{P}\right) \tag{96}$$

then we use Equation 45 and the time derivative of Equation 41. We obtain

$$\rho r \frac{\partial^3 \xi}{\partial t^3} = -4\frac{\partial \xi}{\partial t}\frac{\partial P}{\partial r} + \frac{\partial}{\partial r}\left[P\Gamma_1\left(3\frac{\partial \xi}{\partial t} + r\frac{\partial}{\partial t}\frac{\partial \xi}{\partial r}\right) - \rho(\Gamma_3 - 1)\,\delta\left(\epsilon_{\text{eff}} - \frac{\partial l}{\partial m}\right)\right] \tag{97}$$

Finally, with $\xi(r, t) = \eta(r)\, e^{j\sigma t}$ and after some manipulations we arrive to the *Linear Non-Adiabatic Wave Equation* (LNAWE):

$$j\sigma \mathcal{L}(\xi) - j\sigma^3 \xi = -\frac{1}{r\rho}\frac{\partial}{\partial r}\left[\rho(\Gamma_3 - 1)\left(\delta\epsilon_{\text{eff}} - \frac{\partial \delta l}{\partial m}\right)\right] \tag{98}$$

where the operator $\mathcal{L}$ is exactly the same of Equation 62. The solutions of the LNAWE are similar to those of the LAWE, but σ is in general a complex number with real and imaginary part defined by $\sigma = \omega + j\kappa$ so that $\xi(r, t) = \eta(r)\, e^{j\omega t}\, e^{-\kappa t}$. $\omega = 2\pi/\Pi$ in this case is the angular frequency, not the dimensionless frequency, and represents adiabatic contributions. κ is the *stability coefficient* which determines the rate of growth or decay of pulsations and represents non-adiabatic contributions. The non-adiabatic effects will be more clear if we apply the quasi-adiabatic approximation: $\omega \gg |\kappa|$. In this case, the variational principle allows us to use the solutions of the LAWE to obtain the variation, κ, of σ from the adiabatic frequency. Hence we

introduce in Equation 98 an adiabatic solution, ξ_{ad}, we multiply by the latter and we integrate in $r^2\,dm$ over the whole star:

$$j\sigma\int_0^M \xi_{ad}\mathcal{L}(\xi_{ad})r^2\,dm - j\sigma^3\int_0^M \xi_{ad}\xi_{ad}r^2\,dm = \\ = \underbrace{-\int_0^M \frac{\xi_{ad}}{r\rho}\frac{\partial}{\partial r}\left[\rho(\Gamma_3-1)\left(\delta\epsilon_{eff}-\frac{\partial\delta l}{\partial m}\right)\right]r^2\,dm}_{:=C_{qa}} \quad (99)$$

Since $\omega \gg |\kappa|$, we have $j\sigma^3 \approx \omega^2(j\omega - 3\kappa) = \omega^2(j\sigma - 2\kappa)$. Moreover, we know that $\mathcal{L}(\xi_{ad}) = \omega^2\,\xi_{ad}$ so Equation 99 becomes

$$2\omega^2\kappa\int_0^M \xi_{ad}^2 r^2\,dm = -C_{qa} \quad (100)$$

so that

$$\kappa = -\frac{C_{qa}}{2\omega^2\int_0^M \xi_{ad}^2 r^2\,dm} = -\frac{C_{qa}}{2\omega^2 J} \quad (101)$$

and $\operatorname{sgn}\kappa = -\operatorname{sgn} C_{qa}$ since ω^2, $J > 0$. This means that C_{qa} is fundamental for our understanding of the pulsations' behaviour. This integral can be developed firstly changing the variable from m to r and integrating by parts, and then using Equations 41 and 53; it results

$$C_{qa} = \int_0^M \left(\frac{\delta T}{T}\right)_{ad}\left(\delta\epsilon_{eff}-\frac{\partial\delta l}{\partial m}\right)dm \quad (102)$$

It can be shown that this is equal to $\langle dW/dt\rangle$. The demonstration starts from Equation 93 expanding $P(\partial(\rho^{-1})/\partial t$ until the second order and then combining with Equation 45. Summarizing, in quasi-adiabatic approximation we have $\operatorname{sgn}\kappa = -\operatorname{sgn} C_{qa} = -\operatorname{sgn}\langle dW/dt\rangle$. This fact was expected indeed we said that there is driving when $\langle dW/dt\rangle > 0$ which corresponds to a solution $\xi(r,\,t) = \eta(r)\,e^{j\omega t}\,e^{-\kappa t}$ that grows with time. On the contrary, there is damping if $\langle dW/dt\rangle < 0$ and so $\kappa > 0$.

PHASE LAGS The adiabatic theory can't explain also the phase lags observed between different physical quantities. For example, we can do the separation of variables in Equation 45:

$$\frac{\delta P}{P}(r) = \Gamma_1\frac{\delta\rho}{\rho}(r) - \frac{j}{\sigma}(\Gamma_3-1)\delta\left(\epsilon_{eff}-\frac{\partial l}{\partial m}\right) \quad (103)$$

where the second term to the right is not present in adiabatic approximation, but justifies the phase lag observed between the pressure and density perturbations. Moreover, this phase lag is directly connected with the driving condition of heating during compression.

2.2.6 Driving Mechanisms

In order to identify the possible driving mechanisms we concentrate on Equations 101 and 102. It is clear that the sign of κ is determined by the balance between $\delta\epsilon_{eff}$ and $\partial\delta l/\partial m$, and so between energy generation and energy transfer.

THE ϵ-MECHANISM If the heat gain during compression is due to the increase of ϵ_{eff} then we talk about $\epsilon-$mechanism. This mechanism can work because the energy generation rates strongly depend on temperature which increases during compression. This increase of ϵ_{eff} depends on the oscillation amplitude. It turns out, however, that the expected temperature oscillation amplitudes in the nuclear burning regions of Cepheids RR Lyrae stars are not sufficiently high. Therefore the

$\epsilon-$mechanism is not important for classical pulsators. It can have a significant role in massive stars.

THE κ AND γ MECHANISMS These mechanisms are based on energy transfer so we recall Equation 48. In order to avoid confusion, hereafter we will denote the opacity with κ and the stability coefficient with κ_s. We consider an opacity law of the form $\kappa \propto \rho^u T^{-s}$ which gives

$$\frac{\delta\kappa}{\kappa} = u\frac{\delta\rho}{\rho} - s\frac{\delta T}{T} \tag{104}$$

hence, from Equation 26, we obtain

$$\frac{\delta l}{l} = 4\xi - u\frac{\delta\rho}{\rho} + (s+4)\frac{\delta T}{T} + \left(\frac{\partial \ln T}{\partial m}\right)^{-1}\frac{\partial}{\partial m}\frac{\delta T}{T} \tag{105}$$

Now we find out ξ from Equation 41 and we neglect the terms with spatial derivatives (often negligible compared to the others):

$$\frac{\delta l}{l} \approx -\left[\frac{4}{3}+u\right]\frac{\delta\rho}{\rho} + (s+4)\frac{\delta T}{T} \tag{106}$$

If we work in quasi-adiabatic approximation then we can use Equation 53 to find out $\delta\rho/\rho$; it results

$$\left(\frac{\delta l}{l}\right)_{\text{qa}} \approx \left[(s+4) - \frac{\frac{4}{3}+u}{\Gamma_3 - 1}\right]\frac{\delta T}{T} \tag{107}$$

Finally, outside regions where energy production takes place, we can put $\partial l/\partial m = 0$ so that

$$\left(\frac{\partial \delta l}{\partial m}\right)_{\text{qa}} \approx l\frac{\partial}{\partial m}\left\{\left[(s+4) - \frac{\frac{4}{3}+u}{\Gamma_3 - 1}\right]\frac{\delta T}{T}\right\} \tag{108}$$

We remember that κ_s must be negative to excite oscillations and this implies that during compression ($\delta T/T > 0$) the quantity $\partial\delta l/\partial m$ must be negative too. Therefore, according with Equation 108, good driving regions may be those layers where $s < 0$ or where Γ_3 is small. In the former case the opacity increases with increasing temperature and so traps energy during compression which is realeased during expansion: this is the $\kappa-$mechanism. In the latter case the small value of Γ_3 indicates that a great amount of energy can be gained by the layers in the form of heat: this is the $\gamma-$mechanism. Actually, these two mechanisms work together. In particular, both the conditions on s and Γ_1 are satisfied in partial ionization zones, especially those of H and He. The reason is that the opacity has a bump in partial ionization zones and the degree of ionization increases during compression absorbing a great amount of energy. It turns out that these mechanisms are the origin of pulsations in many types of stars such as Cepheids, RR Lyrae and δ Scutis which are located along the so-called instability strip (see Figure 10).

2.2.7 Other Driving Mechanisms

We have seen that the κ and γ mechanisms lead to pulsational instability only under special conditions. However, there are pulsating stars which do not satisfy those conditions. Hence other mechanisms must occur. We only mention the *Convective Blocking* and the δ mechanisms which are supposed to be active in γ Dor stars and white dwarfs respectively. We highlight, instead, the *stochastic excitation* which is responsible of the oscillations in many stars located below the instability strip, the Sun included. These stars are not intrinsically unstable, but the convective turbulence in their outer layers can constantly excite the pulsations. These *Solar-like oscillations* have been observed not only in main-sequence stars but also in subgiants and red

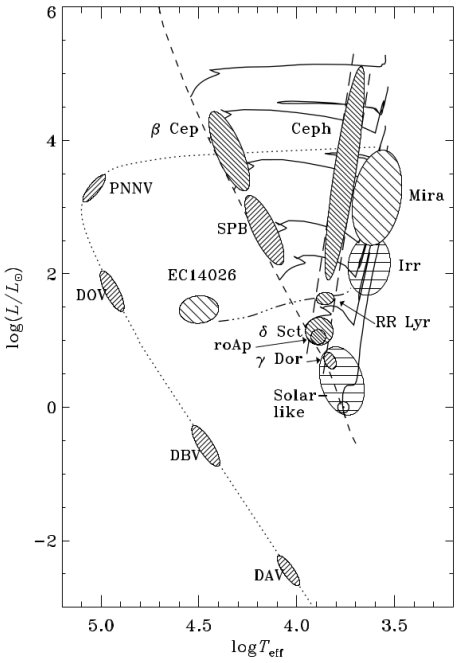

Figure 10: *The different types of pulsating stars in the H-R diagram. Some evolutionary tracks corresponding to* 1, 2, 3, 4, 7, 12 *and* 20 $M_\odot$ *are shown (solid lines). The short-dashed line is the ZAMS, the dot-dashed line is the HB and the dotted line is the path that white dwarfs follow during their cooling process. In particular we can see that Cepheids, RR Lyrae and* δ *Scutis are aligned along the instability strip which is the region enclosed between the two long-dashed lines to the right. Figure taken from Aerts et al. (2010).*

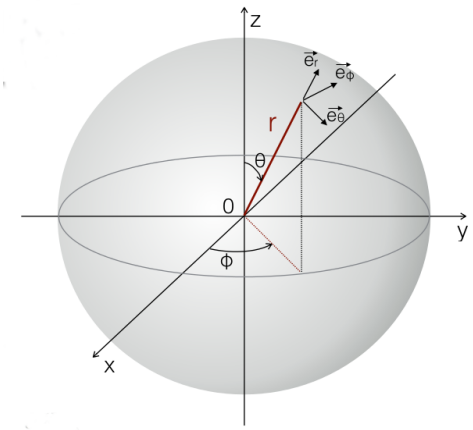

Figure 11.: *The spherical coordinates* r, θ, ϕ *and the unit vectors* $\mathbf{e}_r$, $\mathbf{e}_\theta$, $\mathbf{e}_\phi$. *Credits, "Theoretical Astrophysics: Asteroseismology", J. Montalbán.*

giants. We are going to explore better the properties of solar-like oscillations in the next Section.

2.2.8 The Theory of Non-radial Oscillations

Classical variables clearly show radial pulsations, but stars can pulsate also with non-radial modes. This is the case of the Sun whose non-radial oscillations have been detected also for very high angular degrees. These oscillations are a fundamental resource in order to understand the structure of stellar interiors. Let us develop the basis of the theory behind non-radial oscillations.

We firstly express the perturbation, $\delta\mathbf{r}$ in spherical coordinates (see Figure 11):

$$\delta\mathbf{r} = \delta\mathbf{r}(r,\,\theta,\,\phi,\,t) = \xi_r\,\mathbf{e}_r + \xi_\theta\,\mathbf{e}_\theta + \xi_\phi\,\mathbf{e}_\phi = \delta\mathbf{r}(r,\,\theta,\,\phi)\,e^{j\sigma t} \tag{109}$$

If the perturbation is not purely radial then the linearized equations assume a different form. The linearized continuity equation becomes

$$\frac{\delta\rho}{\rho} + \nabla \cdot \delta\mathbf{r} = 0 \tag{110}$$

$$\frac{\delta\rho}{\rho} + \frac{1}{r^2}\frac{\partial}{\partial r}(r^2\xi_r) + \frac{1}{r\sin\theta}\frac{\partial}{\partial\theta}(\sin\theta\,\xi_\theta) + \frac{1}{r\sin\theta}\frac{\partial\xi_\theta}{\partial\phi} = 0 \tag{111}$$

The linearized momentum equation becomes

$$\rho\frac{\partial^2\delta\mathbf{r}}{\partial t^2} = -\nabla P' - \rho\nabla\psi' + \frac{\rho'}{\rho}\nabla P \tag{112}$$

$$-\rho\sigma^2\delta\mathbf{r} = \left(-\frac{\partial P'}{\partial r} - \rho\frac{\partial\psi'}{\partial r} - \rho' g\right)\mathbf{e}_r + \left(-\frac{\rho}{r}\frac{\partial\psi'}{\partial\theta} - \frac{1}{r}\frac{\partial P'}{\partial\theta}\right)\mathbf{e}_\theta + \left(-\frac{1}{r\sin\theta}\frac{\partial P'}{\partial\phi} - \frac{\rho}{r\sin\theta}\frac{\partial\psi'}{\partial\phi}\right)\mathbf{e}_\phi \tag{113}$$

where P', ψ', ρ' are the Eulerian perturbations of pressure, gravitational potential and density respectively. We have also written the gradients in spherical coordinates and we have used the fact that at the equilibrium $P = P(r)$, $\rho = \rho(r)$ and $\mathbf{g} = \mathbf{g}(r) = -\nabla\psi$. Combining Equations 109 and 113 it is straightforward to derive the following relations:

$$\sigma^2\xi_r = \frac{\partial\psi'}{\partial r} + \frac{\rho'}{\rho}g + \frac{1}{\rho}\frac{\partial P'}{\partial r} \tag{114a}$$

$$\sigma^2\xi_\theta = \frac{1}{r}\frac{\partial}{\partial\theta}\left(\psi' + \frac{P'}{\rho}\right) \tag{114b}$$

$$\sigma^2\xi_\phi = \frac{r}{\sin\theta}\frac{\partial}{\partial\theta}\left(\psi' + \frac{P'}{\rho}\right) \tag{114c}$$

Now, combining Equations 111, 114b and 114c we obtain

$$\frac{\delta\rho}{\rho} + \frac{1}{r^2}\frac{\partial}{\partial r}(r^2\xi_r) - \frac{1}{\sigma^2 r^2}\mathscr{L}^2\left(\psi' + \frac{P'}{\rho}\right) = 0 \tag{115}$$

where the operator $\mathscr{L}^2$ is defined by

$$\mathscr{L}^2 := -\frac{1}{\sin\theta}\frac{\partial}{\partial\theta}\left(\sin\theta\,\frac{\partial}{\partial\theta}\right) - \frac{1}{\sin^2\theta}\frac{\partial^2}{\partial\phi^2} \tag{116}$$

whose eigenfunctions are the spherical harmonics $Y_l^m(\theta, \phi)$:

$$\mathscr{L}^2 Y_l^m(\theta, \phi) = l(l+1)\,Y_l^m(\theta, \phi) \qquad l \in \mathbb{N};\ m \in \mathbb{Z} \mid -l \leq m \leq l \tag{117}$$

where l is the *angular degree* and m is the *azimuthal order*. The linearized Poisson Equation is $\nabla^2\psi' = 4\pi G\rho'$ which can be rewritten as

$$\nabla^2\psi' = \frac{1}{r^2}\frac{\partial}{\partial r}\left(r^2\frac{\partial\psi'}{\partial r}\right) - \frac{1}{r^2}\mathscr{L}^2(\psi') = 4\pi G\rho' \tag{118}$$

We want to solve the system of partial differential equations composed by Equations 114a, 115 and 118. In order to do that we separate the radial variable from the angular

variables. Thus, for a general perturbation X' we write $X'(r,\theta,\phi) = X'_r(r)\,Y_l^m(\theta,\phi)$. If we denote the radial part, $X'_r(r)$, only with X', then the equations just mentioned become

$$\sigma^2\xi_r(r) = \frac{\mathrm{d}\psi'}{\mathrm{d}r} + \frac{\rho'}{\rho}g + \frac{1}{\rho}\frac{\mathrm{d}P'}{\mathrm{d}r} \tag{119a}$$

$$\frac{\delta\rho}{\rho} + \frac{1}{r^2}\frac{\mathrm{d}}{\mathrm{d}r}(r^2\xi_r(r)) - \frac{l(l+1)}{\sigma^2 r^2}\left(\psi' + \frac{P'}{\rho}\right) = 0 \tag{119b}$$

$$\frac{1}{r^2}\frac{\mathrm{d}}{\mathrm{d}r}\left(r^2\frac{\mathrm{d}\psi'}{\mathrm{d}r}\right) - \frac{l(l+1)}{r^2}\psi' = 4\pi G\rho' \tag{119c}$$

Note that the spherical harmonics and the factor $e^{j\sigma t}$ cancel out so all variables only depend on r now and hereafter unless specific indications. This is a system with four unknown variables: $\xi_r(r)$, ψ', ρ' and P'. If we assume adiabatic conditions then we can use the simple relation $\delta P/P = \Gamma_1(\delta\rho/\rho)$ and derive new expressions for $\delta\rho/\rho$ and ρ'/ρ:

$$\frac{\delta\rho}{\rho} = \frac{1}{\Gamma_1}\frac{\delta P}{P} \tag{120}$$

$$\rho' + \delta\mathbf{r}\cdot\nabla\rho = \frac{\rho}{\Gamma_1 P}(P' + \delta\mathbf{r}\cdot\nabla P) \tag{121}$$

$$\rho' + \frac{\mathrm{d}\rho}{\mathrm{d}r}\xi_r = \frac{\rho}{\Gamma_1 P}\left(P' + \frac{\mathrm{d}P}{\mathrm{d}r}\xi_r\right) \tag{122}$$

$$\frac{\rho'}{\rho} = \frac{1}{\Gamma_1}\frac{P'}{P} + \left(\frac{1}{\Gamma_1}\frac{\mathrm{d}\ln P}{\mathrm{d}r} - \frac{\mathrm{d}\ln\rho}{\mathrm{d}r}\right)\xi_r \tag{123}$$

Usually, the following equivalent relations for $\delta\rho/\rho$ and ρ'/ρ are used:

$$\frac{\rho'}{\rho} = \frac{1}{\Gamma_1}\frac{P'}{P} + \frac{N^2}{g}\xi_r \tag{124}$$

$$\frac{\delta\rho}{\rho} = \frac{1}{\Gamma_1}\frac{P'}{P} - \frac{g}{c_s^2}\xi_r \tag{125}$$

where $N^2 = -g\,A_s$ is the square of the so-called *Brunt-Väisälä frequency* and

$$A_s = -\frac{1}{\Gamma_1}\frac{\mathrm{d}\ln P}{\mathrm{d}r} + \frac{\mathrm{d}\ln\rho}{\mathrm{d}r} \tag{126}$$

is the *Schwarzshild discriminant*. It can be shown that the buoyancy force per unit volume acting on a mass element displaced by δr in radial direction with respect to its equilibrium position is $F_b = \rho g A_s \delta r$. At this point it is clear that $A_s > 0$ means instability to convection and $N^2 < 0$. If there is stability to convection then $A_s < 0$ and the mass element oscillates around its equilibrium point with angular frequency $N = \sqrt{-A_s g}$.

Substituting expressions 124 and 125 into Equations 119 and rearranging, it results

$$\frac{1}{\rho}\frac{\mathrm{d}P'}{\mathrm{d}r} + \frac{P'}{\rho c_s^2}g + (N^2 - \sigma^2)\xi_r = -\frac{\mathrm{d}\psi'}{\mathrm{d}r} \tag{127a}$$

$$\frac{1}{r^2}\frac{\mathrm{d}}{\mathrm{d}r}(r^2\xi_r) - \frac{g}{c_s^2}\xi_r + \left(1 - \frac{S_l^2}{\sigma^2}\right)\frac{P'}{\rho c_s^2} = \frac{l(l+1)}{\sigma^2 r^2}\psi' \tag{127b}$$

$$\frac{1}{r^2}\frac{\mathrm{d}}{\mathrm{d}r}\left(r^2\frac{\mathrm{d}\psi'}{\mathrm{d}r}\right) - \frac{l(l+1)}{r^2}\psi' = 4\pi G\rho\left(\frac{P'}{\rho c_s^2} + \frac{N^2}{g}\xi_r\right) \tag{127c}$$

where $S_l^2 = l(l+1)c_s^2/r^2$ is the square of the so-called *Lamb frequency*. In order to solve this system of ODEs we need four boundary conditions (as many as the system's order). We do not consider the case $l = 0$ which corresponds to radial oscillations. Again we request regularity at the center. Consequently, it must be

$$\xi_r \propto r^{l-1} \qquad \text{and} \qquad \frac{P'}{\rho'}\psi' \propto r^l \tag{128}$$

At the surface we impose $\delta\rho = 0$ and so $\delta P = P' + \xi_r \frac{\mathrm{d}P}{\mathrm{d}r} = 0$. Finally for the regularity of ψ' at the surface it must be

$$\frac{\mathrm{d}\psi'}{\mathrm{d}r} + \frac{l(l+1)}{r}\psi' = 0 \tag{129}$$

This is another eigenvalue problem (there are solutions only for certain values of σ^2), but it is not a Sturm-Liouville problem. Therefore the eigenvalues can't be easily ordered as for radial oscillations. However some properties are still present. If we define a new operator $\mathcal{L}_{\mathrm{nr}}$ such that $\mathcal{L}_{\mathrm{nr}}(\delta\mathbf{r}) = \sigma^2\delta\mathbf{r}$ then this operator is linear and self-adjoint. Moreover, the eigenvalues are real, the eigenfunctions are orthonormal. For each pair (l, m) there are infinite eigenvalues, σ^2_{nlm} for which the following relation holds:

$$\sigma^2_{nlm} = \frac{\int_0^M \delta\mathbf{r}^*_{nlm} \cdot \mathcal{L}_{\mathrm{nr}}(\delta\mathbf{r}_{nlm})\,\mathrm{d}m}{\int_0^M \delta\mathbf{r}^*_{nlm} \cdot \delta\mathbf{r}_{nlm}\,\mathrm{d}m} \tag{130}$$

Other properties of non-radial oscillations will be clear if we decompose the displacement $\delta\mathbf{r}$ into two components, radial the first and tangential the second:

$$\delta\mathbf{r}(r, \theta, \phi) = \xi_r(r, \theta, \phi)\mathbf{e}_r + \xi_h(r, \theta, \phi)\mathbf{e}_h \tag{131}$$

where amplitude and direction of the tangential component are defined by $\xi_h(r, \theta, \phi)\mathbf{e}_h = \xi_\theta(r, \theta, \phi)\mathbf{e}_\theta + \xi_\phi(r, \theta, \phi)\mathbf{e}_\phi$. We can separate variables again and from Equations 114b and 114c we obtain:

$$\xi_\theta = \frac{1}{r\sigma^2}\left(\psi' + \frac{P'}{\rho}\right)\frac{\partial Y_l^m(\theta, \phi)}{\partial\theta} \tag{132a}$$

$$\xi_\phi = \frac{1}{r\sigma^2}\left(\psi' + \frac{P'}{\rho}\right)\frac{1}{\sin\theta}\frac{\partial Y_l^m(\theta, \phi)}{\partial\phi} \tag{132b}$$

hence

$$\xi_h(r, \theta, \phi) = \xi_h(r)\left(\frac{\partial Y_l^m(\theta, \phi)}{\partial\theta}\mathbf{e}_\theta + \frac{1}{\sin\theta}\frac{\partial Y_l^m(\theta, \phi)}{\partial\phi}\mathbf{e}_\phi\right) \tag{133}$$

$$\xi_h(r) = \frac{1}{r\sigma^2}\left(\psi' + \frac{P'}{\rho}\right) \tag{134}$$

$$\delta\mathbf{r}(r, \theta, \phi, t) = \left[\xi_r(r)\mathbf{e}_r + \xi_h(r)\left(\mathbf{e}_\theta\frac{\partial}{\partial\theta} + \frac{1}{\sin\theta}\mathbf{e}_\phi\frac{\partial}{\partial\phi}\right)\right] Y_l^m(\theta, \phi)\, e^{j\sigma t} \tag{135}$$

Let's explore in detail the geometrical and physical properties of non-radial oscillations (see also Figure 12):

- The angular degree l is equal to the number of surface nodal lines.
- The azimuthal order m is equal to the number of surface vertical nodal lines (passing through the poles).
- The radial order n is equal to the number of nodes along the radius, i.e. the number of nodal surfaces in the stellar interiors.

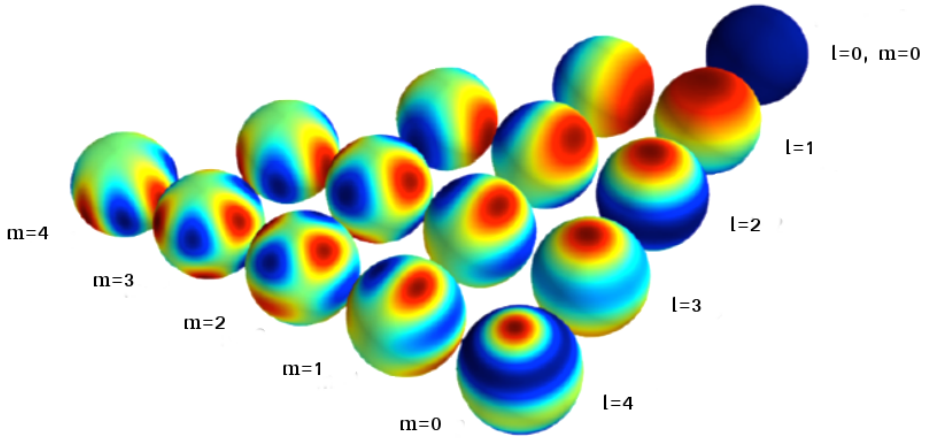

(a)

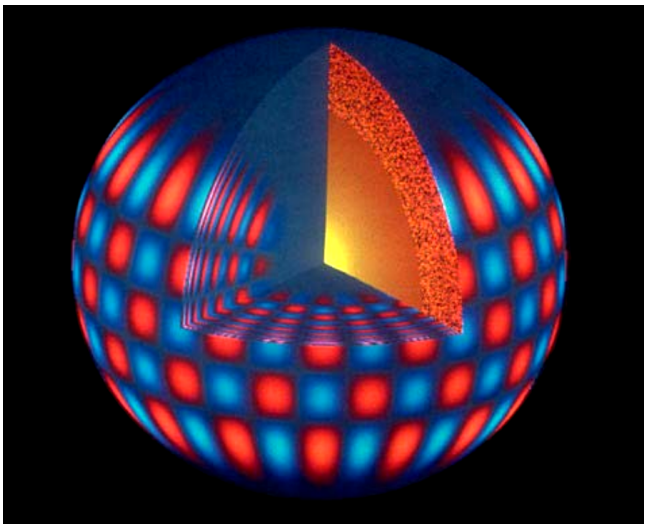

(b)

Figure 12.: *Panel 12a: representation of non-radial oscillations for some values of angular degree and azimuthal order as they appear at the surface. The colours indicate regions expanding or contracting in the radial direction. Note the position of the nodal lines on varying l and m. The case $m = l = 0$ is that of radial pulsations. Figure taken from Beck & Kallinger (2013). Panel 12b: the structure of a non-radial mode inside the star. We can see the nodal surfaces along the radius inside the star and the repetition of the surface pattern at any depth.*

- Nodal lines are not located only at the surface but at all depths.
- We remember that $Y_l^m(\theta, \phi) \propto e^{jm\phi}$ so $\delta\mathbf{r}(r, \theta, \phi, t) \propto e^{j(m\phi+\sigma t)}$. If $m \neq 0$ then $\delta\mathbf{r} \propto \cos(m\phi + \sigma t)$ and consequently waves move around the polar axis with angular phase velocity (i.e. the angular velocity of vertical nodal lines). Instead, $m = 0$ is the case of stationary waves with period $\Pi = 2\pi/\sigma$.
- The azimuthal order does not appear in the eigenvalue problem so $\sigma^2_{nlm} = \sigma^2_{nlm'}$. This degeneration can be broken by effects of rotation and magnetic field.
- Many different oscillations can be active at the same time.

2.3 PRESSURE AND GRAVITY MODES

In order to interpret solutions of the fourth-order system of differential equations for non-radial oscillations, we proceed by successive approximations.

2.3.1 The Cowling Approximation and Trapping

The Cowling Approximation consists in neglecting the perurbation of the gravitational potential, ψ'. This approximation is good for high values of n and l. Indeed, assuming $\psi'(r) \propto e^{jnr}$, Equation 119c becomes

$$\psi' = -4\pi G\rho' \left[n^2 + \frac{l(l+1)}{r^2} \right]^{-1} \tag{136}$$

If we apply this approximation then Equations 127a and 127b become

$$\frac{1}{\rho}\frac{\mathrm{d}P'}{\mathrm{d}r} + \frac{P'}{\rho c_s^2} g + (N^2 - \sigma^2)\xi_r = 0 \tag{137a}$$

$$\frac{1}{r^2}\frac{\mathrm{d}}{\mathrm{d}r}(r^2\xi_r) - \frac{g}{c_s^2}\xi_r + \left(1 - \frac{S_l^2}{\sigma^2}\right)\frac{P'}{\rho c_s^2} = 0 \tag{137b}$$

and $\xi_h = P'/(r\sigma^2\rho)$. As we are going to see, the frequencies N and S_l are crucial. We have only defined the Lamb frequency, but its physical meaning is simple. Let $\mathbf{k} = k_r\mathbf{e}_r + k_h\mathbf{e}_h$ be the wave number, then S_l is the angular frequency of the tangential component: $S_l = k_h c_s$.
Now, since $\frac{1}{\rho}\frac{\mathrm{d}P}{\mathrm{d}r} = -g$ in the unperturbed model and using the definition of the pressure scale height, $H_P = \left(-\frac{1}{\rho}\frac{\mathrm{d}P}{\mathrm{d}r}\right)^{-1}$, it is easy to demonstrate that $g/c_s^2 = (\Gamma_1 H_P)^{-1}$. When this relation is introduced into Equations 137, it results

$$\frac{\mathrm{d}P'}{\mathrm{d}r} = -\frac{P'}{\Gamma_1 H_P} + \sigma^2\rho\left(1 - \frac{N^2}{\sigma^2}\right)\xi_r \tag{138a}$$

$$\frac{2}{r}\xi_r + \frac{\mathrm{d}\xi_r}{\mathrm{d}r} - \frac{1}{\Gamma_1 H_P}\xi_r + \left(1 - \frac{S_l^2}{\sigma^2}\right)\frac{P'}{\rho c_s^2} = 0 \tag{138b}$$

We assume that the scale heights and the radius are much greater than the other quantities, so that

$$\frac{\mathrm{d}P'}{\mathrm{d}r} \simeq \sigma^2\rho\left(1 - \frac{N^2}{\sigma^2}\right)\xi_r \tag{139a}$$

$$\frac{\mathrm{d}\xi_r}{\mathrm{d}r} \simeq \left(\frac{S_l^2}{\sigma^2} - 1\right)\frac{P'}{\rho c_s^2} \tag{139b}$$

At this point, with the same hypothesis, we take the derivative with respect to r of the last equation. It results

$$\frac{\mathrm{d}\xi_r^2}{\mathrm{d}r^2} \simeq \frac{\sigma^2}{c_s^2}\left(\frac{S_l^2}{\sigma^2} - 1\right)\left(1 - \frac{N^2}{\sigma^2}\right)\xi_r \tag{140}$$

Since $\xi_r \propto e^{jk_r r}$, it must be

$$\mathcal{K}(r) := k_r^2 = \frac{\sigma^2}{c_s^2}\left(\frac{S_l^2}{\sigma^2} - 1\right)\left(1 - \frac{N^2}{\sigma^2}\right) \tag{141}$$

and consequently $\|\mathbf{k}\|^2 = k_r^2 + k_h^2 = \mathcal{K}(r) + l(l+1)/r^2$.
Hence there are two possibilities:

- σ^2 is greater than or lower than both S_l^2 and N^2: this implies $\mathcal{K}(r) > 0$ so the solutions are periodic;

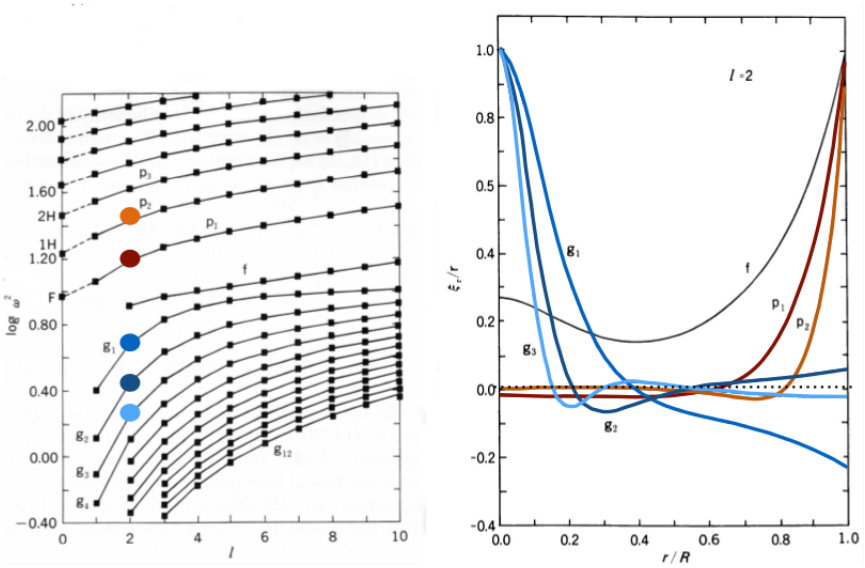

Figure 13.: *Some p- and g-modes computed for a polytropic model with index 3. In the left panel the separation between the two families is clearly visible. Each black square represents a mode. The radial perturbation amplitudes of the modes marked with coloured circles are shown to the right. In the right panel we can verify the behaviour of the radial perturbation amplitude here denoted by ξ_r. Credits, "Theoretical Astrophysics: Asteroseismology", J. Montalbán, adapted from Unno et al. (1989).*

- $S_l^2 < \sigma^2 < N^2$ or $N^2 < \sigma^2 < S_l^2$: this implies $\mathcal{K}(r) < 0$ so the solutions grow or decay exponentially.

Thus the Lamb and the Brunt-Väisälä frequencies have a key role for the propagation of non-radial oscillations. We say that the modes are trapped in regions whose limits are determined by the conditions $\sigma = N, S_l$.

2.3.2 p-modes and g-modes

There are two families of eigenfunctions which are called p- and g-modes. The p-modes are modes supported by pressure forces and have a frequency that increases with n. The g-modes, instead, are supported by gravity and have a frequency that decreases with n. The two families are separated by a surface gravity mode usually denoted by f (see Figure 13). The frequency of f is an upper limit for g-modes and a lower limit for p-modes. Another important difference that we are going to investigate is the propagation region. As boundary condition at the surface we have imposed $\delta P = P' + \xi_r(\partial P/\partial r) = 0$ so

$$\xi_h(R) = \frac{1}{R\sigma^2}\left(\psi'(R) + \frac{P'(R)}{\rho(R)}\right) = \frac{1}{R\sigma^2}\left(\psi'(R) - \xi_r(R)\frac{1}{\rho(R)}\frac{\partial P}{\partial r}\bigg|_{r=R}\right)$$
$$= \frac{1}{R\sigma^2}\left(\psi'(R) + \xi_r(R)g(R)\right) \quad (142)$$

hence, applying the Cowling approximation, we have

$$\frac{\xi_h(R)}{\xi_r(R)} \simeq \frac{g(R)}{R\sigma^2} = \omega^{-2} \quad (143)$$

where ω is the dimensionless frequency already defined in Paragraph 2.2.4. This means that p-modes, i.e. high-frequency modes, usually have a significant radial component at the surface. Let's give a more detailed description of the propagation of these modes. We refer to the *propagation diagram* of Figure 14. In Figure 17 some examples of eigenfunctions of p-modes and g-modes for a solar model are shown.

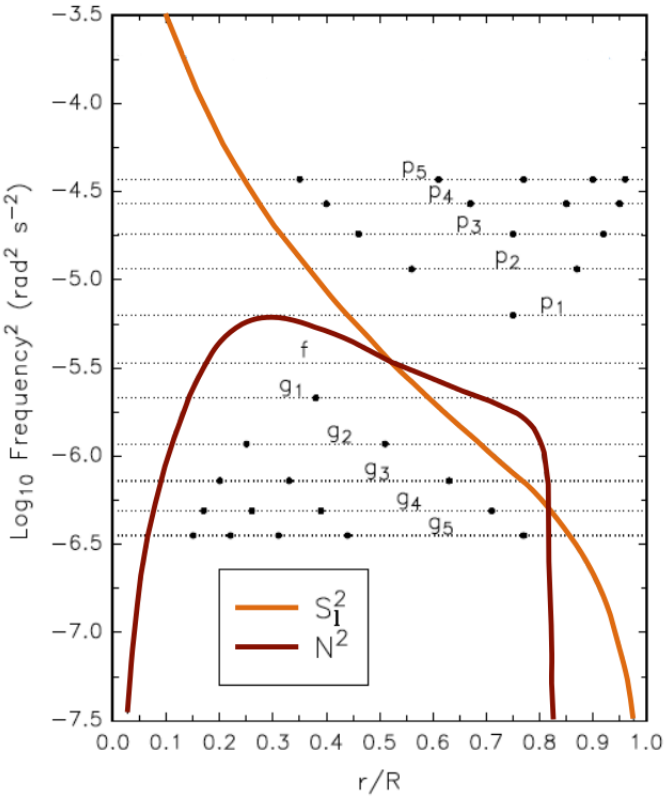

Figure 14.: *An example of propagation diagram similar to the solar one. We can easily identify the regions where p- and g-modes propagate, i.e. above and under the two curves of N^2 and S_l^2 respectively. These regions are often called p- and g-cavity. Credits, "Theoretical Astrophysics: Asteroseismology", J. Montalbán, adapted from Hansen et al. (2004).*

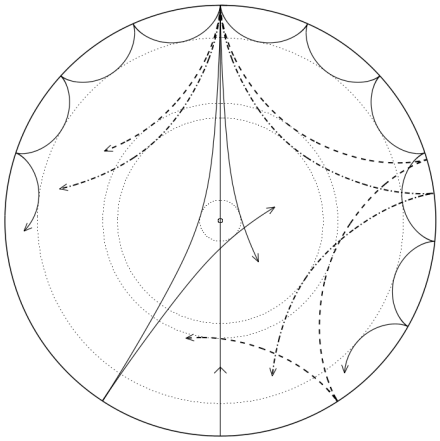

Figure 15.: *A schematic representation of the propagation of some p-modes. Those modes that propagate deeper have lower l or/and higher frequency than those that are confined near the surface. Figure taken from Aerts et al. (2010).*

PROPAGATION OF P-MODES The propagation diagram shows the functions $S_l^2(r)$ and $N^2(r)$. In Figure 14 are also shown some horizontal lines corresponding to the modes' frequencies. We have seen that a mode with angular frequency σ propagates only where σ^2 is greater or lower than both $S_l^2(r)$ and $N^2(r)$. Therefore we can immediately understand that for a star with a propagation diagram like this of Figure 14, there are a group of low-frequency modes, the g-modes, which propagates preferentially in the inner regions and a group at higher frequencies, the p-modes, which propagates in the envelope. Therefore the p-modes have in general lower inertia than the g-modes because of the term $\rho|\xi_n|^2$ (remember the definition of oscillatory moment of inertia, Equation 68).

In order to have an idea of how the p-modes propagate inward from the surface, we can assume for simplicity $\sigma^2 \gg S_l^2 \gg N^2$. Thus

$$\mathcal{K}(r) \simeq \frac{\sigma^2 - S_l^2}{c_s^2} \qquad \longrightarrow \qquad \|\mathbf{k}\|^2 = k_r^2 + k_h^2 = \frac{\sigma^2}{c_s^2} \tag{144}$$

It is clear that the role of the speed of sound is fundamental. Firstly, it is the propagation velocity (since $\|\mathbf{k}\|^2 = \sigma^2/c_s^2$) and it determines the internal radius of the propagation region:

$$\sigma^2 = S_l^2 \qquad \longrightarrow \qquad r_{\text{in}}^2 = \frac{l(l+1)}{\sigma^2} c_s^2(r_{\text{in}}) \tag{145}$$

Moreover, since $c_s(r)$ increases with depth, then $k_r^2 \propto c_s^{-2}$ decreases with depth until it vanishes at $r = r_{\text{in}}$. This means that at $r = r_{\text{in}}$ the wave can move only tangentially with $|\mathbf{k}| = k_h = \sqrt{l(l+1)}/r_{\text{in}}$. At the surface, instead, k_r is considerably greater than k_h. Finally, we highlight that r_{in} depends also on l and σ. We have small values of r_{in} for small values of l or/and for high values of σ and so n. A schematic representation of the propagation of p-modes is given in Figure 15.

PROPAGATION OF G-MODES For simplicity we assume that $\sigma^2 \ll S_l^2, N^2$, so that

$$\mathcal{K}(r) \simeq \frac{l(l+1)}{r^2}\left(\frac{N^2}{\sigma^2} - 1\right) = k_h^2\left(\frac{N^2}{\sigma^2} - 1\right) \qquad \longrightarrow \qquad \sigma^2 = N^2 \frac{k_h^2}{\|\mathbf{k}\|^2} \tag{146}$$

Now we can understand that g-modes can't propagate in convective regions because $N^2 < 0$ and so also $k_r^2 < 0$ here. Moreover, the radius at which the g-modes reflect does not depend on l. Its dependence on σ, instead, is more or less important

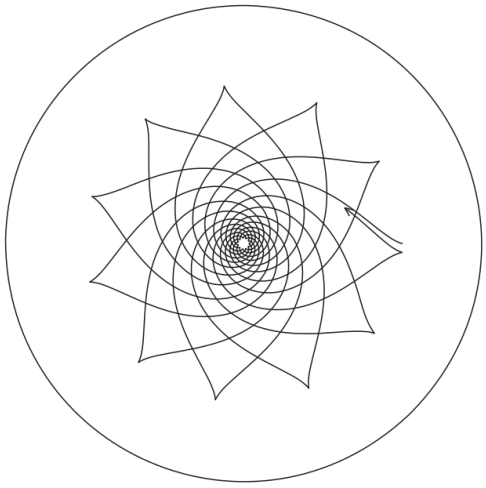

Figure 16.: *A schematic representation of the propagation of a g-mode. Figure taken from Aerts et al. (2010).*

depending on the details of the internal structure of the star and on the domain of σ considered. The radial component of the wave number decreases with σ^2 and consequently the radial order decreases with the frequency too. See Figure 16 for a schematic representation of the propagation of g-modes.

2.4 ASYMPTOTIC THEORY

In this Section we want to study the oscillations pattern under asymptotic approximation.

2.4.1 A second-order differential equation for ξ_r

We firstly derive a useful relation for ξ_r. We start from Equations 137 and we derive the second one without assuming scale heights to be very large. It results

$$\frac{\mathrm{d}^2\xi_r}{\mathrm{d}r^2} = -\left(\frac{2}{r} - \frac{1}{\Gamma_1 H_P}\right)\frac{\mathrm{d}\xi_r}{\mathrm{d}r} - \left[-\frac{2}{r^2} - \frac{\mathrm{d}}{\mathrm{d}r}\left(\frac{1}{\Gamma_1 H_P}\right)\right]\xi_r + \frac{1}{\rho c_s^2}\left(\frac{S_l^2}{\sigma^2} - 1\right)\left[\rho(\sigma^2 - N^2)\xi_r - \frac{1}{\Gamma_1 H_P}P'\right] + \frac{\mathrm{d}}{\mathrm{d}r}\left[\left(\frac{S_l^2}{\sigma^2} - 1\right)\frac{1}{\rho c_s^2}\right]P' \quad (147)$$

and combining with Equations 137 we obtain

$$\frac{\mathrm{d}^2\xi_r}{\mathrm{d}r^2} = -\left(\frac{2}{r} - \frac{1}{\Gamma_1 H_P}\right)\frac{\mathrm{d}\xi_r}{\mathrm{d}r} + \left[-\frac{1}{\Gamma_1 H_P} + \frac{\mathrm{d}}{\mathrm{d}r}\ln\left|\frac{1}{\rho c_s^2}\left(\frac{S_l^2}{\sigma^2} - 1\right)\right|\right]\frac{\mathrm{d}\xi_r}{\mathrm{d}r} + [-\mathcal{K}(r) + \tilde{h}(r)]\xi_r \quad (148)$$

where $\tilde{h}(r)$ is a function of r that gathers all terms not explicitly written. Equation 148 can be written in a more practical form:

$$\frac{\mathrm{d}^2\xi_r}{\mathrm{d}r^2} - \frac{\mathrm{d}\ln f}{\mathrm{d}r}\frac{\mathrm{d}\xi_r}{\mathrm{d}r} + [\mathcal{K}(r) - \tilde{h}(r)]\xi_r = 0 \qquad \text{with } f(r) = \frac{1}{\rho r^2 c_s^2}\left|\frac{S_l^2}{\sigma^2} - 1\right| \quad (149)$$

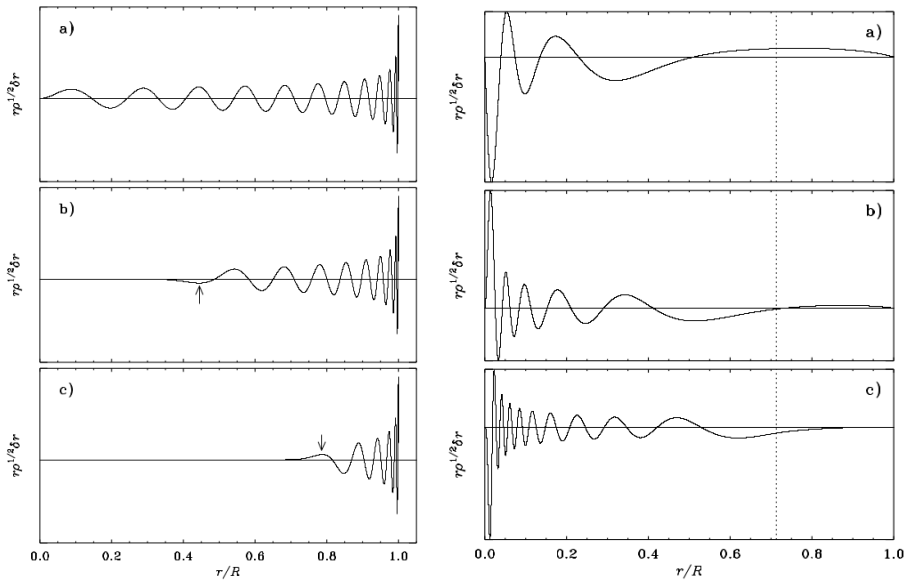

Figure 17.: *Some examples of eigenfunctions of p-modes (panel 17a) and g-modes (panel 17b) for a solar model. Panel 17a: the characteristics of the selected p-modes are a)* $(\sigma, n, l) = (3310\,\mu Hz, 23, 0)$*; b)* $(\sigma, n, l) = (3375\,\mu Hz, 17, 20)$*; c)* $(\sigma, n, l) = (3234\,\mu Hz, 10, 60)$*. For each eigenfunction the asymptotic turning point radius is marked with an arrow. Panel 17b: the characteristics of the selected g-modes are a)* $(\sigma, n, l) = (110\,\mu Hz, -5, 1)$*; b)* $(\sigma, n, l) = (103\,\mu Hz, -10, 2)$*; c)* $(\sigma, n, l) = (100\,\mu Hz, -19, 4)$*. The dotted lines indicate the boundary between core and envelope. Figures taken from Aerts et al. (2010).*

Now we rewrite Equation 149 in terms of the new variable $\hat{A}_r(r) = \xi_r(r) f^{-1/2}$:

$$\frac{\mathrm{d}^2 \hat{A}_r}{\mathrm{d}r^2} + [\mathcal{K}(r) - h(r)]\hat{A}_r = 0 \qquad \text{with } h(r) = \tilde{h}(r) - \frac{1}{2}\frac{\mathrm{d}^2 \ln f}{\mathrm{d}r^2} + \frac{1}{4}\left(\frac{\mathrm{d}\ln f}{\mathrm{d}r}\right)^2 \tag{150}$$

This is the expression we were searching for. It is valid far from the points where $\sigma^2 = S_l^2$ because in their neighbourhoods the logarithmic derivative of f diverges.

2.4.2 The JWKB Analysis

In order to analyze Equation 150 asymptotically, we assume that the solution $\hat{A}_r$ varies rapidly compared with equilibrium quantities. This is called *JWKB analysis*. We thus consider solutions of the form $\hat{A}_r(r) = a(r)e^{j\phi(r)}$ with $\phi(r)$ rapidly varying so that $k_r = \mathrm{d}\psi/\mathrm{d}r$ is large. The amplitude $a(r)$, instead, varies slowly. If we neglect $h(r)$, which is small compared to $\mathcal{K}$, then Equation 150 becomes identical to Equation 140 except for the variable change and the properties of p- and g-modes remain the same. Let's try to substitute $\hat{A}_r(r)$ with $a(r)e^{j\phi(r)}$ in Equation 150 neglecting $h(r)$; it results

$$\frac{1}{2jk_r a}\frac{\mathrm{d}^2 a}{\mathrm{d}r^2} + \frac{1}{a}\frac{\mathrm{d}a}{\mathrm{d}r} + \frac{1}{2k_r}\frac{\mathrm{d}k_r}{\mathrm{d}r} = 0 \tag{151}$$

The asymptotic approximation consists in assuming $a(r) = |k_r|^{-1/2} = |\mathcal{K}(r)|^{-1/4}$ so that $\mathrm{d}^2 a/\mathrm{d}r^2 = 0$, i.e. we neglect $\mathrm{d}^2 a/\mathrm{d}r^2 = 0$. At this point the asymptotic solution is completely determined:

$$\hat{A}_r(r) = A|\mathcal{K}(r)|^{-1/4}\cos\left(\int_{r_t}^{r} \mathcal{K}(r')^{1/2}\,\mathrm{d}r' + \vartheta\right) \qquad \text{for } \mathcal{K}(r) > 0 \tag{152}$$

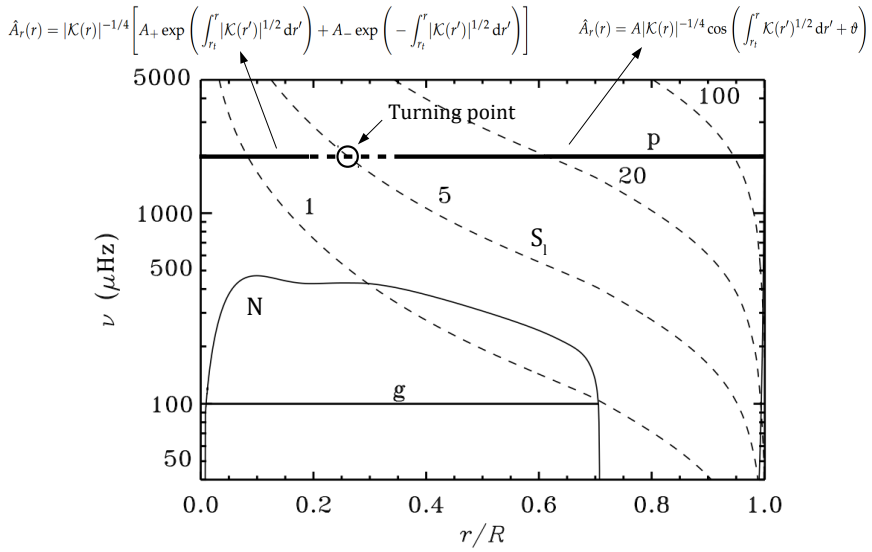

Figure 18.: *Location of the solutions predicted by the JWKB analysis for a p-mode. Figure adapted from the Lecture Notes on Stellar Oscillations of J. Christensen-Dalsgaard available on* http://astro.phys.au.dk/~jcd/oscilnotes/.

and

$$\hat{A}_r(r) = |\mathcal{K}(r)|^{-1/4}\left[A_+ \exp\left(\int_{r_t}^{r}|\mathcal{K}(r')|^{1/2}\,dr'\right) + A_- \exp\left(-\int_{r_t}^{r}|\mathcal{K}(r')|^{1/2}\,dr'\right)\right] \tag{153}$$

for $\mathcal{K}(r) < 0$. The constants A, ϑ, A_+, $A_- \in \mathbb{R}$ can be fixed by boundary conditions. The radius r_t is that of the turning point. In this case we assumed an internal turning point. If an external turning point is present then we can simply exchange the limits of the integral. It is important to remember that r can't be too close to the turning points of p-modes. Again we find oscillatory solutions only for $\mathcal{K}(r) > 0$. To impose the continuity at the connection between exponential and oscillatory solutions leads to the following condition for p-modes:

$$\int_{r_t}^{R}\mathcal{K}(r)^{1/2}\,dr = (n+\alpha)\pi \tag{154}$$

where α is a phase constant fixed by boundary conditions.

2.4.3 Asymptotic Theory for p-modes

We have seen that for $\sigma^2 \gg S_l^2 \gg N^2$ we have $\mathcal{K}(r) \simeq (\sigma^2 - S_l^2)/c_s^2$. Therefore the frequencies of p-modes approximately satisfy the following equation:

$$\int_{r_t}^{R}(\sigma^2 - S_l^2)^{1/2}\frac{dr'}{c_s} = (n+\alpha)\pi \tag{155}$$

with $n \in \mathbb{N}$ and α phase constant fixed by boundary conditions. Equation 155 implicitly determines the frequencies of modes. We write Equation 155 in a more practical form:

$$\int_{r_t}^{R}\left(1 - \frac{L^2c_s^2}{\sigma^2 r^2}\right)^{1/2}\frac{dr}{c_s} = \frac{(n+\alpha)\pi}{\sigma} \qquad \text{with } L^2 = l(l+1) \tag{156}$$

Now we define $w = \sigma/L$ so that

$$\frac{\pi(n+\alpha)}{\sigma} = \int_{r_t}^{R} \left(1 - \frac{c_s^2}{r^2 w^2}\right)^{1/2} \frac{\mathrm{d}r}{c_s} \equiv F(w) \tag{157}$$

where the function $F(w)$ can be derived from observations and then inverted to obtain $c_s(r)$. Now we demonstrate that the second term in the integral of $F(w)$ is negligible for l small, i.e. when the turning point is close to the center.
Let us consider the quantities I, I_1, I_2 defined by

$$I = \int_0^R \frac{\mathrm{d}r}{c_s} - \int_{r_t}^R \left(1 - \frac{c_s^2}{r^2 w^2}\right)^{1/2} \frac{\mathrm{d}r}{c_s} = \underbrace{\int_0^{r_t} \frac{\mathrm{d}r}{c_s}}_{:=I_1} + \underbrace{\int_{r_t}^R \left[1 - \left(1 - \frac{c_s^2}{r^2 w^2}\right)^{1/2}\right] \frac{\mathrm{d}r}{c_s}}_{:=I_2} \tag{158}$$

It can be shown that $\mathrm{d}c_s/\mathrm{d}r$ is zero at the center and, since r_t is assumed small, we can consider $c_s = c_s(r=0)$ between the center and r_r. Thus

$$I_1 = \int_0^{r_t} \frac{\mathrm{d}r}{c_s} \simeq \frac{r_t}{c_s(0)} \simeq \frac{L}{\sigma} = \frac{1}{w} \tag{159}$$

indeed $r_t^2 = l(l+1)c_s^2(r_t)/\sigma^2$ for p-modes. Moreover, the integrand of I_2 is significantly different from zero only near the turning point, so we will take $c_s = c_s(r=0)$ also for the computation of I_2. Applying the variable change $u = c_s/wr$, it results

$$I_2 \simeq \int_1^0 \left[1 - (1-u^2)^{1/2}\right] \left(-\frac{1}{wu^2}\right) \mathrm{d}u = \frac{1}{w}\left(\frac{\pi}{2} - 1\right) \tag{160}$$

Hence $I = I_1 + I_2 = \pi/2w$ and Equation 155 becomes

$$\frac{\pi(n+\alpha)}{\sigma} = \int_0^R \frac{\mathrm{d}r}{c_s} - \frac{L}{\sigma}\frac{\pi}{2} \qquad \longrightarrow \qquad \sigma = \frac{(n + L/2 + \alpha)\pi}{\int_0^R \frac{\mathrm{d}r}{c_s}} \tag{161}$$

Therefore we have derived an interesting formula for the frequencies of p-modes. A more rigorous treatment leads to a very similar expression:

$$\nu_{nl} = \frac{\sigma_{nl}}{2\pi} \simeq \left(n + \frac{l}{2} + \frac{1}{4} + \alpha\right) \Delta\nu \tag{162}$$

where

$$\Delta\nu = \left[2\int_0^R \frac{\mathrm{d}r}{c_s}\right]^{-1} \tag{163}$$

is the *large frequency separation*, a fundamental quantity for Asteroseismology of solar-like oscillators.
Equation 162 predicts that at low l the difference in frequency between two modes with equal l and consecutive n is $\Delta\nu$. Moreover, it is easy to see that $\nu_{nl} \simeq \nu_{n-1,l+2}$. These characteristics have been observed in solar oscillation modes with period of about 5 minutes.

If the variation of c_s near the core is taken into account then it results

$$\nu_{nl} \simeq \left(n + \frac{l}{2} + \frac{1}{4} + \alpha\right)\Delta\nu - (AL^2 - \delta)\frac{\Delta\nu^2}{\nu_{nl}} \tag{164}$$

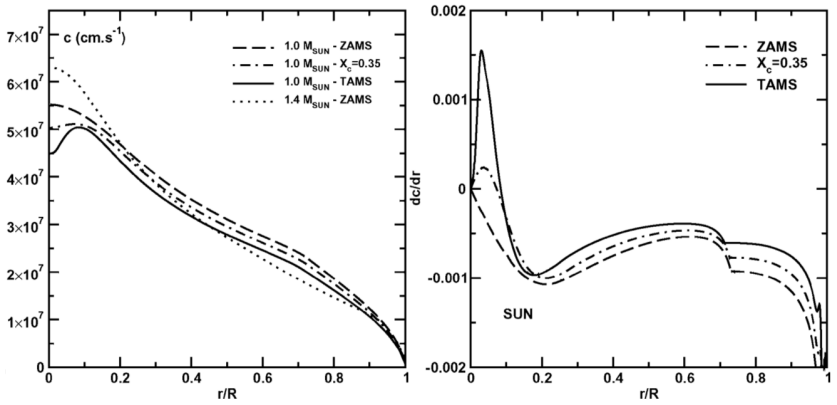

Figure 19.: *The sound speed profile (centre) and the dc/dr profile (right) in $1\,M_\odot$ models, on the ZAMS, in the middle of the MS and at the end of the MS (TAMS). In the TAMS model of $1\,M_\odot$, the speed of sound shows a bowl near the center due to the convective nature of the core. Figure taken from Lebreton & Montalbán (2009).*

where

$$A = \frac{1}{4\pi^2 \Delta\nu}\left[\frac{c_s(R)}{R} - \int_0^R \frac{\mathrm{d}c_s}{\mathrm{d}r}\frac{\mathrm{d}r}{r}\right] \tag{165}$$

and neglecting $c_s(R)/R$ we obtain

$$\delta\nu_{nl} := \nu_{nl} - \nu_{n-1,l+2} \simeq -(4l+6)\frac{\Delta\nu}{4\pi^2\nu_{nl}}\int_0^R \frac{\mathrm{d}c_s}{\mathrm{d}r}\frac{\mathrm{d}r}{r} \tag{166}$$

$$\delta\nu_l := \langle\delta\nu_{nl}\rangle_n \simeq (4l+6)D_0 \tag{167}$$

with

$$D_0 = -\frac{1}{4\pi^2}\left\langle\frac{\Delta\nu}{\nu_{nl}}\right\rangle\int_0^R \frac{\mathrm{d}c_s}{\mathrm{d}r}\frac{\mathrm{d}r}{r} \tag{168}$$

The quantity $\delta\nu_{nl}$ is called *small separation*. We can also write

$$\nu_{nl} \simeq \left(n + \frac{l}{2} + \frac{1}{4} + \alpha\right)\Delta\nu - l(l+1)D_0 \tag{169}$$

The reason why our first derivation was inaccurate is that $-\frac{1}{r}\frac{\mathrm{d}c_s}{\mathrm{d}r}$ and so D_0 are not negligible because of the composition gradient. It is clear that the small separation strongly depends on the core properties.

2.4.4 $(\Delta\nu, D_0)$ Diagrams

While a main-sequence star evolves the hydrogen abundance in the core decreases and μ increases. Hence, since the central temperature does not vary a lot during hydrogen burning, the speed of sound $c_s \propto T/\mu$ decreases. In the inner regions the hydrogen burning is faster so the decrease of c_s is faster too. Consequently the function $c_s(r)$ shows a local minimum at the center and $\mathrm{d}c_s/\mathrm{d}r$ is positive in the core (see Figure 19). Thus inner regions lead to a negative contribution to D_0. This contribution increases with evolution so D_0 decreases with evolution and can be used to estimate the evolution stage of the star. On the other hand $\Delta\nu \propto \tau_{\mathrm{dyn}}^{-1} \propto \sqrt{\overline{\rho}}$. These considerations allow us to use a $(\Delta\nu, D_0)$ diagram as an H-R diagram (see Figure 20).

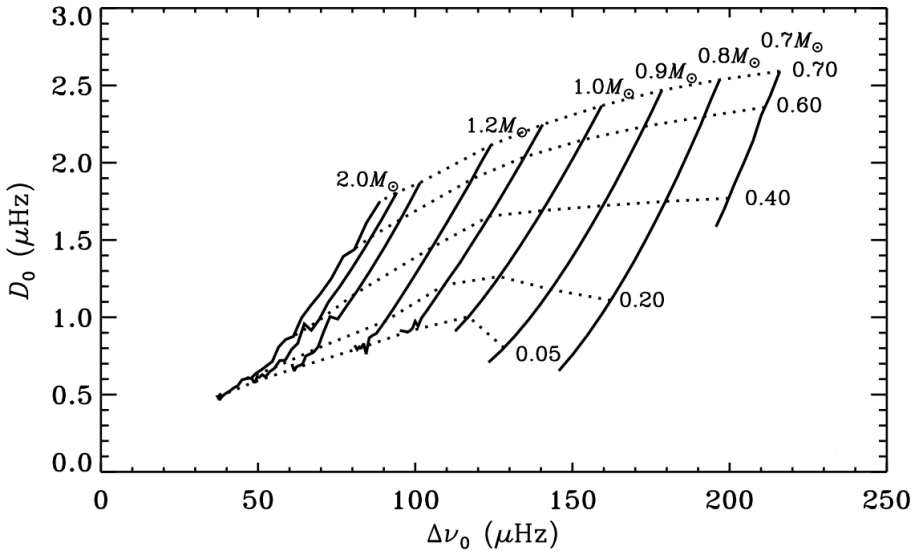

Figure 20.: $(\Delta\nu, D_0)$ *diagram showing evolutionary tracks (filled lines) of stars with masses* 0.7, 0.8, 0.9, 1.0, 1.2, 2.0 $M_\odot$. *The large separation, here denoted by* $\Delta\nu_0$, *has been computed averaging the difference between modes with* $l = 0$ *and consecutive* n. *The dotted lines are curves of constant central hydrogen abundance whose value is reported to the right. Figure taken from the Lecture Notes on Stellar Oscillations of J. Christensen-Dalsgaard available on* `http://astro.phys.au.dk/~jcd/oscilnotes/`.

2.4.5 Asymptotic Theory for g-modes

We have seen that in the case of g-modes with $\sigma^2 \ll S_l^2, N^2$ we can write

$$\mathcal{K}(r) \simeq \frac{l(l+1)}{r^2}\left(\frac{N^2}{\sigma^2} - 1\right) \tag{170}$$

Since g-modes usually are confined between two zeros, say r_1 and r_2, of $\mathcal{K}(r)$, then an expression similar to Equation 155 holds:

$$\int_{r_1}^{r_2} \mathcal{K}(r)^{1/2}\,\mathrm{d}r = \int_{r_1}^{r_2} L\left(\frac{N^2}{\sigma^2} - 1\right)^{1/2}\frac{\mathrm{d}r}{r} = (n + \alpha_g)\pi \tag{171}$$

Thus we can write

$$\frac{n + \alpha_g}{L} = G(\sigma) \qquad \text{with } G(\sigma) = \frac{1}{\pi}\int_{r_1}^{r_2}\left(\frac{N^2}{\sigma^2} - 1\right)^{1/2}\frac{\mathrm{d}r}{r} \tag{172}$$

Clearly r_1 and r_2 are the positions of the turning points of the g-cavity, but they are well-defined only if $N^2(r)$ has a single maximum, $N^2_{\max}$, as we are assuming. Equation 172 gives the following results:

$$\lim_{\sigma \to N_{\max}} G(\sigma) = 0 \qquad \lim_{L\to\infty} \sigma = N_{\max} \tag{173}$$

Consequently for high n and low l the frequency is much lower than N in the g-cavity and we can treat the inner regions near r_1 as we have done for p-modes by using the proportionality of N with r near the center. However the expansion at the outer turning point needs a complicated method. We only report the final result:

$$\sigma_{nl} \simeq \frac{L\int_{r_1}^{r_2} N\frac{\mathrm{d}r}{r}}{\pi(n + l/2 + \alpha_g)} \tag{174}$$

therefore

$$\Pi_{nl} = \frac{2\pi}{\sigma_{nl}} \simeq \frac{2\pi^2(n + l/2 + \alpha_g)}{\sqrt{l(l+1)}\int_{r_1}^{r_2} N\frac{dr}{r}} = \frac{n + l/2 + \alpha_g}{\sqrt{l(l+1)}}\Pi_0 \tag{175}$$

where

$$\Pi_0 := \frac{2\pi^2}{\int_{r_1}^{r_2} N\frac{dr}{r}} \tag{176}$$

Hence g-modes with equal l and consecutive n are (approximately) equally spaced in period:

$$\Delta\Pi_{nl} = \Pi_{nl} - \Pi_{n-1,l} \simeq \frac{\Pi_0}{\sqrt{l(l+1)}} \tag{177}$$

Since N increases with evolution then we expect a decrease of Π_0 and so also of $\Delta\Pi_l$. This fact implies an increase of the number of g-modes per frequency interval.

2.4.6 The propagation diagram during the main sequence and beyond.

As a main-sequence star evolves, it contracts and a composition gradient builds up because of the hydrogen burning. These facts lead to an increase of N near the core center (see Figure 21a). Consequently, the characteristic frequency of p-modes decreases and the maximum frequency permitted of g-modes increases leading to a significant overlap between the frequency domains of p and g cavities, in particular in the domain of solar-like oscillators. When the width of the region, called *evanescent zone* (see Figure 21b), which separates the g-cavity from the p-cavity is thin enough, then there might be some modes propagating in both the two cavities. In this case we talk about mixed modes. Mixed modes are important because they carry information about the near-core structure and have a detectable amplitude at the surface. As we are going to see, mixed modes are especially useful for asteroseismology of RGB and red-clump stars. Figure 22 shows propagation diagrams of a 1.5 $M_\odot$ star during the RGB and helium-core-burning (HeCB) phases. We can see that the maximum Brunt-Väisälä frequency increases during the RGB phase and the peak moves toward the center as the star approaches the RGB tip. Both these effects imply a higher value of $\int N\frac{dr}{r}$ and so lower Π_0 and $\Delta\Pi$ according to Equations 176 and 177. In the HeCB phase the propagation diagram shows the presence of a convective core. In fact N^2 is negative until the border of the core where it suddenly increases because of the composition gradient. Moreover, the lower central concentration leads to lower values of N than during the RGB phase. This fact provides a powerful method to discriminate between RGB and RC stars, the former having lower period spacing than the latter. The number of mixed modes by frequency interval increases with $\int N\frac{dr}{r}$ and their expected amplitude decrease with their inertia and hence with the importance of the evanescent region (see e.g. Montalbán et al. 2013; Montalbán & Noels 2013).

2.4.7 Echelle Diagram

In order to investigate in detail the properties of the frequency spectrum of oscillations it is useful to introduce the *Echelle Diagram*. In this diagram, frequencies are introduced by expressing them as

$$\nu_{nl} = \nu_0 + k\Delta\nu + \tilde{\nu}_{nl} \tag{178}$$

where ν_0 is a suitable reference frequency and k is an integer such that $\tilde{\nu}_{nl} \in [0, \Delta\nu[$. An Echelle diagram has $\tilde{\nu}_{nl}$ on the $x-$axis and $\nu_0 + k\Delta\nu$ on the $y-$axis. If the asymptotic relation 164 had been exactly satisfied then in Echelle diagrams we would have seen the points representing the modes organized in perfectly vertical lines. These vertical lines, called *ridges*, actually are bent a little (see Figure 23). Each ridge corresponds to a different value of l. Therefore in Echelle diagrams are visible both the large and the small separation, the former being the frequency separation

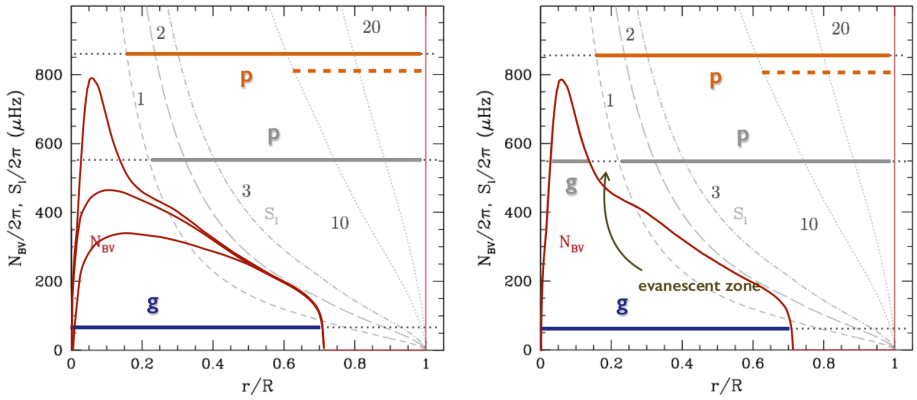

Figure 21.: *Panel 21a: Propagation diagram during the evolution along the main sequence. The thin, light coloured lines illustrate the function $S_l(r/R)$ for the indicated values of the angular degree. Red solid lines show the behaviour of $N(r/R)$ at different evolutionary stages along the main sequence. The frequency N (here denoted by N_{BV}) increases as the star evolves and at a certain point mixed modes can appear as shown in Panel 21b. Credits, "Theoretical Astrophysics: Asteroseismology", J. Montalbán.*

between two subsequent modes belonging to the same ridge (i.e. with the same angular degree) and the latter being defined as the difference $\nu_{nl} - \nu_{n-1,l+2}$.

Figures 24 and 25 present, instead, the Echelle diagram of a 1.5 $M_\odot$ star throughout its evolution starting from the main sequence until the HeCB phase. When the star leaves the main sequence, mixed modes appear in the spectrum modifying the organization of modes in ridges. As the star evolves along the RGB, the evanescent zone becomes wider and the coupling between p and g cavities decreases. As a consequence, highly p-dominated modes appear with a significant amplitude, and the corresponding Echelle diagram recovers the usual aspect with almost vertical ridges corresponding to different angular degrees (see Figures 24 and 25, points dimension is proportional to the mode amplitude). At the HeCB phase, the vertical structure disappear again, since the smaller evanescent region allows mixed modes to appear again.

2.4.8 Solar-like Oscillations and Scaling Relations

We report now the results obtained for the Sun as representative case of all solar-like oscillators (see horizontally barred regions in Figure 10). Figure 26 shows schematically the solar oscillation modes. The 5-minutes modes have been observed for sure while the detection of g-modes has not been confirmed yet. The 5-minutes oscillations are p-modes of radial order between 1 and 20 and angular degree between 0 and 1500. The so-called *fundamental mode f* has been observed for high angular degrees. Keeping l fixed the p-modes are always above the f-mode.
The power spectrum of low-angular degree solar oscillations is shown in Figure 27. It has been obtained thanks to Doppler velocity measurements in disk-integrated light. The amplitudes distribution is peaked around the frequency $\nu_{\max,\odot} \simeq 3100\,\mu$Hz. There are velocity amplitudes up to tens of cm/s and brightness variations up to 8 ppm. In Panel 27b the large and small separations are clearly visible. The large separation of the Sun is about 135 μHz.

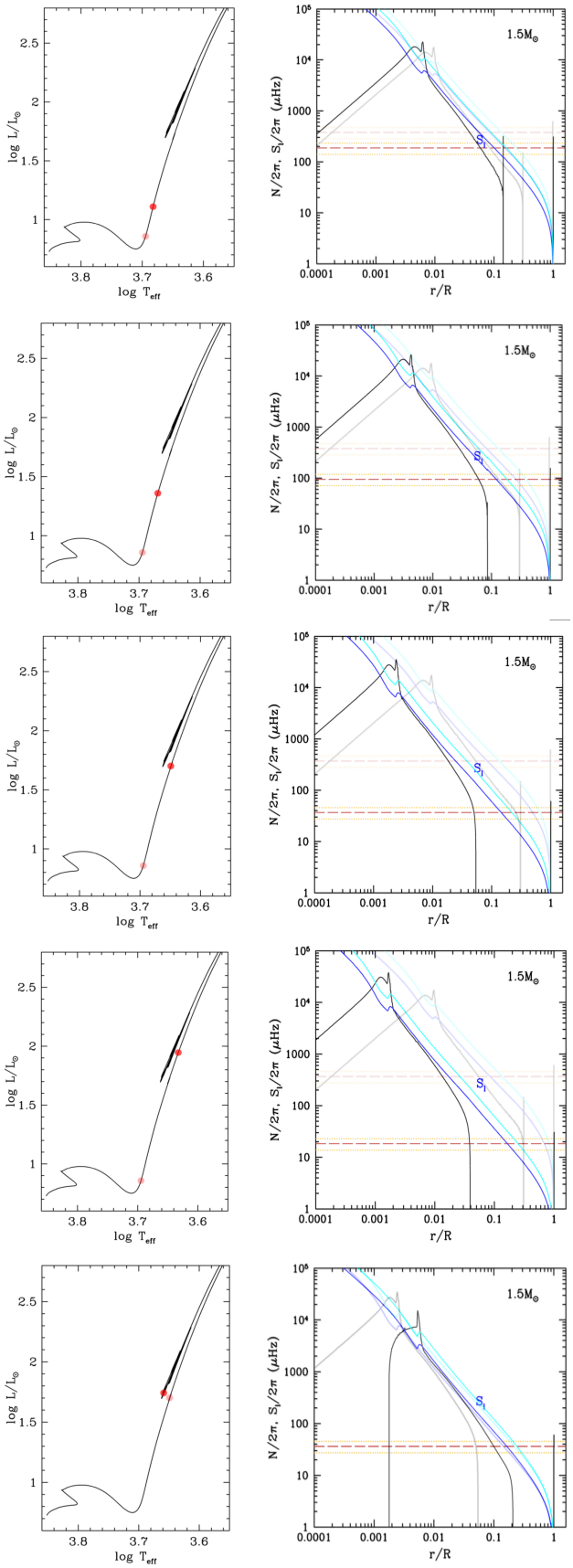

Figure 22.: *Propagation diagram of a* $1.5\,M_{\odot}$ *star during the RGB and the HeCB phases. Figures taken from Montalbán (2013).*

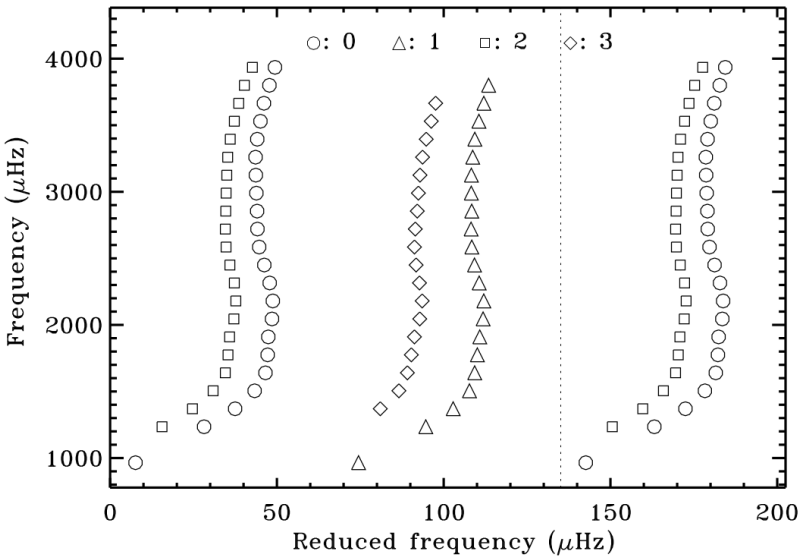

Figure 23.: *Echelle diagram for observed solar frequencies obtained with the* ***Bi****rmingham* ***S****olar* ***O****scillation* ***N****etwork (BiSON) (Chaplin et al. 2002), plotted with* $\nu_0 = 830\,\mu$Hz *and* $\Delta\nu = 135\,\mu$Hz*. Circles, triangles, squares and diamonds are used for modes of degree* $l = 0$, 1, 2 *and* 3*, respectively. For clarity the points for* $l = 0$ *and* 2 *have been repeated in the right-hand part of the diagram; the dotted vertical line indicates* $\Delta\nu$*. Figure taken from the Lecture Notes on Stellar Oscillations of J. Christensen-Dalsgaard available on* `http://astro.phys.au.dk/~jcd/oscilnotes/`.

SCALING RELATIONS The following homology relations hold:

$$\begin{cases} \dfrac{P}{P_\odot} = \left(\dfrac{M}{M_\odot}\right)^{2}\left(\dfrac{R}{R_\odot}\right)^{-4} \\ \dfrac{\rho}{\rho_\odot} = \left(\dfrac{M}{M_\odot}\right)\left(\dfrac{R}{R\odot}\right)^{-3} \end{cases} \longrightarrow \quad \frac{c_s}{c_{s,\odot}} = \left(\frac{M}{M_\odot}\right)^{1/2}\left(\frac{R}{R_\odot}\right)^{-1/2} \tag{179}$$

Now, as shown in Ulrich (1986), if we approximate $\Delta\nu$ with $(2R/c_s)^{-1}$ then we obtain

$$\frac{\Delta\nu}{\Delta\nu_\odot} = \left(\frac{M}{M_\odot}\right)^{1/2}\left(\frac{R}{R_\odot}\right)^{-3/2} \tag{180}$$

Moreover, the semi-empirical relation $\nu_{\max} \propto g/\sqrt{T_{\rm eff}}$ holds (Brown et al. 1991), hence

$$\frac{\nu_{\max}}{\nu_{\max,\odot}} = \left(\frac{M}{M_\odot}\right)\left(\frac{R}{R_\odot}\right)^{-2}\left(\frac{T_{\rm eff}}{T_{\rm eff,\odot}}\right)^{-1/2} \tag{181}$$

Therefore, if we measure $T_{\rm eff}$, $\nu_{\max}$ and $\Delta\nu$ then we can estimate the mass and radius of a star with Equations 180 and 181:

$$\frac{R}{R_\odot} = \left(\frac{\nu_{\max}}{\nu_{\max,\odot}}\right)\left(\frac{\Delta\nu}{\Delta\nu_\odot}\right)^{-2}\left(\frac{T_{\rm eff}}{T_{\rm eff,\odot}}\right)^{1/2} \tag{182a}$$

$$\frac{M}{M_\odot} = \left(\frac{\nu_{\max}}{\nu_{\max,\odot}}\right)^{3}\left(\frac{\Delta\nu}{\Delta\nu_\odot}\right)^{-4}\left(\frac{T_{\rm eff}}{T_{\rm eff,\odot}}\right)^{3/2} \tag{182b}$$

which are usually called *asteroseismic scaling relations* (Kjeldsen & Bedding 1995). Obviously this is not a rigorous method to derive mass and radius of stars, but it works quite well and predicts correctly the decrease of $\nu_{\max}$ and $\Delta\nu$ with evolution.

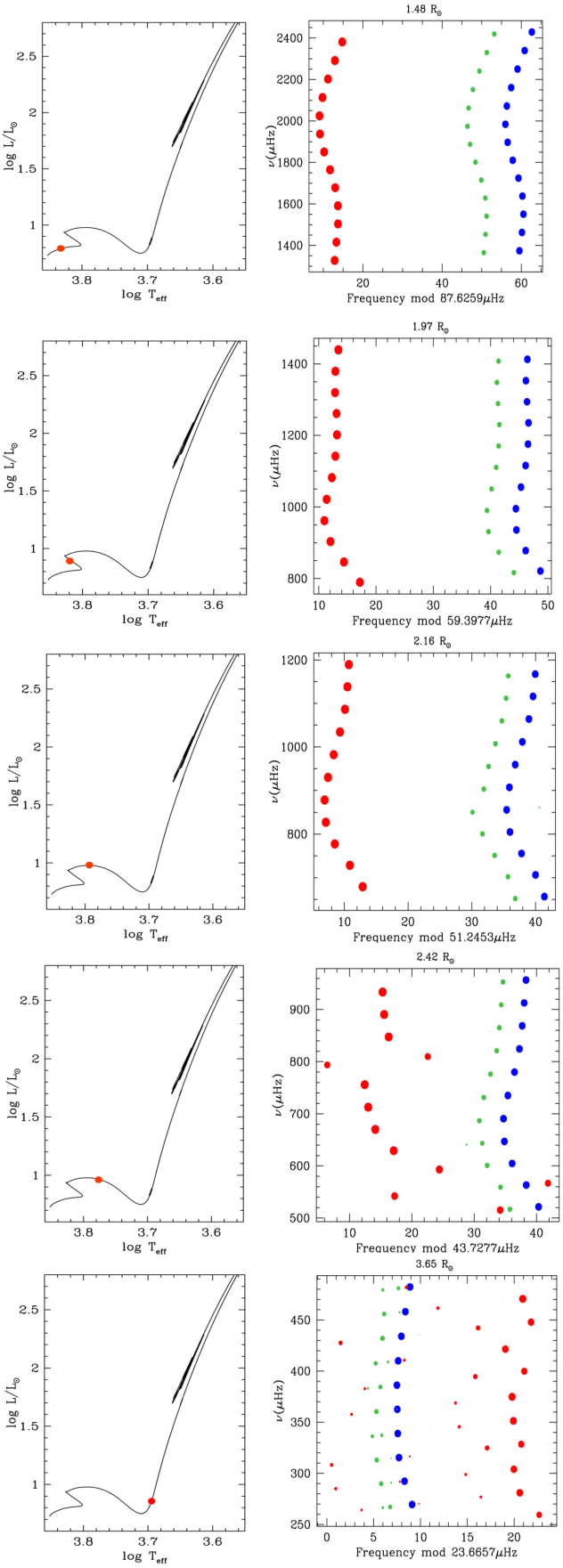

Figure 24.: *Echelle diagram of a* $1.5\,M_{\odot}$ *star during its evolution (Part I). Blue, red and green points represent modes with angular degree* $l = 0, 1, 2$ *respectively. Figures taken from Montalbán (2013).*

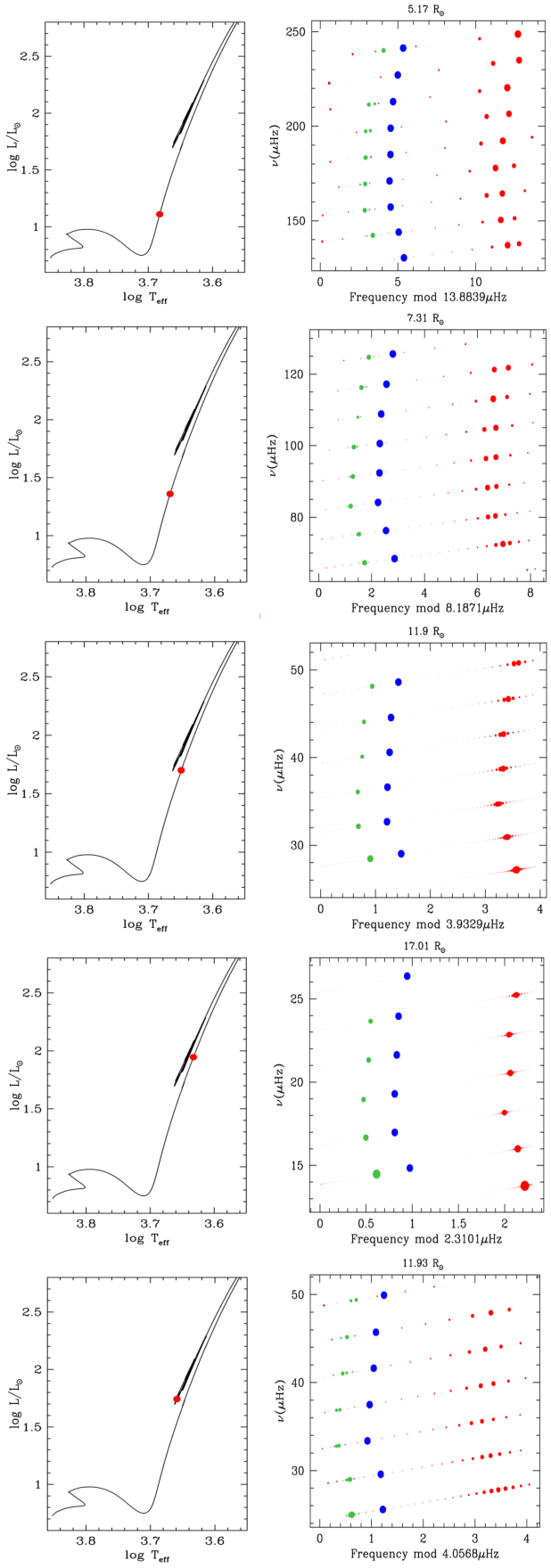

Figure 25.: *Echelle diagram of a* $1.5\,M_{\odot}$ *star during its evolution (Part II). Blue, red and green points represent modes with angular degree* $l = 0, 1, 2$ *respectively. Figures taken from Montalbán (2013).*

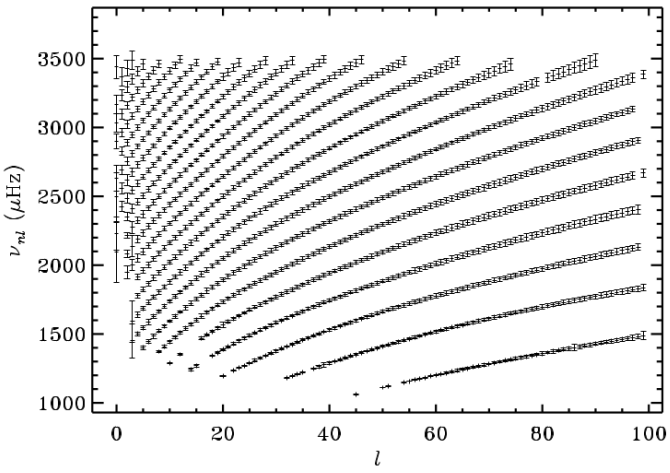

(a)

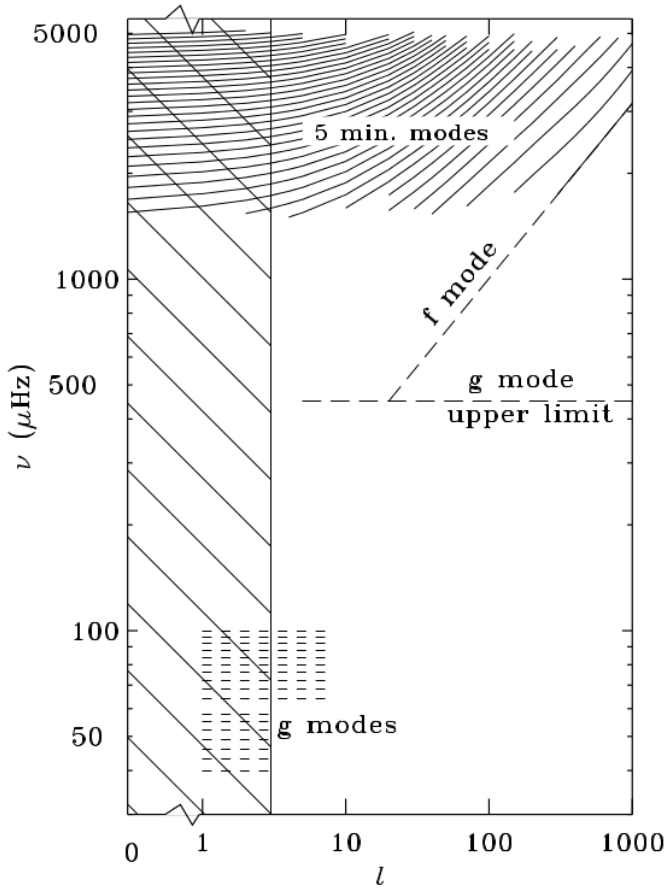

(b)

Figure 26.: *Panel 26a: observed solar p-modes' frequencies as a function of l. The 1000σ error bars are shown. Modes with the same radial order n are aligned and form a ridge. The lowest ridge corresponds to n = 1. Panel 26b: schematic representation of solar oscillations. The 5-minutes modes are the p-modes. The f-mode and g-modes whose detection has been claimed, but not confirmed are also shown. The hatched region indicates the values of l of the modes that can be observed in disk-integrated light. Indeed this observational technique averages out modes of high angular degree. Figures taken from the Lecture Notes on Stellar Oscillations of J. Christensen-Dalsgaard available on* `http://astro.phys.au.dk/~jcd/oscilnotes/`.

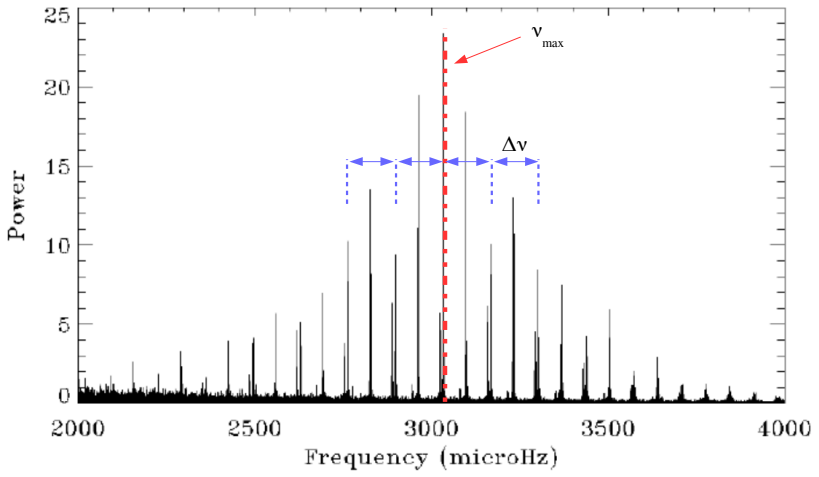

(a)

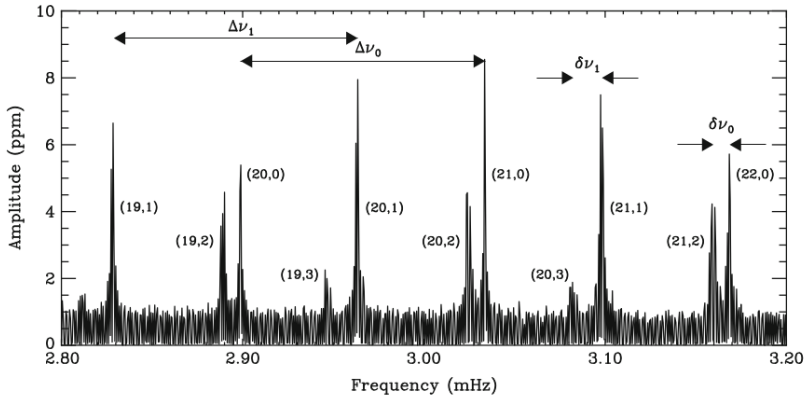

(b)

Figure 27.: *Panel 27a: the power spectrum of low-angular degree solar oscillations. It has been obtained thanks to Doppler velocity measurements in disk-integrated light acquired by the BiSON Network. We can see the typical gaussian shape of a spectrum dominated by stochastically excited modes: centered at a frequency ν_{max} and showing the regularities predicted by the asymptotic theory. Panel 27b: zoom of the central region around* 3100 μHz. *For each mode the radial order and the angular degree are indicated. The estimates $\Delta\nu_0$ and $\Delta\nu_1$ of the large separation and the small separation $\delta\nu_0$ and $\delta\nu_1$ are clearly visible. Figure taken from Aerts et al. (2010).*

The uncertainties of the estimates provided by these scaling relations are just over 10% in mass and about 5.5% in radius. Moreover, scaling relations provide an immediate and model-independent method for stellar parameters estimation. We remember that the mass and the radius are extremely important stellar parameters because allow the estimate of the age and the absolute magnitude and so of the distance.

2.5 OBSERVATIONAL ASTEROSEISMOLOGY

2.5.1 Observational Techniques

What we need to do Asteroseismology are the frequencies of stellar pulsations. Stellar oscillations can be observed through photometric measurements of the stellar flux variations or through spectroscopic measurements of Doppler velocity variations. Of course different oscillation modes are active at the same time in general. Therefore, once the time series has been obtained, then a Fourier analysis is necessary to identify the modes. Although we have a good understanding of the frequency spectrum, we can't say the same for what concerns the oscillation amplitudes so almost all the information come from the frequency pattern. Note that, except for the Sun and very few cases, we can observe stars only in disk-integrated light so the modes with high angular degree cancel out and can't be observed. Also for stars whose disk can be resolved high-degree modes have not been detected yet. Let us summarize the main characteristics of the photometric and spectroscopic techniques. The typical observational results are reported in Tables 1 and 2.

PHOTOMETRY

- Working principle: precise measurement of stellar intensity variations mainly due to temperature variations.
- Precision level achieved: a few parts per million with space telescopes.
- Main noise sources: Poisson noise. The signal-to-noise ratio (S/N) goes with the square root of the number of photons collected. However, if we increase too much the observation time then the frequency resolution of the spectrum and the Nyquist frequency decrease so the identification of modes becomes more difficult. Therefore the study of variability for faint stars requires large telescopes able to collect a large number of photons in a short time. For bright stars the most important source of noise may not be the Poisson noise, but atmospheric and instrumental effects or errors introduced during data reduction and analysis.
- The photometric amplitudes are not the same for every passband because of the stellar spectrum shape: many stars show higher intensity variations in the blue than in the red. Moreover, the photometric amplitudes and their phases at different wavelengths depend on the mode geometry. This property is useful for mode identification.

SPECTROSCOPY

- Working principle: precise measurements of line profile variations mainly due to Doppler velocity variations.
- Precision level achieved: a few cm/s with ground-based telescopes.
- Instrumental requirements: ideally a line profile should be sampled with 50 points in wavelength and with a S/N above 200. Spectra with such resolutions can only be obtained from ground-based telescopes.
- Main noise sources: Poisson noise and low-frequency noise due to temperature, pressure and humidity changes in the spectrograph during the observation.

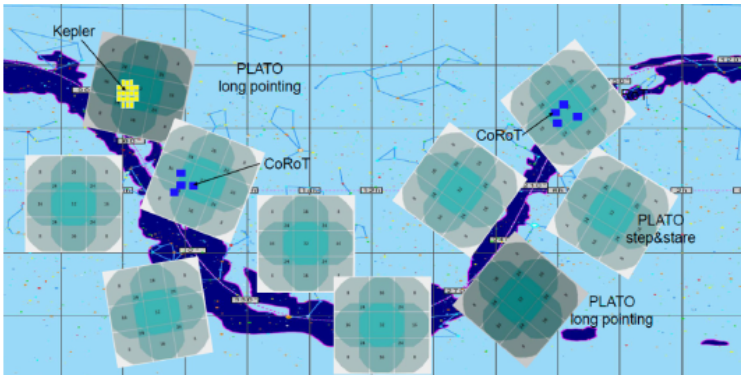

Figure 28.: *Schematic comparison of PLATO 2.0, CoRoT and Kepler's fields of view and observational strategy. Figure taken from the PLATO Assessment Study Report (Yellow Book), ESA/SRE(2013)5.*

2.5.2 Observations of Stellar Oscillations across the H-R Diagram

Although variable stars are more concentrated along the instability strip, if we look at Figure 10 it is clear that stellar oscillations have been observed at any evolution stage. We report in Tables 1 and 2 the main characteristics of the various types of pulsating stars. In the tables 'F' stands for fundamental radial mode, 'FO' for first radial overtone and 'S' for strange mode oscillations. The S-modes are exited in strong non-adiabatic conditions due to a great enhancement of the opacity in the partial ionization zones of helium (the second one) and of heavy elements (Aerts et al. 2010). An important update in Tables 1 and 2 should be done: during the last years a great variety of mixed-modes has been observed in red giants, opening a window to the study of stellar interiors.

2.5.3 The CoRoT Mission

The CoRoT (**Co**nvection, **Ro**tation and planetary **T**ransits) Mission is one of the most important space missions for Asteroseismology and exoplanet hunting together with the Kepler/K2 Mission. CoRoT started scientific operations on 2 February 2007 and continuously observed star fields in the Milky Way (see Figure 28) for periods of up to 6 months. The mission ended on 17 June 2014. The satellite carries an afocal telescope with a 27-cm lens and a wide-field camera composed of four CCDs that provides a precision of 10^{-6} mag. The pointing accuracy is of 0.5″ and a field of view of $2.8^\circ \times 2.8^\circ$. Table 3 summarizes the main programme details of the mission for what concerns primary asteroseismic targets. Although stars observed during exoplanet hunting have lower luminosities, their light curves have been used to study stellar variability too.

2.5.4 The Kepler and K2 Missions

The Kepler and K2 Missions have been providing the largest collection of light curves with the quality level requested for Asteroseismology. The K2 Mission is the extension of the Kepler Mission. The spacecraft hosts a 0.95 m aperture Schmidt telescope and a CCD array. Originally there were 42 CCDs organized in 21 modules, but three of the modules have no longer been working since August 2016. Each module covers 5 square degrees on the sky for a total field of view of 116 square degrees. Figure 31 shows the single field that was observed during the prime Kepler mission. Kepler observes in only one, broad bandpass ranging from 420 to 900 nm. Figure 32 shows the Kepler bandpass compared to the CoRoT's one and others. The Kepler Mission, launched in March 2009, had as primary objective the detection of exoplanet transits in particular around Sun-like stars. Kepler monitored more than 150 000 stars for about four years. Observations cadence can be of 30 min or 1 min depending on the purpose (e.g. 5-minutes oscillations of a star like the Sun need

Table 1.: *Basic properties of main sequence, giant and compact pulsators. Table taken from Aerts et al. (2010).*

Class name	Other names in the literature	Mode Type	Period Ranges	Amplitudes (brightness)	Amplitudes (velocity)	$\log T_{\rm eff}$ [K] approx. range	$\log L/L_\odot$ approx. range
Solar-like	main sequence	p	3 to 10 min	few ppm	$< 50\,$cm/s	[3.70, 3.82]	$[-0.5, 1.0]$
pulsator	red giants	p	few hours	few tens ppm	few m/s	[3.65, 3.70]	$[-0.5, 2.0]$
γ Dor	slowly pulsating F	g	8 h to 5 d	$< 50\,$mmag	$< 5\,$km/s	[3.83, 3.90]	[0.7, 1.1]
δ Sct	SX Phe (Pop. II)	p	15 min to 8 h	$< 0.3\,$mag	$< 10\,$km/s	[3.82, 3.95]	[0.6, 2.0]
roAp	-	p	5 to 22 min	$< 10\,$mmag	$< 10\,$km/s	[3.82, 3.93]	[0.8, 1.5]
SPB	53 Per	g	0.5 to 5 d	$< 50\,$mmag	$< 15\,$km/s	[4.05, 4.35]	[2.0, 4.0]
β Cep	β CMa, ζ Oph (SpT O)	p, g	1 to 12 h (p)	$< 0.1\,$mag	$< 20\,$km/s	[4.25, 4.50]	[3.2, 5.0]
	53 Per		few days (g)	$< 0.01\,$mag	$< 10\,$km/s		
pulsating Be	λ Eri, SPBe	p, g	0.1 to 5 d	$< 20\,$mmag	$< 20\,$km/s	[4.05, 4.50]	[2.0, 5.0]
pre-MS pulsator	pulsating T Tauri	p	1 to 8 h	$< 5\,$mmag			
	pulsating Herbig Ae/Be	p	1 to 8 h	$< 5\,$mmag			
	pulsating T Tauri	g	8 h to 5 d	$< 5\,$mmag			
p-mode sdBV	EC14026, V361 Hya	p	80 to 800 s	$< 0.1\,$mag		[4.20, 4.50]	[1.2, 2.2]
g-mode sdBV	PG1716 + 426	g	0.5 to 3 h	$< 0.01\,$mag		[4.40, 4.60]	[1.2, 2.6]
	Betsy star, IpsdBV						
PNNV	ZZLep, [WCE]	g	5 h to 5 d	$< 0.3\,$mag			
GW Vir	DOV, PG1159	g	5 to 80 min	$< 0.2\,$mag		[4.80, 5.10]	[1.5, 3.5]
DBV	V777 Her	g	2 to 16 min	$< 0.2\,$mag		[4.40, 4.60]	$[-1.0, 0.7]$
DAV	ZZ Ceti	g	0.5 to 25 min	$< 0.2\,$mag		[3.95, 4.15]	$[-2.6, -2.2]$

Table 2.: *Basic properties of supergiant pulsators. Table taken from Aerts et al. (2010).*

Class name	Other names in the literature	Mode Type	Period Ranges	Amplitudes (brightness)	Amplitudes (velocity)	$\log T_{\rm eff}$ [K] approx. range	$\log L/L_\odot$ approx. range
RR Lyr	RRab	F	~ 0.5 d	< 1.5 mag	< 30 km/s	[3.78, 3.88]	[1.4, 1.7]
	RRc	FO	~ 0.3 d	< 0.5 mag	< 10 km/s		
	RRd	F+FO	0.3 to 0.5 d	< 0.2 mag	< 10 km/s		
Type II Cepheid	W Vir	F	10 to 30 d	< 1 mag	< 30 km/s	[3.70, 3.90]	[2.0, 4.0]
	BL Her	F	1 to 5 d	< 1 mag	< 30 km/s		
RV Tauri	RVa, RVb	F?	30 to 150 d	< 3 mag	< 30 km/s	[3.60, 3.90]	[3.2, 4.2]
Type I Cepheid	-	F	1 to 50 d	< 1 mag	< 30 km/s	[3.55, 3.85]	[2.0, 5.5]
	s-Cepheid	FO	< 20 d	< 0.1 mag	< 10 km/s		
Mira	SRa, SRb	$l = 0$	> 80 d	< 8 mag		[3.45, 3.75]	[2.5, 4.0]
	SRc	$l = 0$	> 80 d	< 1 mag			
	SRd	$l = 0$	< 80 d	< 1 mag			
PVSG (SpT A)	α Cyg	g, S?	10 to 100 d	< 0.3 mag	< 20 km/s	[3.45, 4.00]	[2.5, 4.5]
PVSG (SpT B)	SPBsg	g	1 to 10 d	< 0.3 mag	< 20 km/s	[4.00, 4.50]	[4.3, 5.8]
LBV	S Dor	g, S	2 to 40 d	< 0.1 mag		[3.80, 4.20]	[5.5, 6.5]
WR	WC, WN	g, S	1 h to 5 d	< 0.2 mag		[4.40, 4.70]	[4.5, 6.0]
HdC	R CrB	g?	40 to 100 d	< 0.05 mag	< 10 km/s	[3.50, 4.20]	[3.5, 4.5]
eHe	PV Tel	S	~ 20 d				
	V652 Her	g, S?	~ 0.1 d				
	V2076 Oph	g, S?	0.5 to 8 d				

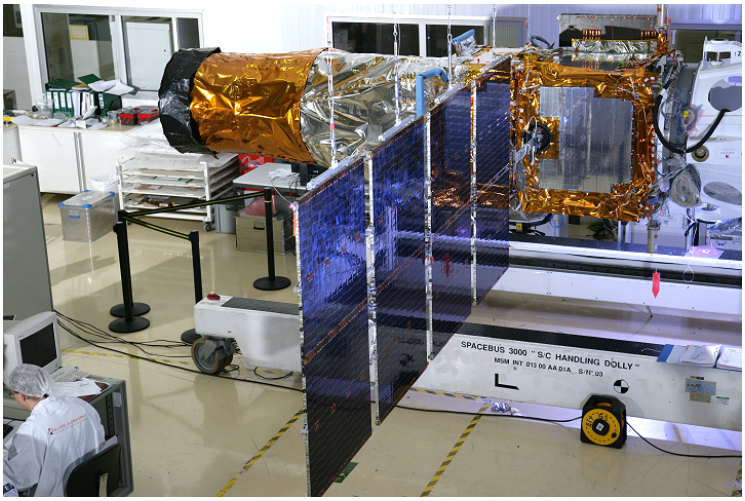

Figure 29.: *Mechanical tests on the solar panels of the CoRoT satellite. Figure taken from the official site of the CoRoT Mission:* https://corot.cnes.fr/en/COROT/index.htm.

Table 3.: *Programme details of the CoRoT Mission for what concerns primary asteroseismic targets.*

	Long runs	Short runs
Observing run duration	150 d	$20 \div 30$ d
Number of stars per run	10	10
Magnitude	[6, 9]	[6, 9]
Number of observing runs	5	$5 \div 10$
Frequency resolution	0.1 μHz	0.6 μHz
Total number of targets	50	$50 \div 100$
Spectral types	mostly A, F, G	all

the short cadence to be detected). After the loss of a second reaction wheel in May 2013 the Kepler Mission was interrupted, the pointing being possible only within the orbital plane of the spacecraft. For this reason in May 2014 the K2 Mission started and it will end in 2017 or 2018. The fields observed during this mission are illustrated in Figure 33: they are located along the spacecraft's orbital plane which is near to the ecliptic's plane. For each field of view there is a dedicated observational campaign that last for about 80 days. Observations' cadence possibilities are the same of Kepler Mission. The activities of this second mission are also mainly involved in planet hunting and stellar polulations studies.

2.6 ENSEMBLE ASTEROSEISMOLOGY

2.6.1 The APOKASC Catalog

Low density red giants show solar-like oscillations with periods of a few days or weeks. Therefore these oscillations can be detected with the Kepler long cadence. We have seen that asteroseismic data can be used to estimate masses and radii of stars if the effective temperature is also available. Then the luminosity $L = 4\pi R^2 \sigma T_{\text{eff}}^4$ can be easily computed. Moreover, by taking into account bolometric correction and extinction the distance can be estimated too.
The APOKASC catalog gathers more than 10 000 giants with asteroseismic and spectroscopic parameters together with measured apparent magnitudes in several passbands (e.g. SDSS *griz* and DDO51 from KIC team, JHK_s from 2MASS, the Kepler magnitude K_p). The asteroseismic data are provided by the Kepler Asteroseismic Science Consortium (KASC) and the spectroscopic ones by the Apache Point Obsrvatory Galactic Evolution Experiment (APOGEE). The stars of APOKASC have

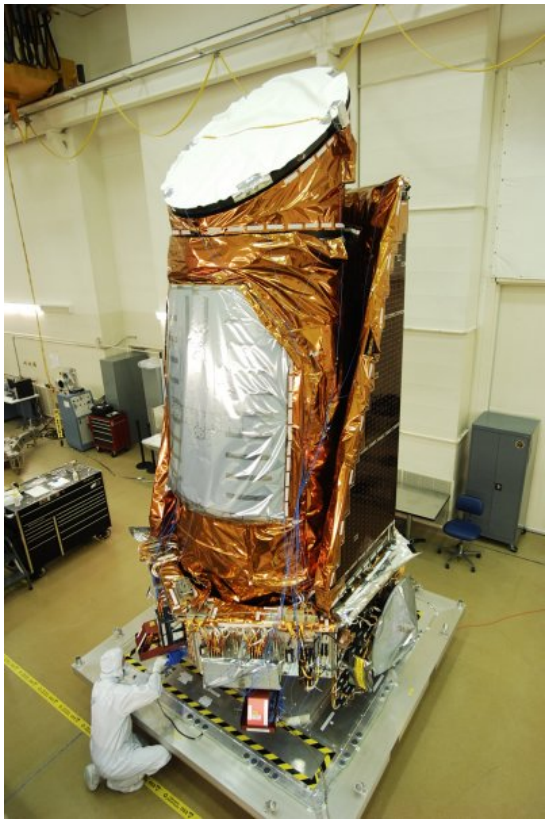

Figure 30.: *The Kepler Space Telescope. Figure taken from the official site of the Kepler & K2 Science Center:* https://keplerscience.arc.nasa.gov/.

apparent magnitude in the H band between 7 and 11. Some of these stars belong to the open clusters NGC6791 and NGC6819. Information of about 2000 stars of the APOKASC catalog are freely available (Pinsonneault et al. 2014). This catalog allows us to derive precise distances of stars located far from the Solar Neighbourhood and so to study Galactic Archaeology.

2.6.2 Asteroseismology of Stellar Populations

Such a wide catalog makes possible the application of Asteroseismology to the study of stellar populations. This involves studying similarities and differences in groups of stars by using asteroseismic diagrams, in which two properties of the oscillation spectra are plotted against one another. A classic example of asteroseismic diagram is that of Figure 35. This diagram demonstrates that $\Delta\nu$ and ν_{max} are almost proportional according to Equations 182. Along the RGB $\Delta\nu$ and ν_{max} decrease together with temperature as shown in Figures 35, 36 and 37. Another important asteroseismic diagram is the $\Delta\nu - \Delta\Pi$ diagram (see Figure 38) which allows us to easily distinguish between red-clump and red-giant-branch stars thanks to the sensitivity of $\Delta\Pi$ to the near-core structure. Many interesting articles which analyze the fields and the stellar clusters observed by Kepler, K2 and CoRoT are present in literature (see e.g. Corsaro et al. 2012; Miglio et al. 2013; Anders et al. 2017; Miglio et al. 2016; Stello et al. 2016).

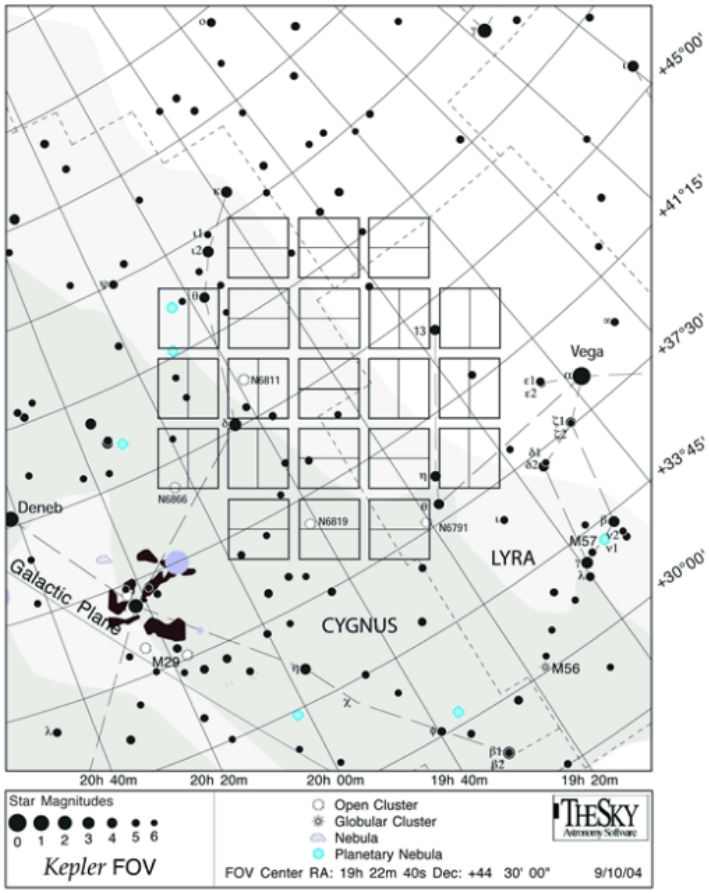

Figure 31.: *The field that was observed during the prime Kepler mission. Figure taken from the official site of the Kepler & K2 Science Center:* https://keplerscience.arc.nasa.gov/.

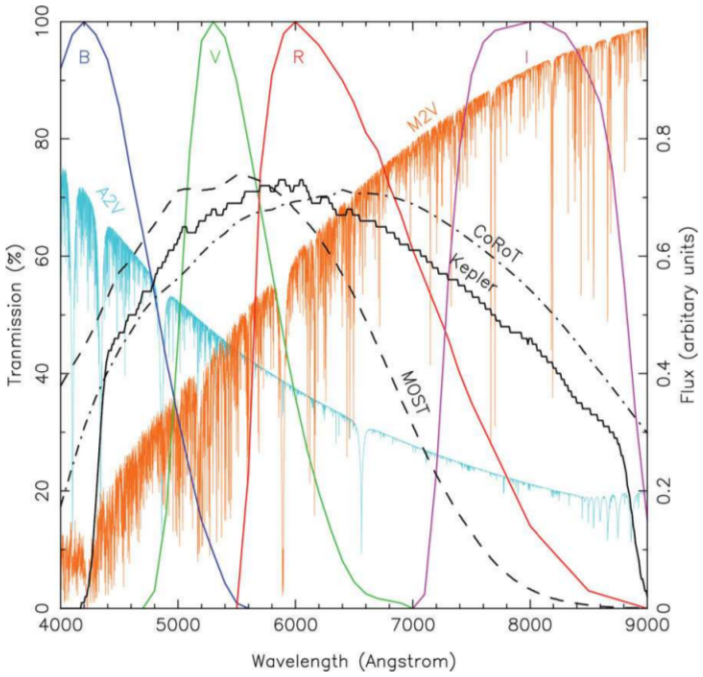

Figure 32.: *The Kepler bandpass. The response curves of MOST, CoRoT and Johnson B, V, R, I filters are shown for comparison. The Johnson's passbands have been scaled so that their maximum is at* 100% *transmission. The spectra of an A2V star and of a M2V star, scaled to have equal flux in the V passband, are also shown. Figure taken from Rowe et al. (2009).*

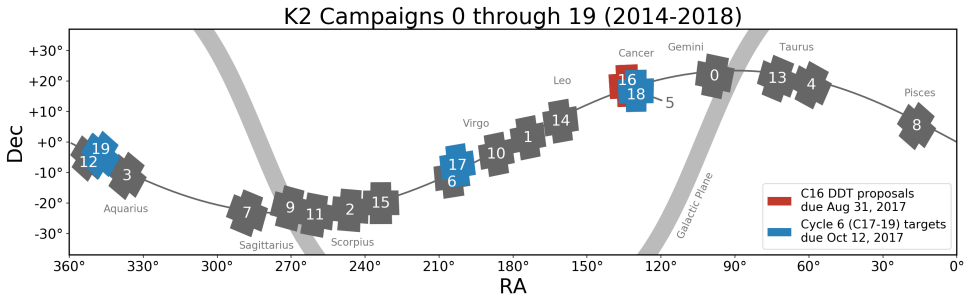

Figure 33.: *The fields observed during the campaigns of the K2 Mission until 2018. Figure taken from the official site of the Kepler & K2 Science Center:* https://keplerscience.arc.nasa.gov/.

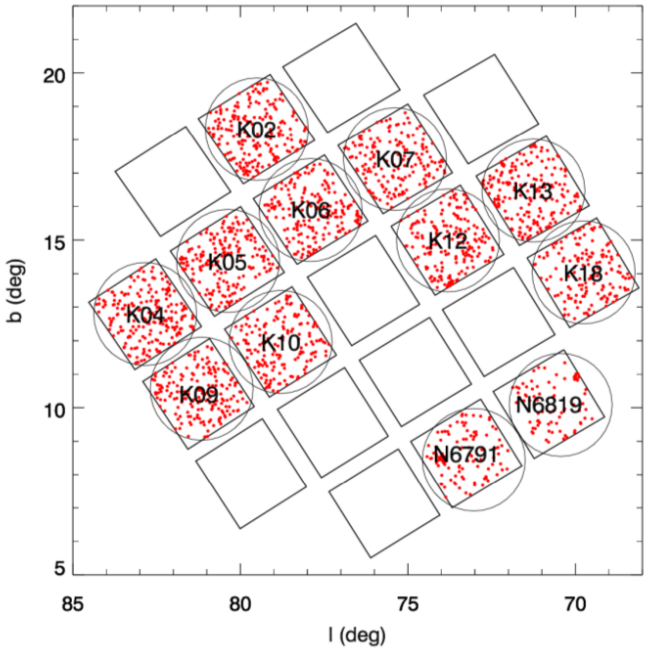

Figure 34.: *Kepler fields (squares) and fields covered by APOKASC (circles). The red points mark the positions of the stars whose data are freely available. Figure taken from Rodrigues et al. (2014).*

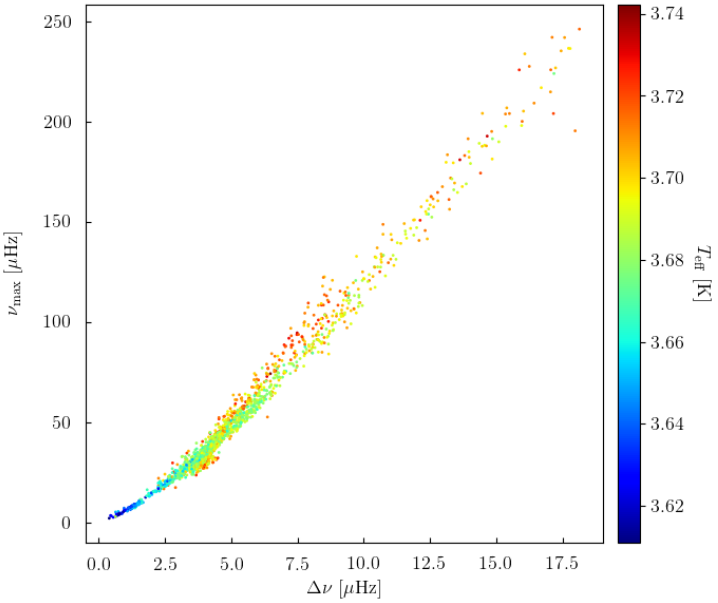

Figure 35.: *The stars of the APOKASC catalog in the $\Delta\nu$-ν_{max} diagram. These two quantities decrease during evolution, indeed cooler stars are preferentially close to the $(0, 0)$ point.*

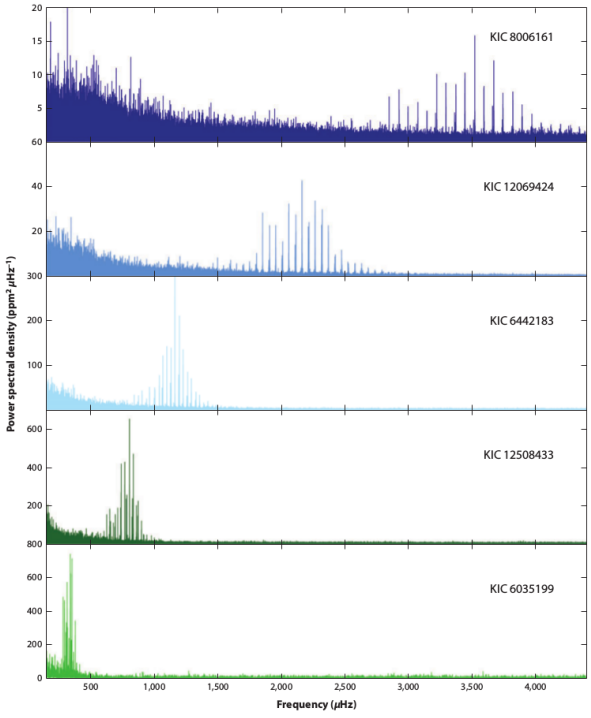

Figure 36.: *Solar-like oscillation spectra of five stars observed by Kepler, using its short-cadence data. The masses of these stars are all around 1 $M_\odot$. The top two stars KIC 8006161 and KIC 12069424 (16 Cyg A) are main-sequence stars. The third and fourth stars down—KIC 6442183 (HD 183159) and KIC 12508433 are subgiants. The bottom star (KIC 6035199) lies at the base of the RGB. The decrease of ν_{max} from the main sequence until the base of the RGB is clearly visible. Figure taken from Chaplin & Miglio (2013).*

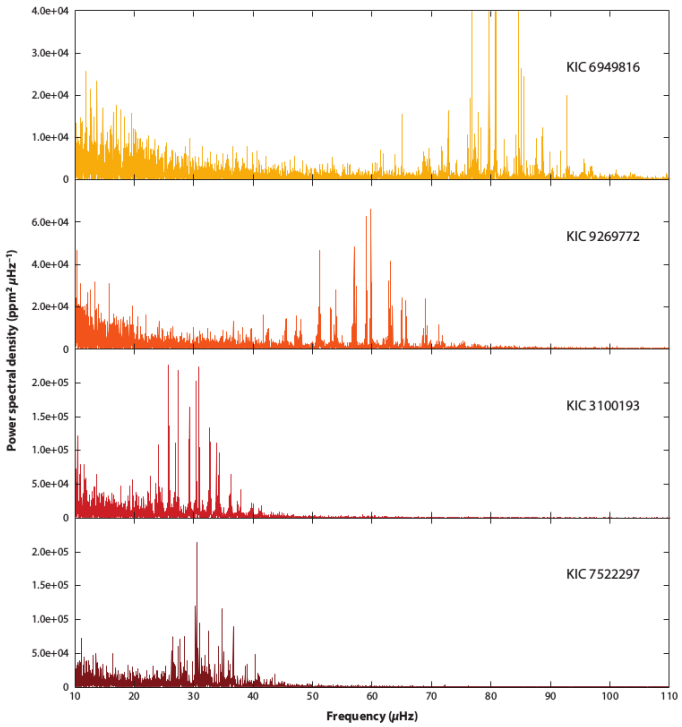

Figure 37.: *Solar-like oscillation spectra of four stars observed by Kepler, using its long-cadence data. The masses of these stars are all around* $1\,M_{\odot}$*. KIC 6949816 and KIC 9269772 are both first-ascent RGB stars. KIC 3100193 and KIC 7522297 are, respectively, RGB and RC stars sharing similar surface properties. The decrease of* ν_{max} *moving up from the bottom of the RGB is clearly visible. Figure taken from Chaplin & Miglio (2013).*

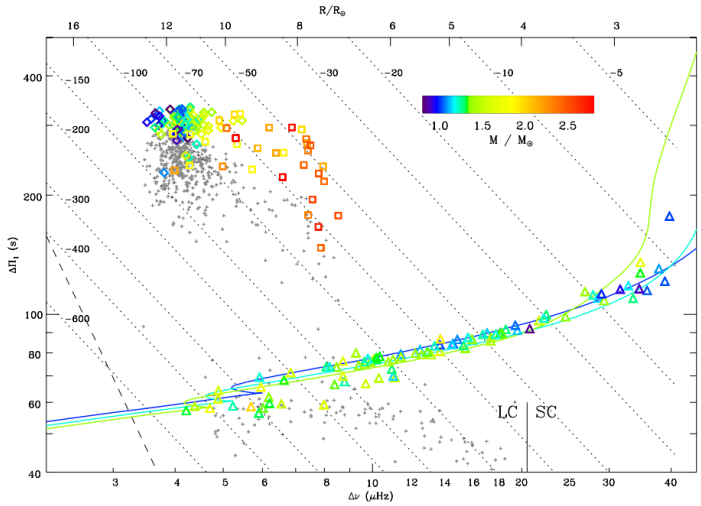

Figure 38.: *Gravity-mode period spacing* $\Delta\Pi_1$ *as a function of the pressure-mode large frequency spacing* $\Delta\nu$*. Kepler's long-cadence data (LC) have* $\Delta\nu \leq 20.4\,\mu$Hz*. RGB stars are indicated by triangles; clump stars by diamonds; secondary clump stars by squares. Uncertainties in both parameters are smaller than the symbol size. The seismic estimate of the mass is given by the color code. Small gray crosses indicate the bumped periods* $\Delta\Pi_{\rm obs}$ *measured by Mosser et al. (2011). Dotted lines are* n_g *isolines. The dashed line in the lower left corner indicates the formal frequency resolution limit. The upper x-axis gives an estimate of the stellar radius for a star whose* $\nu_{\rm max}$ *is related to* $\Delta\nu$ *according to the mean scaling relation* $\nu_{\rm max} = (\Delta\nu/0.28)^{1.33}$ *(both frequencies in μHz). The solid colored lines correspond to a grid of stellar models with masses of* 1, 1.2 *and* $1.4\,M_{\odot}$*, from the ZAMS to the tip of the RGB. Figure taken from Mosser et al. (2012a).*

3 THE TRILEGAL AND THE PARAM CODES

3.1 STELLAR POPULATION SYNTHESIS WITH TRILEGAL

Let us suppose to look at a certain surface element of the sky with galactic coordinates (l, b) and solid angle $\mathrm{d}\Omega$. The number counts of stars in a given bin of apparent x-magnitude $[m_x, m_x + \mathrm{d}m_x]$ is given by

$$N(m_x, l, b) = \left(\int_0^\infty r^2 \rho(\mathbf{r}) \phi(M_x, \mathbf{r}) \mathrm{d}r \right) \mathrm{d}m_x \, \mathrm{d}\Omega \tag{183}$$

where r is the distance along the line of sight, $\mathbf{r} = (l, b, r)$, $\rho(\mathbf{r})$ is the stellar density and $\phi(M_x, \mathbf{r})$ is the intrinsic luminosity function, i.e. the distribution of stellar absolute magnitudes, at the position $\mathbf{r}$. The aim of stellar population synthesis is to find ρ and ϕ such that the predicted number counts is in good agreement with observations in a volume as large as possible. We can simplify the problem by expressing the density as the sum of three different contributions belonging to each galaxy component (disk, halo and bulge):

$$\rho = \rho_d + \rho_h + \rho_b \tag{184}$$

Each of these components have a density distribution that can be written rather easily. Moreover, we can assume that the luminosity functions are independent of $\mathbf{r}$, i.e. $\phi(M_x, \mathbf{r}) = \phi(M_x)$, for each of these components. The TRILEGAL (TRIdimensional modeL of thE GALaxy) code implements a *population synthesis Galaxy star count model*. Such models, starting from a set of evolutionary tracks and suitable distributions of stellar masses, ages and metallicities, assume a theoretical $\phi(M)$. The stellar density is also expressed as a function of stellar parameters like age and metallicity. TRILEGAL was originally thought to be able to simulate star counts in several passband systems and for both very shallow and very deep photometric data. The synthetic photometry and bolometric corrections are derived from an extended library of stellar spectra. On the other hand, complete evolutionary sequences are necessary to cover a wide range of magnitudes.
Let us describe schematically the working principle of TRILEGAL (see Figure 39). The input datasets are:

- tables of stellar evolutionary tracks comprehensive of bolometric magnitudes, effective temperatures, surface gravity, core mass, surface chemical composition and asteroseismic parameters;
- tables of bolometric corrections for all the passbands considered;
- the initial mass function (IMF), ϕ_m;
- star formation rate (SFR), $\psi(t)$, and age-metallicity relation (AMR), $Z(t)$, for each Galaxy component;
- stellar densities and V-extinction as a function of $\mathbf{r}$, i.e. the geometry of the Galaxy components.

A single run of TRILEGAL executes the following steps:

- Equation 183 is used to predict the number counts in each bin of distance modulus;

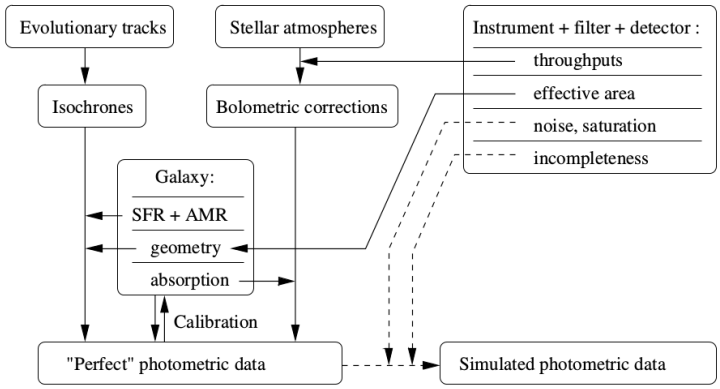

Figure 39.: *A general scheme of the TRILEGAL code. The solid arrows refer to steps which are performed inside TRILEGAL and they lead to the simulation of perfect (i.e. without errors) photometric data. External scripts can perform additional steps (dashed lines) to simulate instrumental errors. Figure taken from Girardi et al. (2005).*

- for each simulated star the stellar age, metallicity and mass are singled out by using SFR, AMR and IMF;
- the intrinsic properties (luminosity, effective temperature, surface gravity, etc.) of the star are derived by interpolating them in the grid of evolutionary tracks, for the selected initial mass, age, and metallicity;
- the apparent magnitudes are derived by taking into account bolometric corrections, distance modulus and extinction.

The interpolation in the grid of evolutionary tracks is explained below (see Girardi et al. 2005; Girardi 2016, for further details).

3.2 MESA STELLAR MODELS WITH OVERSHOOTING

In this work we consider three different evolutionary models computed with the MESA[1] (Modules for Experiments in Stellar Astrophysics) code. The evolutionary tracks were computed by Ben Cooke, currently student at the University of Birmingham, with the physical inputs described in Bossini et al. (2015). These three models are characterized by three different overshooting parameters during the H-core burning phase. Convective overshooting and Asteroseismology are indeed strictly connected. In particular, the period spacing, $\Delta\Pi_1$, of gravity modes with $l = 1$ is sensitive to the near-core structure. For sure $\Delta\Pi_1$ can be used to discriminate between stars in helium-core-burning and in RGB phases. Indeed, as we can see in the Figures of Section 3.4, HeCB stars have a period spacing larger of about $\sim 200 \div 300$ s than that of RGB stars. Then, after the early-AGB phase, it decreases to similar or smaller values. We want to understand if the choice of the evolutionary model, i.e. our lack of information about the overshooting phenomenon, leads to significant systematic errors in the estimates of masses, radii and ages of stars. As parameter estimation method we use a Bayesian method implemented by the PARAM code which is described in Section 3.5. We investigate both the cases where the period spacing is available or not as prior information.
The physical inputs used to compute the evolutionary tracks with the MESA code are:

- computation starting from the zero-age main sequence (ZAMS) up to the first thermal pulse of the asymptotic giant branch (TP-AGB);

1 Paxton et al. (2013)

- Grevesse & Noels (1993) heavy elements partition;
- the OPAL equation of state (Rogers & Nayfonov 2002) and OPAL opacities (Iglesias & Rogers 1996) augmented by low-temperature opacities from Ferguson et al. (2005). C-O enhanced opacity tables are considered during the helium-core burning (HeCB) phase;
- a table of nuclear reaction rates as in (NACRE, Angulo et al. 1999);
- the Krishna Swamy (1966) model for the atmosphere;
- MLT for the treatment of convection;
- overshooting during the main sequence ($\alpha_{\rm OV,H} = 0.0, 0.1, 0.2$) and penetrative convection during the HeCB phase ($\alpha_{\rm OV,He} = 0.5$) are taken into account in accordance with Maeder (1975) step function scheme;
- element diffusion, mass loss and rotational mixing are not taken into account;
- the formula $Z = Z_\odot\, 10^{[Fe/H]}$ with $Z_\odot = 0.01756$ is used to convert metallicities $[Fe/H]$ into mass fraction of heavy metals, Z;
- the helium initial mass fraction, Y, is settled by

$$Y = Y_P + \frac{\Delta Y}{\Delta Z} Z \tag{185}$$

  where $Y_p = 0.2485$ is the primordial helium abundance and $\Delta Y/\Delta Z = (Y_\odot - Y_p)/Z_\odot = 1.007$.

Table 4 summarizes the properties of the models considered and the set of evolutionary tracks used as input for TRILEGAL. In addition to the age, the effective temperature and the luminosity, also $\Delta\nu$ and $\Delta\Pi$ are computed along the evolutionary tracks. The period spacing is exactly that given by the MESA code. Instead, the $\Delta\nu$ computed by MESA is substituted by an average large frequency separation, $\langle\Delta\nu\rangle$, which is as close as possible to the observational measurement. More precisely, for each model along the tracks, the individual radial mode frequencies are computed with the GYRE code (Townsend & Teitler 2013). A weight w is assigned to the radial frequencies ν_n according to the relation:

$$w = \exp\left[-\frac{(\nu_n - \nu_{\rm max})^2}{2\sigma^2}\right] \qquad \text{with } \sigma = 0.66\,\nu_{\rm max}^{0.88} \tag{186}$$

as described in Mosser et al. (2012b). Finally, $\langle\Delta\nu\rangle$ is derived by a linear fitting of the radial fequencies as a function of the radial order n.

3.2.1 EEPs and interpolation.

TRILEGAL needs as input a set of evolutionary tracks and the positions of the Equivalent Evolutionary Points (EEPs) which mark specific events along the evolutionary track. The EEPs are important in order to do a correct interpolation in the grid of evolutionary tracks. In Figure 40 are shown some evolutionary tracks of the MESA model without overshooting together with their EEPs. When a star have intermediate values of mass, age and metallicity then TRILEGAL perform an interpolation between the nearest pairs of equivalent evolutionary points. Interpolations are linear with $\log M$, $\log\tau$, and $[M/H]$ being the independent variables.

Z_0	Y_0	$M[M_\odot]$	Maximum mass step$[M_\odot]$
0.00176	0.25027	0.6 ÷ 3.0	0.2
0.00312	0.25164	0.6 ÷ 3.0	0.2
0.00555	0.25409	0.6 ÷ 3.0	0.2
0.00987	0.25844	0.6 ÷ 3.0	0.2
0.01756	0.26618	0.8 ÷ 3.0	0.3
0.03123	0.27994	1.0 ÷ 3.0	0.2
0.05553	0.30441	1.0 ÷ 3.0	0.3

Table 4.: *Initial compositions and mass range of the MESA evolutionary tracks with overshooting parameters* $\alpha_{\rm OV,H} = 0.0$ *and* $\alpha_{\rm OV,He} = 0.5$. *Grids of evolutionary tracks with the same combinations of* Z_0, Y_0 *and* M *have been computed for* $\alpha_{\rm OV,H} = 0.1$ *and* 0.2.

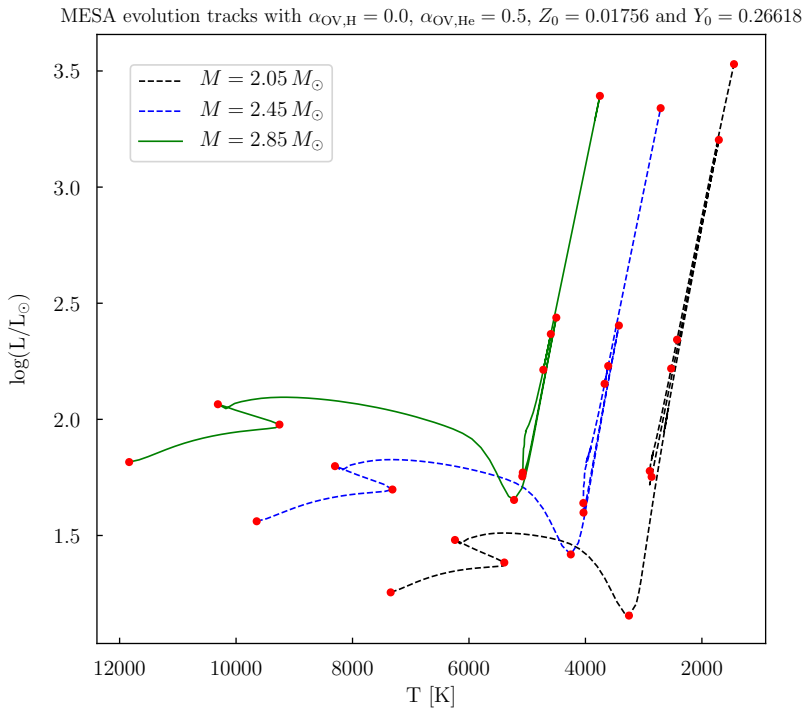

Figure 40.: *Three MESA evolutionary tracks with initial parameters* $\alpha_{\rm OV,H} = 0.0$, $\alpha_{\rm OV,He} = 0.5$, $Z_0 = 0.01756$, $Y_0 = 0.26618$ *and masses* $M = 2.05, 2.45, 2.85\,M_\odot$. $\alpha_{\rm OV,H}$ *and* $\alpha_{\rm OV,He}$ *are the overshooting parameters during the H-core burning and the He-core burning phases respectively. For clarity the dashed blue track and the dashed black one have been shifted toward lower temperatures by* 1000 *K and* 2000 *K respectively. The red points are the EEPs. They mark important evolution stages such as the beginning of the main-sequence phase or the base and the tip of the red-giant branch.*

3.3 ISOCHRONE FITTING OF THE OPEN CLUSTERS NGC6791, NGC6819 AND M67

We want to apply our analysis to artificial stars belonging to simulated stellar clusters or Galaxy fields. We chose the open clusters NGC6791, NGC6819 and M67. The first two have already been observed by Kepler and the latter has been observed during the K2 Mission. We simulated also an high-latitude Kepler field. In order to simulate these open clusters we have to derive the global properties (e.g. age and metallicity) with the isochrone fitting method. Figures from 41 to 49 show the isochrone fitting of the colour-magnitude diagrams (CMDs) of the already mentioned open clusters. The straight line of isochrones which connects the tip-RBG region and the red clump is representative of the helium-flash that stars of this range of masses undergo. See the captions for further details. In Table 5 we summarize the final estimates of the global parameters. Just from these figures we can see that models with convective overshooting during the main sequence in general fit better the CMDs of stellar clusters. However, it is difficult to identify the correct value of the overshooting parameter only by using the isochrone fitting method. Asteroseismology may provide better constraints to overshooting. Anyway, all observational tests about overshooting must be based on its effects on stellar evolution. Let us list the main ones:

- the main sequence lasts for a longer time because of the larger amount of hydrogen available: this fact leads to the difference near the turn-off point between isochrones of models with and without overshooting;

- a larger increase in luminosity and radius during the main sequence affecting again the isochrone's shape around the turn-off;

- at the end of the main sequence the hydrogen-exhausted core mass is greater than in the case without overshooting: this means larger luminosities and shorter lifetimes during all post-main-sequence phases except for the HeCB phase of low-mass stars that undergo the helium-flash.

In particular the connection between asteroseismic parameters and age may guide us toward a good estimate of the overshooting parameter.

Cluster	Age [Gyr]	Z	μ_0	$E(B-V)$
NGC6819	1.8	0.02	12.1	0.14
NGC6791	7.0	0.03	13.1	0.18
M67	3.5	0.019	9.7	0.015

Table 5.: *Final estimates of the global parameters of the open clusters NGC6819, NGC6791 and M67.*

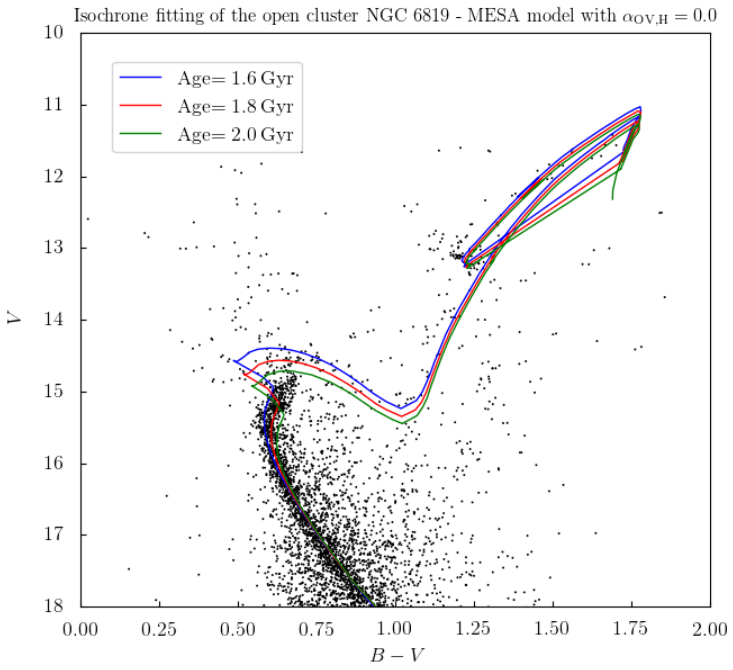

Figure 41.: *Isochrone fitting of the CMD of NGC6819. The UBV photometry has been taken from the WEBDA catalog: https://www.univie.ac.at/webda/. The isochrones belong to the MESA model with overshooting parameter* $\alpha_{OV,H} = 0.0$. *The final estimates of the global parameters are: Age= 1.8 Gyr,* $Z = 0.02$, $\mu_0 = 12.1$, $E(B-V) = 0.14$. *These global parameters are suitable even if we adopt* $\alpha_{OV,H} = 0.1, 0.2$.

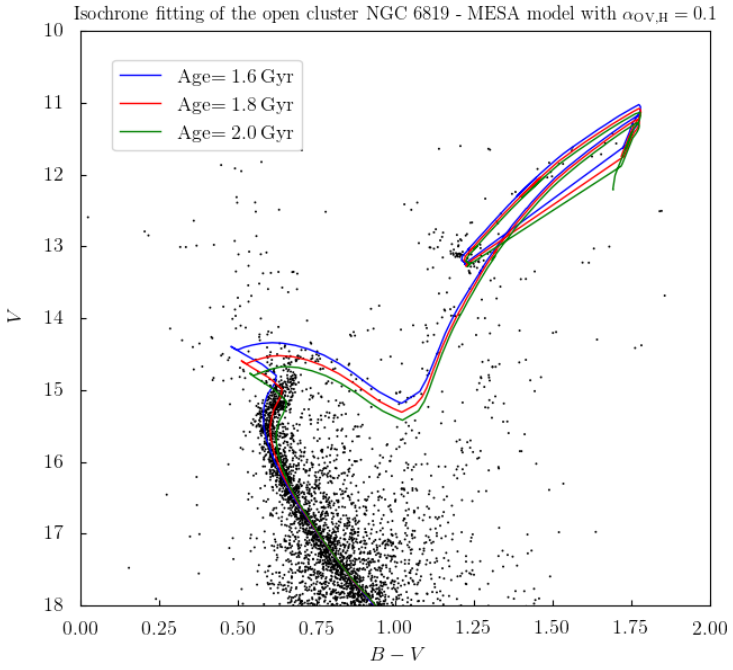

Figure 42.: *Isochrone fitting of the CMD of NGC6819. The UBV photometry has been taken from the WEBDA catalog. The isochrones belong to the MESA model with overshooting parameter* $\alpha_{OV,H} = 0.1$.

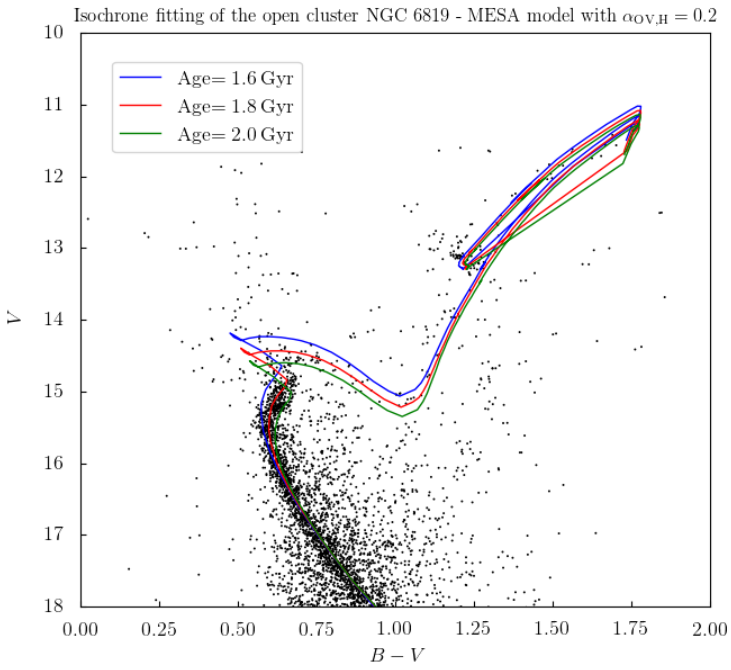

Figure 43.: *Isochrone fitting of the CMD of NGC6819. The UBV photometry has been taken from the WEBDA catalog. The isochrones belong to the MESA model with overshooting parameter* $\alpha_{OV,H} = 0.2$.

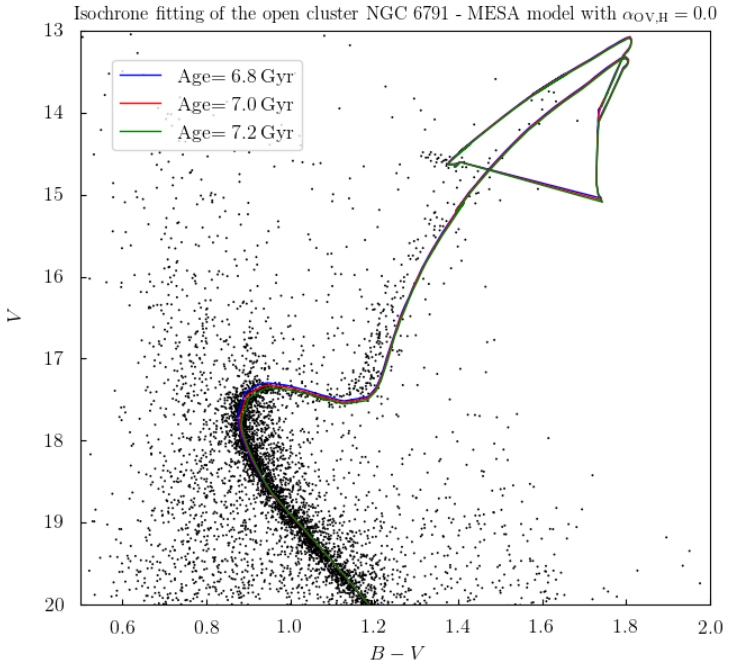

Figure 44.: *Isochrone fitting of the CMD of NGC6791. The UBV photometry has been taken from Stetson et al. (2003). The isochrones belong to the MESA model with overshooting parameter* $\alpha_{OV,H} = 0.0$. *The final estimates of the global parameters are: Age= 7.0 Gyr,* $Z = 0.03$, $\mu_0 = 13.1$, $E(B-V) = 0.18$. *These global parameters are suitable even if we adopt* $\alpha_{OV,H} = 0.1, 0.2$.

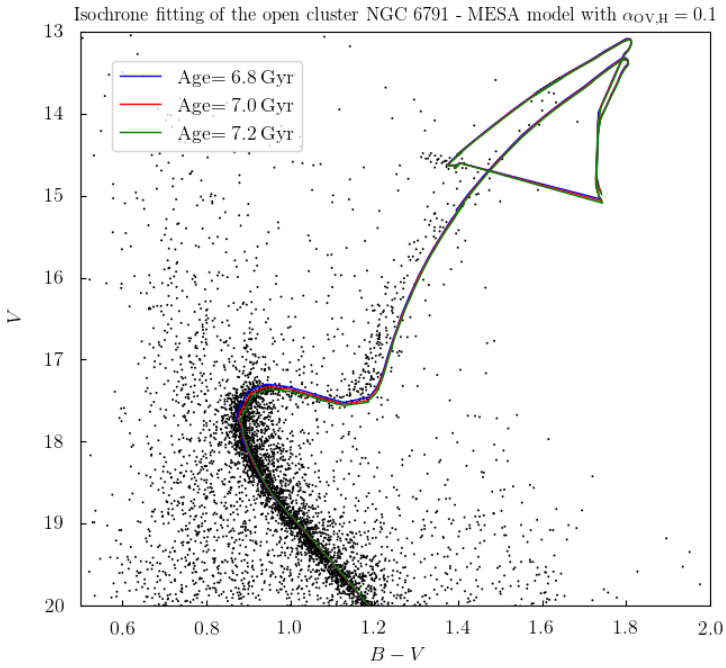

Figure 45.: *Isochrone fitting of the CMD of NGC6791. The UBV photometry has been taken from Stetson et al. (2003). The isochrones belong to the MESA model with overshooting parameter* $\alpha_{OV,H} = 0.1$.

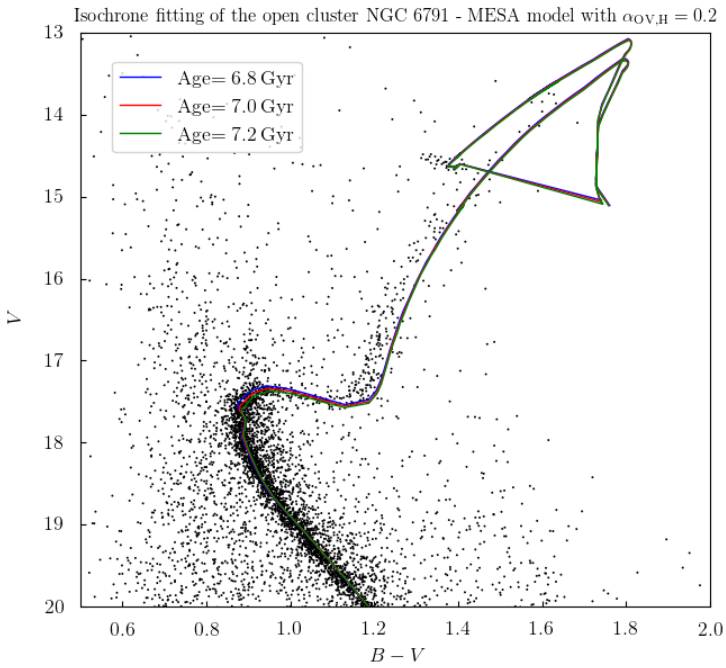

Figure 46.: *Isochrone fitting of the CMD of NGC6791. The UBV photometry has been taken from Stetson et al. (2003). The isochrones belong to the MESA model with overshooting parameter* $\alpha_{OV,H} = 0.2$.

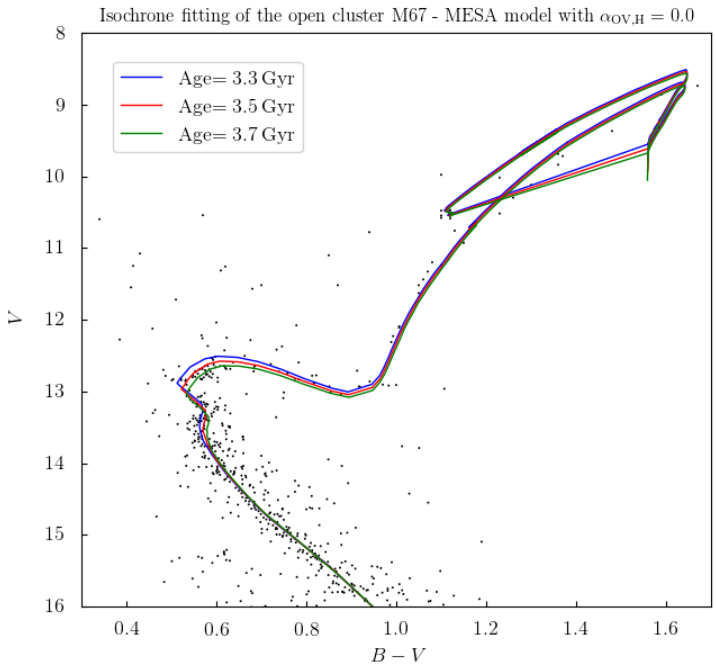

Figure 47.: *Isochrone fitting of the CMD of M67. The UBV photometry has been taken from Montgomery et al. (1993). The isochrones belong to the MESA model with overshooting parameter* $\alpha_{OV,H} = 0.0$. *The final estimates of the global parameters are: Age=* 3.5 *Gyr,* $Z = 0.019$, $\mu_0 = 9.7$, $E(B - V) = 0.015$. *These global parameters are suitable even if we adopt* $\alpha_{OV,H} = 0.1, 0.2$.

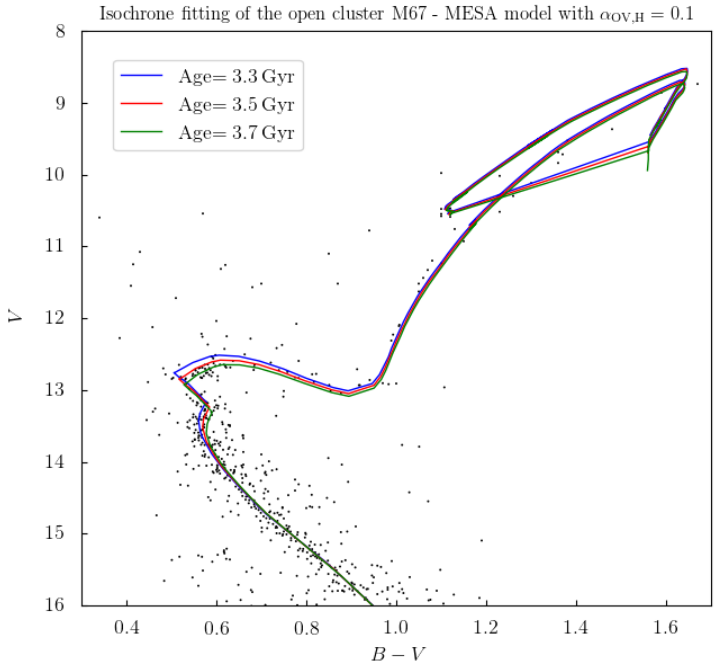

Figure 48.: *Isochrone fitting of the CMD of M67. The UBV photometry has been taken from the Montgomery et al. (1993). The isochrones belong to the MESA model with overshooting parameter* $\alpha_{OV,H} = 0.1$.

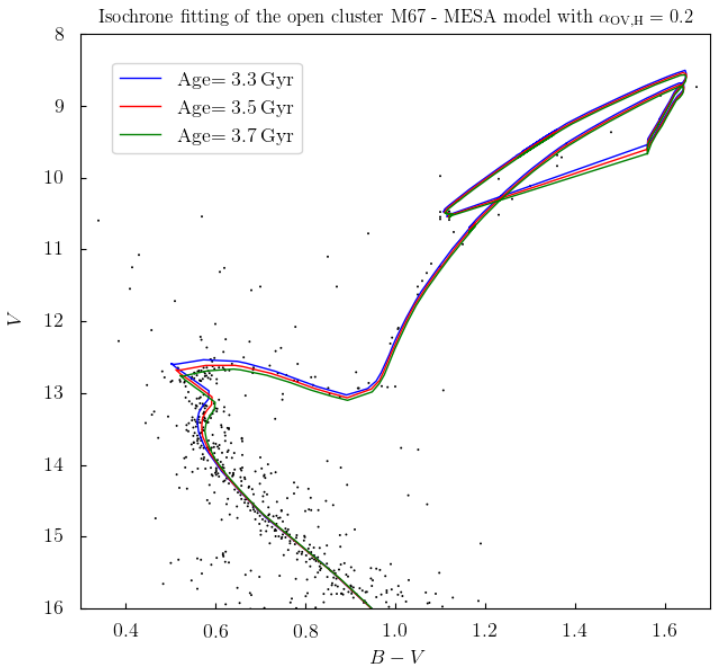

Figure 49.: *Isochrone fitting of the CMD of M67. The UBV photometry has been taken from the Montgomery et al. (1993). The isochrones belong to the MESA model with overshooting parameter* $\alpha_{OV,H} = 0.2$.

3.4 SIMULATIONS WITH TRILEGAL

Now we have all the necessary input parameters to simulate these open clusters with TRILEGAL (except for the total mass which has been chosen to give number counts in agreement with observations). A standard deviation of 0.1 Gyr for the clusters' ages has been adopted in the simulations. The following pictures show some results of the simulations. Figures from 50 to 52 refer to the open clusters and Figure 53 refer to a region of the sky of 0.5 $\deg^2$ representative of the Kepler field with central galactic coordinates $(l, b) = (76.98, 19.84)$. See the captions for further details.

3.5 THE PARAM CODE

The asteroseismic scaling relations 182 provide rather good estimates of masses and radii when $\Delta\nu$, ν_{max} and T_{eff} are available. The derivation of masses and radii through these scaling relations is called *direct method*. However, even better estimates can be achieved with the so-called *grid-based* or *Bayesian methods*. This improvement is due to two main reasons: firstly the scaling relations assume that stars are all homologous to the Sun leading in some cases to significant errors in mass and so in age; secondly the grid-based methods can take into account additional information such as the period spacing $\Delta\Pi$ of mixed modes. The PARAM code implements a Bayesian method which works as follows (da Silva et al. 2006; Rodrigues et al. 2014, 2017):

- the code receive as input a grid of evolutionary tracks like those described in Chapter 3;
- the code receive the measurements of the known star's parameters (we used T_{eff}, $\Delta\nu$, ν_{max}, $[M/H]$ and also $\Delta\Pi$ in some cases), let us denote with $\mathbf{y}$ this set of measurements. We note that TRILEGAL derives $\Delta\nu$ and $\Delta\Pi$ by interpolation and ν_{max} by using the scaling relation $\nu_{max} \propto g/\sqrt{T_{eff}}$;

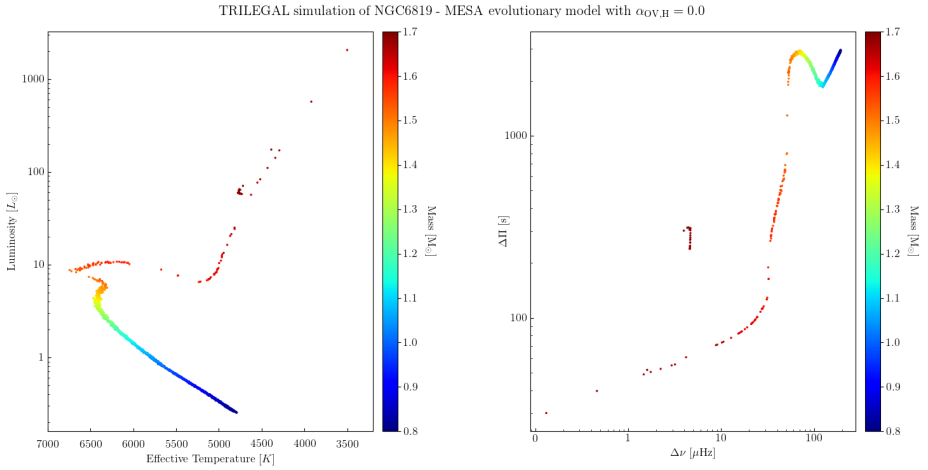

(a)

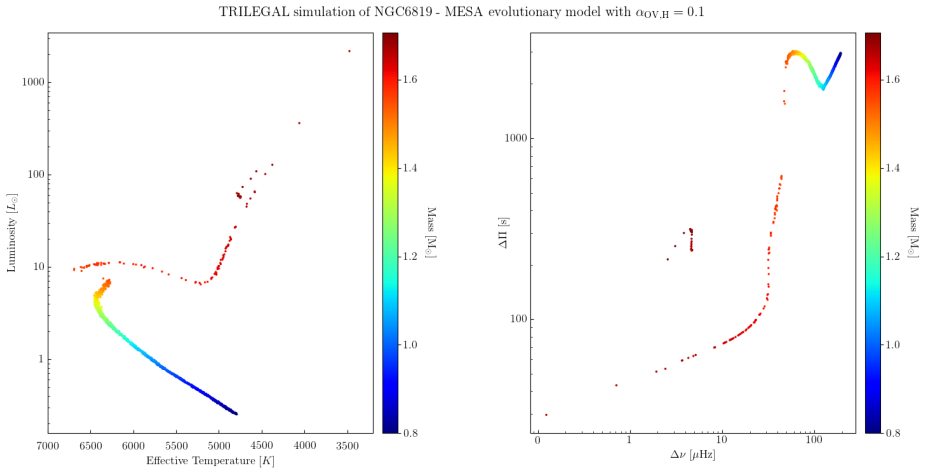

(b)

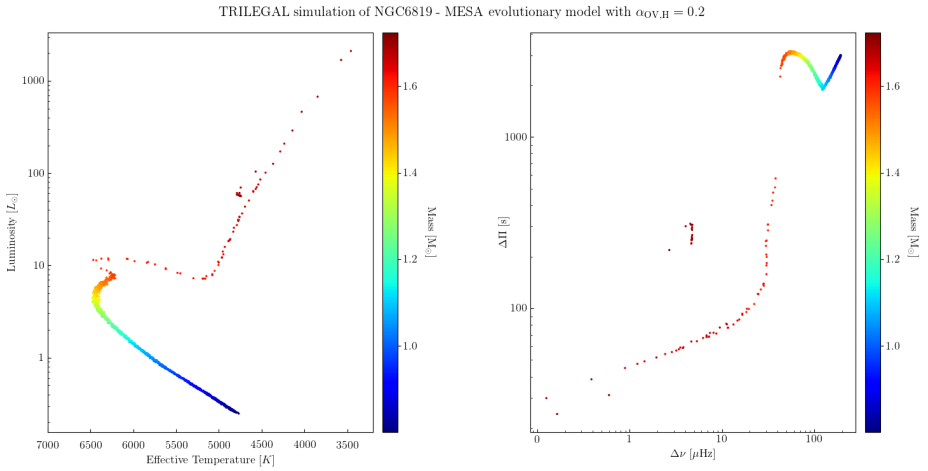

(c)

Figure 50.: *TRILEGAL simulations of NGC6819 with MESA evolutionary models. A total mass of 7400 $M_\odot$ has been settled.*

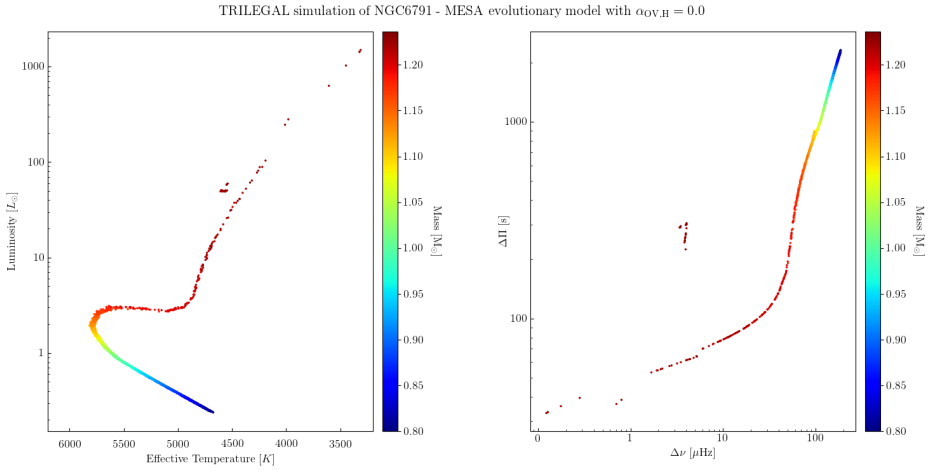

(a)

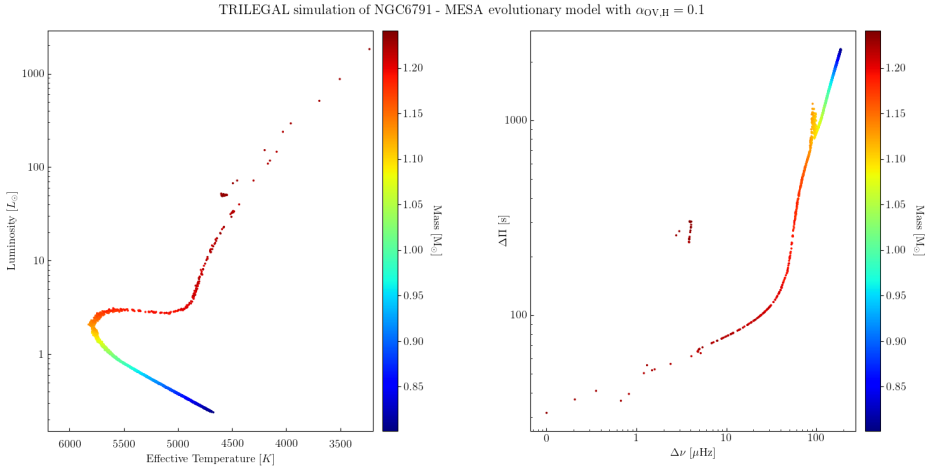

(b)

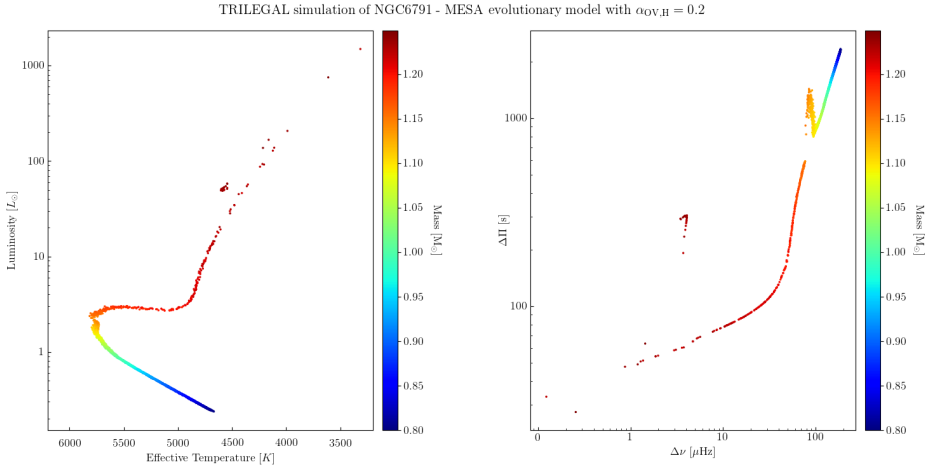

(c)

Figure 51.: *TRILEGAL simulations of NGC6791 with MESA evolutionary models. A total mass of 21800 $M_\odot$ has been settled.*

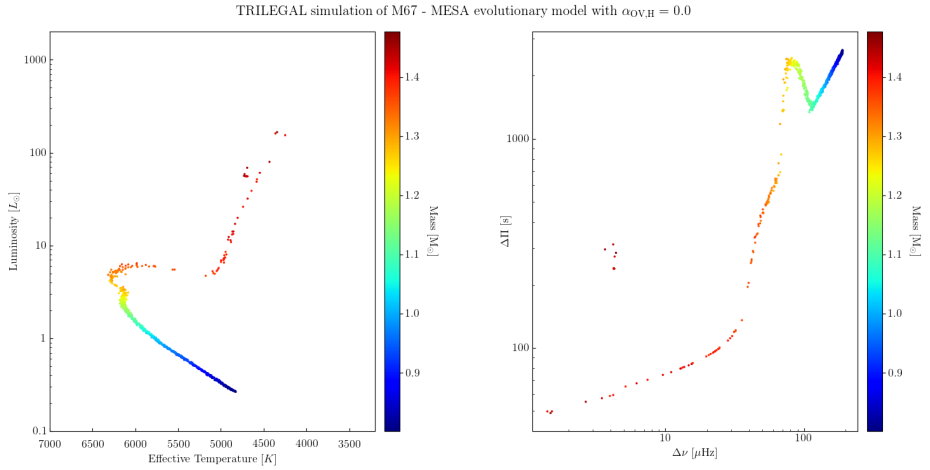

(a)

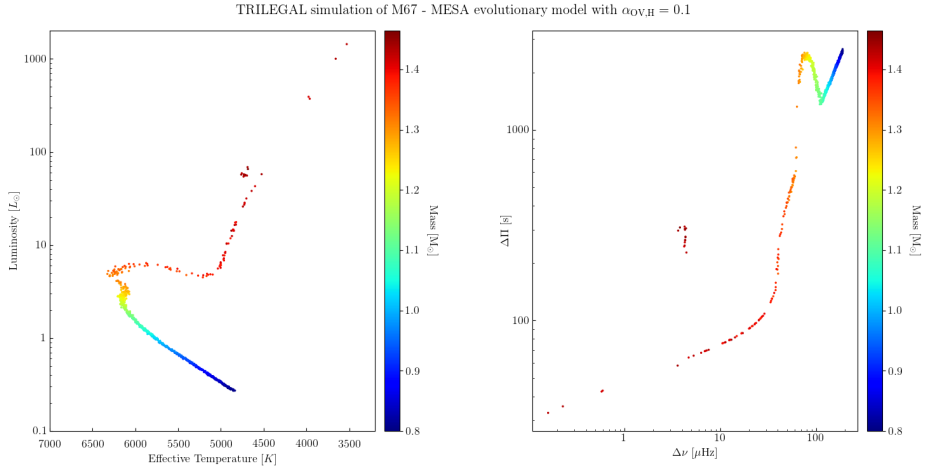

(b)

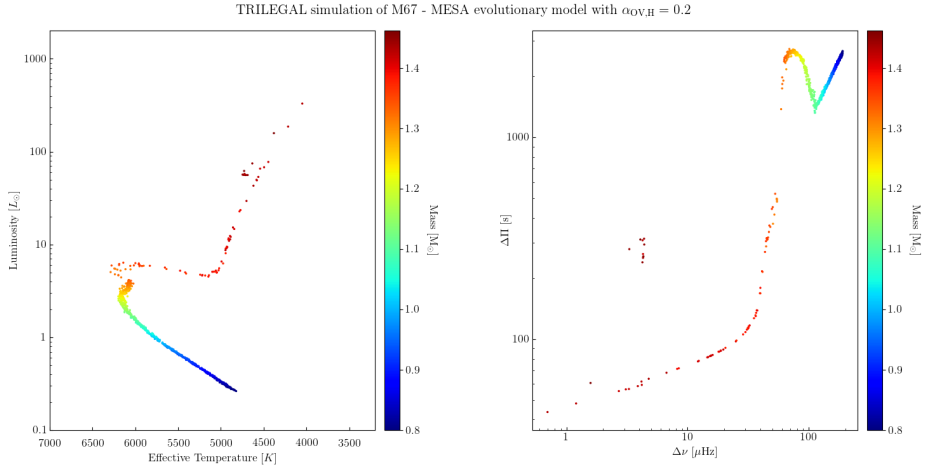

(c)

Figure 52.: *TRILEGAL simulations of M67 with MESA evolutionary models. A total mass of* $5000\,M_\odot$ *has been settled.*

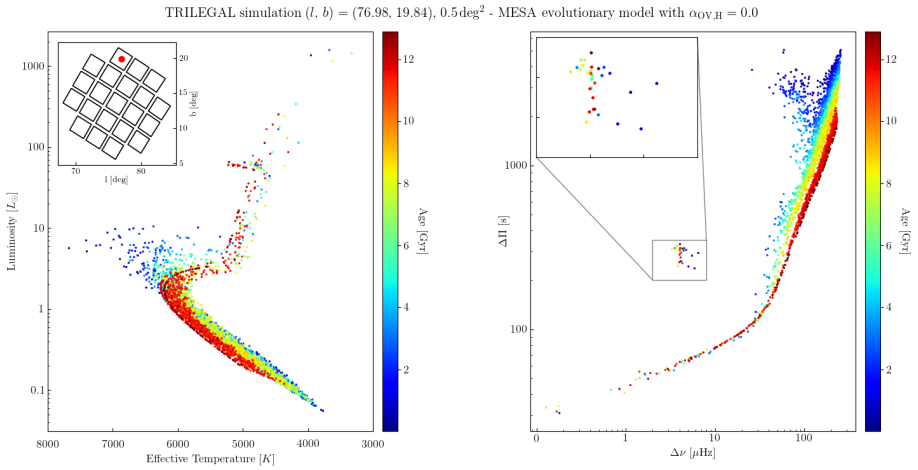

(a)

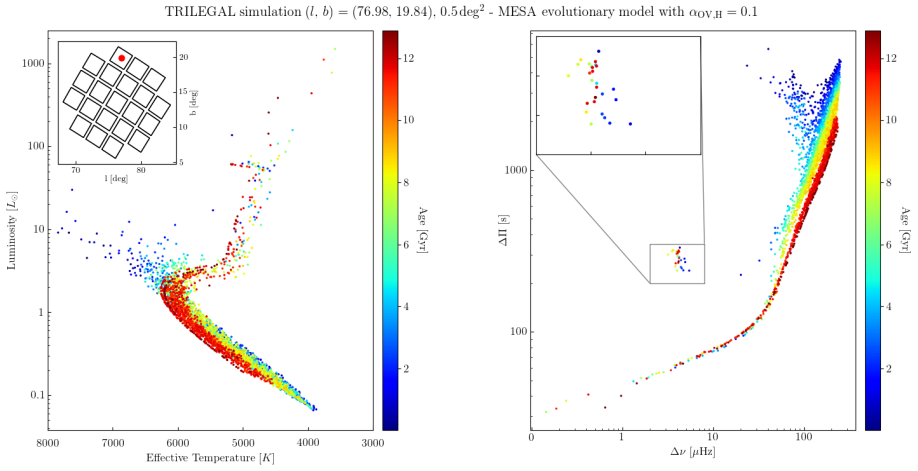

(b)

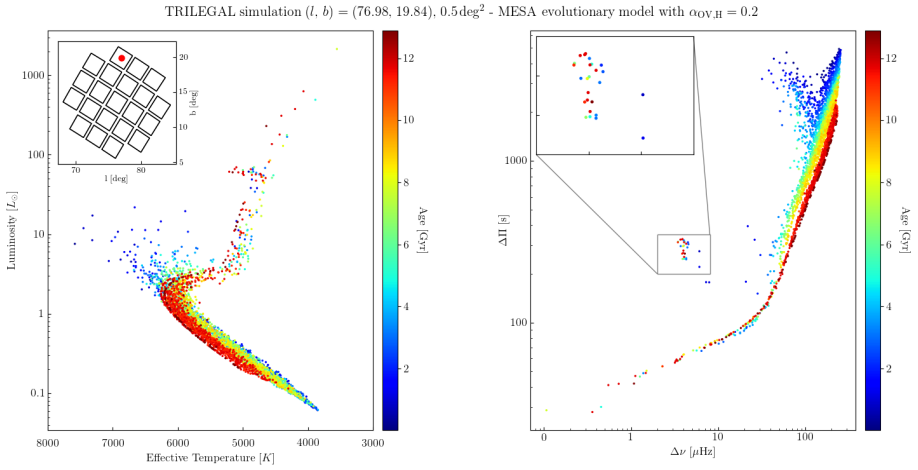

(c)

Figure 53.: *TRILEGAL simulations of a field with MESA evolutionary models. The central coordinates of the field are* $(l, b) = (76.98, 19.84)$ *an its area is of* $0.5\,deg^2$. *The corresponding Kepler field is marked with a red point in the insets of the left panels.*

- if we assume that the uncertainties in $\mathbf{y}$ are normally distributed then the Likelihood function can be written as

$$p(\langle \mathbf{y} \rangle, \mathbf{x}) = \mathcal{L}(\langle \mathbf{y} \rangle, \mathcal{I}(\mathbf{x})) = \prod_i \frac{1}{\sqrt{2\pi}\sigma_{y_i}} \exp\left(- \frac{(\langle y_i \rangle - y_i)^2}{2\sigma_{y_i}^2} \right) \tag{187}$$

  where $\langle y_i \rangle$ and $\sigma_{y_i}^2$ are the mean values and standard deviations of the input parameters respectively. The vector $\mathbf{x} = (M, R, \log g, \tau, M_\lambda)$ is the set of output parameters, i.e. what we would like to compute. $\mathbf{x}$ and $\mathbf{y}$ are connected through the isochrones derived from the grid of evolutionary tracks: $\mathbf{y} = \mathcal{I}(\mathbf{x})$;

- the code computes the Likelihood functions and the prior function, $p(\mathbf{x})$, which is given by

$$p(\mathbf{x}) = p(M)\, p(\tau)\, p([M/H]) \tag{188}$$

  where the priors in age and metallicity are uniform distributions in the interval $[10^6, 10^10]$ yr and the prior in mass is given by the initial mass function derived in Chabrier (2001), but corrected for the mass lost close to the tip of the RGB (see Miglio et al. 2012, for details);

- the code computes the posterior probability:

$$p(\mathbf{x}|\mathbf{y}) = \frac{p(\mathbf{y}|\mathbf{x})\, p(\mathbf{x})}{p(\mathbf{y})} \tag{189}$$

  where $p(\mathbf{y})$ is a normalization factor, independent of $\mathbf{x}$, which do not modify the shape of the posterior probability and so it can be ignored;

- finally the code computes the marginal distributions $p(x_i|\langle \mathrm{y} \rangle)$ by integrating $p(\mathbf{x}|\mathbf{y})$ over all output parameters, except for x_i.

The marginal distributions are the probability density functions of the output parameters. We can use the mode or the median of these distributions as our parameters' estimates (in this work we will use the mode). The uncertainties of our estimates are provided by computing 68 percent credible intervals. The interpolation between the input evolutionary tracks is done with the same method used by TRILEGAL (described in more detail in Marigo et al. 2017). Many tests have been executed in order to check and explore the potentialities of PARAM (see Rodrigues et al. 2014, 2017).

3.6 SIMULATIONS WITH PARAM

The choice of one among the three MESA models available and so the choice of the overshooting parameter may lead to systematic errors in the determination of stellar parameters. We want to quantify these errors when the Bayesian method of PARAM is applied. In order to do that, we adopted the following procedure:

- we choose a TRILEGAL simulation among those showed above;
- for each artificial star we take its effective temperature, metallicity and asteroseismic parameters (firstly we use $\Delta\nu$ and $\nu_{\max}$ for all stars and then we repeat the whole procedure by taking also $\Delta\Pi$, but only for RGB and HeCB stars);
- we assign uncertainties to the input parameters according to the typical values in literature and in the APOKASC and Vrard's catalogs: 90 K in effective temperature, 0.1 dex in metallicity 2% in $\Delta\nu$ and $\Delta\Pi$ and 2.5% in $\nu_{\max}$;
- we run PARAM with a grid of evolutionary tracks corresponding to one of the three MESA models and not necessarily the same of the TRILEGAL simulation;

- PARAM tries to recover the original parameters of the artificial stars (mass, radius and age in particular) by using only the information about temperature, metallicity and asteroseismic parameters;
- as a result, PARAM gives the estimates of the recovered stellar parameters with their credible intervals.

This procedure has been repeated for all possible combinations of TRILEGAL simulations and PARAM input models. We are going to present and analyze the results of these computations in Chapter 4.

4 ANALYSIS AND CONCLUSIONS

4.1 ERROR DEFINITIONS AND PLOTS DESCRIPTION

The estimates of stellar parameters provided by PARAM are affected by two kinds of error. The first contribution comes directly by the application of the Bayesian method and it is determined by the shape and width of posterior probability density functions. The second contribution comes from the choice of the stellar model, and so of the overshooting parameter in our case, given as input to PARAM. We will take the mode of posteriors as parameter estimates.
Let us define some quantities which will be useful in order to distinguish and evaluate these two contributions. Let E_P be the PARAM estimate of a stellar parameter (the mode of its posterior) and E_T its original value in the TRILEGAL simulation. We will consider only mass, radius and age. Let E_{68U} and E_{68L} be the upper and lower limits respectively of the 68% credible interval of its posterior. We quantify the first contribution to error by

$$\sigma_{bm} = \frac{(E_{68U} - E_{68L})/2}{E_P} \tag{190}$$

and the second one by

$$\sigma_{sys} = \frac{E_P - E_T}{E_T} \tag{191}$$

and by its absolute value. The distributions of σ_{bm} and σ_{sys} are showed in two series of plots, all gathered in the Appendices. Hereafter we will refer to σ_{bm} as "PARAM error". The plots of the first series (see Appendix A) are like that of Figures 54 and 56. Each plot refers to a specific TRILEGAL simulation indicated in the main title. For each TRILEGAL simulation there are three different plots for distributions of masses, radii and ages. The parameter the plot refers to is also written in the main title. The graph to the left shows the H-R diagram of the TRILEGAL simulation. The artificial stars are divided into different groups depending on their evolutionary stage. We will consider only stars belonging to main sequence and sub-giant branch (label '1' of the colorbar), to red-giant branch (label '3') and those in HeCB phase (label '4'). The 3×3 matrix of graphs to the right represents the distributions of percentage errors, σ_{bm} [%], of PARAM results for the chosen stellar parameter and for all PARAM input grids available. Distributions of the first column were obtained when PARAM received the grid of evolutionary tracks computed with the MESA code and adopting $\alpha_{\mathrm{OV,H}} = 0.0$. The distributions of the second and the third columns were obtained when $\alpha_{\mathrm{OV,H}} = 0.1, 0.2$ was adopted respectively. Stars belonging to a certain evolutionary stage take part of the distributions of the dedicated row (note the label 'ES' = Evolutionary Stage on the far right-hand side). Finally, blue distributions are obtained when only $\Delta\nu$ and $\nu_{\max}$ are used as asteroseismic parameter in input to PARAM. Red distributions, instead, are obtained when $\Delta\Pi$ is added to the set of input information (note that these distributions are not present in the last row because $\Delta\Pi$ can't be measured for main-sequence stars and hardly for sub-giants). In each graph of the matrix the medians, written in the same colour of the distribution they represent, are reported. The plots of the second series, gathered in Appendix B, are similar (see Figures 55 and 57), but they show the distributions of the percentage systematic errors, σ_{sys} [%]. In this case, denoted by Me_{abs}, the medians of the distributions of $|\sigma_{sys}|$ [%] are also reported.

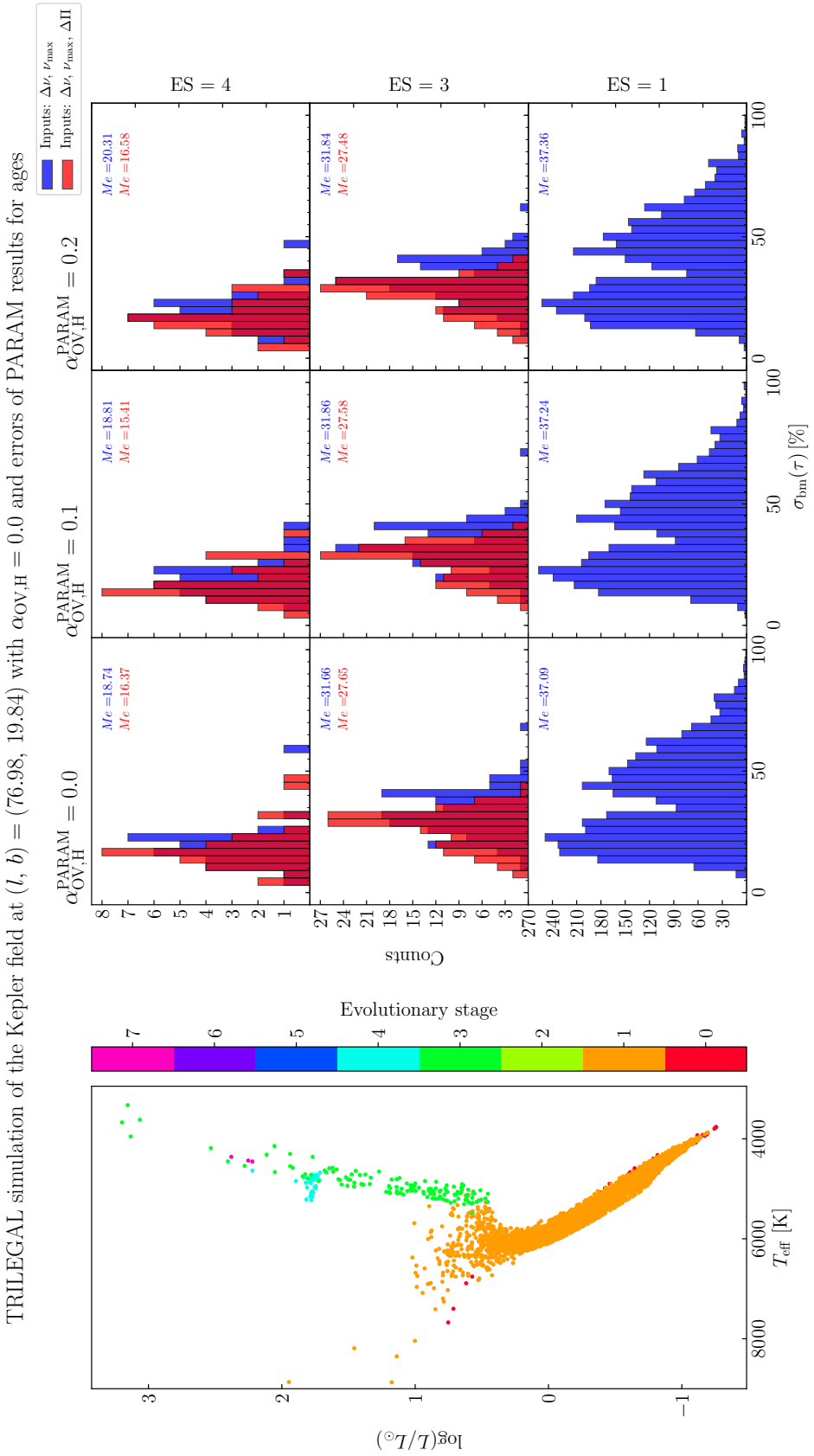

Figure 54.: *Distributions of PARAM errors for ages for the TRILEGAL simulation of the Kepler field with* $\alpha_{\mathrm{OV,H}} = 0.0$.

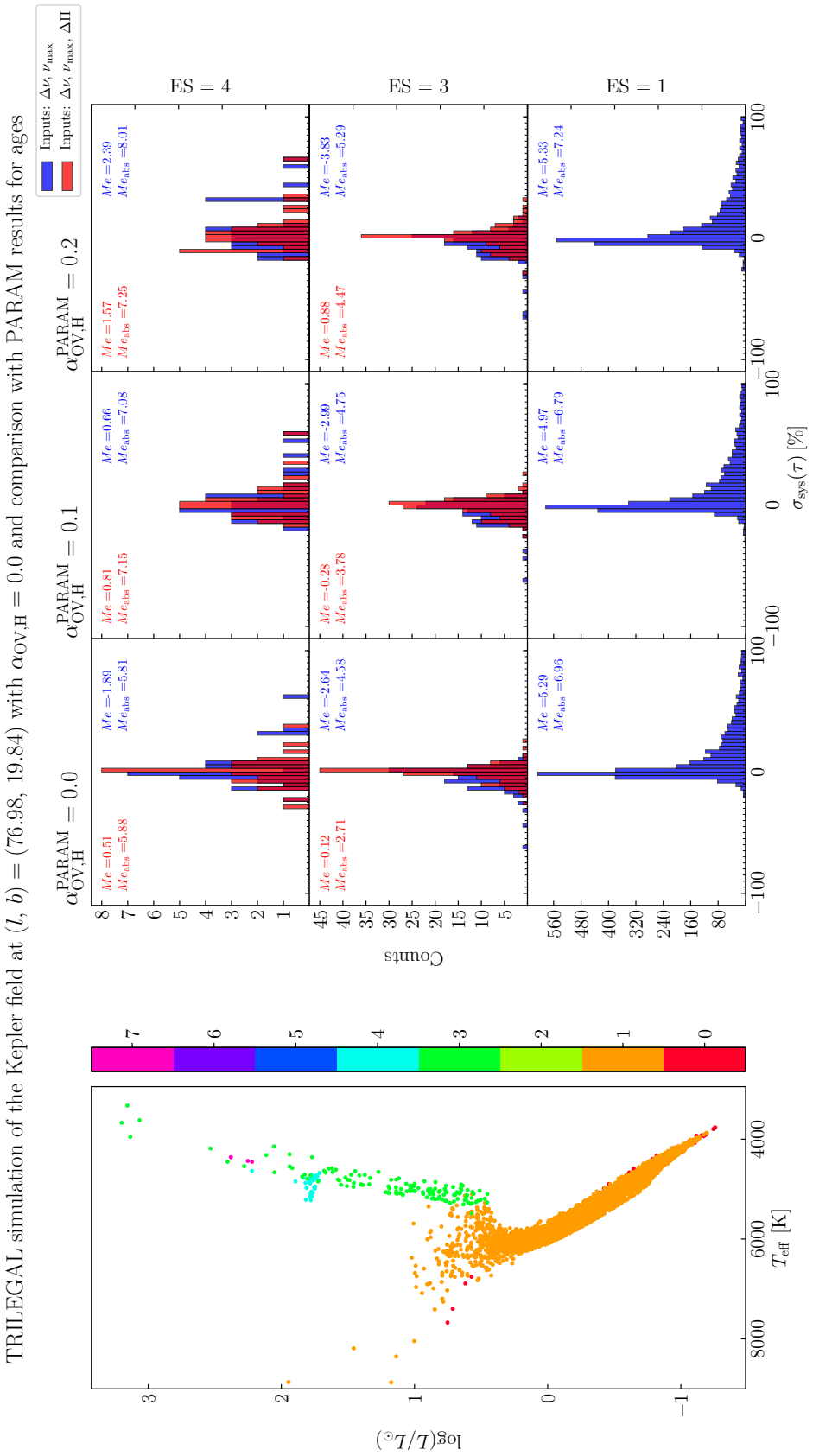

Figure 55.: *Distributions of systematic errors for ages for the TRILEGAL simulation of the Kepler field with* $\alpha_{\mathrm{OV,H}} = 0.0$.

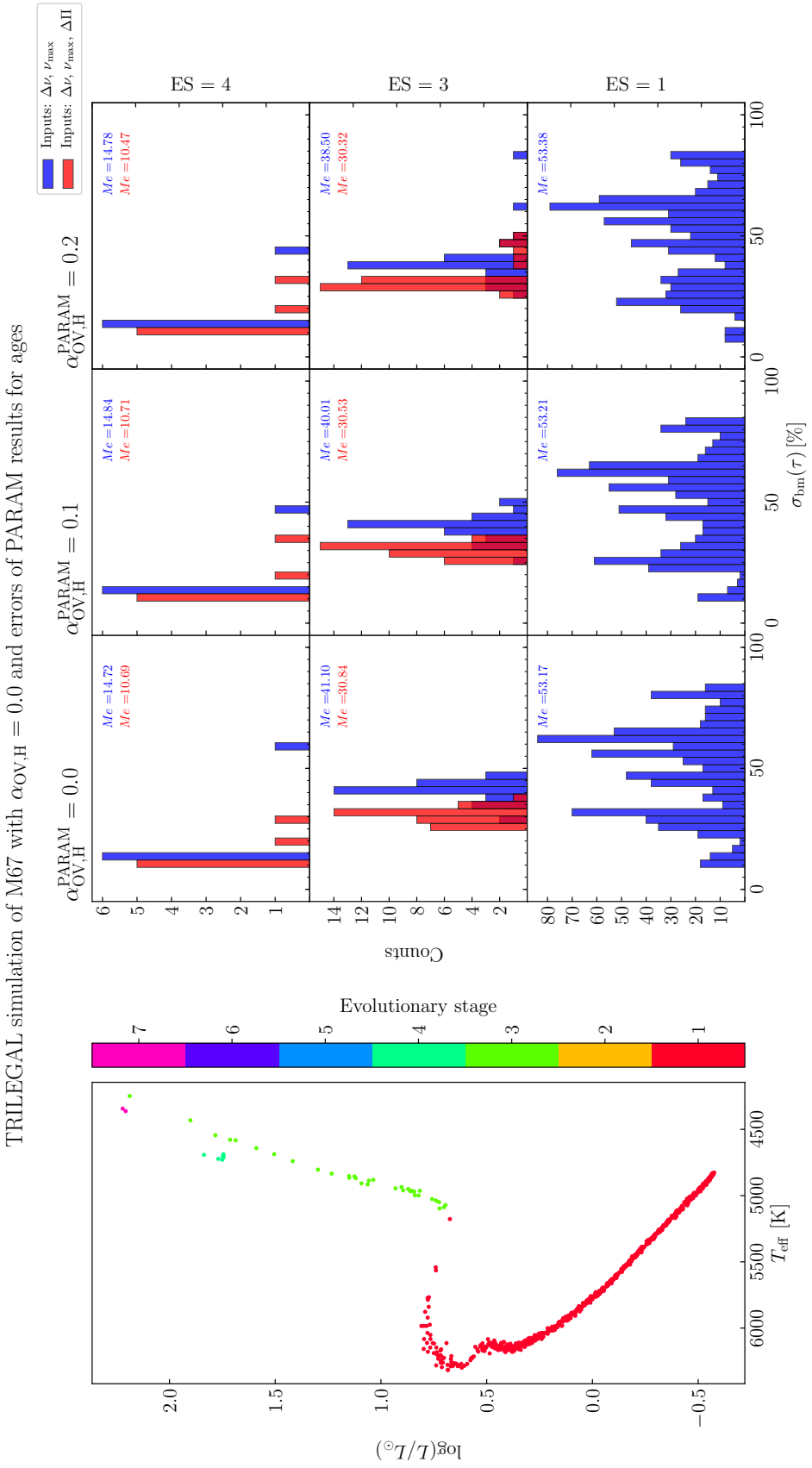

Figure 56.: *Distributions of PARAM errors for ages for the TRILEGAL simulation of M67 with* $\alpha_{OV,H} = 0.0$.

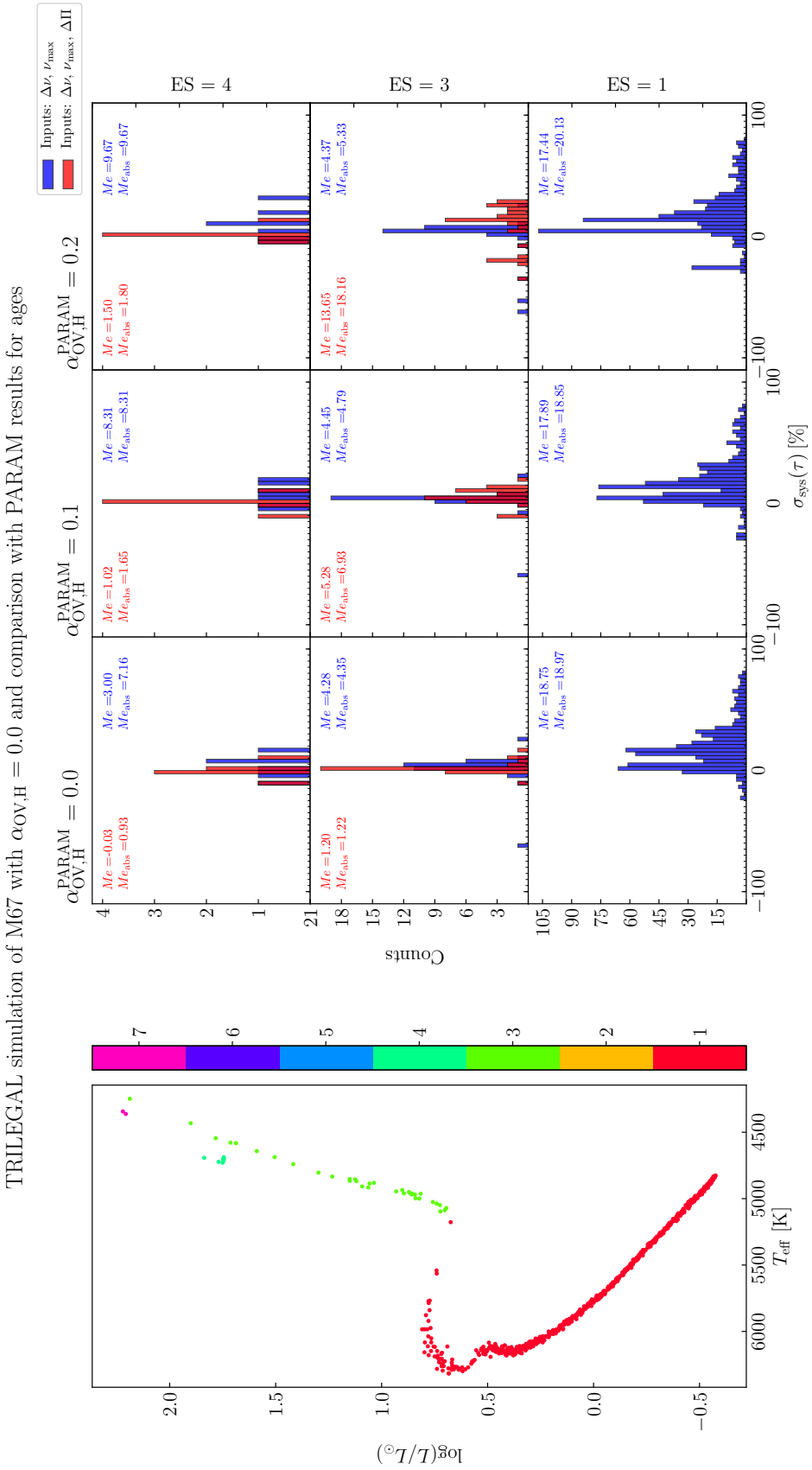

Figure 57.: *Distributions of systematic errors for ages for the TRILEGAL simulation of M67 with* $\alpha_{OV,H} = 0.0$.

4.2 ANALYSIS

From the plots in Appendix A and B we can outline some general aspects:

- PARAM errors are in general lower than 10 % in mass, lower than 5 % in radius and lower than 40 % in age except for low main-sequence stars which have even greater age errors and often lead to multimodal distributions;
- PARAM errors are in general reduced when $\Delta\Pi$ is also used as input information. This is true especially for the age estimates of RGB stars whose errors decrease of 10 % or even more. Moreover, without using $\Delta\Pi$, PARAM errors distributions for RGB stars in the Kepler field are bimodal. The reason is that PARAM can't distinguish well between red-clump stars and nearby RGB stars only by using $\Delta\nu$ and $\nu_{\max}$. In open clusters, distributions do not have a clear bimodal shape because of the lower star counts than the field;
- for HeCB and RGB stars PARAM errors do not change a lot on varying the overshooting parameter in PARAM. This fact was expected because, in the mass range of our artificial stars, the evolutionary tracks with different overshooting parameters differ to each other until the base of the RGB and then are similar;
- systematic errors in general contribute to the total error less than PARAM ones, but they are not negligible;
- systematic errors are never null, even if the evolutionary grids of TRILEGAL and PARAM coincide. The reason is that the choice of the grid is not the only source of systematic errors, e.g. the mode of posteriors might not be a good indicator in case of multi-peaked distributions;
- if only $\Delta\nu$ and $\nu_{\max}$ are used, then systematic errors do not change a lot on varying the overshooting parameter in PARAM;
- there are few stars in HeCB phase so it should be better to repeat the entire analysis accumulating artificial stars from many TRILEGAL simulations with same inputs before doing statistics with HeCB stars. However, since almost all our artificial stars undergo the helium-flash, we do not expect estimates of their parameters to be influenced by effects of overshooting;
- the choice of the correct overshooting parameter is important especially for RGB stars of open clusters: it leads to decreases of systematic errors up to about 18 % in age, 6 % in mass and 2.5 % in radius.

Note that the addition of $\Delta\Pi$ leads in some cases to greater systematic errors. However, to use only $\Delta\nu$ and $\nu_{\max}$ is not a good strategy because PARAM errors are much higher in that case.

4.3 CONCLUSIONS AND FUTURE PERSPECTIVES

Our aim was to quantify systematic errors introduced by the choice of the overshooting parameter, $\alpha_{\mathrm{OV,H}}$, to adopt for computing the evolutionary grid used as input to the Bayesian method implemented by the PARAM code. The results of our work show that in general they contribute to the total error less than PARAM ones, but they are not negligible. This is true especially for RGB stars, for which we have observed decreases of systematic errors up to about 18 % in age, 6 % in mass and 2.5 % in radius. Therefore, the choice of the correct overshooting parameter might be important, in particular for galaxy evolution and for stellar clusters, whose ages are assumed to be close to their stars ages. A lot of work should be done in order to investigate deeper behaviours of systematic errors. Other evolutionary grids and other mass ranges and compositions should be considered. Moreover, looking at the

incoming measurements of parallaxes from Gaia satellite (Lindegren et al. 2016), the entire analysis should be repeated by adding the absolute magnitude as known input information for PARAM. Next in the future, the PLATO Mission will provide great improvements in stellar parameters estimation thanks to detection of individual oscillation frequencies. In such a way it will be possible to go beyond the use of $\Delta\nu$, ν_{max} and $\Delta\Pi$ which only describe the global aspects of solar-like oscillations pattern.

BIBLIOGRAPHY

Aerts, C., Christensen-Dalsgaard, J., & Kurtz, D. W. 2010, Asteroseismology

Anders, F., Chiappini, C., Rodrigues, T. S., et al. 2017, A&A, 597, A30

Angulo, C., Arnould, M., Rayet, M., et al. 1999, Nuclear Physics A, 656, 3

Baglin, A. & Fridlund, M. 2006, in ESA Special Publication, Vol. 1306, ESA Special Publication, ed. M. Fridlund, A. Baglin, J. Lochard, & L. Conroy, 11

Beck, P. G. & Kallinger, T. 2013, Sterne und Weltraum, 52, 50

Borucki, W., Koch, D., Batalha, N., et al. 2009, in IAU Symposium, Vol. 253, Transiting Planets, ed. F. Pont, D. Sasselov, & M. J. Holman, 289–299

Bossini, D., Miglio, A., Salaris, M., et al. 2015, MNRAS, 453, 2290

Brown, T. M., Gilliland, R. L., Noyes, R. W., & Ramsey, L. W. 1991, ApJ, 368, 599

Catelan, M. & Smith, H. A. 2015, Pulsating Stars

Chabrier, G. 2001, ApJ, 554, 1274

Chaplin, W. J., Elsworth, Y., Isaak, G. R., et al. 2002, MNRAS, 336, 979

Chaplin, W. J. & Miglio, A. 2013, ARA&A, 51, 353

Corsaro, E., Stello, D., Huber, D., et al. 2012, ApJ, 757, 190

Cox, J. P. 1980, Theory of stellar pulsation

da Silva, L., Girardi, L., Pasquini, L., et al. 2006, A&A, 458, 609

D'Antona, F. & Mazzitelli, I. 1994, ApJS, 90, 467

Ferguson, J. W., Alexander, D. R., Allard, F., et al. 2005, ApJ, 623, 585

Girardi, L. 2016, Astronomische Nachrichten, 337, 871

Girardi, L., Groenewegen, M. A. T., Hatziminaoglou, E., & da Costa, L. 2005, A&A, 436, 895

Grevesse, N. & Noels, A. 1993, in Origin and Evolution of the Elements, ed. N. Prantzos, E. Vangioni-Flam, & M. Casse, 15–25

Hansen, C. J., Kawaler, S. D., & Trimble, V. 2004, Stellar interiors : physical principles, structure, and evolution

Iglesias, C. A. & Rogers, F. J. 1996, ApJ, 464, 943

Kippenhahn, R. & Weigert, A. 1990, Stellar Structure and Evolution, 192

Kjeldsen, H. & Bedding, T. R. 1995, A&A, 293, 87

Krishna Swamy, K. S. 1966, ApJ, 145, 174

Lebreton, Y. & Montalbán, J. 2009, in IAU Symposium, Vol. 258, The Ages of Stars, ed. E. E. Mamajek, D. R. Soderblom, & R. F. G. Wyse, 419–430

Lindegren, L., Lammers, U., Bastian, U., et al. 2016, A&A, 595, A4

Maeder, A. 1975, A&A, 40, 303

Maeder, A. & Meynet, G. 1987, A&A, 182, 243

Marigo, P., Girardi, L., Bressan, A., et al. 2017, ApJ, 835, 77

Miglio, A., Brogaard, K., Stello, D., Chaplin, W. J., & et al. 2012, MNRAS, 419, 2077

Miglio, A., Chaplin, W. J., Brogaard, K., et al. 2016, MNRAS, 461, 760

Miglio, A., Chiappini, C., Morel, T., et al. 2013, MNRAS, 429, 423

Montalbán, J. 2013, in Asteroseismology of Stellar Populations in the Milky Way, 6

Montalbán, J., Miglio, A., Noels, A., et al. 2013, ApJ, 766, 118

Montalbán, J. & Noels, A. 2013, in European Physical Journal Web of Conferences, Vol. 43, European Physical Journal Web of Conferences, 03002

Montgomery, K. A., Marschall, L. A., & Janes, K. A. 1993, AJ, 106, 181

Mosser, B., Barban, C., Montalbán, J., et al. 2011, A&A, 532, A86

Mosser, B., Elsworth, Y., Hekker, S., et al. 2012a, A&A, 537, A30

Mosser, B., Goupil, M. J., Belkacem, K., et al. 2012b, A&A, 540, A143

Paxton, B., Cantiello, M., Arras, P., et al. 2013, ApJS, 208, 4

Pinsonneault, M., et al., et al., et al. 2014, submitted to ApJS

Rauer, H., Catala, C., Aerts, C., et al. 2014, Experimental Astronomy, 38, 249

Ricker, G. R., Latham, D. W., Vanderspek, R. K., et al. 2009, in Bulletin of the American Astronomical Society, Vol. 41, American Astronomical Society Meeting Abstracts #213, 193

Rodrigues, T. S., Bossini, D., Miglio, A., et al. 2017, MNRAS, 467, 1433

Rodrigues, T. S., Girardi, L., Miglio, A., et al. 2014, MNRAS, 445, 2758

Rogers, F. J. & Nayfonov, A. 2002, ApJ, 576, 1064

Rowe, J. F., Matthews, J. M., Seager, S., et al. 2009, in IAU Symposium, Vol. 253, Transiting Planets, ed. F. Pont, D. Sasselov, & M. J. Holman, 121–127

Salaris, M. & Cassisi, S. 2005, Evolution of Stars and Stellar Populations, 400

Stello, D., Vanderburg, A., Casagrande, L., et al. 2016, ApJ, 832, 133

Stetson, P. B., Bruntt, H., & Grundahl, F. 2003, PASP, 115, 413

Townsend, R. H. D. & Teitler, S. A. 2013, MNRAS, 435, 3406

Ulrich, R. K. 1986, ApJ, 306, L37

Unno, W., Osaki, Y., Ando, H., Saio, H., & Shibahashi, H. 1989, Nonradial oscillations of stars

Appendices

A PARAM ERRORS

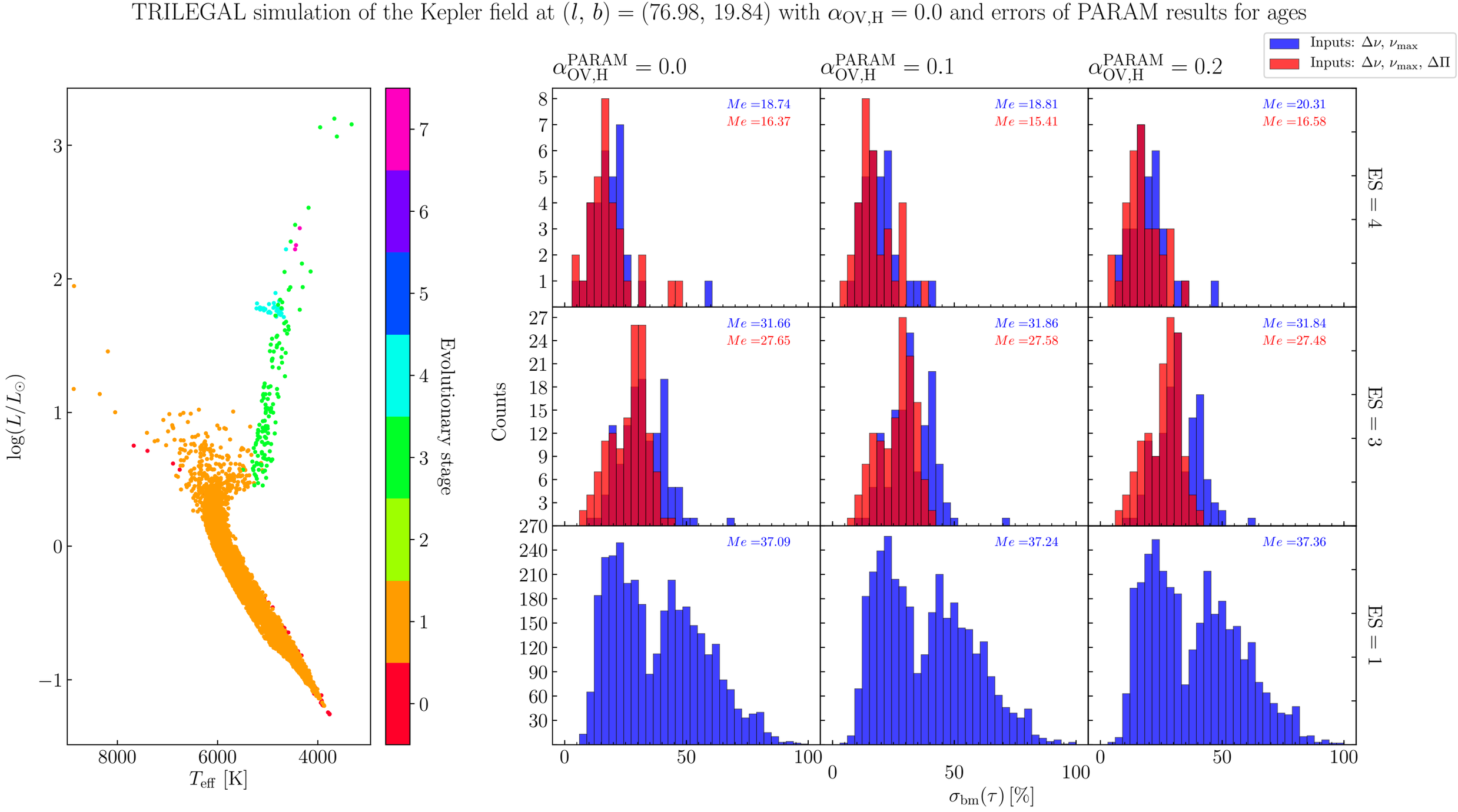
TRILEGAL simulation of the Kepler field at (l, b) = (76.98, 19.84) with $\alpha_{\rm OV,H} = 0.0$ and errors of PARAM results for ages
Inputs: $\Delta\nu$, $\nu_{\rm max}$
Inputs: $\Delta\nu$, $\nu_{\rm max}$, $\Delta\Pi$
$\alpha_{\rm OV,H}^{\rm PARAM} = 0.0$
$\alpha_{\rm OV,H}^{\rm PARAM} = 0.1$
$\alpha_{\rm OV,H}^{\rm PARAM} = 0.2$
$\log(L/L_\odot)$
$T_{\rm eff}$ [K]
Evolutionary stage
Counts
$\sigma_{\rm bm}(\tau)$ [%]
ES = 4
ES = 3
ES = 1
Me =18.74
Me =16.37
Me =18.81
Me =15.41
Me =20.31
Me =16.58
Me =31.66
Me =27.65
Me =31.86
Me =27.58
Me =31.84
Me =27.48
Me =37.09
Me =37.24
Me =37.36

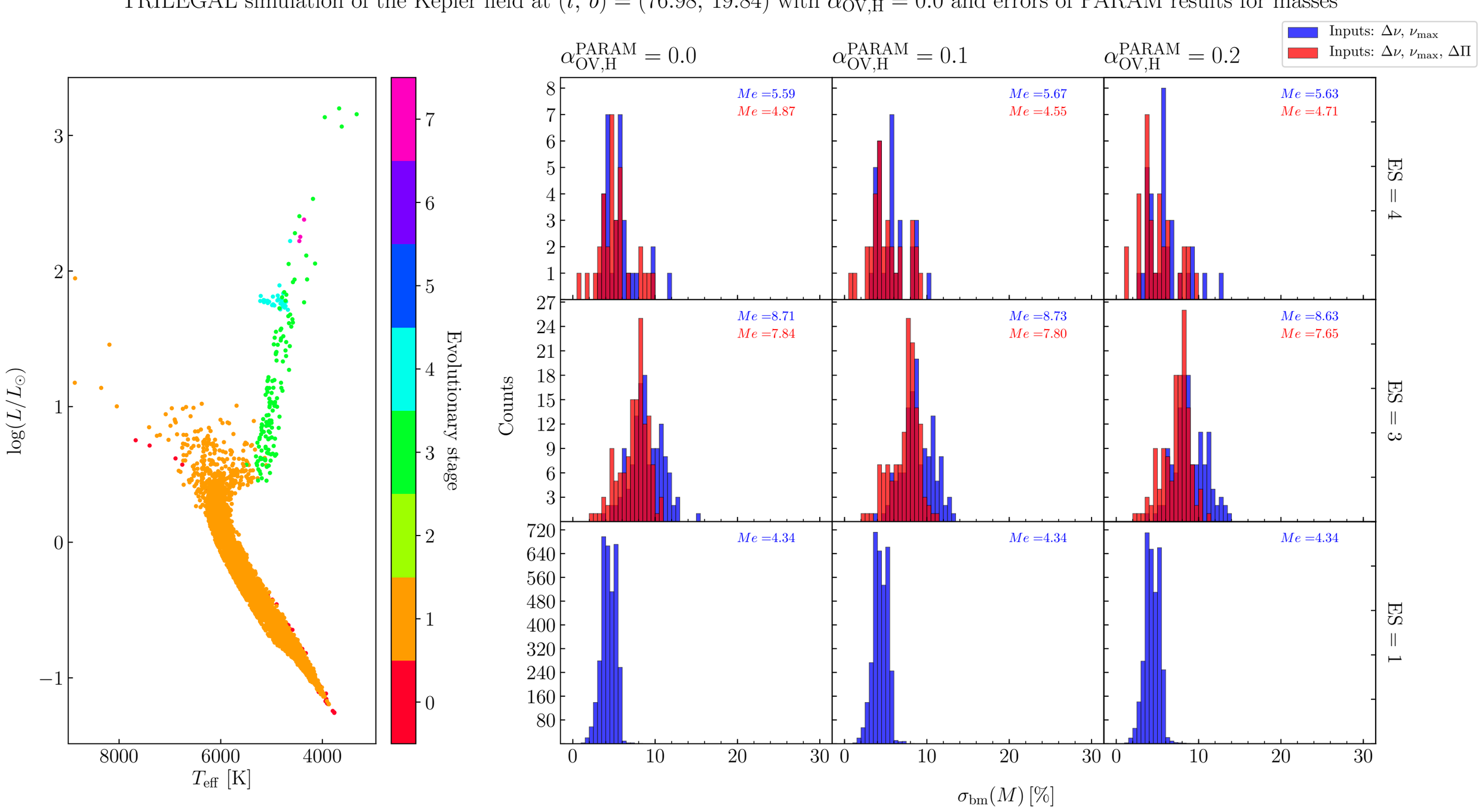
TRILEGAL simulation of the Kepler field at (l, b) = (76.98, 19.84) with $\alpha_{\rm OV,H} = 0.0$ and errors of PARAM results for masses
$\log(L/L_\odot)$
$T_{\rm eff}$ [K]
Evolutionary stage
$\alpha_{\rm OV,H}^{\rm PARAM} = 0.0$
$\alpha_{\rm OV,H}^{\rm PARAM} = 0.1$
$\alpha_{\rm OV,H}^{\rm PARAM} = 0.2$
Inputs: $\Delta\nu$, $\nu_{\rm max}$
Inputs: $\Delta\nu$, $\nu_{\rm max}$, $\Delta\Pi$
Me =5.59
Me =4.87
Me =5.67
Me =4.55
Me =5.63
Me =4.71
Me =8.71
Me =7.84
Me =8.73
Me =7.80
Me =8.63
Me =7.65
Me =4.34
Me =4.34
Me =4.34
ES = 4
ES = 3
ES = 1
Counts
$\sigma_{\rm bm}(M)$ [%]

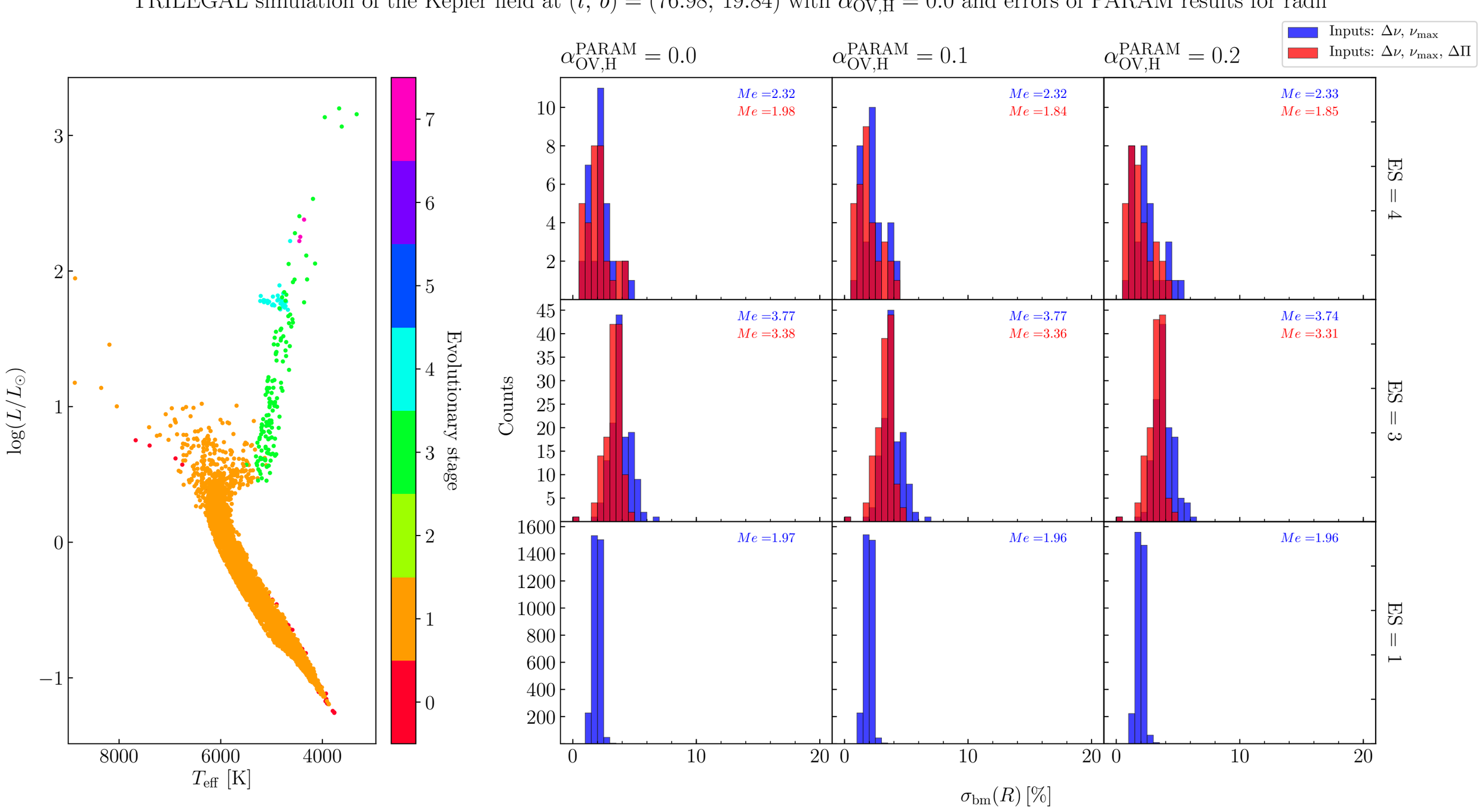
TRILEGAL simulation of the Kepler field at (l, b) = (76.98, 19.84) with $\alpha_{\rm OV,H} = 0.0$ and errors of PARAM results for radii
Inputs: $\Delta\nu$, $\nu_{\rm max}$
Inputs: $\Delta\nu$, $\nu_{\rm max}$, $\Delta\Pi$
$\alpha_{\rm OV,H}^{\rm PARAM} = 0.0$
$\alpha_{\rm OV,H}^{\rm PARAM} = 0.1$
$\alpha_{\rm OV,H}^{\rm PARAM} = 0.2$
$\log(L/L_\odot)$
$T_{\rm eff}$ [K]
Evolutionary stage
Counts
$\sigma_{\rm bm}(R)$ [%]
ES = 4
ES = 3
ES = 1
Me =2.32
Me =1.98
Me =2.32
Me =1.84
Me =2.33
Me =1.85
Me =3.77
Me =3.38
Me =3.77
Me =3.36
Me =3.74
Me =3.31
Me =1.97
Me =1.96
Me =1.96

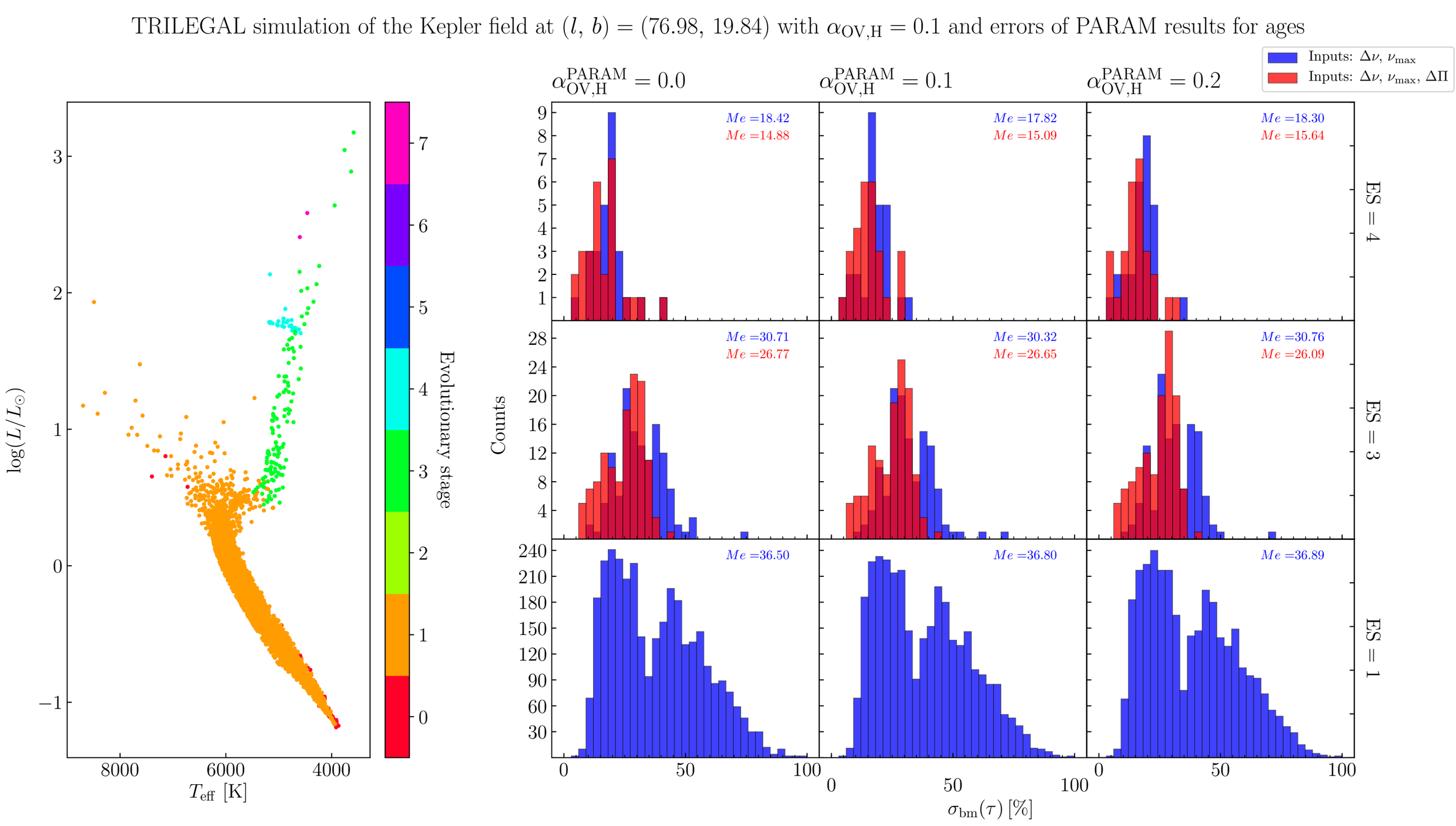
TRILEGAL simulation of the Kepler field at (l, b) = (76.98, 19.84) with $\alpha_{\rm OV,H} = 0.1$ and errors of PARAM results for ages
Inputs: $\Delta\nu$, $\nu_{\rm max}$
Inputs: $\Delta\nu$, $\nu_{\rm max}$, $\Delta\Pi$
$\alpha_{\rm OV,H}^{\rm PARAM} = 0.0$
$\alpha_{\rm OV,H}^{\rm PARAM} = 0.1$
$\alpha_{\rm OV,H}^{\rm PARAM} = 0.2$
$\log(L/L_\odot)$
$T_{\rm eff}$ [K]
Evolutionary stage
Counts
$\sigma_{\rm bm}(\tau)$ [%]
ES = 4
ES = 3
ES = 1
Me =18.42
Me =14.88
Me =17.82
Me =15.09
Me =18.30
Me =15.64
Me =30.71
Me =26.77
Me =30.32
Me =26.65
Me =30.76
Me =26.09
Me =36.50
Me =36.80
Me =36.89

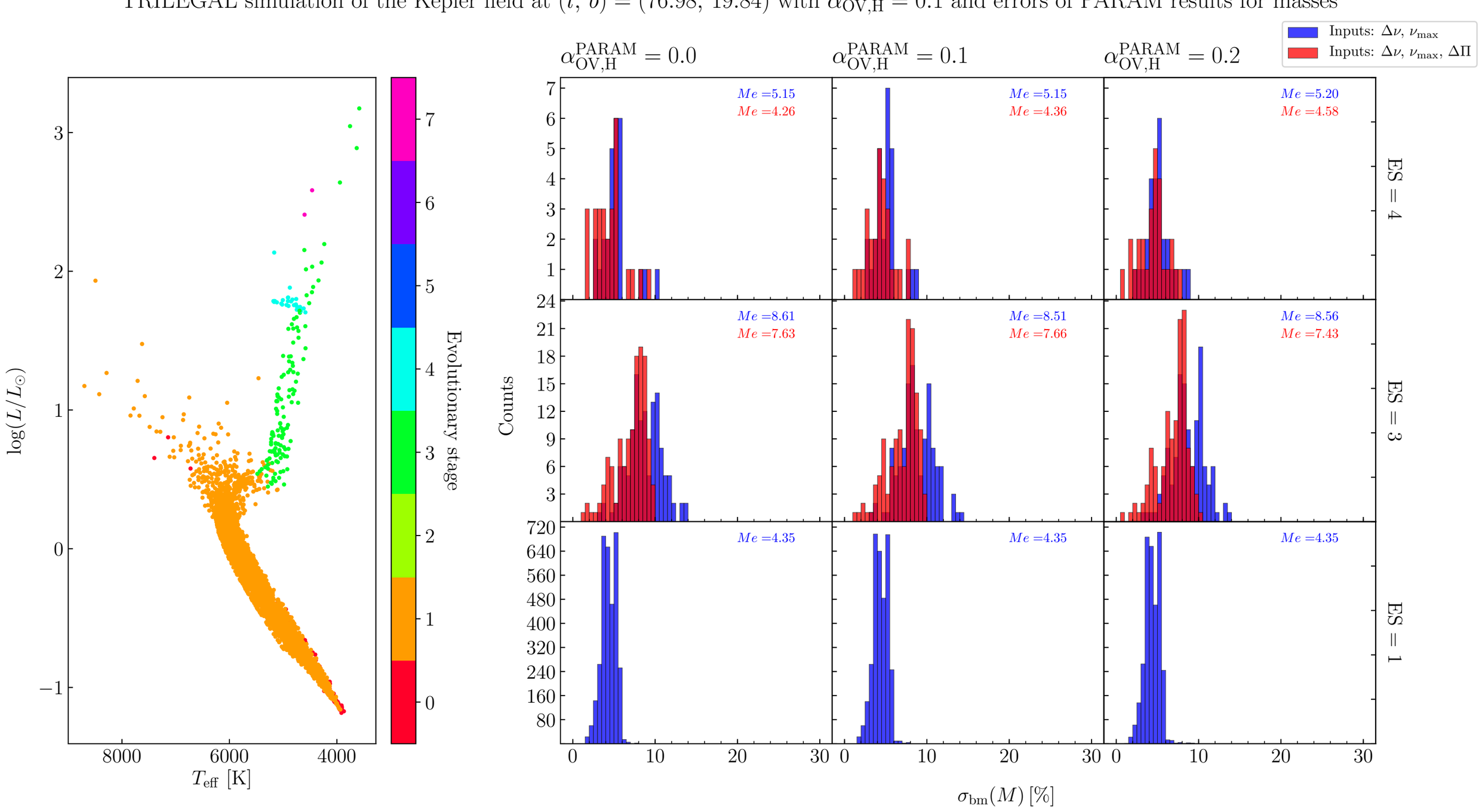
TRILEGAL simulation of the Kepler field at (l, b) = (76.98, 19.84) with $\alpha_{\rm OV,H} = 0.1$ and errors of PARAM results for masses
$\log(L/L_\odot)$
$T_{\rm eff}$ [K]
Evolutionary stage
$\alpha^{\rm PARAM}_{\rm OV,H} = 0.0$
$\alpha^{\rm PARAM}_{\rm OV,H} = 0.1$
$\alpha^{\rm PARAM}_{\rm OV,H} = 0.2$
Inputs: $\Delta\nu$, $\nu_{\rm max}$
Inputs: $\Delta\nu$, $\nu_{\rm max}$, $\Delta\Pi$
Me =5.15
Me =4.26
Me =5.15
Me =4.36
Me =5.20
Me =4.58
Me =8.61
Me =7.63
Me =8.51
Me =7.66
Me =8.56
Me =7.43
Me =4.35
Me =4.35
Me =4.35
ES = 4
ES = 3
ES = 1
Counts
$\sigma_{\rm bm}(M)$ [%]

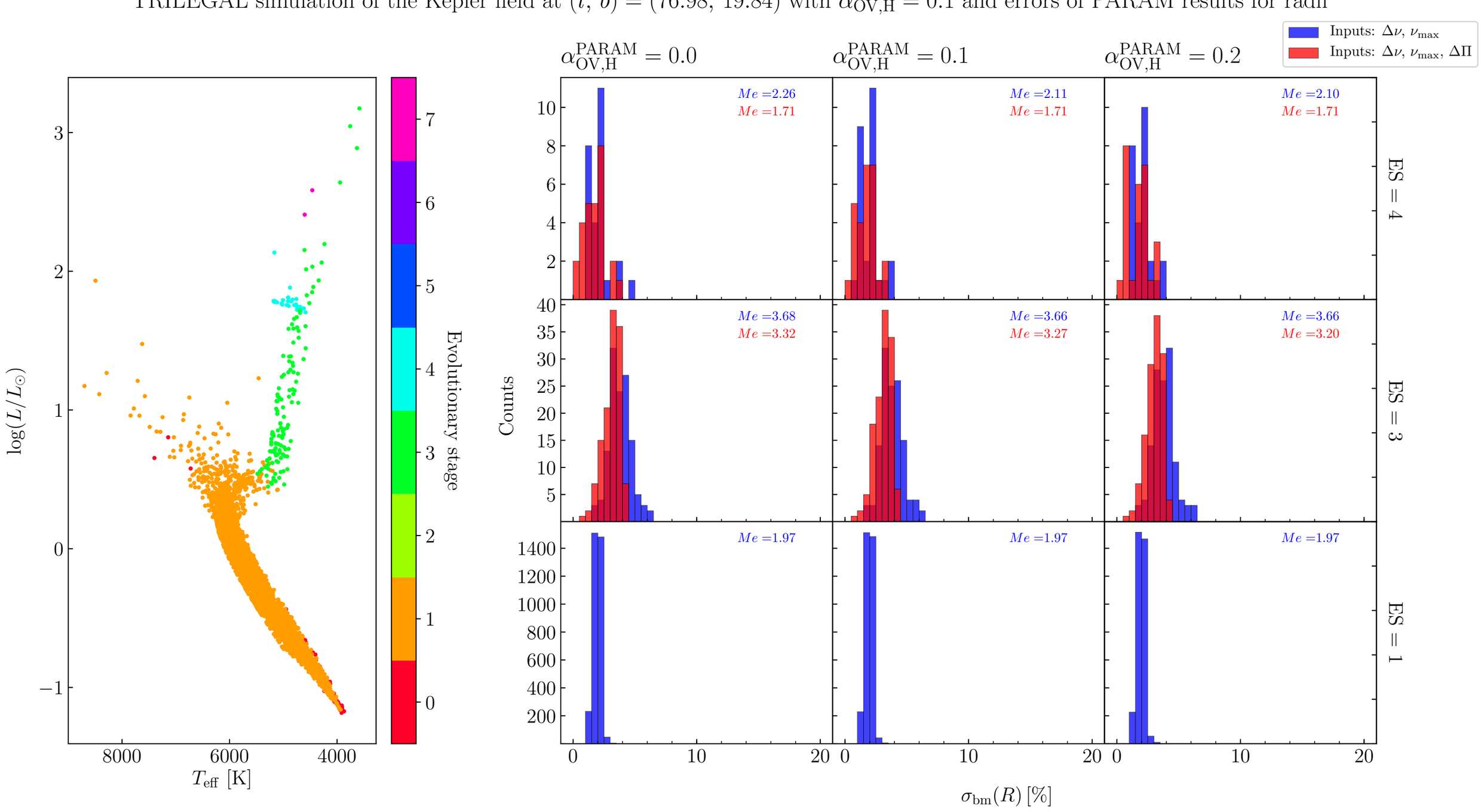
TRILEGAL simulation of the Kepler field at $(l, b) = (76.98, 19.84)$ with $\alpha_{\rm OV,H} = 0.1$ and errors of PARAM results for radii
Inputs: $\Delta\nu$, $\nu_{\rm max}$
Inputs: $\Delta\nu$, $\nu_{\rm max}$, $\Delta\Pi$
$\alpha_{\rm OV,H}^{\rm PARAM} = 0.0$
$\alpha_{\rm OV,H}^{\rm PARAM} = 0.1$
$\alpha_{\rm OV,H}^{\rm PARAM} = 0.2$
Me =2.26
Me =1.71
Me =2.11
Me =1.71
Me =2.10
Me =1.71
Me =3.68
Me =3.32
Me =3.66
Me =3.27
Me =3.66
Me =3.20
Me =1.97
Me =1.97
Me =1.97
ES = 4
ES = 3
ES = 1
Counts
$\sigma_{\rm bm}(R)$ [%]
$\log(L/L_\odot)$
$T_{\rm eff}$ [K]
Evolutionary stage

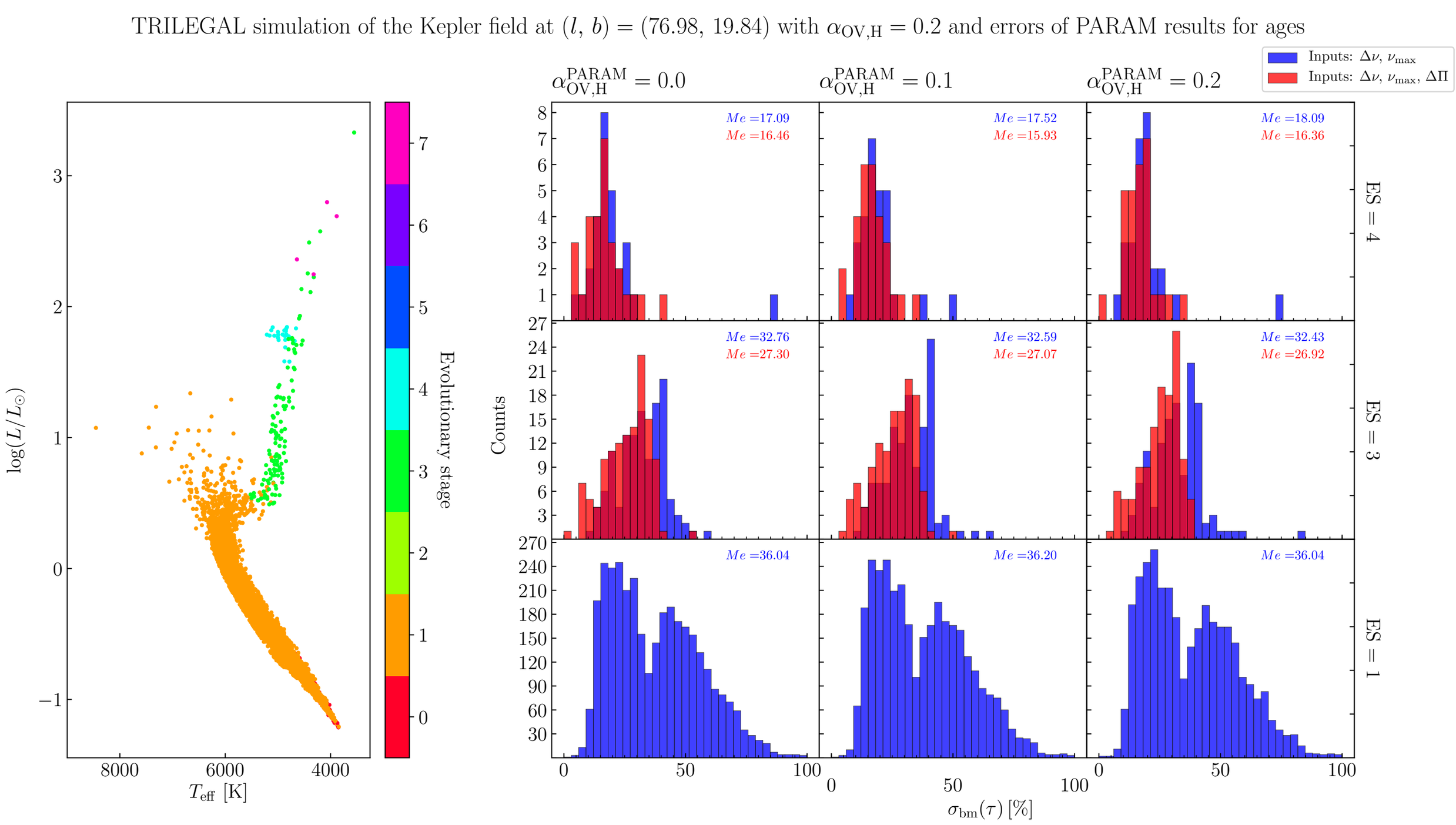
TRILEGAL simulation of the Kepler field at (l, b) = (76.98, 19.84) with $\alpha_{\rm OV,H} = 0.2$ and errors of PARAM results for ages
Inputs: $\Delta\nu$, $\nu_{\rm max}$
Inputs: $\Delta\nu$, $\nu_{\rm max}$, $\Delta\Pi$
$\alpha_{\rm OV,H}^{\rm PARAM} = 0.0$
$\alpha_{\rm OV,H}^{\rm PARAM} = 0.1$
$\alpha_{\rm OV,H}^{\rm PARAM} = 0.2$
$\log(L/L_\odot)$
$T_{\rm eff}$ [K]
Evolutionary stage
Counts
$\sigma_{\rm bm}(\tau)$ [%]
ES = 4
ES = 3
ES = 1
Me =17.09
Me =16.46
Me =17.52
Me =15.93
Me =18.09
Me =16.36
Me =32.76
Me =27.30
Me =32.59
Me =27.07
Me =32.43
Me =26.92
Me =36.04
Me =36.20
Me =36.04

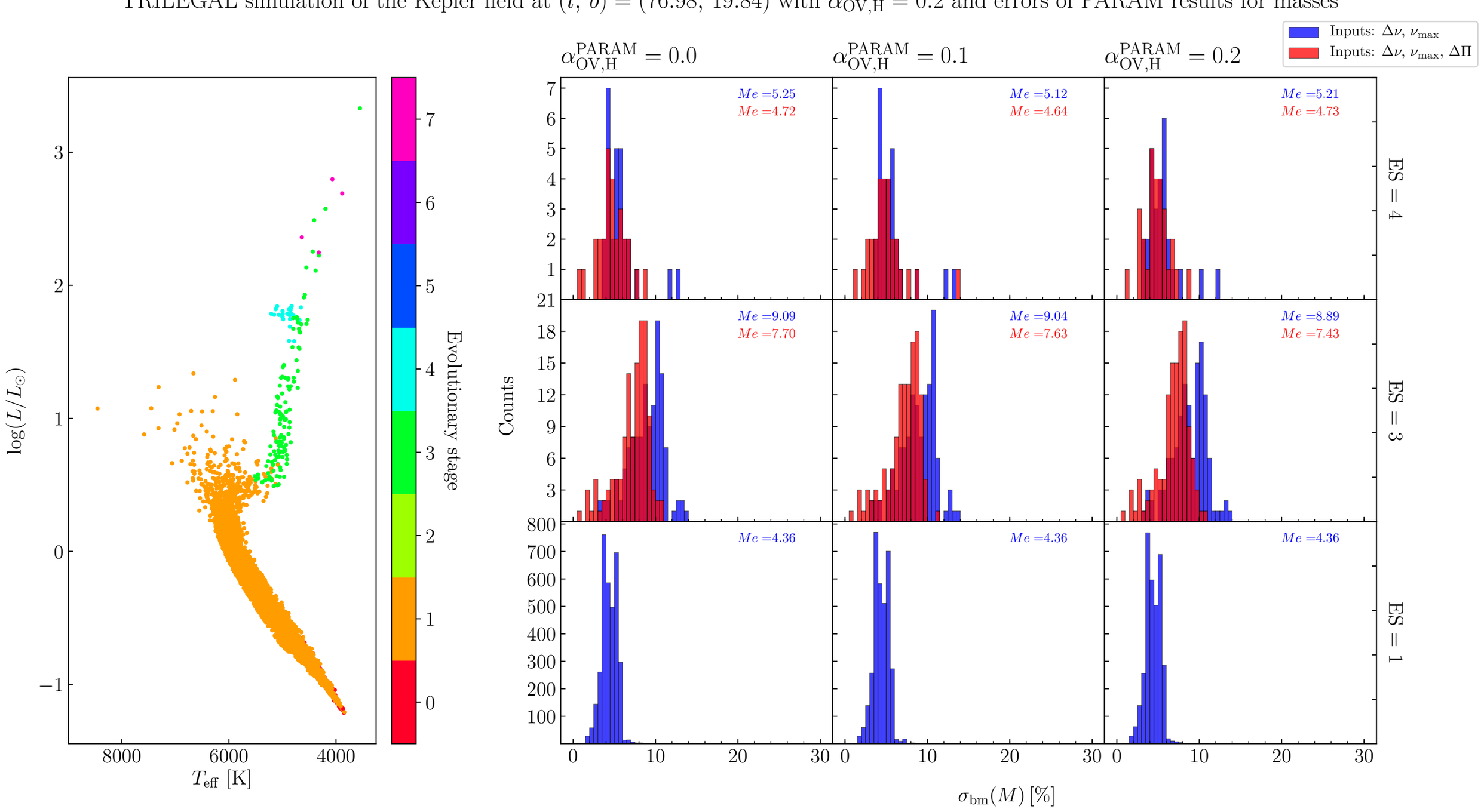
TRILEGAL simulation of the Kepler field at (l, b) = (76.98, 19.84) with $\alpha_{\rm OV,H} = 0.2$ and errors of PARAM results for masses
$\log(L/L_\odot)$
$T_{\rm eff}$ [K]
Evolutionary stage
$\alpha_{\rm OV,H}^{\rm PARAM} = 0.0$
$\alpha_{\rm OV,H}^{\rm PARAM} = 0.1$
$\alpha_{\rm OV,H}^{\rm PARAM} = 0.2$
Inputs: $\Delta\nu$, $\nu_{\rm max}$
Inputs: $\Delta\nu$, $\nu_{\rm max}$, $\Delta\Pi$
Me =5.25
Me =4.72
Me =5.12
Me =4.64
Me =5.21
Me =4.73
Me =9.09
Me =7.70
Me =9.04
Me =7.63
Me =8.89
Me =7.43
Me =4.36
Me =4.36
Me =4.36
ES = 4
ES = 3
ES = 1
Counts
$\sigma_{\rm bm}(M)$ [%]

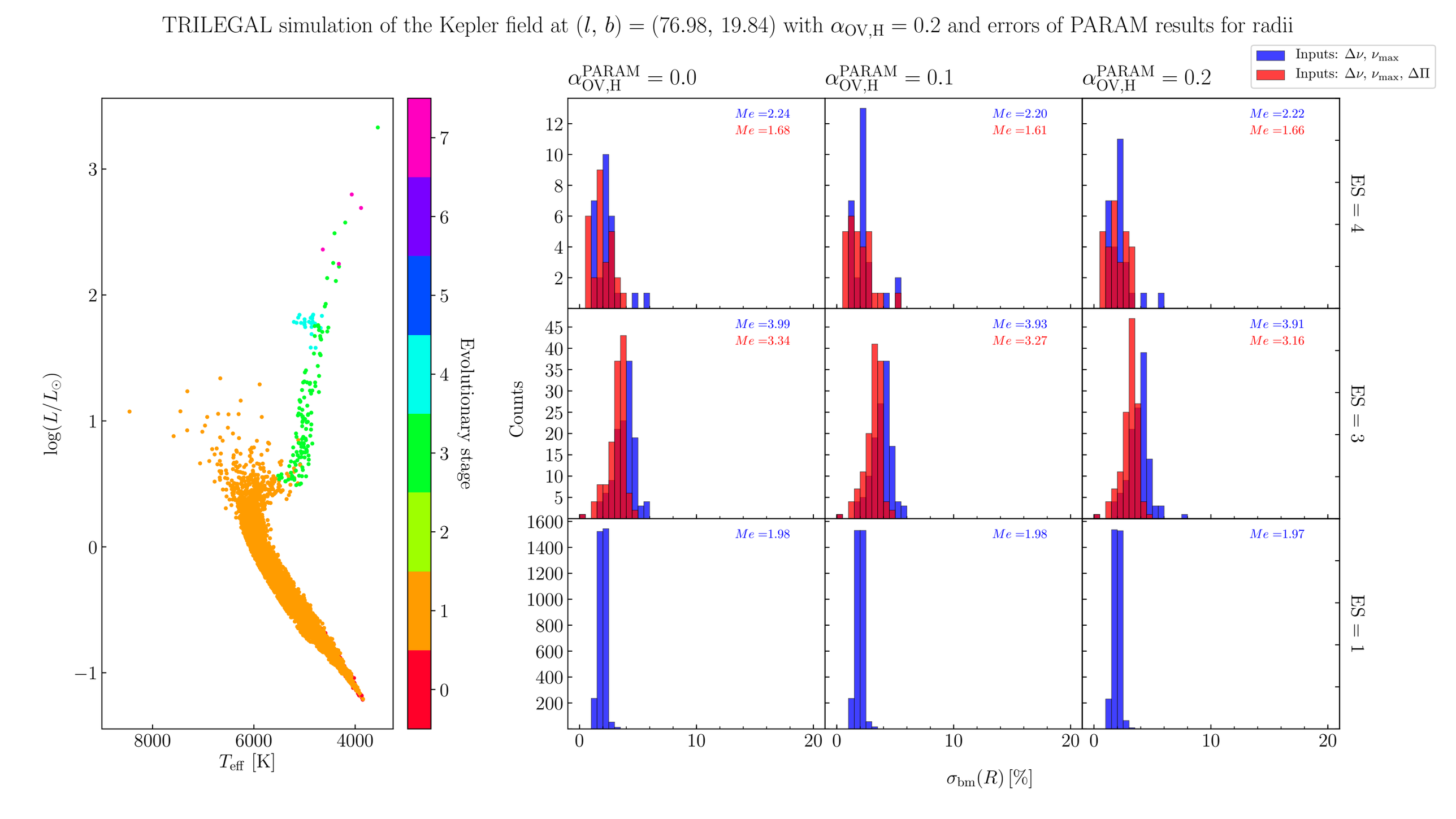
TRILEGAL simulation of the Kepler field at $(l, b) = (76.98, 19.84)$ with $\alpha_{\rm OV,H} = 0.2$ and errors of PARAM results for radii
$\log(L/L_\odot)$
$T_{\rm eff}$ [K]
Evolutionary stage
$\alpha_{\rm OV,H}^{\rm PARAM} = 0.0$
$\alpha_{\rm OV,H}^{\rm PARAM} = 0.1$
$\alpha_{\rm OV,H}^{\rm PARAM} = 0.2$
Inputs: $\Delta\nu$, $\nu_{\rm max}$
Inputs: $\Delta\nu$, $\nu_{\rm max}$, $\Delta\Pi$
Me =2.24
Me =1.68
Me =2.20
Me =1.61
Me =2.22
Me =1.66
Me =3.99
Me =3.34
Me =3.93
Me =3.27
Me =3.91
Me =3.16
Me =1.98
Me =1.98
Me =1.97
ES = 4
ES = 3
ES = 1
Counts
$\sigma_{\rm bm}(R)$ [%]

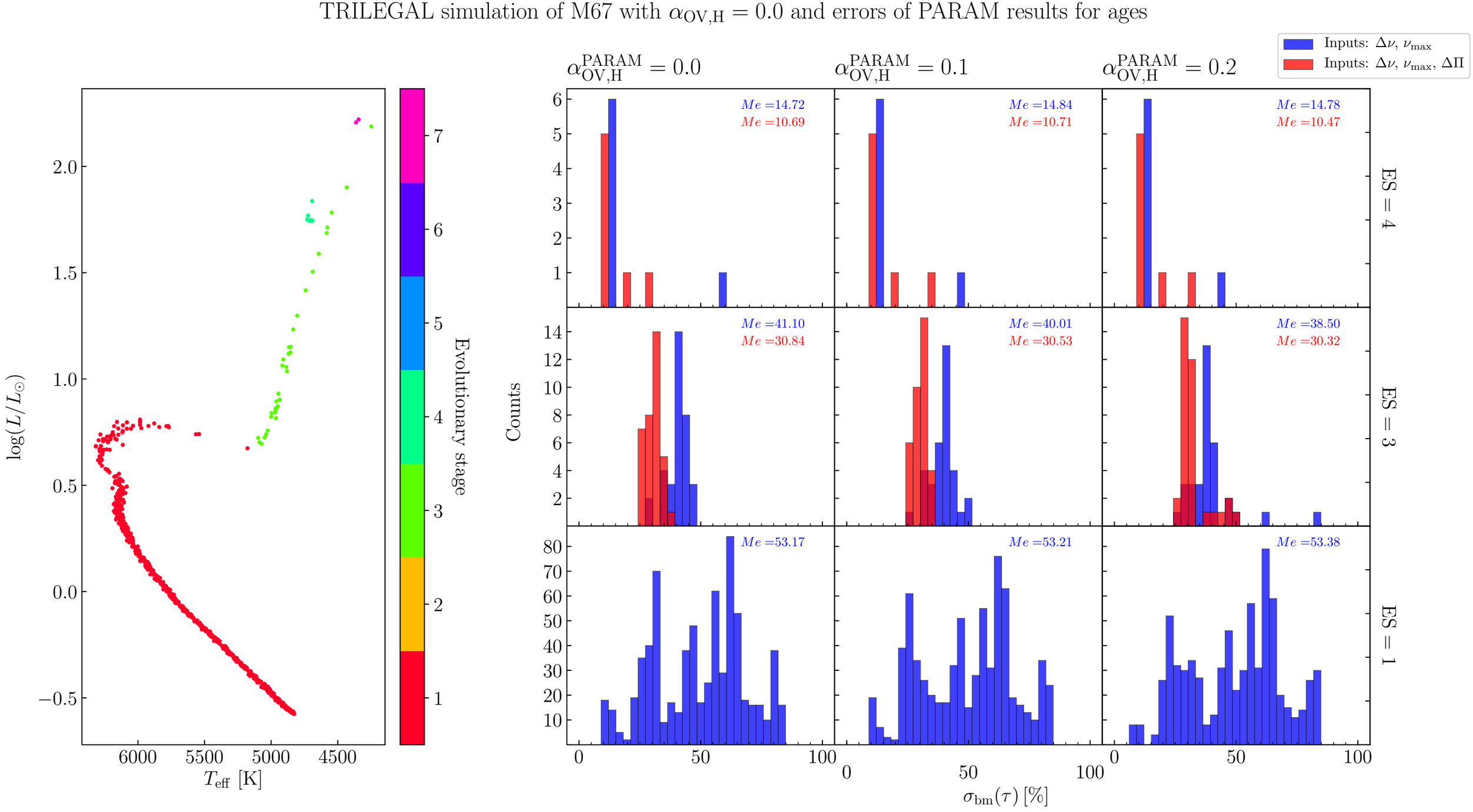
TRILEGAL simulation of M67 with $\alpha_{\rm OV,H} = 0.0$ and errors of PARAM results for ages
Inputs: $\Delta\nu$, $\nu_{\rm max}$
Inputs: $\Delta\nu$, $\nu_{\rm max}$, $\Delta\Pi$
$\alpha_{\rm OV,H}^{\rm PARAM} = 0.0$
$\alpha_{\rm OV,H}^{\rm PARAM} = 0.1$
$\alpha_{\rm OV,H}^{\rm PARAM} = 0.2$
$\log(L/L_\odot)$
$T_{\rm eff}$ [K]
Evolutionary stage
Counts
$\sigma_{\rm bm}(\tau)$ [%]
ES = 4
ES = 3
ES = 1
Me =14.72
Me =10.69
Me =14.84
Me =10.71
Me =14.78
Me =10.47
Me =41.10
Me =30.84
Me =40.01
Me =30.53
Me =38.50
Me =30.32
Me =53.17
Me =53.21
Me =53.38

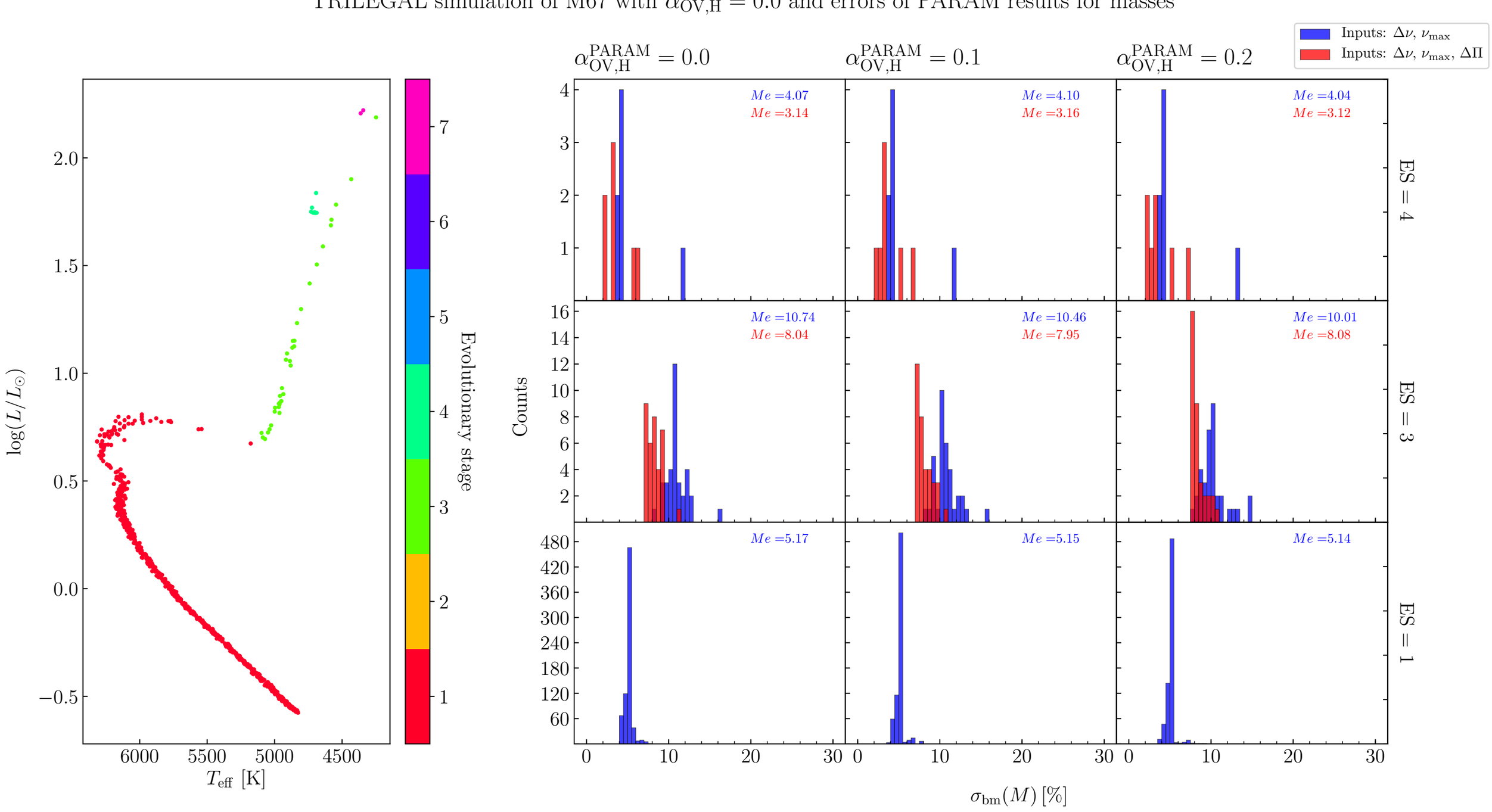
TRILEGAL simulation of M67 with $\alpha_{\rm OV,H} = 0.0$ and errors of PARAM results for masses
Inputs: $\Delta\nu$, $\nu_{\rm max}$
Inputs: $\Delta\nu$, $\nu_{\rm max}$, $\Delta\Pi$
$\alpha_{\rm OV,H}^{\rm PARAM} = 0.0$
$\alpha_{\rm OV,H}^{\rm PARAM} = 0.1$
$\alpha_{\rm OV,H}^{\rm PARAM} = 0.2$
$\log(L/L_\odot)$
$T_{\rm eff}$ [K]
Evolutionary stage
Counts
$\sigma_{\rm bm}(M)$ [%]
ES = 4
ES = 3
ES = 1
Me =4.07
Me =3.14
Me =4.10
Me =3.16
Me =4.04
Me =3.12
Me =10.74
Me =8.04
Me =10.46
Me =7.95
Me =10.01
Me =8.08
Me =5.17
Me =5.15
Me =5.14

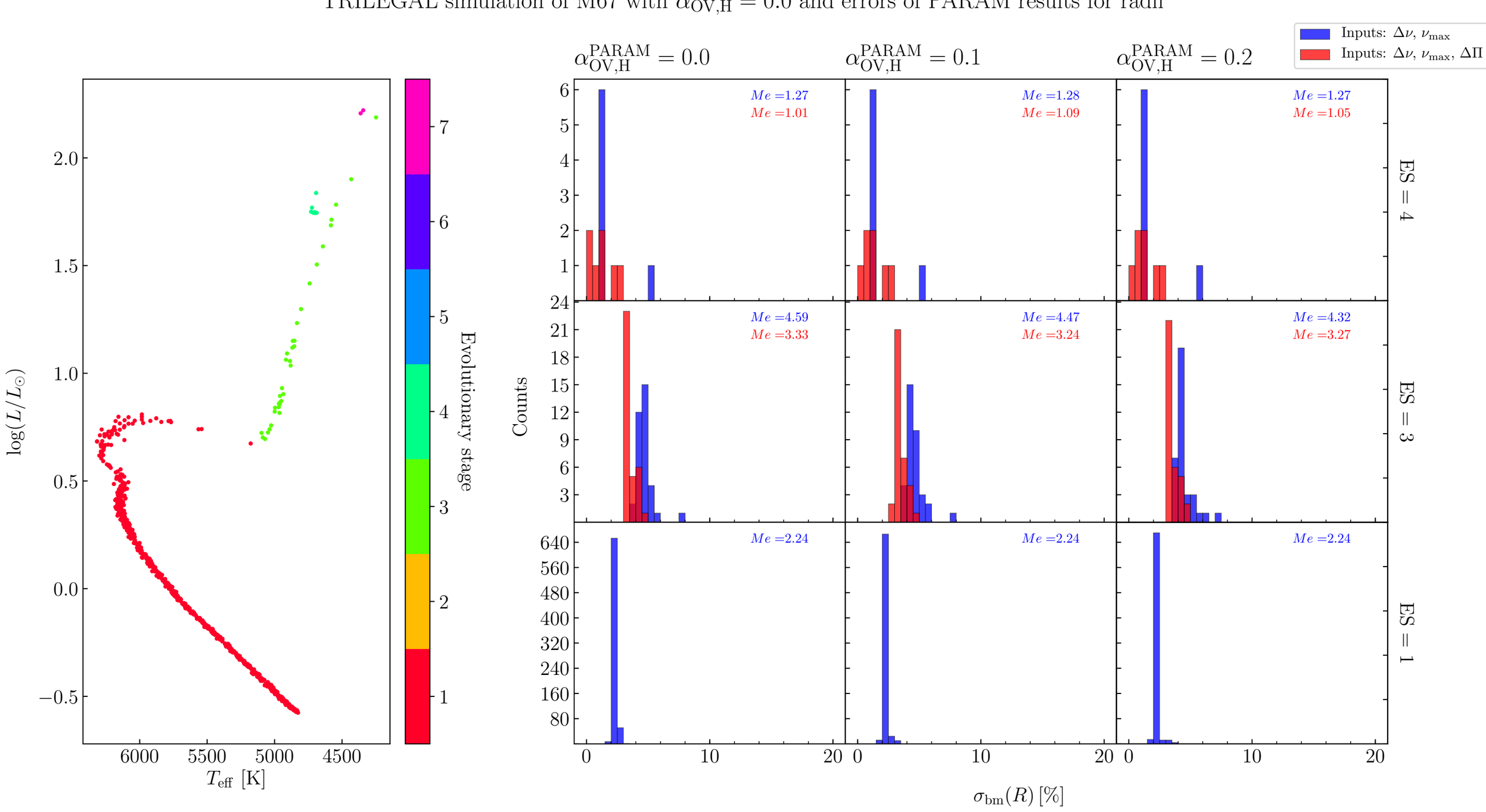
TRILEGAL simulation of M67 with $\alpha_{\rm OV,H} = 0.0$ and errors of PARAM results for radii
Inputs: $\Delta\nu$, $\nu_{\rm max}$
Inputs: $\Delta\nu$, $\nu_{\rm max}$, $\Delta\Pi$
$\alpha_{\rm OV,H}^{\rm PARAM} = 0.0$
$\alpha_{\rm OV,H}^{\rm PARAM} = 0.1$
$\alpha_{\rm OV,H}^{\rm PARAM} = 0.2$
$\log(L/L_\odot)$
$T_{\rm eff}$ [K]
Evolutionary stage
Counts
$\sigma_{\rm bm}(R)$ [%]
ES = 4
ES = 3
ES = 1
Me =1.27
Me =1.01
Me =1.28
Me =1.09
Me =1.27
Me =1.05
Me =4.59
Me =3.33
Me =4.47
Me =3.24
Me =4.32
Me =3.27
Me =2.24
Me =2.24
Me =2.24

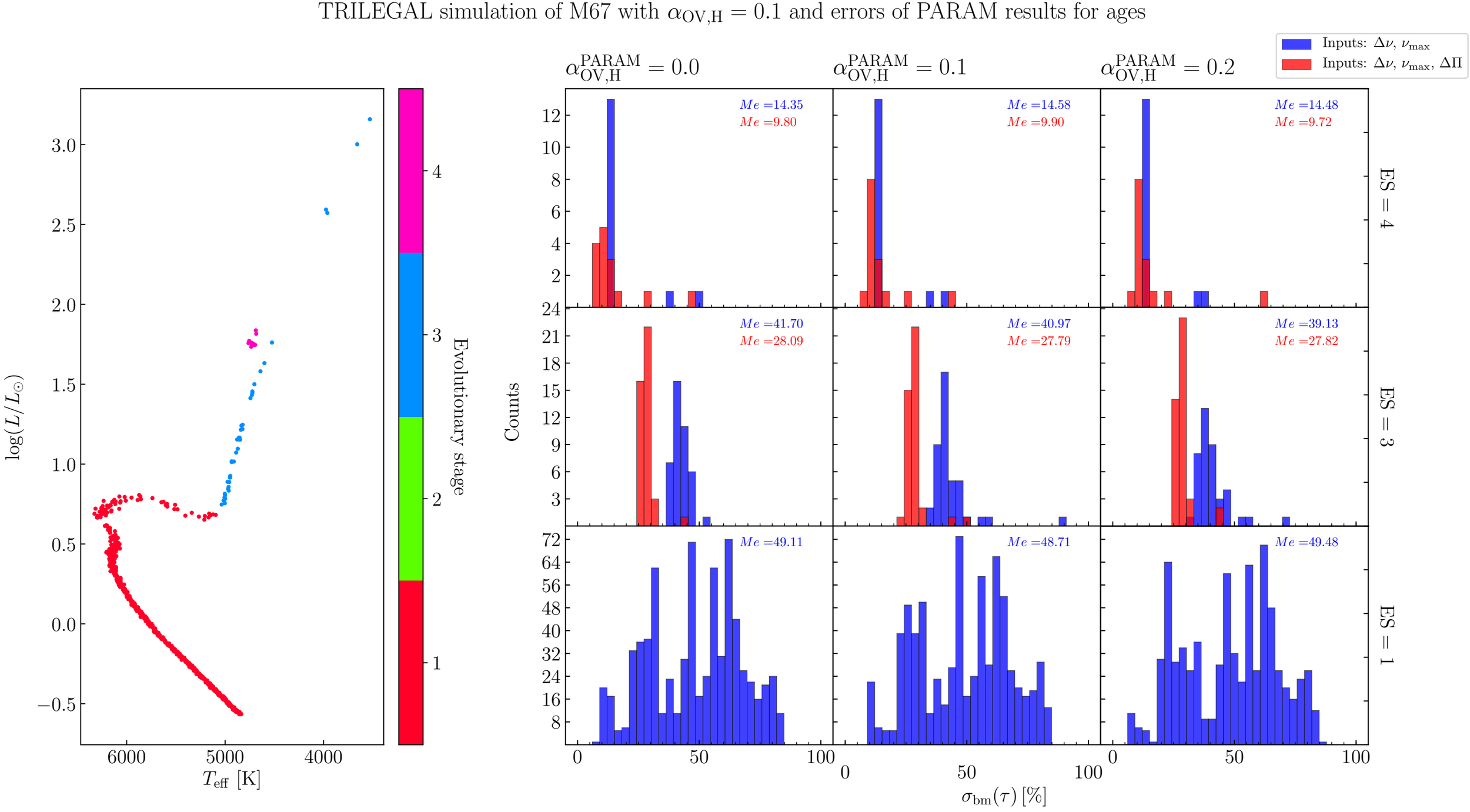
TRILEGAL simulation of M67 with $\alpha_{\rm OV,H} = 0.1$ and errors of PARAM results for ages
Inputs: $\Delta\nu$, $\nu_{\rm max}$
Inputs: $\Delta\nu$, $\nu_{\rm max}$, $\Delta\Pi$
$\alpha_{\rm OV,H}^{\rm PARAM} = 0.0$
$\alpha_{\rm OV,H}^{\rm PARAM} = 0.1$
$\alpha_{\rm OV,H}^{\rm PARAM} = 0.2$
Me =14.35
Me =9.80
Me =14.58
Me =9.90
Me =14.48
Me =9.72
Me =41.70
Me =28.09
Me =40.97
Me =27.79
Me =39.13
Me =27.82
Me =49.11
Me =48.71
Me =49.48
ES = 4
ES = 3
ES = 1
Counts
$\sigma_{\rm bm}(\tau)$ [%]
$\log(L/L_\odot)$
$T_{\rm eff}$ [K]
Evolutionary stage

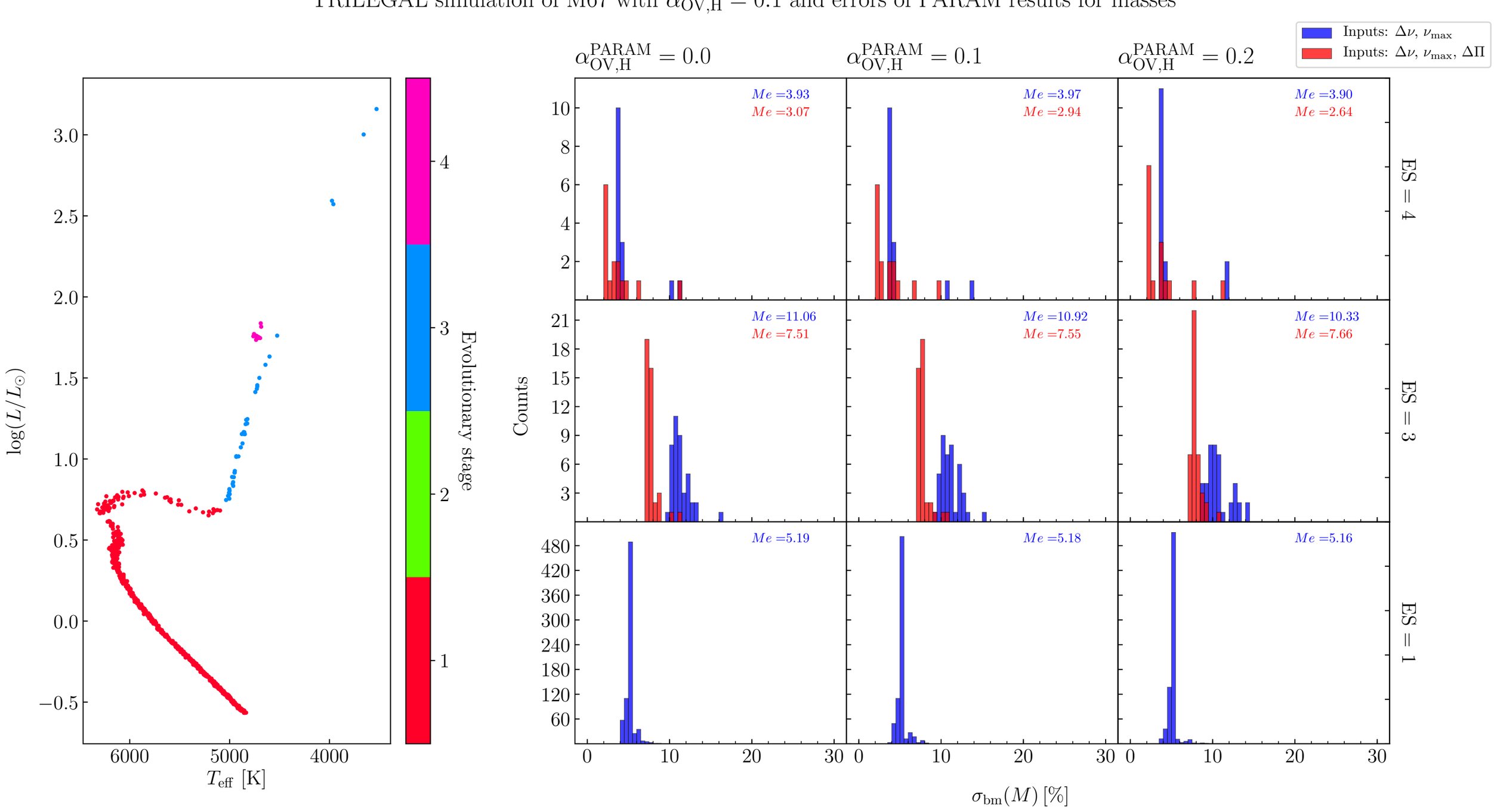
TRILEGAL simulation of M67 with $\alpha_{\rm OV,H} = 0.1$ and errors of PARAM results for masses
Inputs: $\Delta\nu$, $\nu_{\rm max}$
Inputs: $\Delta\nu$, $\nu_{\rm max}$, $\Delta\Pi$
$\alpha_{\rm OV,H}^{\rm PARAM} = 0.0$
$\alpha_{\rm OV,H}^{\rm PARAM} = 0.1$
$\alpha_{\rm OV,H}^{\rm PARAM} = 0.2$
$\log(L/L_\odot)$
$T_{\rm eff}$ [K]
Evolutionary stage
Counts
$\sigma_{\rm bm}(M)$ [%]
ES = 4
ES = 3
ES = 1
Me =3.93
Me =3.07
Me =3.97
Me =2.94
Me =3.90
Me =2.64
Me =11.06
Me =7.51
Me =10.92
Me =7.55
Me =10.33
Me =7.66
Me =5.19
Me =5.18
Me =5.16

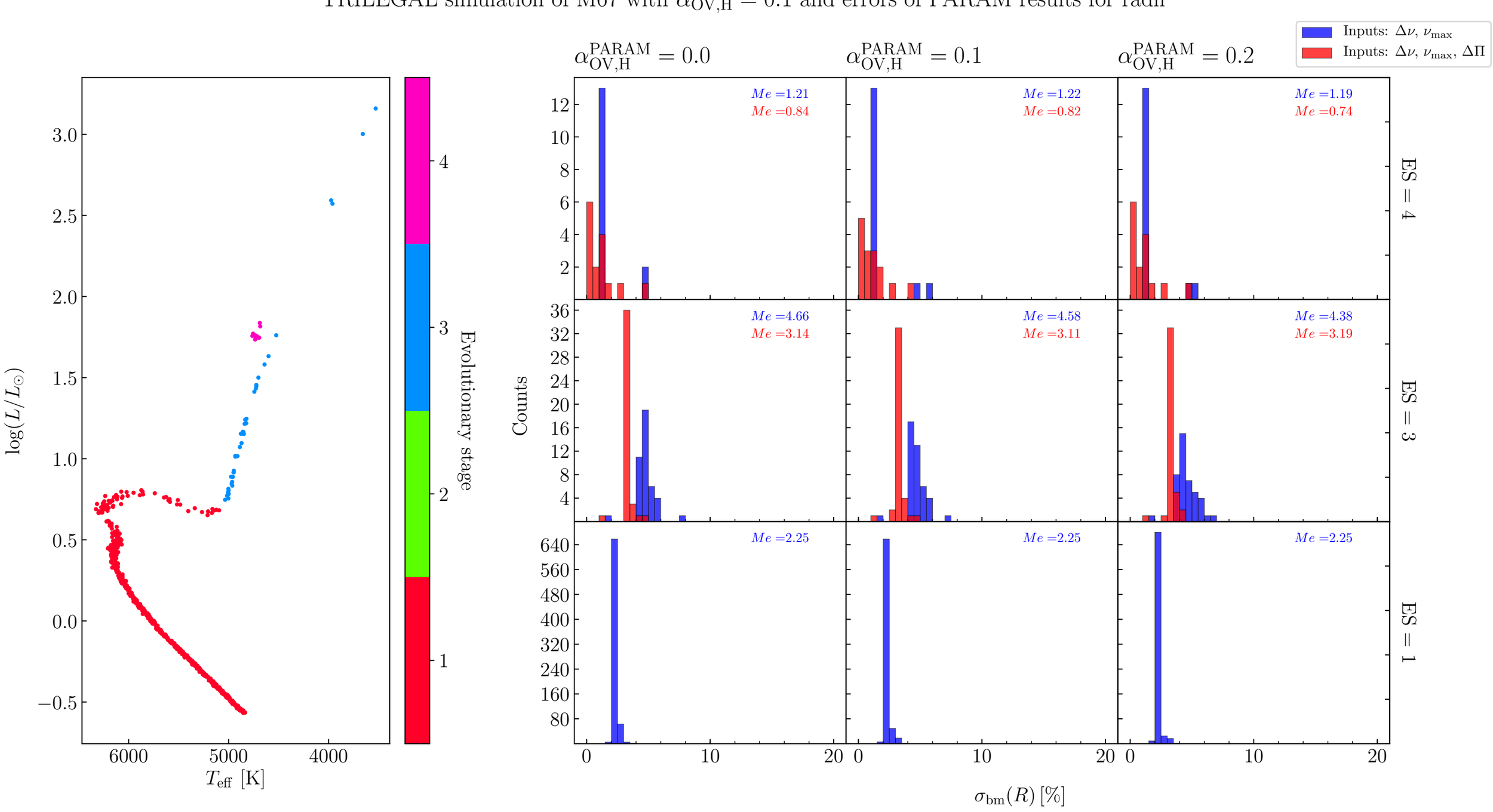
TRILEGAL simulation of M67 with $\alpha_{\rm OV,H} = 0.1$ and errors of PARAM results for radii
Inputs: $\Delta\nu$, $\nu_{\rm max}$
Inputs: $\Delta\nu$, $\nu_{\rm max}$, $\Delta\Pi$
$\alpha_{\rm OV,H}^{\rm PARAM} = 0.0$
$\alpha_{\rm OV,H}^{\rm PARAM} = 0.1$
$\alpha_{\rm OV,H}^{\rm PARAM} = 0.2$
$\log(L/L_\odot)$
$T_{\rm eff}$ [K]
Evolutionary stage
Counts
$\sigma_{\rm bm}(R)$ [%]
ES = 4
ES = 3
ES = 1
Me =1.21
Me =0.84
Me =1.22
Me =0.82
Me =1.19
Me =0.74
Me =4.66
Me =3.14
Me =4.58
Me =3.11
Me =4.38
Me =3.19
Me =2.25
Me =2.25
Me =2.25

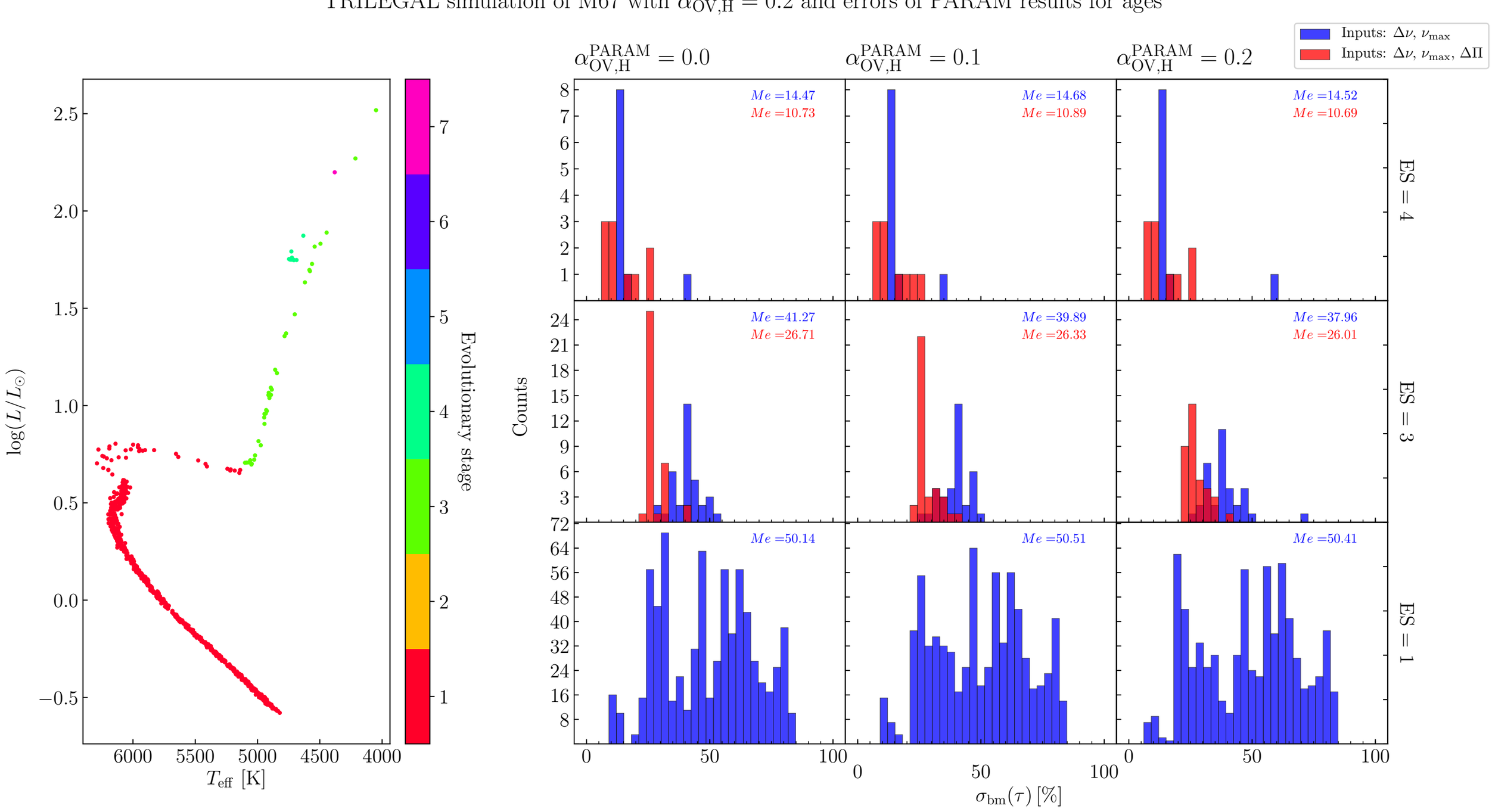
TRILEGAL simulation of M67 with $\alpha_{\rm OV,H} = 0.2$ and errors of PARAM results for ages
Inputs: $\Delta\nu$, $\nu_{\rm max}$
Inputs: $\Delta\nu$, $\nu_{\rm max}$, $\Delta\Pi$
$\alpha_{\rm OV,H}^{\rm PARAM} = 0.0$
$\alpha_{\rm OV,H}^{\rm PARAM} = 0.1$
$\alpha_{\rm OV,H}^{\rm PARAM} = 0.2$
$\log(L/L_\odot)$
$T_{\rm eff}$ [K]
Evolutionary stage
Counts
$\sigma_{\rm bm}(\tau)$ [%]
ES = 4
ES = 3
ES = 1
Me =14.47
Me =10.73
Me =14.68
Me =10.89
Me =14.52
Me =10.69
Me =41.27
Me =26.71
Me =39.89
Me =26.33
Me =37.96
Me =26.01
Me =50.14
Me =50.51
Me =50.41

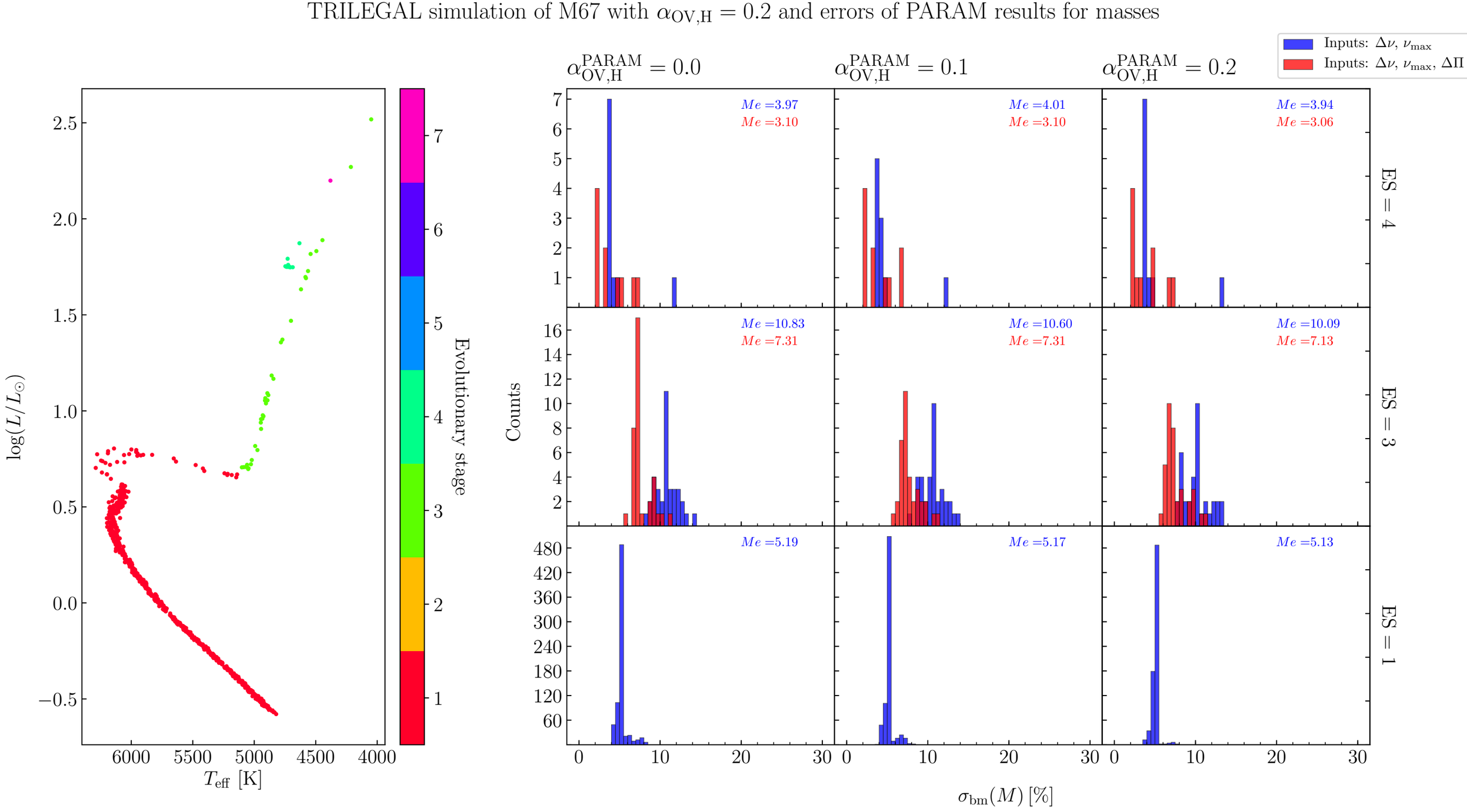
TRILEGAL simulation of M67 with $\alpha_{\rm OV,H} = 0.2$ and errors of PARAM results for masses
Inputs: $\Delta\nu$, $\nu_{\rm max}$
Inputs: $\Delta\nu$, $\nu_{\rm max}$, $\Delta\Pi$
$\alpha_{\rm OV,H}^{\rm PARAM} = 0.0$
$\alpha_{\rm OV,H}^{\rm PARAM} = 0.1$
$\alpha_{\rm OV,H}^{\rm PARAM} = 0.2$
$\log(L/L_\odot)$
$T_{\rm eff}$ [K]
Evolutionary stage
Counts
$\sigma_{\rm bm}(M)$ [%]
ES = 4
ES = 3
ES = 1
Me =3.97
Me =3.10
Me =4.01
Me =3.10
Me =3.94
Me =3.06
Me =10.83
Me =7.31
Me =10.60
Me =7.31
Me =10.09
Me =7.13
Me =5.19
Me =5.17
Me =5.13

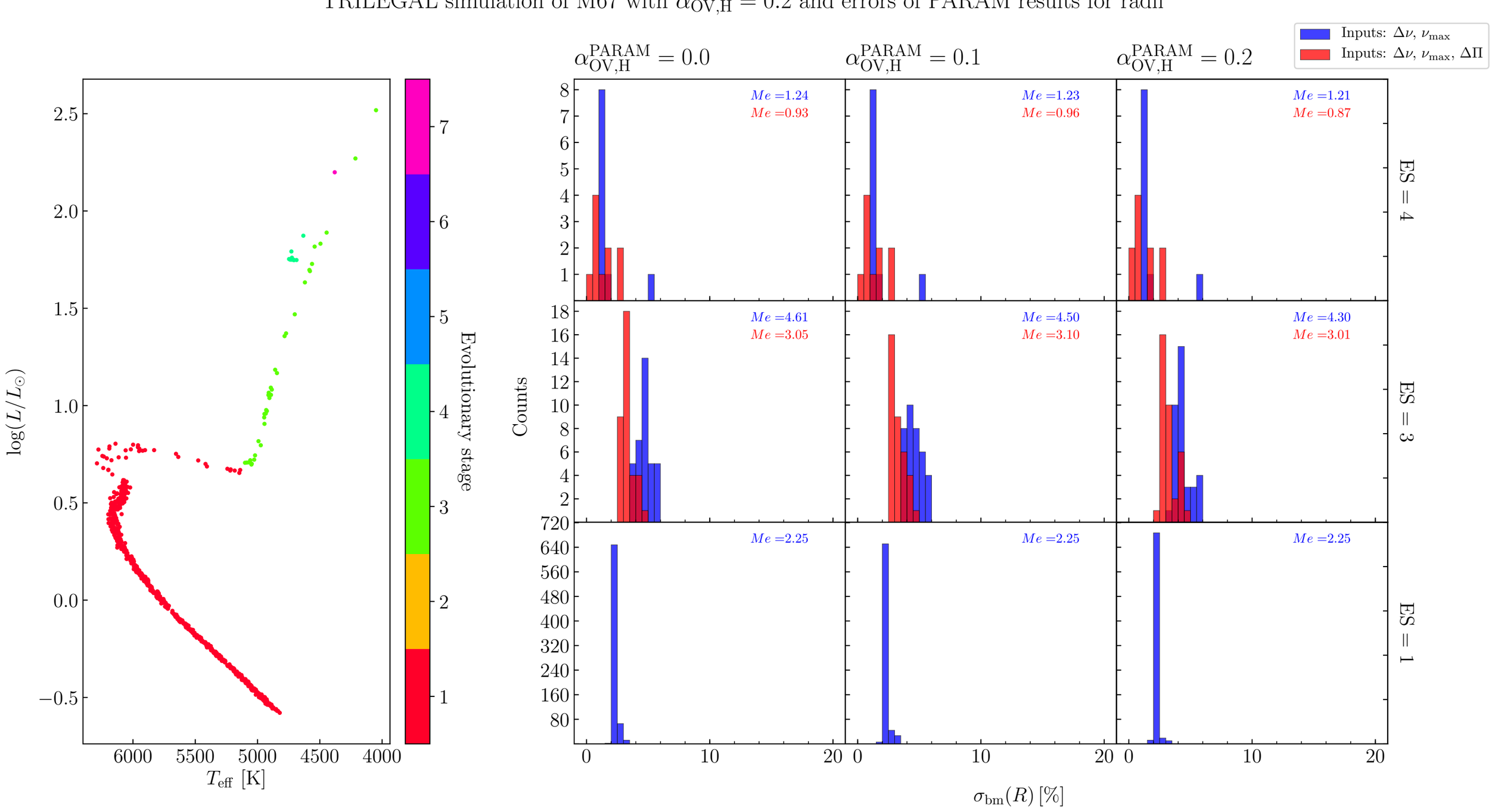
TRILEGAL simulation of M67 with $\alpha_{\rm OV,H} = 0.2$ and errors of PARAM results for radii
$\log(L/L_\odot)$
$T_{\rm eff}$ [K]
Evolutionary stage
$\alpha_{\rm OV,H}^{\rm PARAM} = 0.0$
$\alpha_{\rm OV,H}^{\rm PARAM} = 0.1$
$\alpha_{\rm OV,H}^{\rm PARAM} = 0.2$
Inputs: $\Delta\nu$, $\nu_{\rm max}$
Inputs: $\Delta\nu$, $\nu_{\rm max}$, $\Delta\Pi$
ES = 4
ES = 3
ES = 1
Counts
$\sigma_{\rm bm}(R)$ [%]
Me =1.24
Me =0.93
Me =1.23
Me =0.96
Me =1.21
Me =0.87
Me =4.61
Me =3.05
Me =4.50
Me =3.10
Me =4.30
Me =3.01
Me =2.25
Me =2.25
Me =2.25

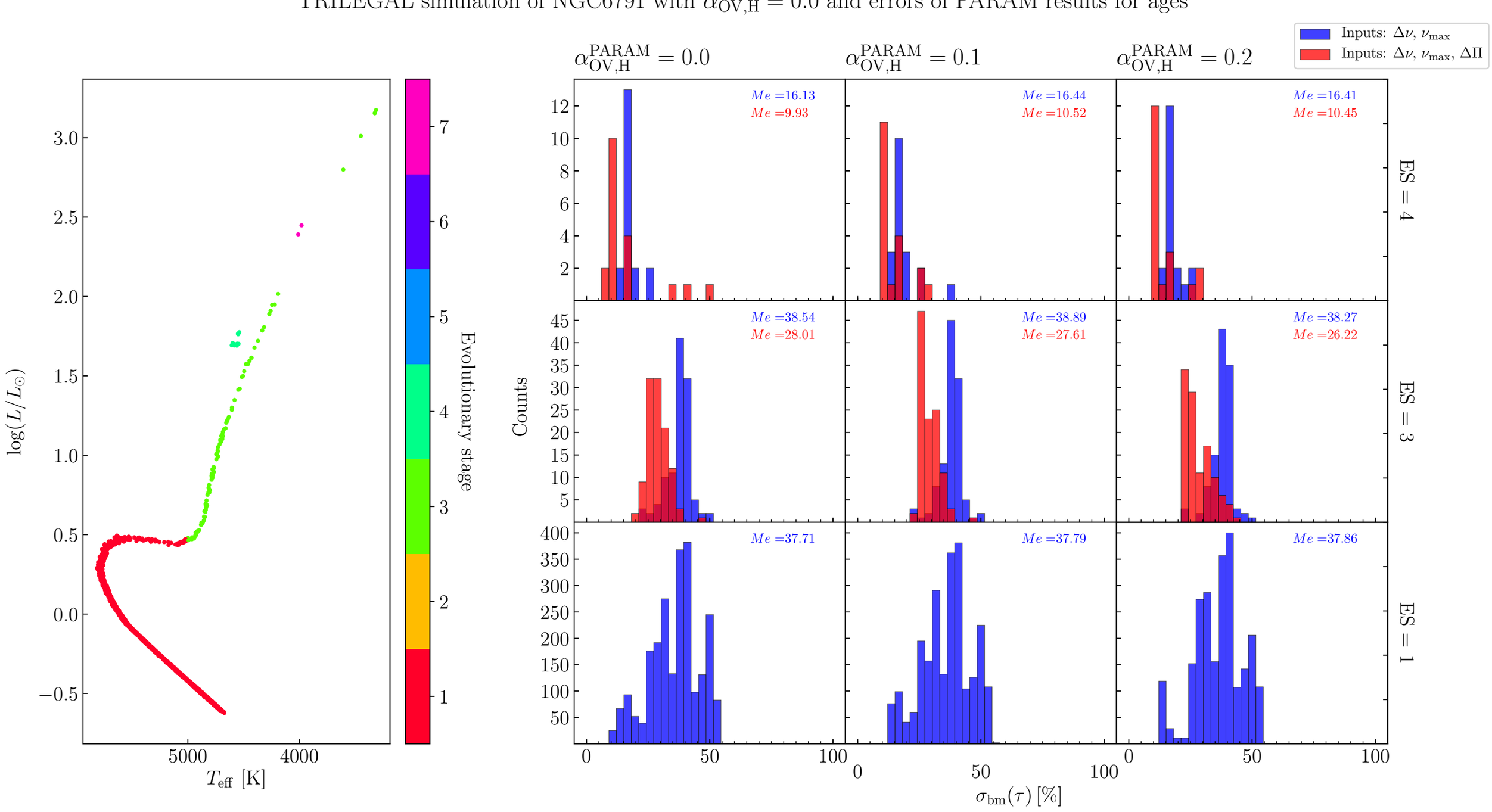
TRILEGAL simulation of NGC6791 with $\alpha_{\rm OV,H} = 0.0$ and errors of PARAM results for ages
Inputs: $\Delta\nu$, $\nu_{\rm max}$
Inputs: $\Delta\nu$, $\nu_{\rm max}$, $\Delta\Pi$
$\alpha_{\rm OV,H}^{\rm PARAM} = 0.0$
$\alpha_{\rm OV,H}^{\rm PARAM} = 0.1$
$\alpha_{\rm OV,H}^{\rm PARAM} = 0.2$
Me =16.13
Me =9.93
Me =16.44
Me =10.52
Me =16.41
Me =10.45
Me =38.54
Me =28.01
Me =38.89
Me =27.61
Me =38.27
Me =26.22
Me =37.71
Me =37.79
Me =37.86
ES = 4
ES = 3
ES = 1
Counts
$\sigma_{\rm bm}(\tau)$ [%]
$\log(L/L_\odot)$
$T_{\rm eff}$ [K]
Evolutionary stage

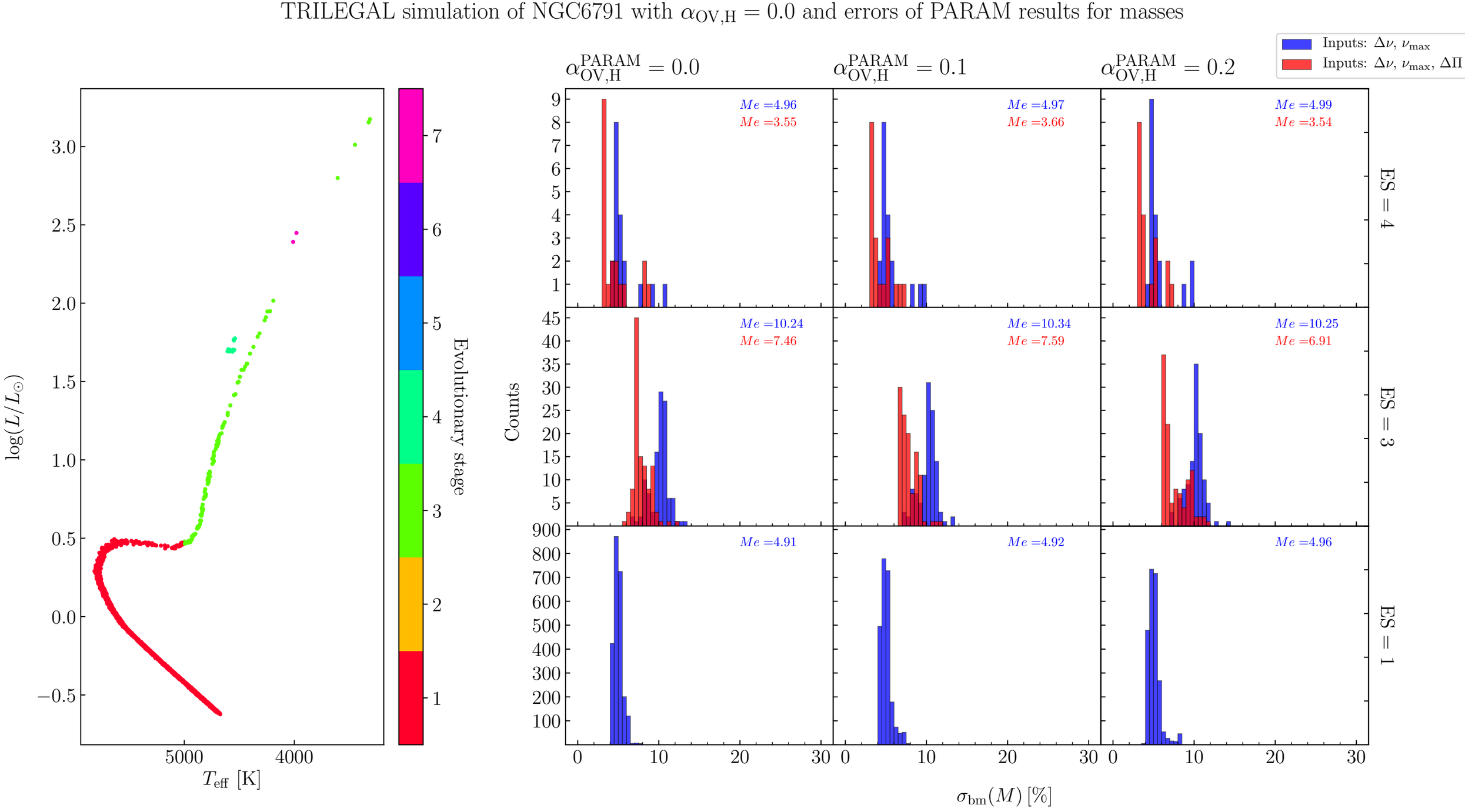
TRILEGAL simulation of NGC6791 with $\alpha_{\rm OV,H} = 0.0$ and errors of PARAM results for masses
Inputs: $\Delta\nu$, $\nu_{\rm max}$
Inputs: $\Delta\nu$, $\nu_{\rm max}$, $\Delta\Pi$
$\alpha_{\rm OV,H}^{\rm PARAM} = 0.0$
$\alpha_{\rm OV,H}^{\rm PARAM} = 0.1$
$\alpha_{\rm OV,H}^{\rm PARAM} = 0.2$
ES = 4
ES = 3
ES = 1
Me =4.96
Me =3.55
Me =4.97
Me =3.66
Me =4.99
Me =3.54
Me =10.24
Me =7.46
Me =10.34
Me =7.59
Me =10.25
Me =6.91
Me =4.91
Me =4.92
Me =4.96
Counts
$\sigma_{\rm bm}(M)$ [%]
$\log(L/L_\odot)$
$T_{\rm eff}$ [K]
Evolutionary stage

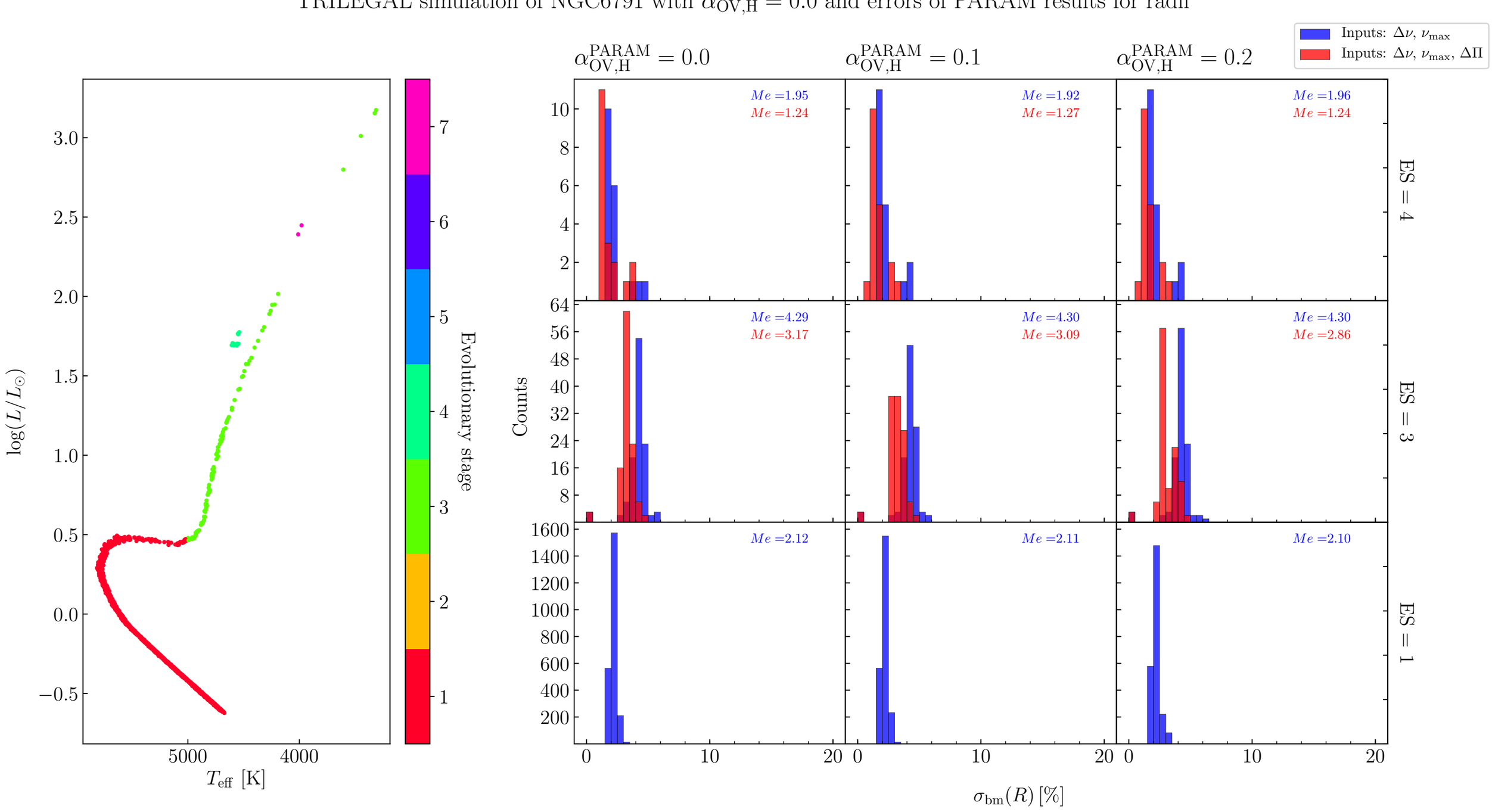
TRILEGAL simulation of NGC6791 with $\alpha_{\rm OV,H} = 0.0$ and errors of PARAM results for radii
Inputs: $\Delta\nu$, $\nu_{\rm max}$
Inputs: $\Delta\nu$, $\nu_{\rm max}$, $\Delta\Pi$
$\alpha_{\rm OV,H}^{\rm PARAM} = 0.0$
$\alpha_{\rm OV,H}^{\rm PARAM} = 0.1$
$\alpha_{\rm OV,H}^{\rm PARAM} = 0.2$
Me =1.95
Me =1.24
Me =1.92
Me =1.27
Me =1.96
Me =1.24
Me =4.29
Me =3.17
Me =4.30
Me =3.09
Me =4.30
Me =2.86
Me =2.12
Me =2.11
Me =2.10
ES = 4
ES = 3
ES = 1
Counts
$\sigma_{\rm bm}(R)$ [%]
$\log(L/L_\odot)$
$T_{\rm eff}$ [K]
Evolutionary stage

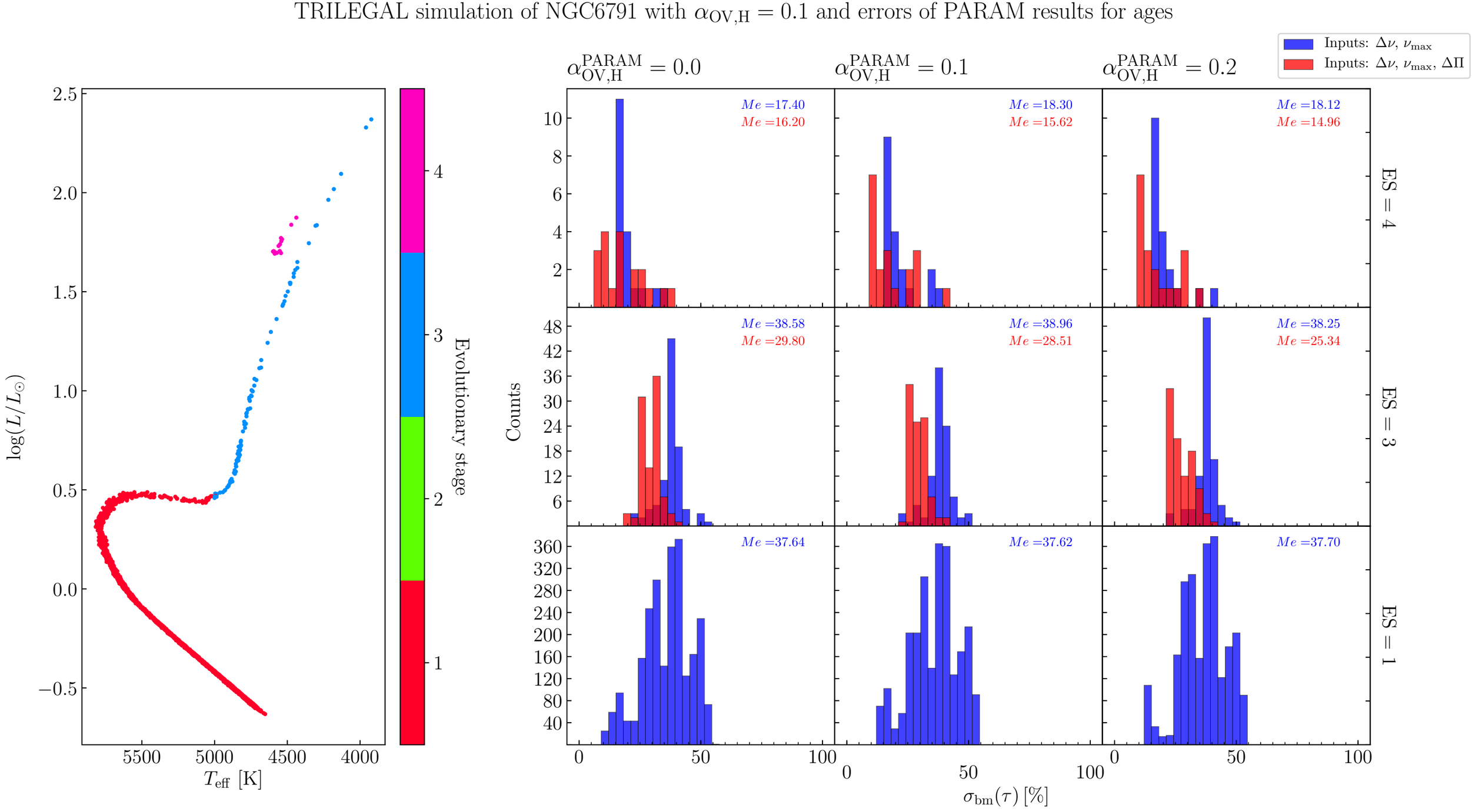
TRILEGAL simulation of NGC6791 with $\alpha_{\rm OV,H} = 0.1$ and errors of PARAM results for ages
Inputs: $\Delta\nu$, $\nu_{\rm max}$
Inputs: $\Delta\nu$, $\nu_{\rm max}$, $\Delta\Pi$
$\alpha_{\rm OV,H}^{\rm PARAM} = 0.0$
$\alpha_{\rm OV,H}^{\rm PARAM} = 0.1$
$\alpha_{\rm OV,H}^{\rm PARAM} = 0.2$
ES = 4
ES = 3
ES = 1
Me =17.40
Me =16.20
Me =18.30
Me =15.62
Me =18.12
Me =14.96
Me =38.58
Me =29.80
Me =38.96
Me =28.51
Me =38.25
Me =25.34
Me =37.64
Me =37.62
Me =37.70
Counts
$\sigma_{\rm bm}(\tau)$ [%]
$\log(L/L_\odot)$
$T_{\rm eff}$ [K]
Evolutionary stage

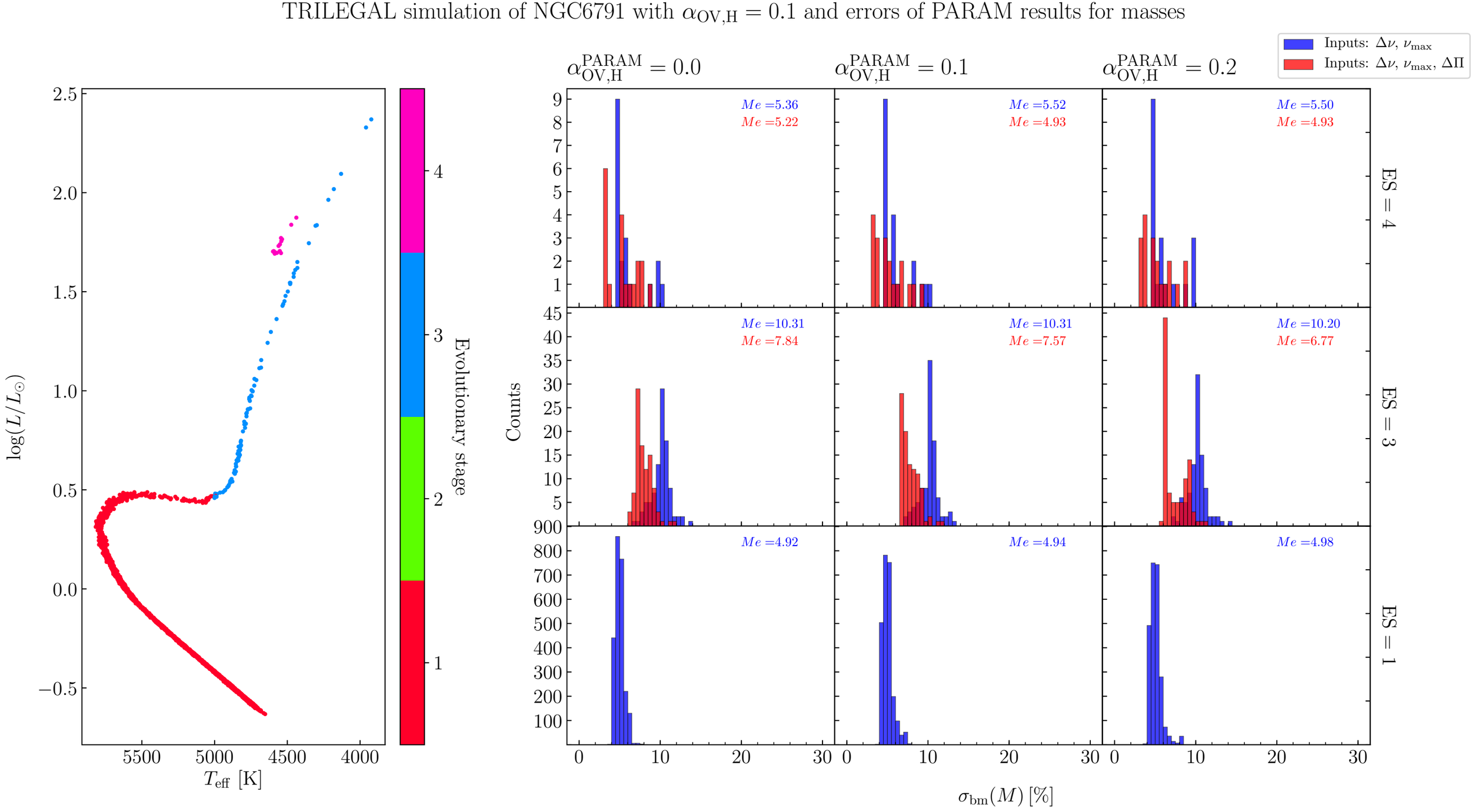
TRILEGAL simulation of NGC6791 with $\alpha_{\rm OV,H} = 0.1$ and errors of PARAM results for masses
Inputs: $\Delta\nu$, $\nu_{\rm max}$
Inputs: $\Delta\nu$, $\nu_{\rm max}$, $\Delta\Pi$
$\alpha_{\rm OV,H}^{\rm PARAM} = 0.0$
$\alpha_{\rm OV,H}^{\rm PARAM} = 0.1$
$\alpha_{\rm OV,H}^{\rm PARAM} = 0.2$
ES = 4
ES = 3
ES = 1
Me =5.36
Me =5.22
Me =5.52
Me =4.93
Me =5.50
Me =4.93
Me =10.31
Me =7.84
Me =10.31
Me =7.57
Me =10.20
Me =6.77
Me =4.92
Me =4.94
Me =4.98
Counts
$\sigma_{\rm bm}(M)$ [%]
$\log(L/L_\odot)$
$T_{\rm eff}$ [K]
Evolutionary stage

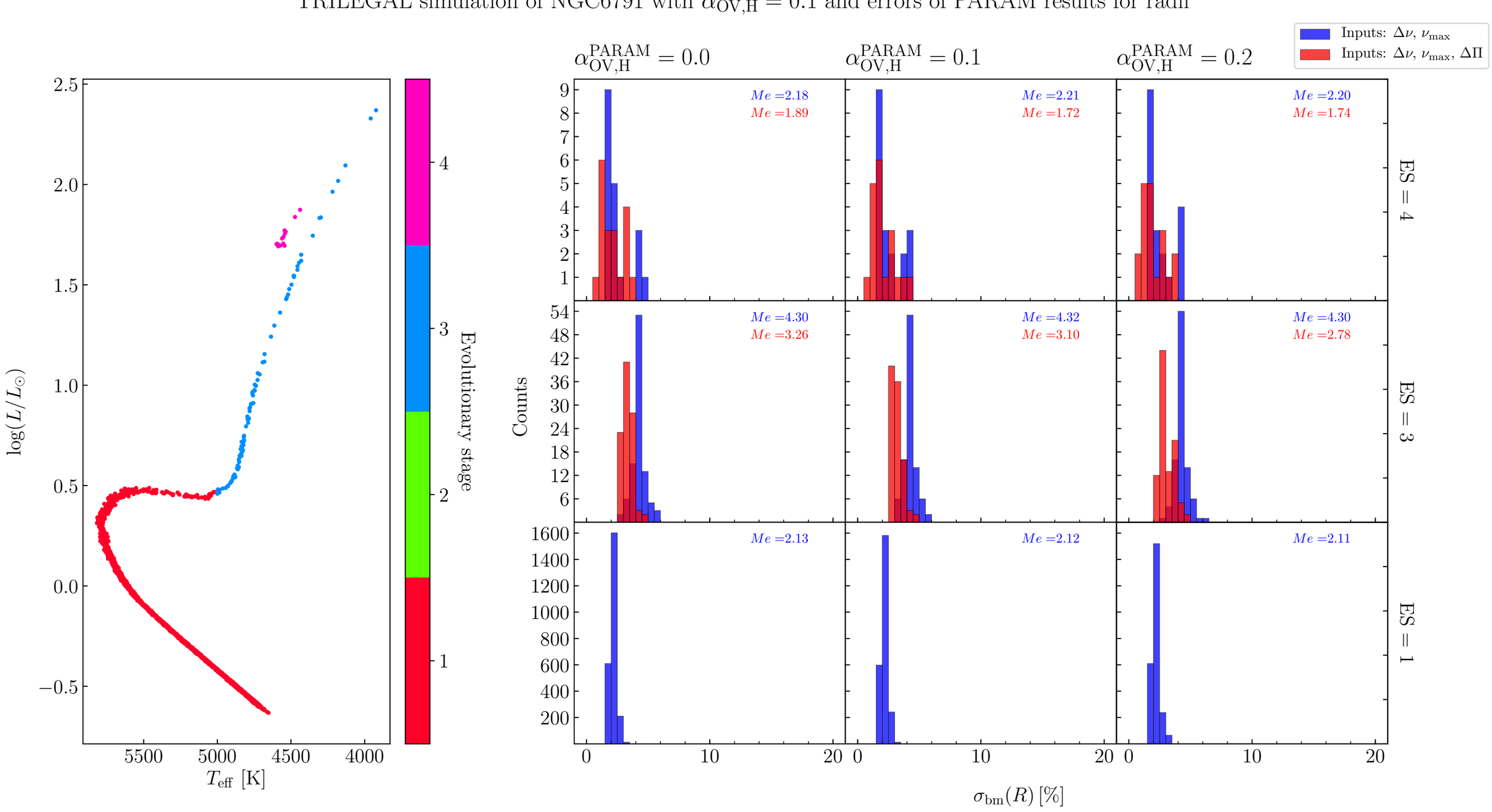
TRILEGAL simulation of NGC6791 with $\alpha_{\rm OV,H} = 0.1$ and errors of PARAM results for radii
$\log(L/L_\odot)$
$T_{\rm eff}$ [K]
Evolutionary stage
$\alpha_{\rm OV,H}^{\rm PARAM} = 0.0$
$\alpha_{\rm OV,H}^{\rm PARAM} = 0.1$
$\alpha_{\rm OV,H}^{\rm PARAM} = 0.2$
Inputs: $\Delta\nu$, $\nu_{\rm max}$
Inputs: $\Delta\nu$, $\nu_{\rm max}$, $\Delta\Pi$
Me =2.18
Me =1.89
Me =2.21
Me =1.72
Me =2.20
Me =1.74
Me =4.30
Me =3.26
Me =4.32
Me =3.10
Me =4.30
Me =2.78
Me =2.13
Me =2.12
Me =2.11
ES = 4
ES = 3
ES = 1
Counts
$\sigma_{\rm bm}(R)$ [%]

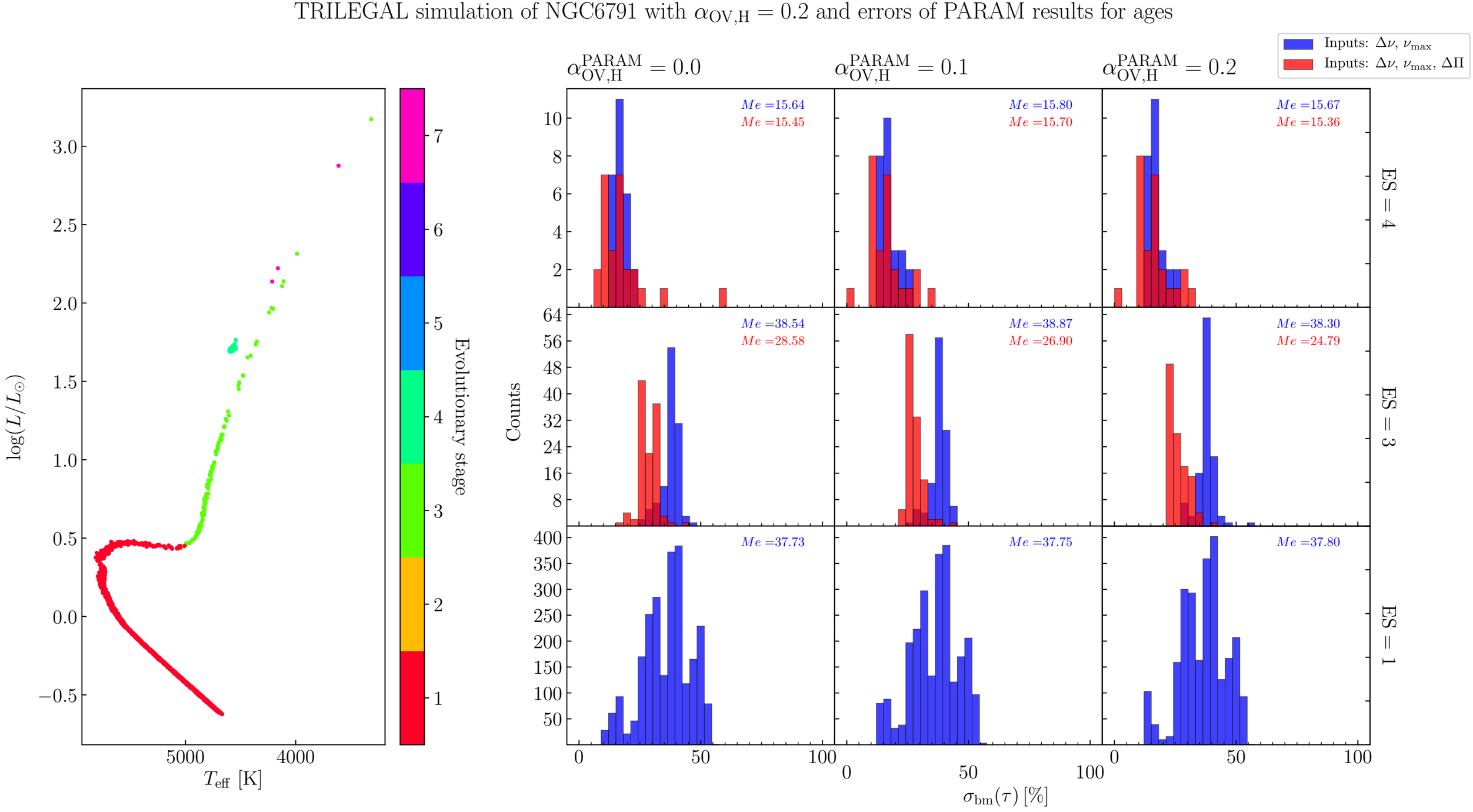
TRILEGAL simulation of NGC6791 with $\alpha_{\rm OV,H} = 0.2$ and errors of PARAM results for ages
Inputs: $\Delta\nu$, $\nu_{\rm max}$
Inputs: $\Delta\nu$, $\nu_{\rm max}$, $\Delta\Pi$
$\alpha_{\rm OV,H}^{\rm PARAM} = 0.0$
$\alpha_{\rm OV,H}^{\rm PARAM} = 0.1$
$\alpha_{\rm OV,H}^{\rm PARAM} = 0.2$
Me =15.64
Me =15.45
Me =15.80
Me =15.70
Me =15.67
Me =15.36
Me =38.54
Me =28.58
Me =38.87
Me =26.90
Me =38.30
Me =24.79
Me =37.73
Me =37.75
Me =37.80
ES = 4
ES = 3
ES = 1
Counts
$\sigma_{\rm bm}(\tau)$ [%]
$\log(L/L_\odot)$
$T_{\rm eff}$ [K]
Evolutionary stage

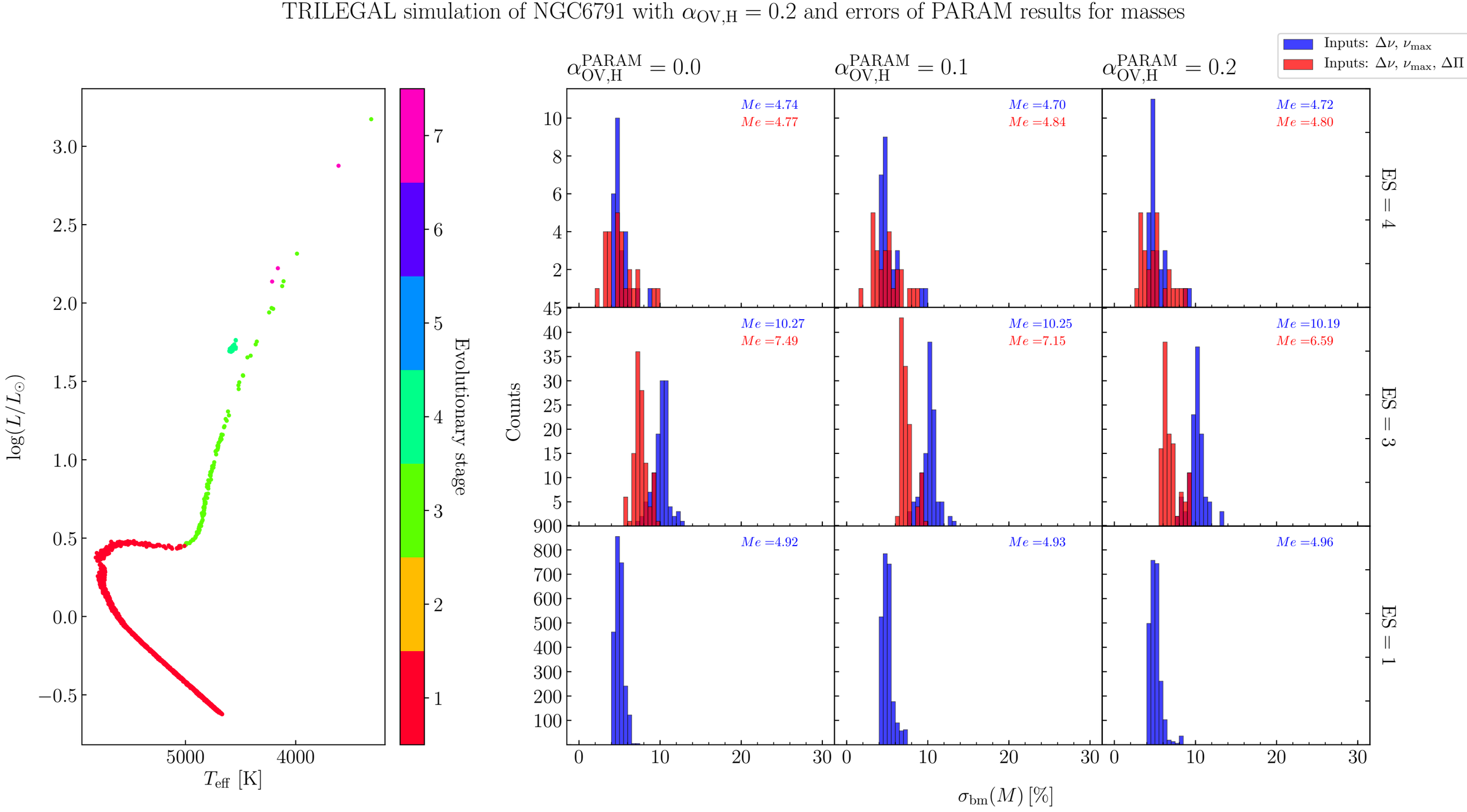
TRILEGAL simulation of NGC6791 with $\alpha_{\rm OV,H} = 0.2$ and errors of PARAM results for masses
Inputs: $\Delta\nu$, $\nu_{\rm max}$
Inputs: $\Delta\nu$, $\nu_{\rm max}$, $\Delta\Pi$
$\alpha_{\rm OV,H}^{\rm PARAM} = 0.0$
$\alpha_{\rm OV,H}^{\rm PARAM} = 0.1$
$\alpha_{\rm OV,H}^{\rm PARAM} = 0.2$
ES = 4
ES = 3
ES = 1
Me =4.74
Me =4.77
Me =4.70
Me =4.84
Me =4.72
Me =4.80
Me =10.27
Me =7.49
Me =10.25
Me =7.15
Me =10.19
Me =6.59
Me =4.92
Me =4.93
Me =4.96
Counts
$\sigma_{\rm bm}(M)$ [%]
$\log(L/L_\odot)$
$T_{\rm eff}$ [K]
Evolutionary stage

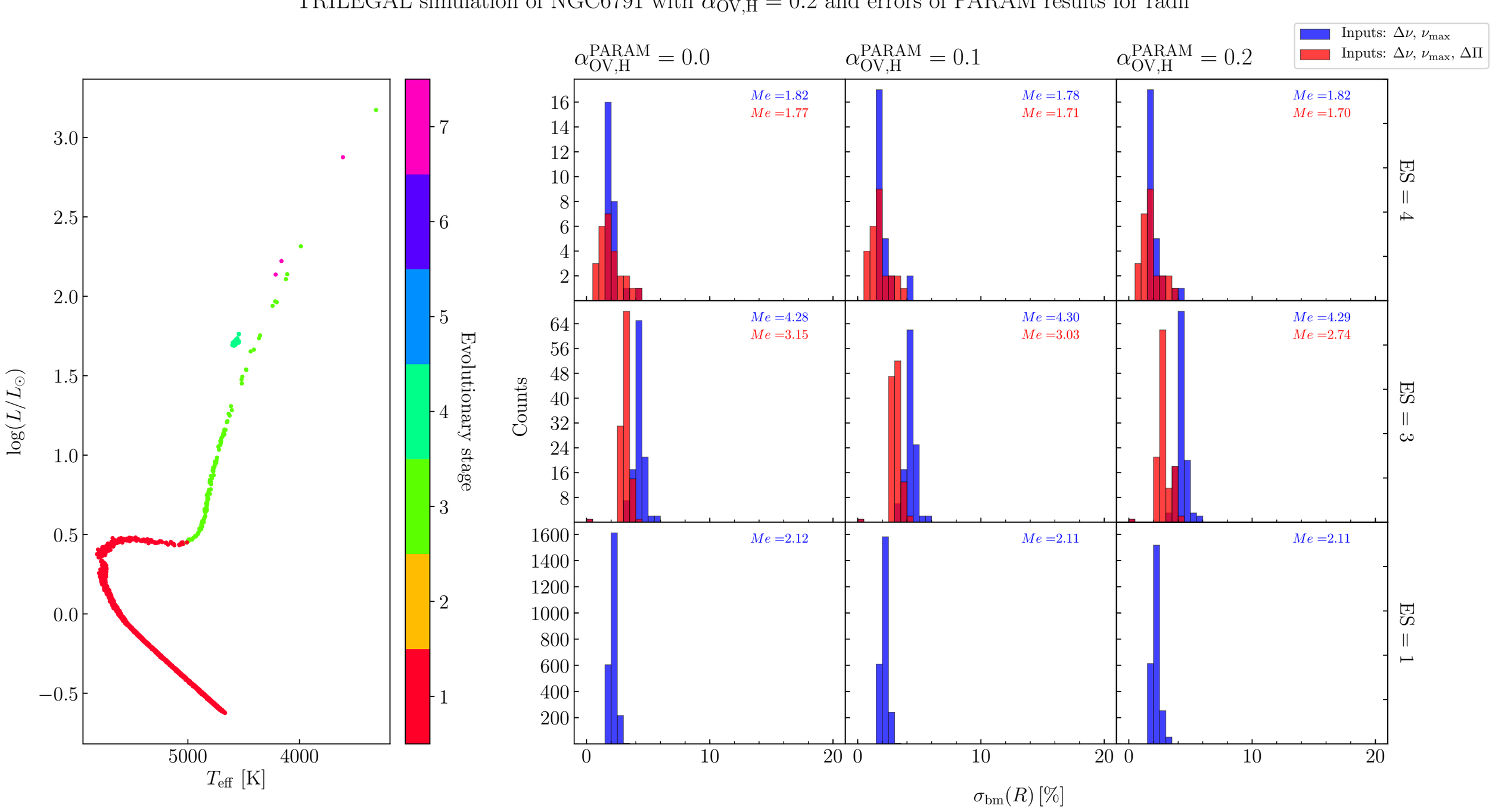
TRILEGAL simulation of NGC6791 with $\alpha_{\rm OV,H} = 0.2$ and errors of PARAM results for radii
Inputs: $\Delta\nu$, $\nu_{\rm max}$
Inputs: $\Delta\nu$, $\nu_{\rm max}$, $\Delta\Pi$
$\alpha_{\rm OV,H}^{\rm PARAM} = 0.0$
$\alpha_{\rm OV,H}^{\rm PARAM} = 0.1$
$\alpha_{\rm OV,H}^{\rm PARAM} = 0.2$
$\log(L/L_\odot)$
$T_{\rm eff}$ [K]
Evolutionary stage
Counts
$\sigma_{\rm bm}(R)$ [%]
ES = 4
ES = 3
ES = 1
Me =1.82
Me =1.77
Me =1.78
Me =1.71
Me =1.82
Me =1.70
Me =4.28
Me =3.15
Me =4.30
Me =3.03
Me =4.29
Me =2.74
Me =2.12
Me =2.11
Me =2.11

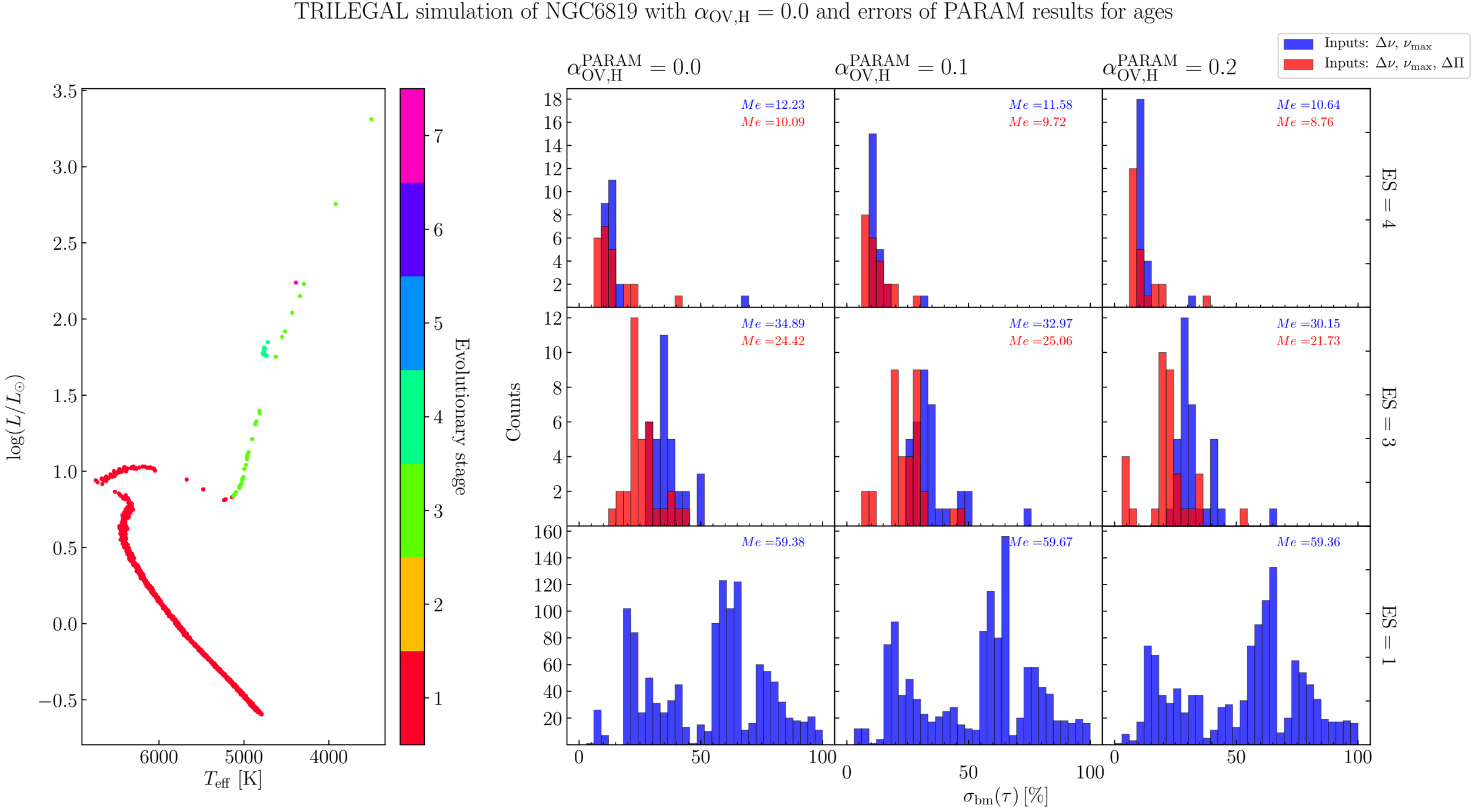
TRILEGAL simulation of NGC6819 with $\alpha_{\rm OV,H} = 0.0$ and errors of PARAM results for ages
Inputs: $\Delta\nu$, $\nu_{\rm max}$
Inputs: $\Delta\nu$, $\nu_{\rm max}$, $\Delta\Pi$
$\alpha_{\rm OV,H}^{\rm PARAM} = 0.0$
$\alpha_{\rm OV,H}^{\rm PARAM} = 0.1$
$\alpha_{\rm OV,H}^{\rm PARAM} = 0.2$
Me =12.23
Me =10.09
Me =11.58
Me =9.72
Me =10.64
Me =8.76
Me =34.89
Me =24.42
Me =32.97
Me =25.06
Me =30.15
Me =21.73
Me =59.38
Me =59.67
Me =59.36
ES = 4
ES = 3
ES = 1
Counts
$\sigma_{\rm bm}(\tau)$ [%]
$\log(L/L_\odot)$
$T_{\rm eff}$ [K]
Evolutionary stage

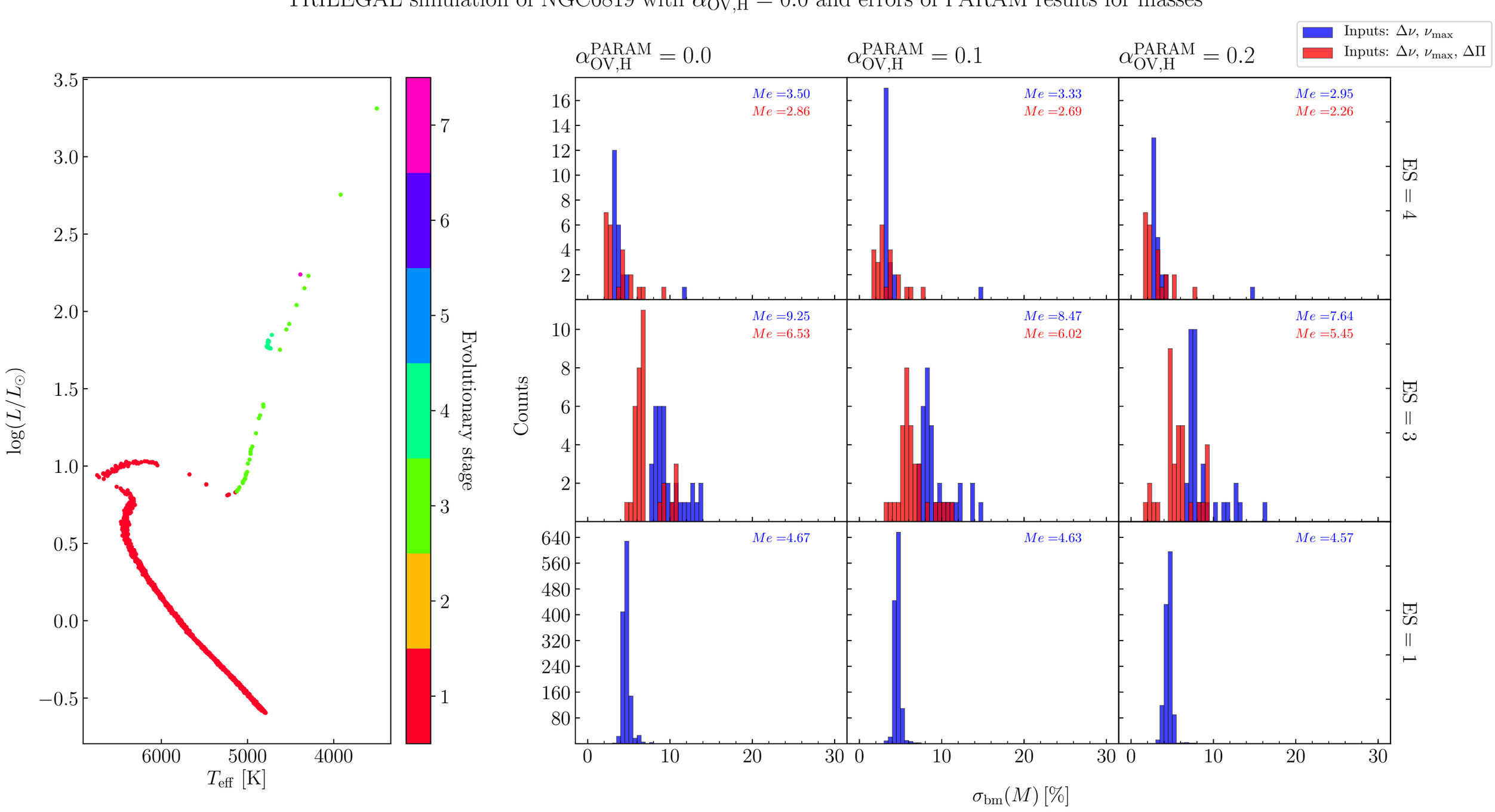
TRILEGAL simulation of NGC6819 with $\alpha_{\rm OV,H} = 0.0$ and errors of PARAM results for masses
Inputs: $\Delta\nu$, $\nu_{\rm max}$
Inputs: $\Delta\nu$, $\nu_{\rm max}$, $\Delta\Pi$
$\alpha_{\rm OV,H}^{\rm PARAM} = 0.0$
$\alpha_{\rm OV,H}^{\rm PARAM} = 0.1$
$\alpha_{\rm OV,H}^{\rm PARAM} = 0.2$
Me =3.50
Me =2.86
Me =3.33
Me =2.69
Me =2.95
Me =2.26
Me =9.25
Me =6.53
Me =8.47
Me =6.02
Me =7.64
Me =5.45
Me =4.67
Me =4.63
Me =4.57
ES = 4
ES = 3
ES = 1
Counts
$\sigma_{\rm bm}(M)$ [%]
$\log(L/L_\odot)$
$T_{\rm eff}$ [K]
Evolutionary stage

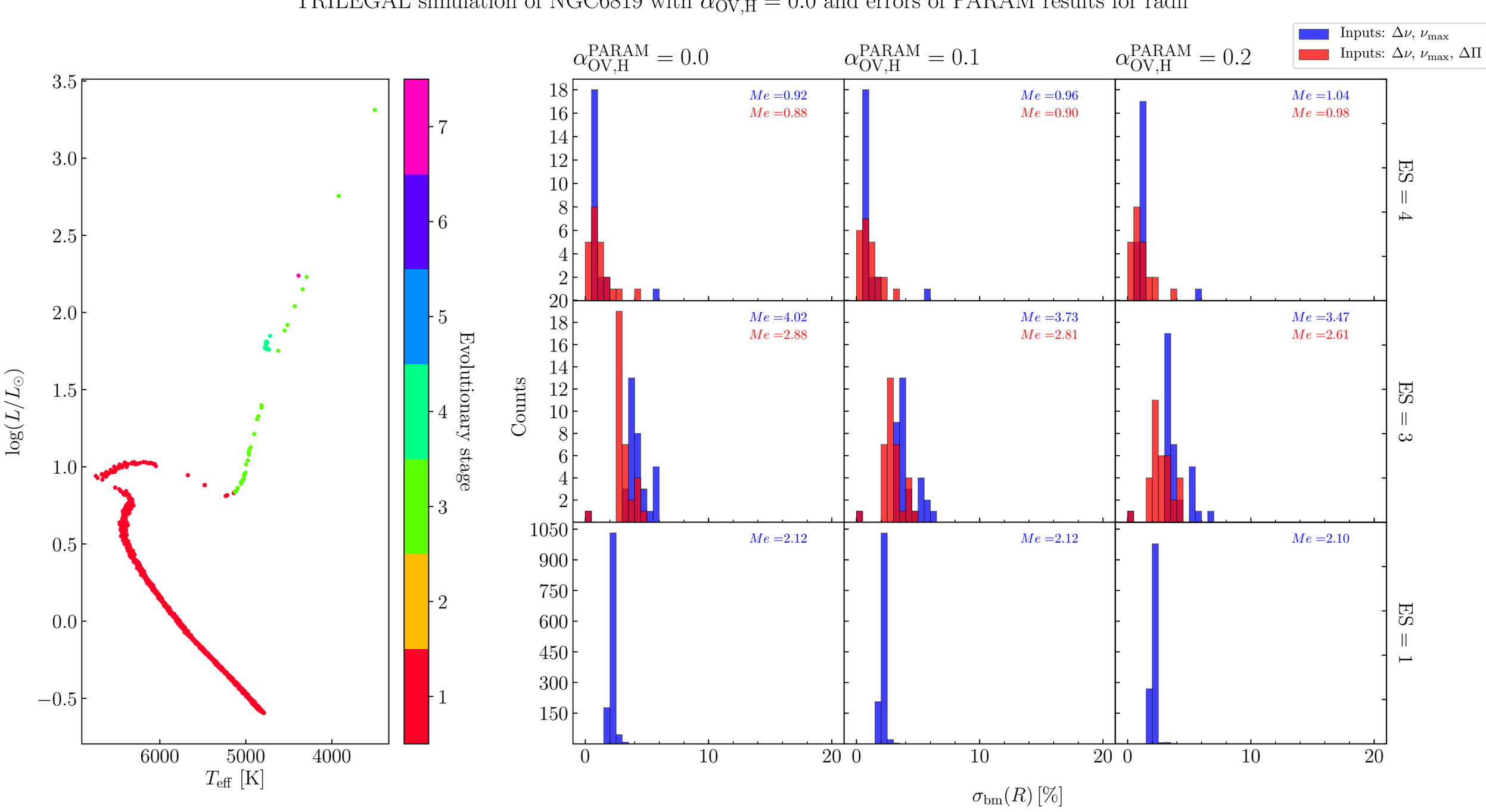
TRILEGAL simulation of NGC6819 with $\alpha_{\rm OV,H} = 0.0$ and errors of PARAM results for radii
Inputs: $\Delta\nu$, $\nu_{\rm max}$
Inputs: $\Delta\nu$, $\nu_{\rm max}$, $\Delta\Pi$
$\alpha_{\rm OV,H}^{\rm PARAM} = 0.0$
$\alpha_{\rm OV,H}^{\rm PARAM} = 0.1$
$\alpha_{\rm OV,H}^{\rm PARAM} = 0.2$
$\log(L/L_\odot)$
$T_{\rm eff}$ [K]
Evolutionary stage
Counts
$\sigma_{\rm bm}(R)$ [%]
ES = 4
ES = 3
ES = 1
Me =0.92
Me =0.88
Me =0.96
Me =0.90
Me =1.04
Me =0.98
Me =4.02
Me =2.88
Me =3.73
Me =2.81
Me =3.47
Me =2.61
Me =2.12
Me =2.12
Me =2.10

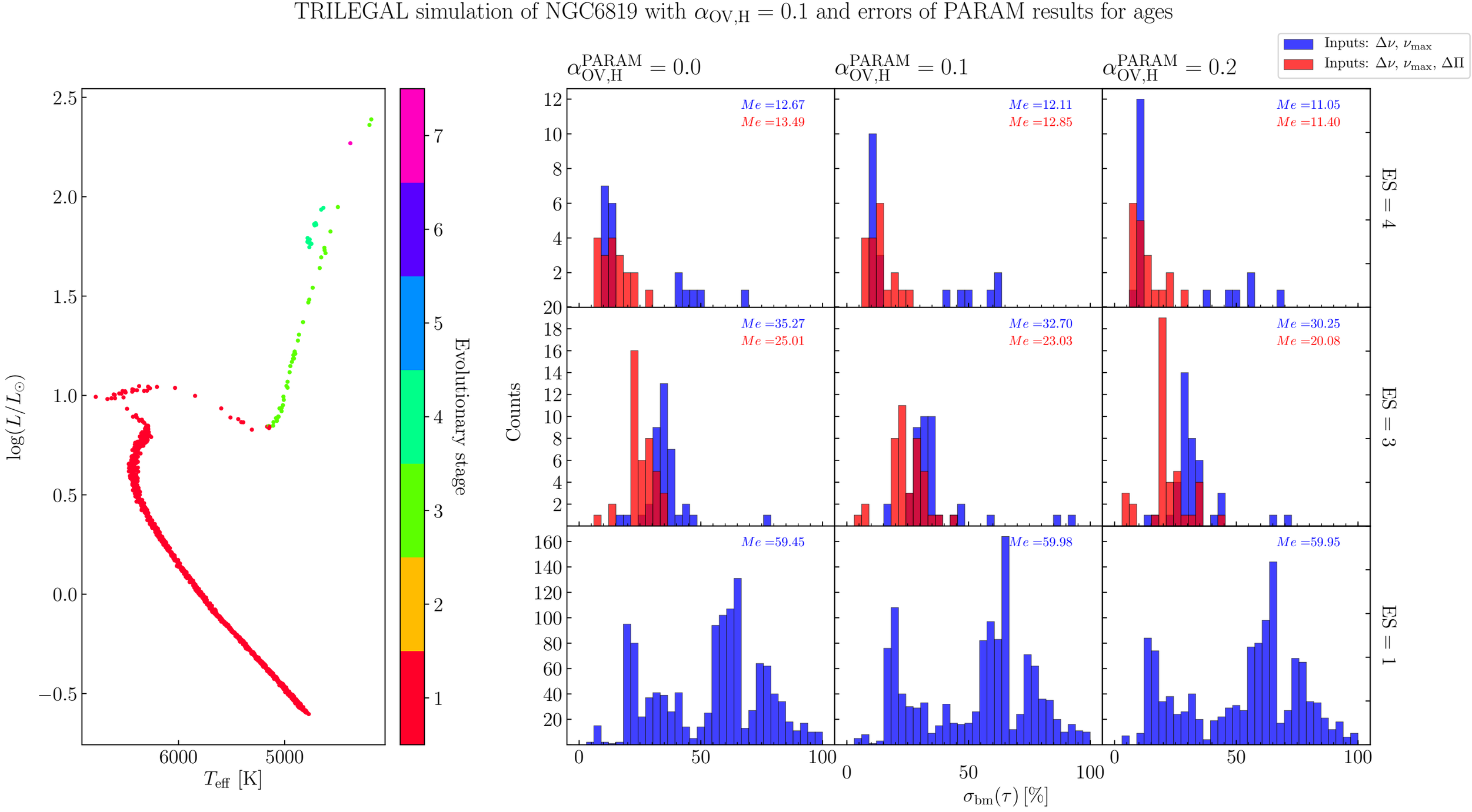
TRILEGAL simulation of NGC6819 with $\alpha_{\rm OV,H} = 0.1$ and errors of PARAM results for ages
Inputs: $\Delta\nu$, $\nu_{\rm max}$
Inputs: $\Delta\nu$, $\nu_{\rm max}$, $\Delta\Pi$
$\alpha_{\rm OV,H}^{\rm PARAM} = 0.0$
$\alpha_{\rm OV,H}^{\rm PARAM} = 0.1$
$\alpha_{\rm OV,H}^{\rm PARAM} = 0.2$
Me =12.67
Me =13.49
Me =12.11
Me =12.85
Me =11.05
Me =11.40
Me =35.27
Me =25.01
Me =32.70
Me =23.03
Me =30.25
Me =20.08
Me =59.45
Me =59.98
Me =59.95
ES = 4
ES = 3
ES = 1
Counts
$\sigma_{\rm bm}(\tau)$ [%]
$\log(L/L_\odot)$
$T_{\rm eff}$ [K]
Evolutionary stage

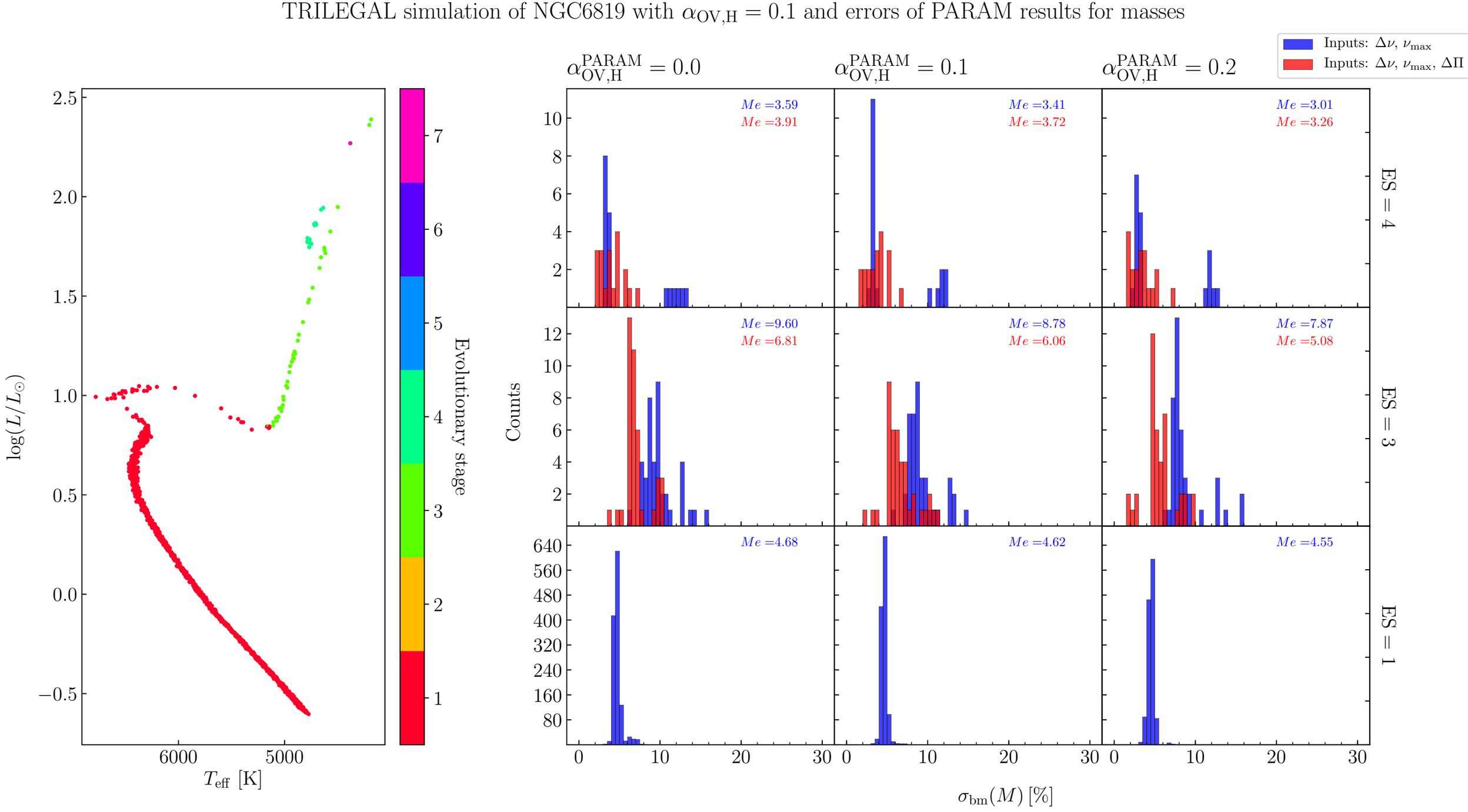
TRILEGAL simulation of NGC6819 with $\alpha_{\rm OV,H} = 0.1$ and errors of PARAM results for masses
$\alpha_{\rm OV,H}^{\rm PARAM} = 0.0$
$\alpha_{\rm OV,H}^{\rm PARAM} = 0.1$
$\alpha_{\rm OV,H}^{\rm PARAM} = 0.2$
Inputs: $\Delta\nu$, $\nu_{\rm max}$
Inputs: $\Delta\nu$, $\nu_{\rm max}$, $\Delta\Pi$
$\log(L/L_\odot)$
$T_{\rm eff}$ [K]
Evolutionary stage
Counts
$\sigma_{\rm bm}(M)$ [%]
ES = 4
ES = 3
ES = 1
Me =3.59
Me =3.91
Me =3.41
Me =3.72
Me =3.01
Me =3.26
Me =9.60
Me =6.81
Me =8.78
Me =6.06
Me =7.87
Me =5.08
Me =4.68
Me =4.62
Me =4.55

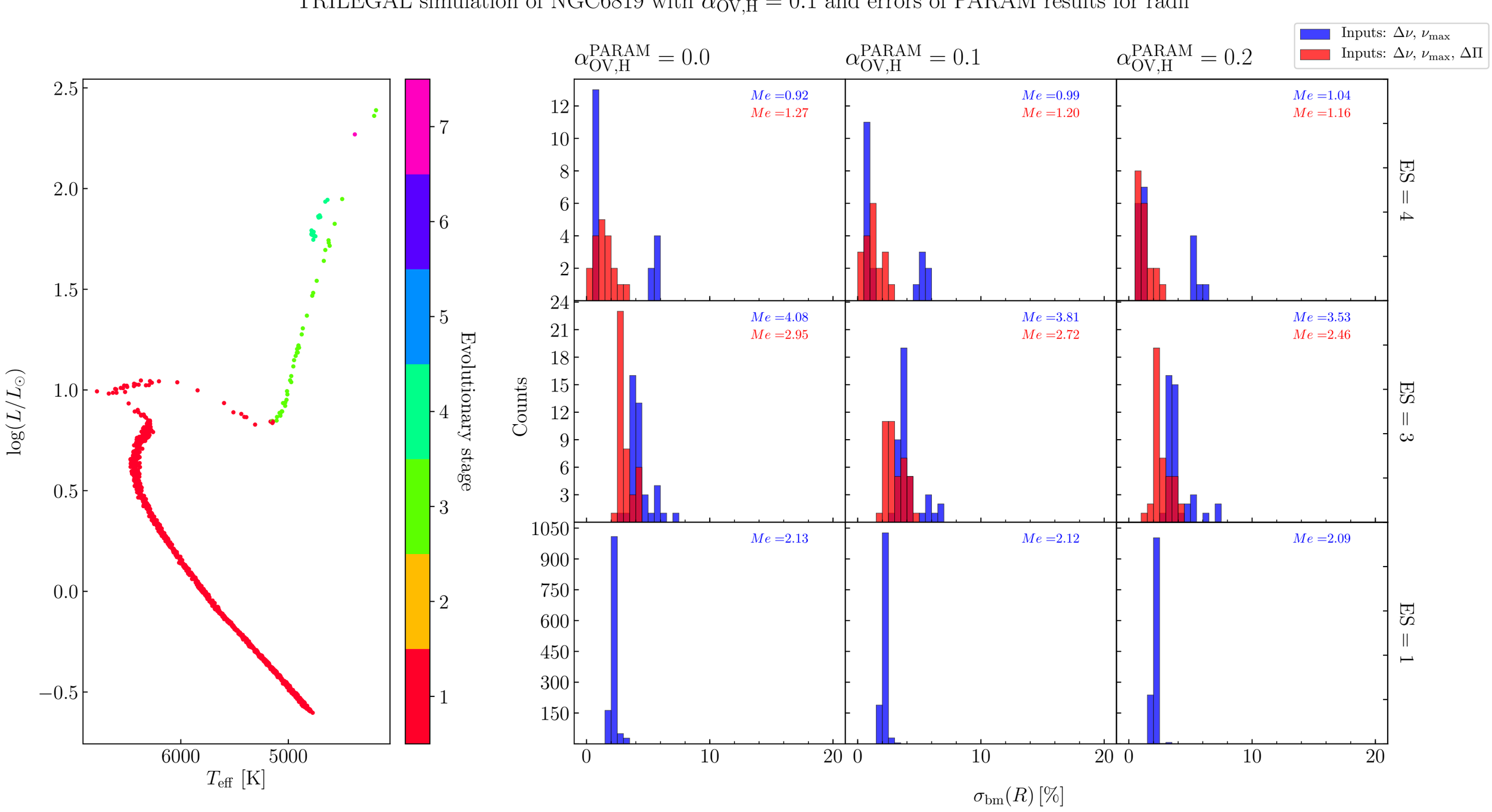
TRILEGAL simulation of NGC6819 with $\alpha_{\rm OV,H} = 0.1$ and errors of PARAM results for radii
Inputs: $\Delta\nu$, $\nu_{\rm max}$
Inputs: $\Delta\nu$, $\nu_{\rm max}$, $\Delta\Pi$
$\alpha_{\rm OV,H}^{\rm PARAM} = 0.0$
$\alpha_{\rm OV,H}^{\rm PARAM} = 0.1$
$\alpha_{\rm OV,H}^{\rm PARAM} = 0.2$
Me =0.92
Me =1.27
Me =0.99
Me =1.20
Me =1.04
Me =1.16
Me =4.08
Me =2.95
Me =3.81
Me =2.72
Me =3.53
Me =2.46
Me =2.13
Me =2.12
Me =2.09
ES = 4
ES = 3
ES = 1
Counts
$\sigma_{\rm bm}(R)$ [%]
$\log(L/L_\odot)$
$T_{\rm eff}$ [K]
Evolutionary stage

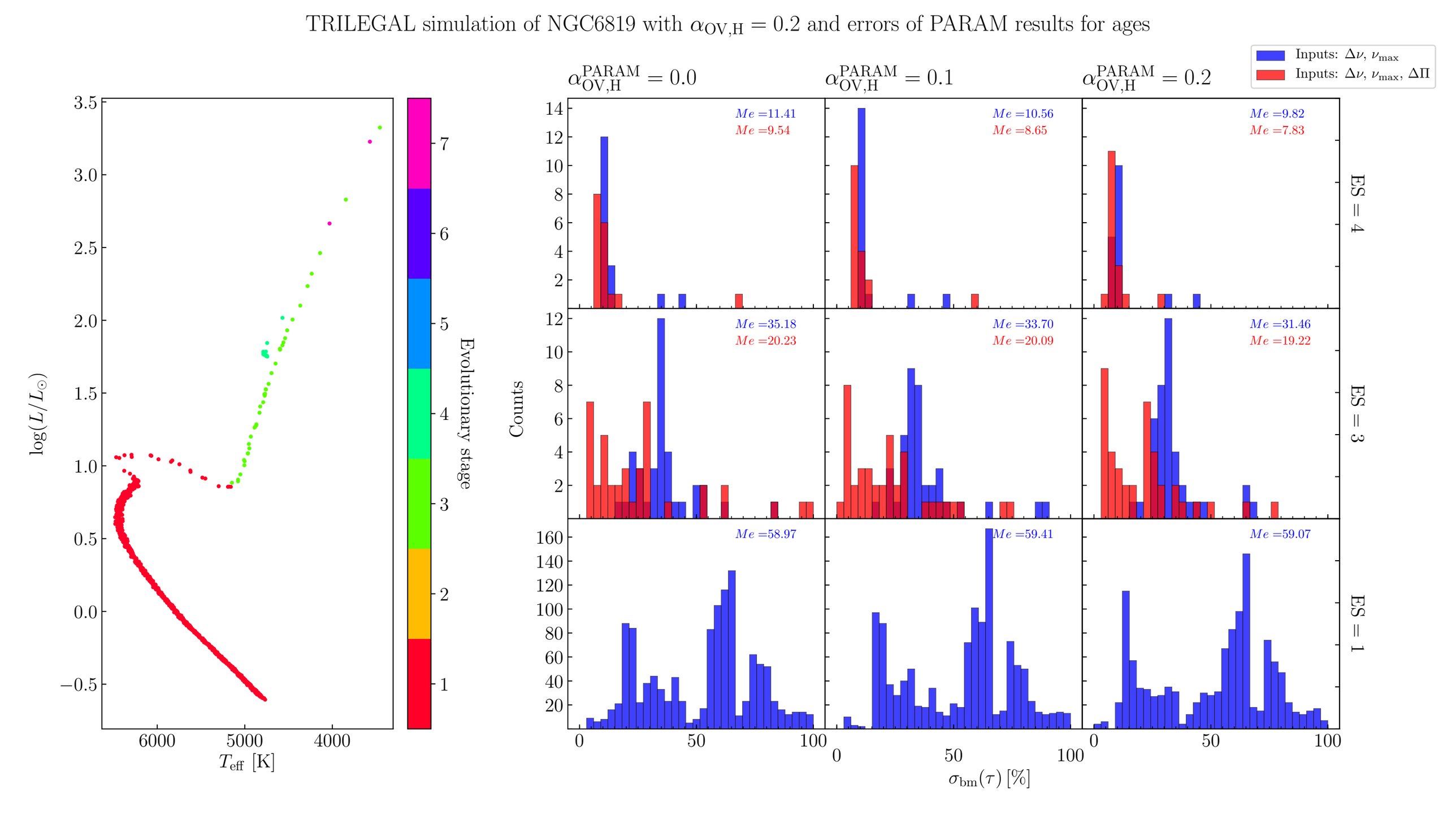
TRILEGAL simulation of NGC6819 with $\alpha_{\rm OV,H} = 0.2$ and errors of PARAM results for ages
Inputs: $\Delta\nu$, $\nu_{\rm max}$
Inputs: $\Delta\nu$, $\nu_{\rm max}$, $\Delta\Pi$
$\alpha_{\rm OV,H}^{\rm PARAM} = 0.0$
$\alpha_{\rm OV,H}^{\rm PARAM} = 0.1$
$\alpha_{\rm OV,H}^{\rm PARAM} = 0.2$
$\log(L/L_\odot)$
$T_{\rm eff}$ [K]
Evolutionary stage
Counts
$\sigma_{\rm bm}(\tau)$ [%]
ES = 4
ES = 3
ES = 1
Me =11.41
Me =9.54
Me =10.56
Me =8.65
Me =9.82
Me =7.83
Me =35.18
Me =20.23
Me =33.70
Me =20.09
Me =31.46
Me =19.22
Me =58.97
Me =59.41
Me =59.07

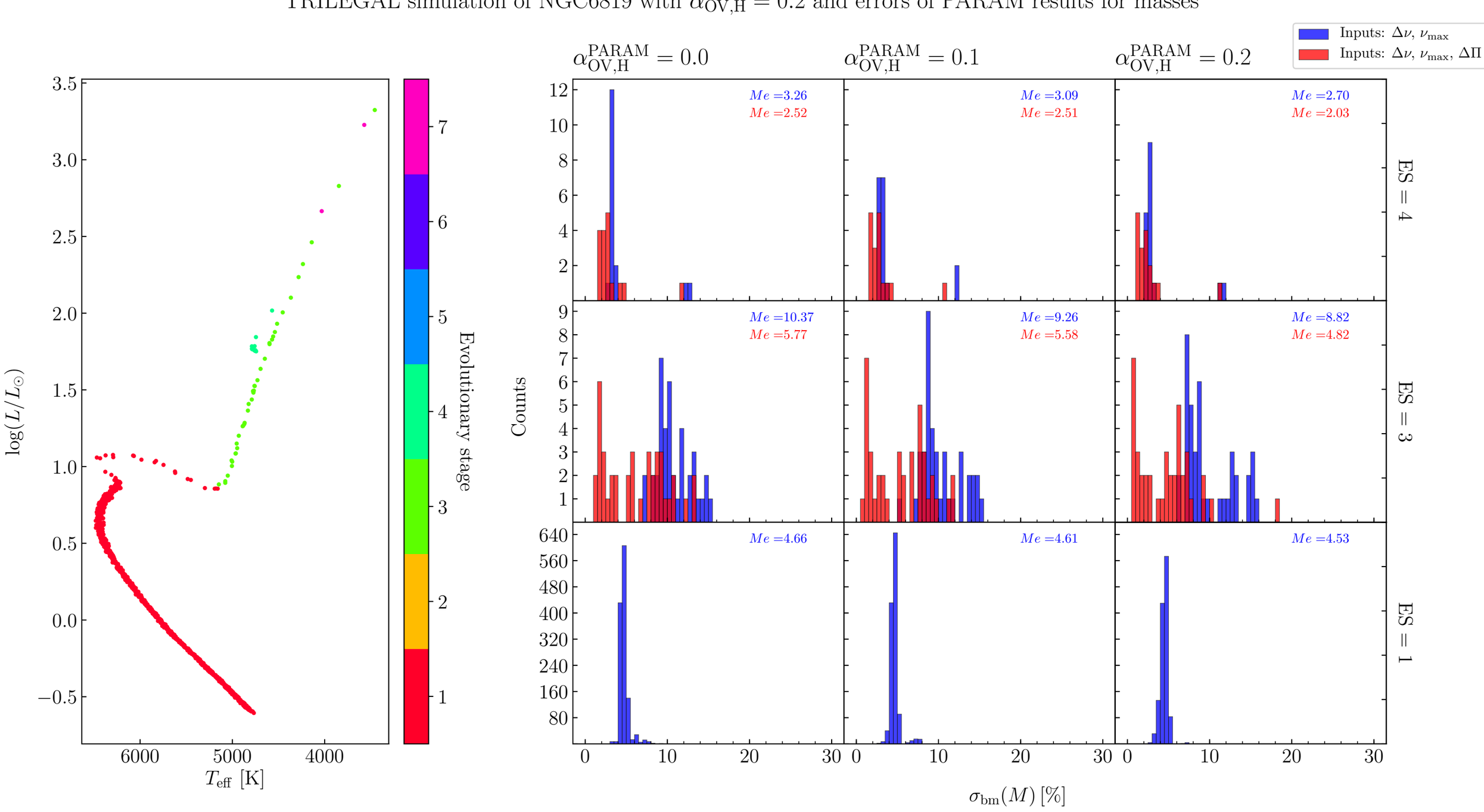
TRILEGAL simulation of NGC6819 with $\alpha_{\rm OV,H} = 0.2$ and errors of PARAM results for masses
Inputs: $\Delta\nu$, $\nu_{\rm max}$
Inputs: $\Delta\nu$, $\nu_{\rm max}$, $\Delta\Pi$
$\alpha_{\rm OV,H}^{\rm PARAM} = 0.0$
$\alpha_{\rm OV,H}^{\rm PARAM} = 0.1$
$\alpha_{\rm OV,H}^{\rm PARAM} = 0.2$
$\log(L/L_\odot)$
$T_{\rm eff}$ [K]
Evolutionary stage
Counts
$\sigma_{\rm bm}(M)$ [%]
ES = 4
ES = 3
ES = 1
Me =3.26
Me =2.52
Me =3.09
Me =2.51
Me =2.70
Me =2.03
Me =10.37
Me =5.77
Me =9.26
Me =5.58
Me =8.82
Me =4.82
Me =4.66
Me =4.61
Me =4.53

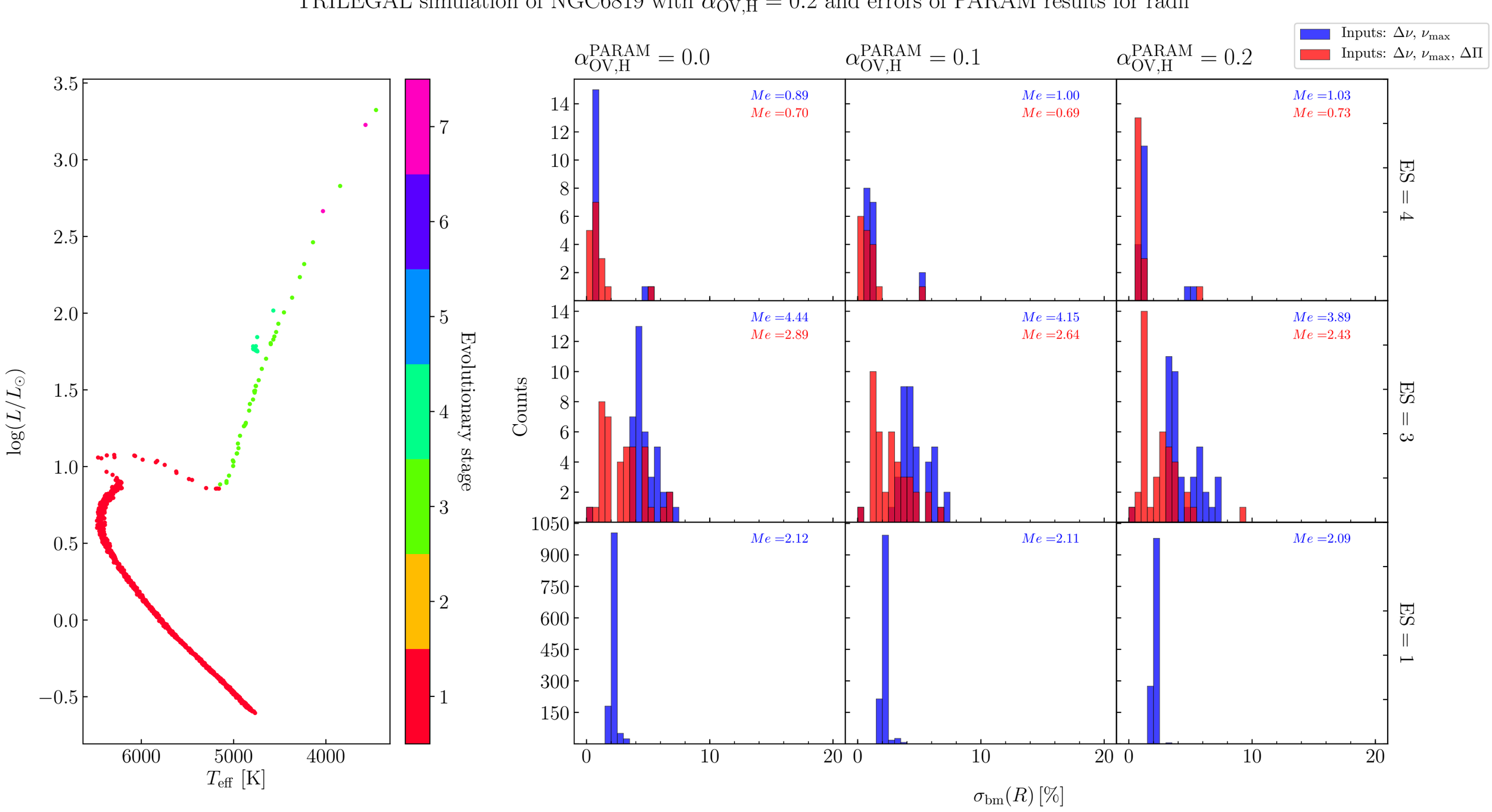
TRILEGAL simulation of NGC6819 with $\alpha_{\rm OV,H} = 0.2$ and errors of PARAM results for radii
$\log(L/L_\odot)$
$T_{\rm eff}$ [K]
Evolutionary stage
$\alpha_{\rm OV,H}^{\rm PARAM} = 0.0$
$\alpha_{\rm OV,H}^{\rm PARAM} = 0.1$
$\alpha_{\rm OV,H}^{\rm PARAM} = 0.2$
Inputs: $\Delta\nu$, $\nu_{\rm max}$
Inputs: $\Delta\nu$, $\nu_{\rm max}$, $\Delta\Pi$
ES = 4
ES = 3
ES = 1
Counts
$\sigma_{\rm bm}(R)$ [%]
Me =0.89
Me =0.70
Me =1.00
Me =0.69
Me =1.03
Me =0.73
Me =4.44
Me =2.89
Me =4.15
Me =2.64
Me =3.89
Me =2.43
Me =2.12
Me =2.11
Me =2.09

B | SYSTEMATIC ERRORS

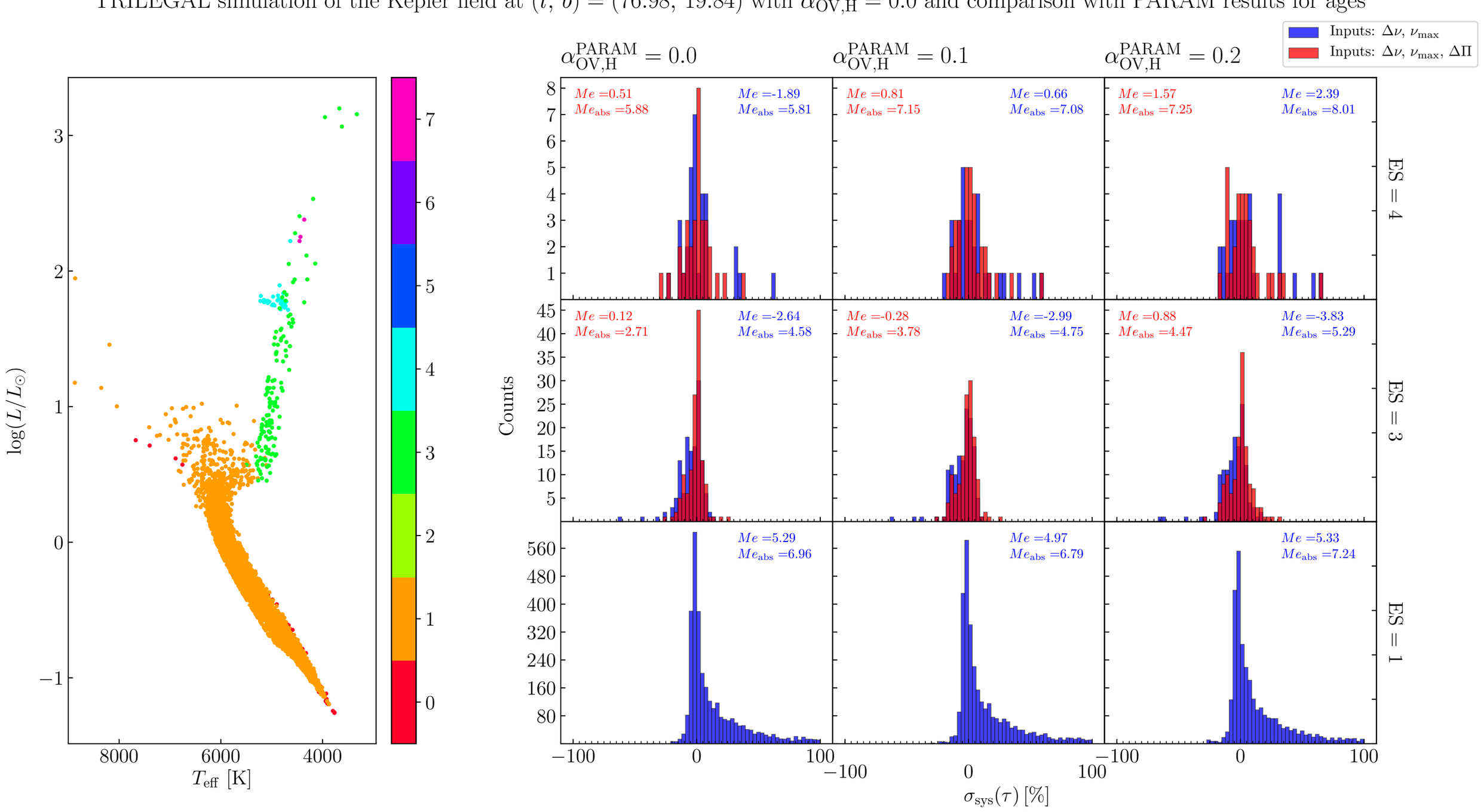
TRILEGAL simulation of the Kepler field at (l, b) = (76.98, 19.84) with $\alpha_{\rm OV,H} = 0.0$ and comparison with PARAM results for ages
Inputs: Δν, $\nu_{\rm max}$
Inputs: Δν, $\nu_{\rm max}$, ΔΠ
$\alpha_{\rm OV,H}^{\rm PARAM} = 0.0$
$\alpha_{\rm OV,H}^{\rm PARAM} = 0.1$
$\alpha_{\rm OV,H}^{\rm PARAM} = 0.2$
ES = 4
ES = 3
ES = 1
Counts
$\sigma_{\rm sys}(\tau)$ [%]
$\log(L/L_\odot)$
$T_{\rm eff}$ [K]
Me =0.51
Me$_{\rm abs}$ =5.88
Me =-1.89
Me$_{\rm abs}$ =5.81
Me =0.81
Me$_{\rm abs}$ =7.15
Me =0.66
Me$_{\rm abs}$ =7.08
Me =1.57
Me$_{\rm abs}$ =7.25
Me =2.39
Me$_{\rm abs}$ =8.01
Me =0.12
Me$_{\rm abs}$ =2.71
Me =-2.64
Me$_{\rm abs}$ =4.58
Me =-0.28
Me$_{\rm abs}$ =3.78
Me =-2.99
Me$_{\rm abs}$ =4.75
Me =0.88
Me$_{\rm abs}$ =4.47
Me =-3.83
Me$_{\rm abs}$ =5.29
Me =5.29
Me$_{\rm abs}$ =6.96
Me =4.97
Me$_{\rm abs}$ =6.79
Me =5.33
Me$_{\rm abs}$ =7.24

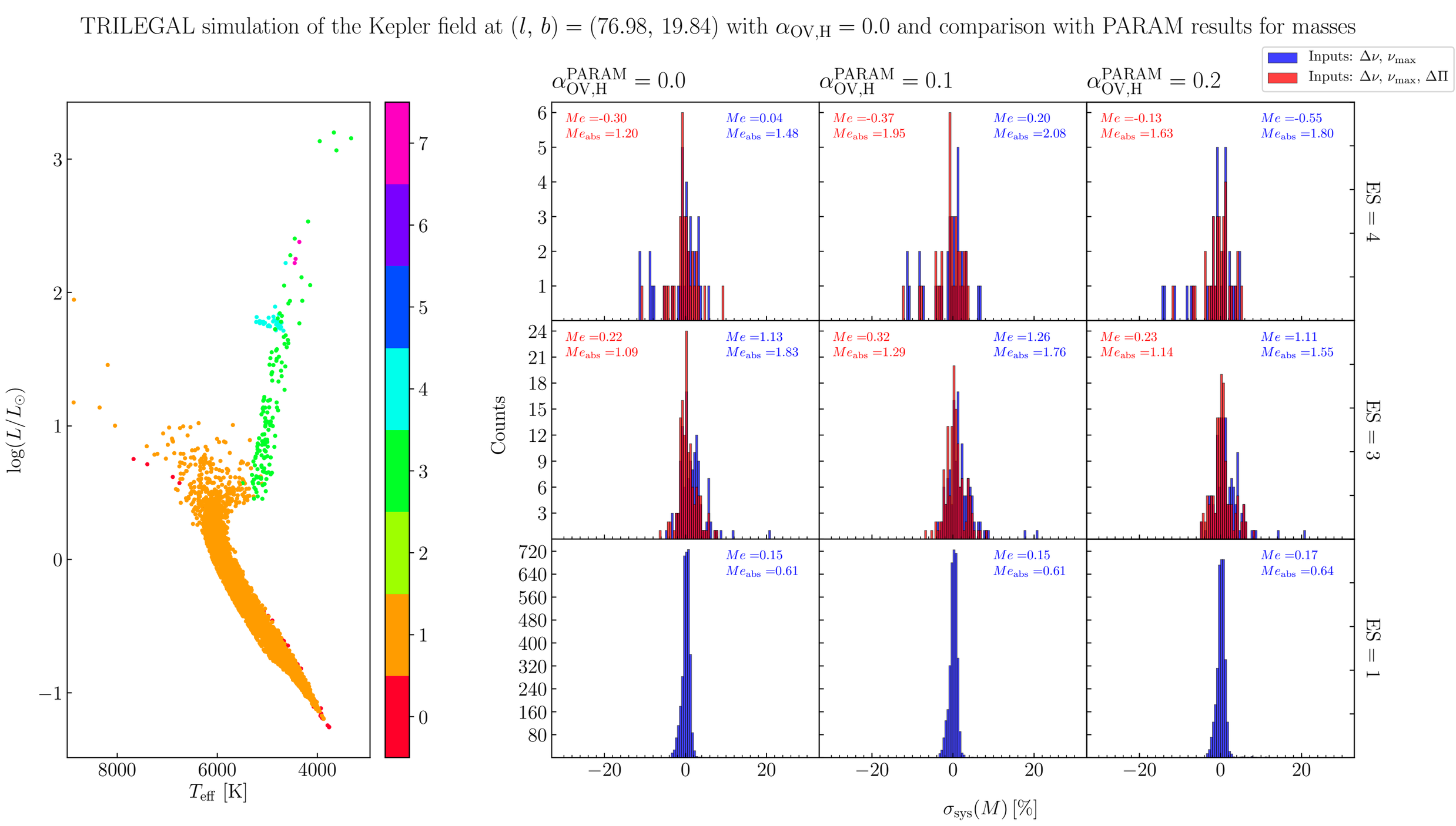
TRILEGAL simulation of the Kepler field at $(l, b) = (76.98, 19.84)$ with $\alpha_{\rm OV,H} = 0.0$ and comparison with PARAM results for masses
Inputs: $\Delta\nu$, $\nu_{\rm max}$
Inputs: $\Delta\nu$, $\nu_{\rm max}$, $\Delta\Pi$
$\alpha_{\rm OV,H}^{\rm PARAM} = 0.0$
$\alpha_{\rm OV,H}^{\rm PARAM} = 0.1$
$\alpha_{\rm OV,H}^{\rm PARAM} = 0.2$
$\log(L/L_\odot)$
$T_{\rm eff}$ [K]
Counts
$\sigma_{\rm sys}(M)$ [%]
ES = 4
ES = 3
ES = 1
Me =-0.30
Me$_{\rm abs}$ =1.20
Me =0.04
Me$_{\rm abs}$ =1.48
Me =-0.37
Me$_{\rm abs}$ =1.95
Me =0.20
Me$_{\rm abs}$ =2.08
Me =-0.13
Me$_{\rm abs}$ =1.63
Me =-0.55
Me$_{\rm abs}$ =1.80
Me =0.22
Me$_{\rm abs}$ =1.09
Me =1.13
Me$_{\rm abs}$ =1.83
Me =0.32
Me$_{\rm abs}$ =1.29
Me =1.26
Me$_{\rm abs}$ =1.76
Me =0.23
Me$_{\rm abs}$ =1.14
Me =1.11
Me$_{\rm abs}$ =1.55
Me =0.15
Me$_{\rm abs}$ =0.61
Me =0.15
Me$_{\rm abs}$ =0.61
Me =0.17
Me$_{\rm abs}$ =0.64

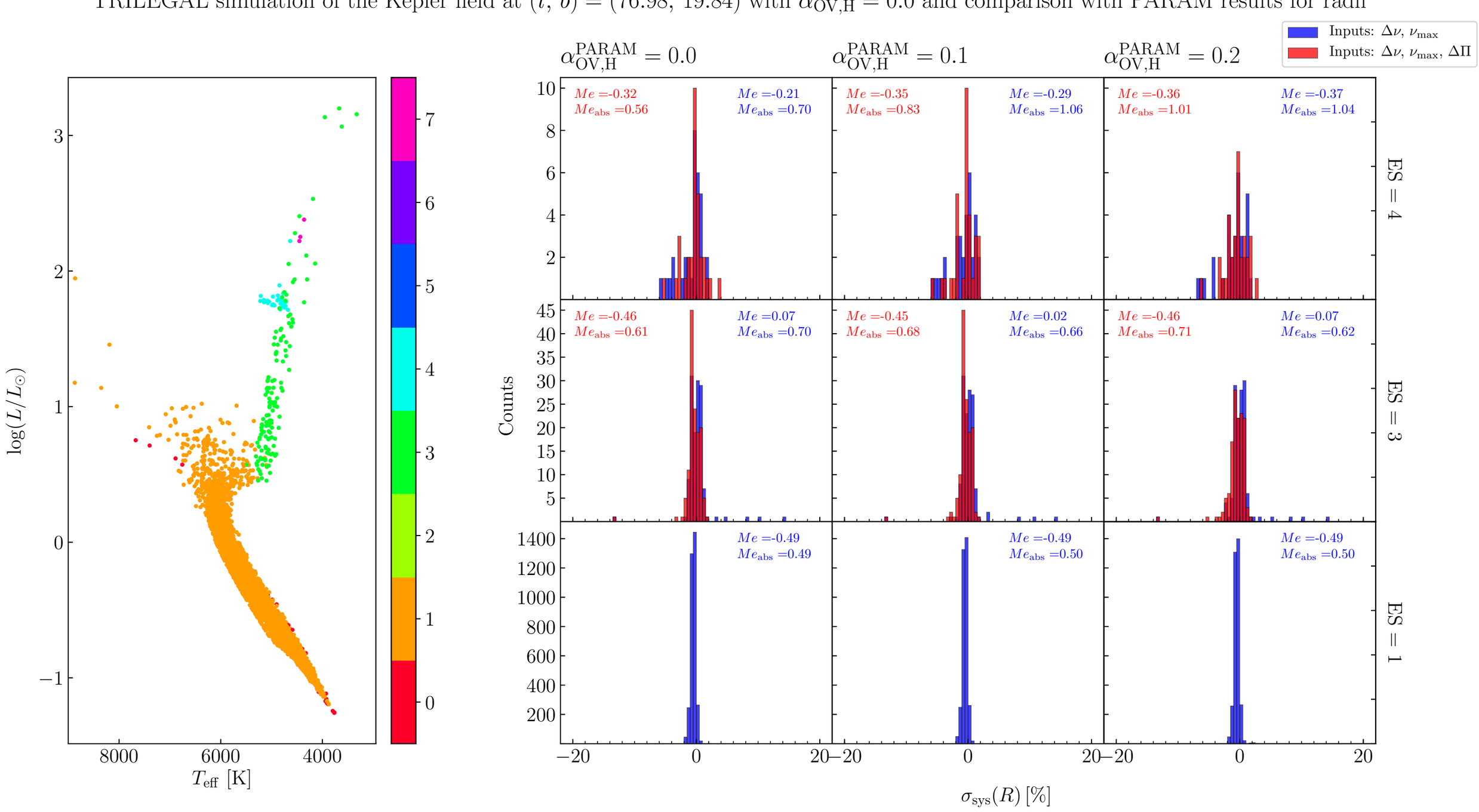
TRILEGAL simulation of the Kepler field at $(l, b) = (76.98, 19.84)$ with $\alpha_{\rm OV,H} = 0.0$ and comparison with PARAM results for radii
$\log(L/L_\odot)$
$T_{\rm eff}$ [K]
$\alpha_{\rm OV,H}^{\rm PARAM} = 0.0$
$\alpha_{\rm OV,H}^{\rm PARAM} = 0.1$
$\alpha_{\rm OV,H}^{\rm PARAM} = 0.2$
Inputs: $\Delta\nu$, $\nu_{\rm max}$
Inputs: $\Delta\nu$, $\nu_{\rm max}$, $\Delta\Pi$
ES = 4
ES = 3
ES = 1
Counts
$\sigma_{\rm sys}(R)$ [%]
Me =-0.32
Me$_{\rm abs}$ =0.56
Me =-0.21
Me$_{\rm abs}$ =0.70
Me =-0.35
Me$_{\rm abs}$ =0.83
Me =-0.29
Me$_{\rm abs}$ =1.06
Me =-0.36
Me$_{\rm abs}$ =1.01
Me =-0.37
Me$_{\rm abs}$ =1.04
Me =-0.46
Me$_{\rm abs}$ =0.61
Me =0.07
Me$_{\rm abs}$ =0.70
Me =-0.45
Me$_{\rm abs}$ =0.68
Me =0.02
Me$_{\rm abs}$ =0.66
Me =-0.46
Me$_{\rm abs}$ =0.71
Me =0.07
Me$_{\rm abs}$ =0.62
Me =-0.49
Me$_{\rm abs}$ =0.49
Me =-0.49
Me$_{\rm abs}$ =0.50
Me =-0.49
Me$_{\rm abs}$ =0.50

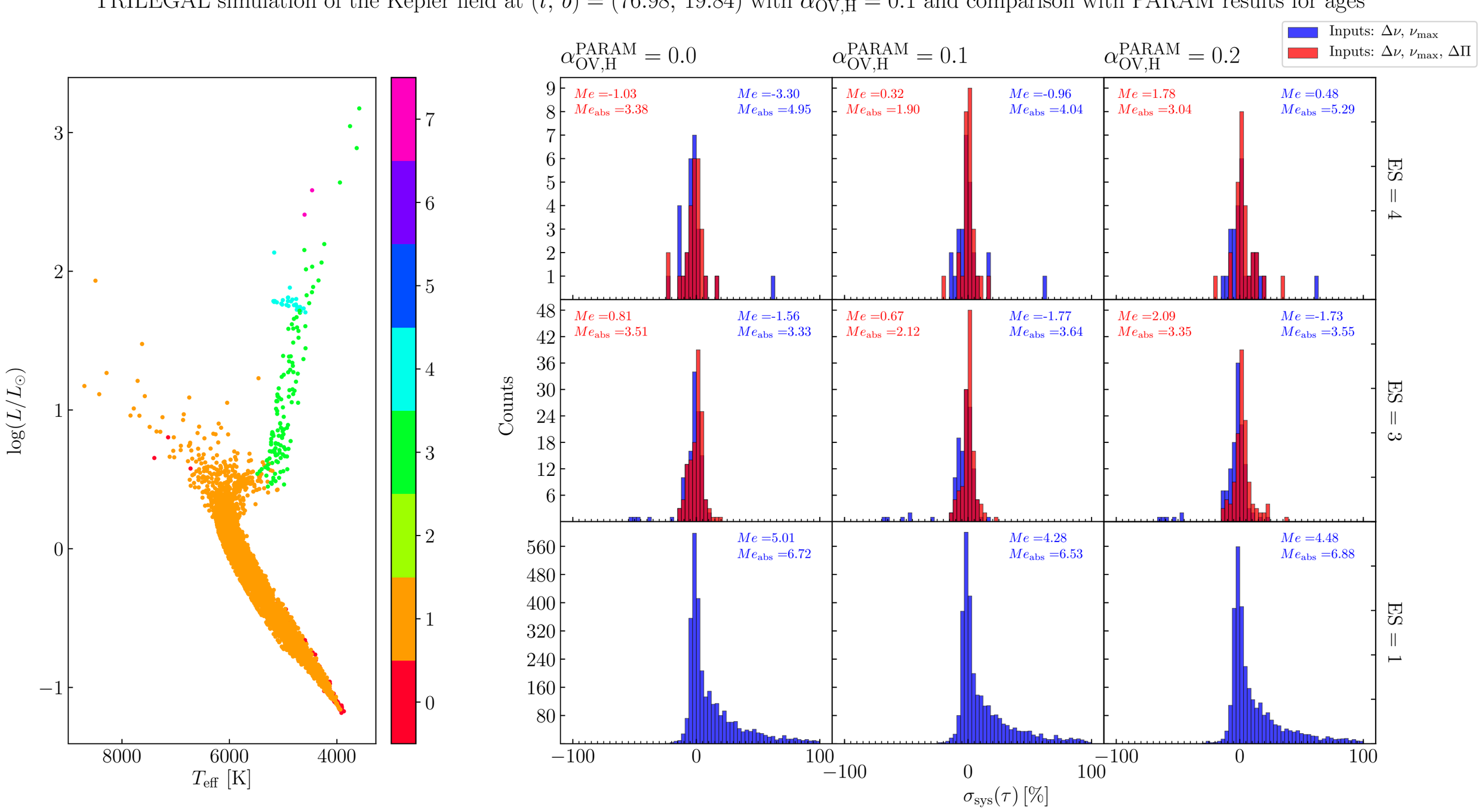
TRILEGAL simulation of the Kepler field at (l, b) = (76.98, 19.84) with $\alpha_{\rm OV,H} = 0.1$ and comparison with PARAM results for ages
$\log(L/L_\odot)$
$T_{\rm eff}$ [K]
$\alpha_{\rm OV,H}^{\rm PARAM} = 0.0$
$\alpha_{\rm OV,H}^{\rm PARAM} = 0.1$
$\alpha_{\rm OV,H}^{\rm PARAM} = 0.2$
Inputs: $\Delta\nu$, $\nu_{\rm max}$
Inputs: $\Delta\nu$, $\nu_{\rm max}$, $\Delta\Pi$
ES = 4
ES = 3
ES = 1
Counts
$\sigma_{\rm sys}(\tau)$ [%]
Me =-1.03
Me$_{\rm abs}$ =3.38
Me =-3.30
Me$_{\rm abs}$ =4.95
Me =0.32
Me$_{\rm abs}$ =1.90
Me =-0.96
Me$_{\rm abs}$ =4.04
Me =1.78
Me$_{\rm abs}$ =3.04
Me =0.48
Me$_{\rm abs}$ =5.29
Me =0.81
Me$_{\rm abs}$ =3.51
Me =-1.56
Me$_{\rm abs}$ =3.33
Me =0.67
Me$_{\rm abs}$ =2.12
Me =-1.77
Me$_{\rm abs}$ =3.64
Me =2.09
Me$_{\rm abs}$ =3.35
Me =-1.73
Me$_{\rm abs}$ =3.55
Me =5.01
Me$_{\rm abs}$ =6.72
Me =4.28
Me$_{\rm abs}$ =6.53
Me =4.48
Me$_{\rm abs}$ =6.88

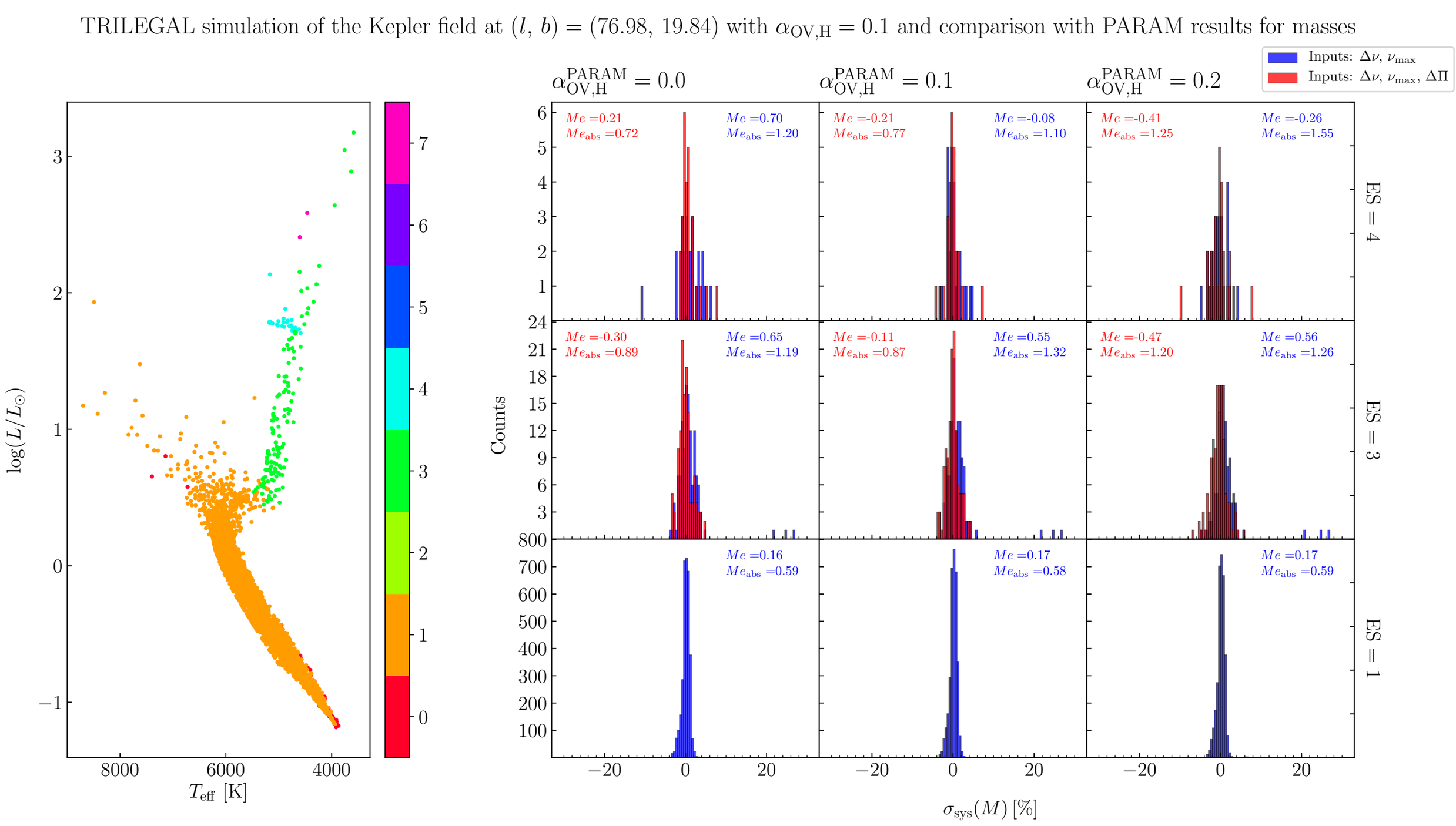
TRILEGAL simulation of the Kepler field at $(l, b) = (76.98, 19.84)$ with $\alpha_{\rm OV,H} = 0.1$ and comparison with PARAM results for masses
$\log(L/L_\odot)$
$T_{\rm eff}$ [K]
Inputs: $\Delta\nu$, $\nu_{\rm max}$
Inputs: $\Delta\nu$, $\nu_{\rm max}$, $\Delta\Pi$
$\alpha_{\rm OV,H}^{\rm PARAM} = 0.0$
$\alpha_{\rm OV,H}^{\rm PARAM} = 0.1$
$\alpha_{\rm OV,H}^{\rm PARAM} = 0.2$
ES = 4
ES = 3
ES = 1
Counts
$\sigma_{\rm sys}(M)$ [%]
Me =0.21
Me$_{\rm abs}$ =0.72
Me =0.70
Me$_{\rm abs}$ =1.20
Me =-0.21
Me$_{\rm abs}$ =0.77
Me =-0.08
Me$_{\rm abs}$ =1.10
Me =-0.41
Me$_{\rm abs}$ =1.25
Me =-0.26
Me$_{\rm abs}$ =1.55
Me =-0.30
Me$_{\rm abs}$ =0.89
Me =0.65
Me$_{\rm abs}$ =1.19
Me =-0.11
Me$_{\rm abs}$ =0.87
Me =0.55
Me$_{\rm abs}$ =1.32
Me =-0.47
Me$_{\rm abs}$ =1.20
Me =0.56
Me$_{\rm abs}$ =1.26
Me =0.16
Me$_{\rm abs}$ =0.59
Me =0.17
Me$_{\rm abs}$ =0.58
Me =0.17
Me$_{\rm abs}$ =0.59

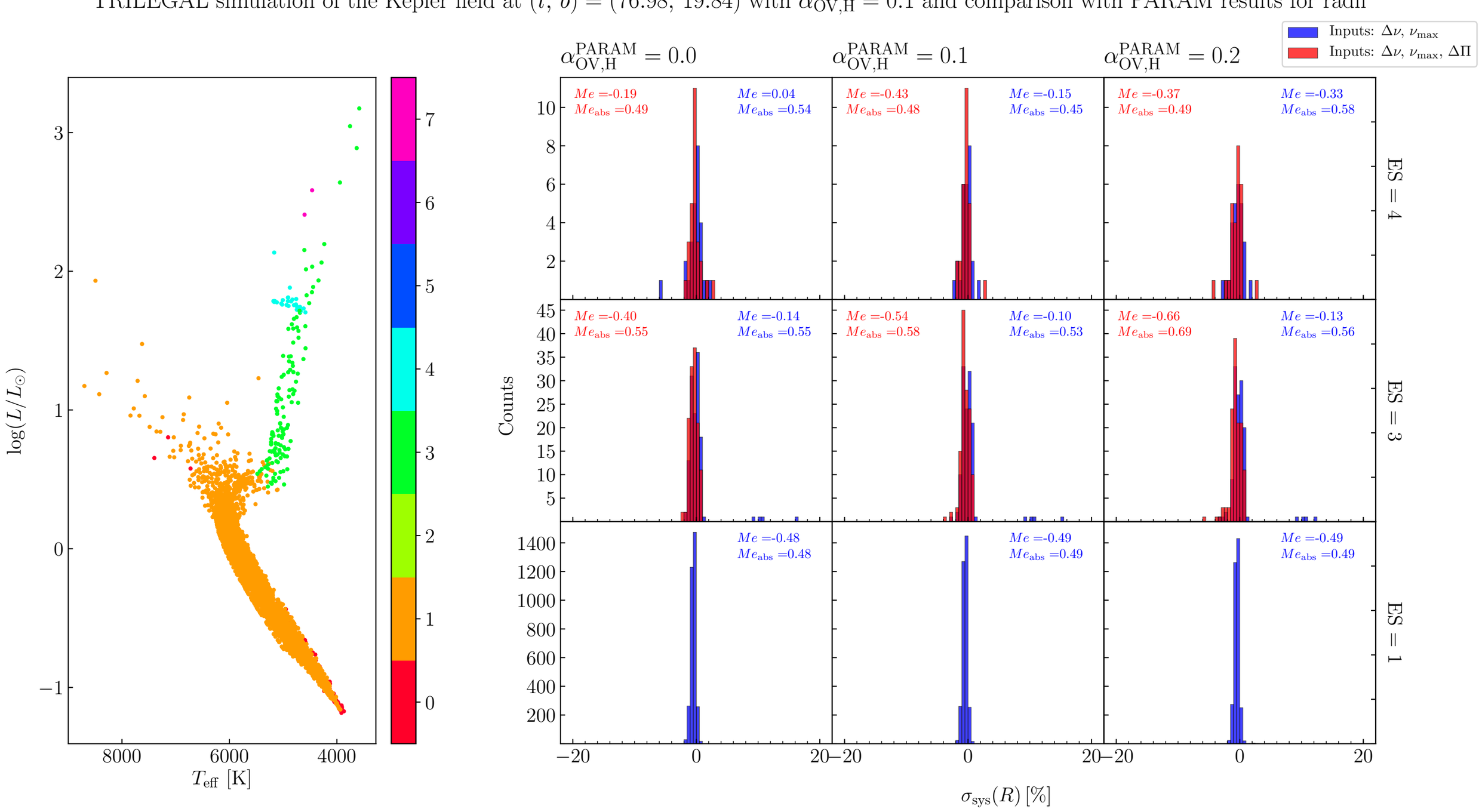
TRILEGAL simulation of the Kepler field at $(l, b) = (76.98, 19.84)$ with $\alpha_{\rm OV,H} = 0.1$ and comparison with PARAM results for radii
$\log(L/L_\odot)$
$T_{\rm eff}$ [K]
$\alpha_{\rm OV,H}^{\rm PARAM} = 0.0$
$\alpha_{\rm OV,H}^{\rm PARAM} = 0.1$
$\alpha_{\rm OV,H}^{\rm PARAM} = 0.2$
Inputs: $\Delta\nu$, $\nu_{\rm max}$
Inputs: $\Delta\nu$, $\nu_{\rm max}$, $\Delta\Pi$
ES = 4
ES = 3
ES = 1
Counts
$\sigma_{\rm sys}(R)$ [%]
Me =-0.19
Me$_{\rm abs}$ =0.49
Me =0.04
Me$_{\rm abs}$ =0.54
Me =-0.43
Me$_{\rm abs}$ =0.48
Me =-0.15
Me$_{\rm abs}$ =0.45
Me =-0.37
Me$_{\rm abs}$ =0.49
Me =-0.33
Me$_{\rm abs}$ =0.58
Me =-0.40
Me$_{\rm abs}$ =0.55
Me =-0.14
Me$_{\rm abs}$ =0.55
Me =-0.54
Me$_{\rm abs}$ =0.58
Me =-0.10
Me$_{\rm abs}$ =0.53
Me =-0.66
Me$_{\rm abs}$ =0.69
Me =-0.13
Me$_{\rm abs}$ =0.56
Me =-0.48
Me$_{\rm abs}$ =0.48
Me =-0.49
Me$_{\rm abs}$ =0.49
Me =-0.49
Me$_{\rm abs}$ =0.49

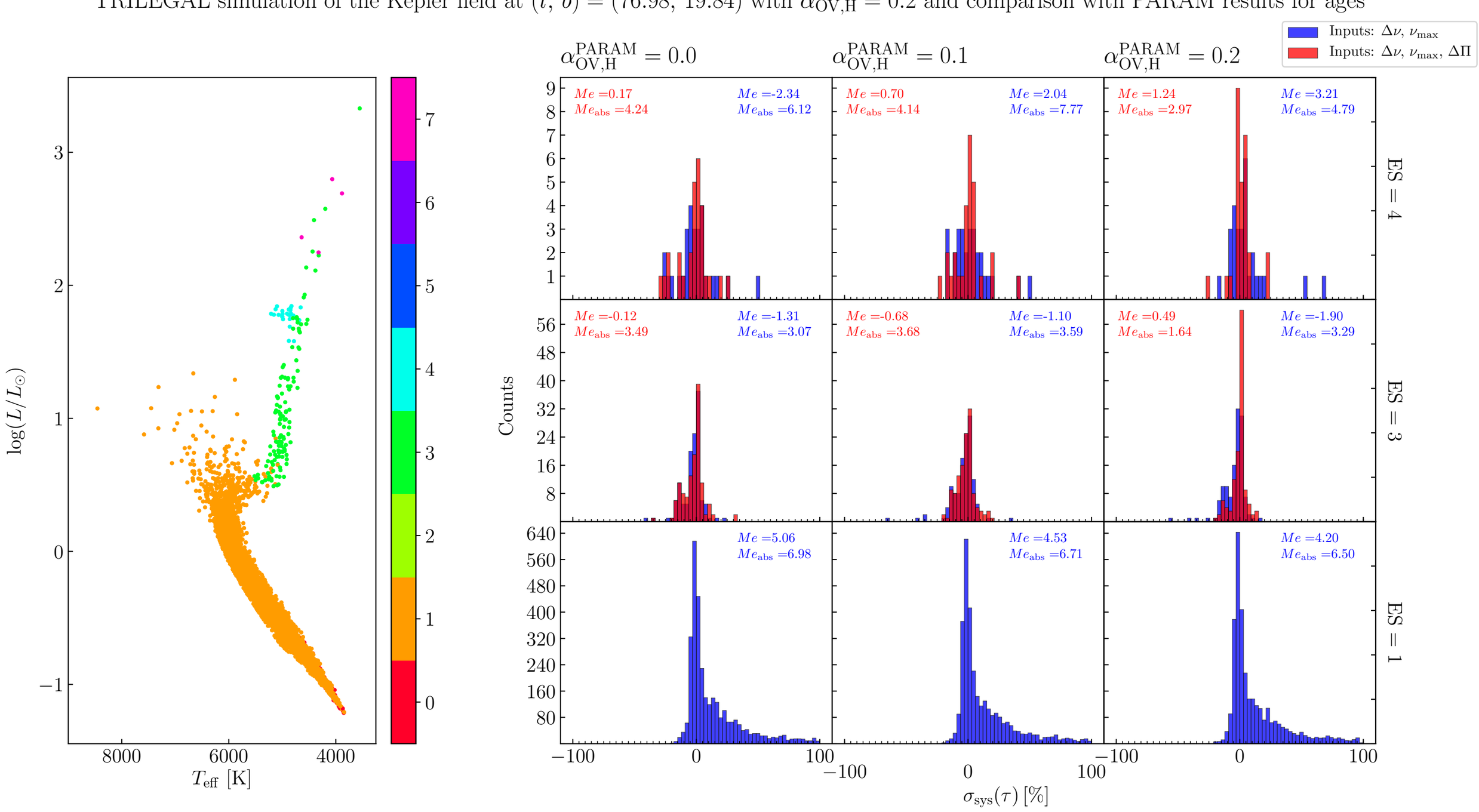
TRILEGAL simulation of the Kepler field at (l, b) = (76.98, 19.84) with $\alpha_{\rm OV,H} = 0.2$ and comparison with PARAM results for ages
Inputs: $\Delta\nu$, $\nu_{\rm max}$
Inputs: $\Delta\nu$, $\nu_{\rm max}$, $\Delta\Pi$
$\alpha_{\rm OV,H}^{\rm PARAM} = 0.0$
$\alpha_{\rm OV,H}^{\rm PARAM} = 0.1$
$\alpha_{\rm OV,H}^{\rm PARAM} = 0.2$
ES = 4
ES = 3
ES = 1
Counts
$\log(L/L_\odot)$
$T_{\rm eff}$ [K]
$\sigma_{\rm sys}(\tau)$ [%]
Me =0.17
Me$_{\rm abs}$ =4.24
Me =-2.34
Me$_{\rm abs}$ =6.12
Me =0.70
Me$_{\rm abs}$ =4.14
Me =2.04
Me$_{\rm abs}$ =7.77
Me =1.24
Me$_{\rm abs}$ =2.97
Me =3.21
Me$_{\rm abs}$ =4.79
Me =-0.12
Me$_{\rm abs}$ =3.49
Me =-1.31
Me$_{\rm abs}$ =3.07
Me =-0.68
Me$_{\rm abs}$ =3.68
Me =-1.10
Me$_{\rm abs}$ =3.59
Me =0.49
Me$_{\rm abs}$ =1.64
Me =-1.90
Me$_{\rm abs}$ =3.29
Me =5.06
Me$_{\rm abs}$ =6.98
Me =4.53
Me$_{\rm abs}$ =6.71
Me =4.20
Me$_{\rm abs}$ =6.50

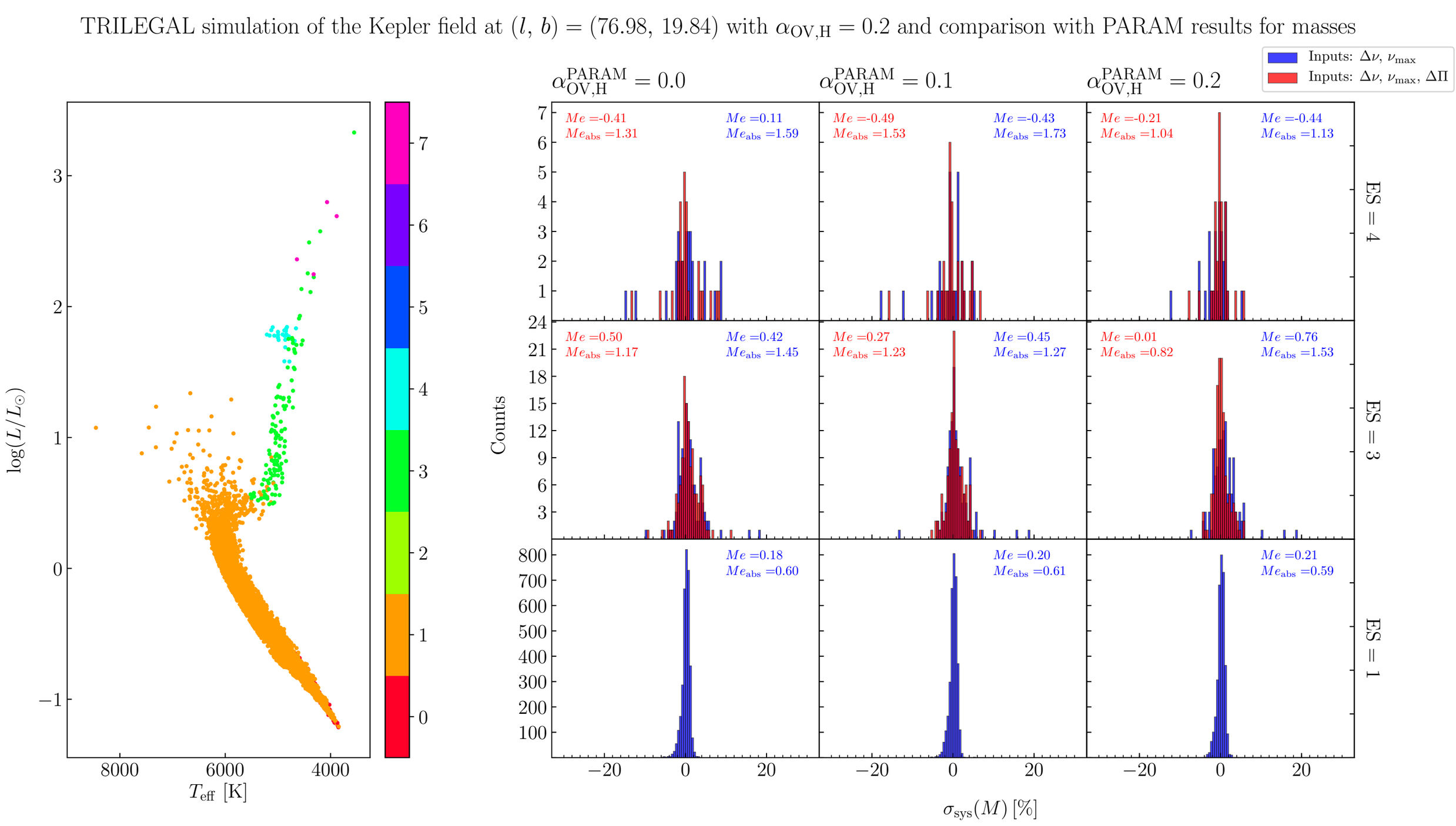
TRILEGAL simulation of the Kepler field at $(l, b) = (76.98, 19.84)$ with $\alpha_{\rm OV,H} = 0.2$ and comparison with PARAM results for masses
$\log(L/L_\odot)$
$T_{\rm eff}$ [K]
Inputs: $\Delta\nu$, $\nu_{\rm max}$
Inputs: $\Delta\nu$, $\nu_{\rm max}$, $\Delta\Pi$
$\alpha_{\rm OV,H}^{\rm PARAM} = 0.0$
$\alpha_{\rm OV,H}^{\rm PARAM} = 0.1$
$\alpha_{\rm OV,H}^{\rm PARAM} = 0.2$
ES = 4
ES = 3
ES = 1
Counts
$\sigma_{\rm sys}(M)$ [%]
Me =-0.41
Me$_{\rm abs}$ =1.31
Me =0.11
Me$_{\rm abs}$ =1.59
Me =-0.49
Me$_{\rm abs}$ =1.53
Me =-0.43
Me$_{\rm abs}$ =1.73
Me =-0.21
Me$_{\rm abs}$ =1.04
Me =-0.44
Me$_{\rm abs}$ =1.13
Me =0.50
Me$_{\rm abs}$ =1.17
Me =0.42
Me$_{\rm abs}$ =1.45
Me =0.27
Me$_{\rm abs}$ =1.23
Me =0.45
Me$_{\rm abs}$ =1.27
Me =0.01
Me$_{\rm abs}$ =0.82
Me =0.76
Me$_{\rm abs}$ =1.53
Me =0.18
Me$_{\rm abs}$ =0.60
Me =0.20
Me$_{\rm abs}$ =0.61
Me =0.21
Me$_{\rm abs}$ =0.59

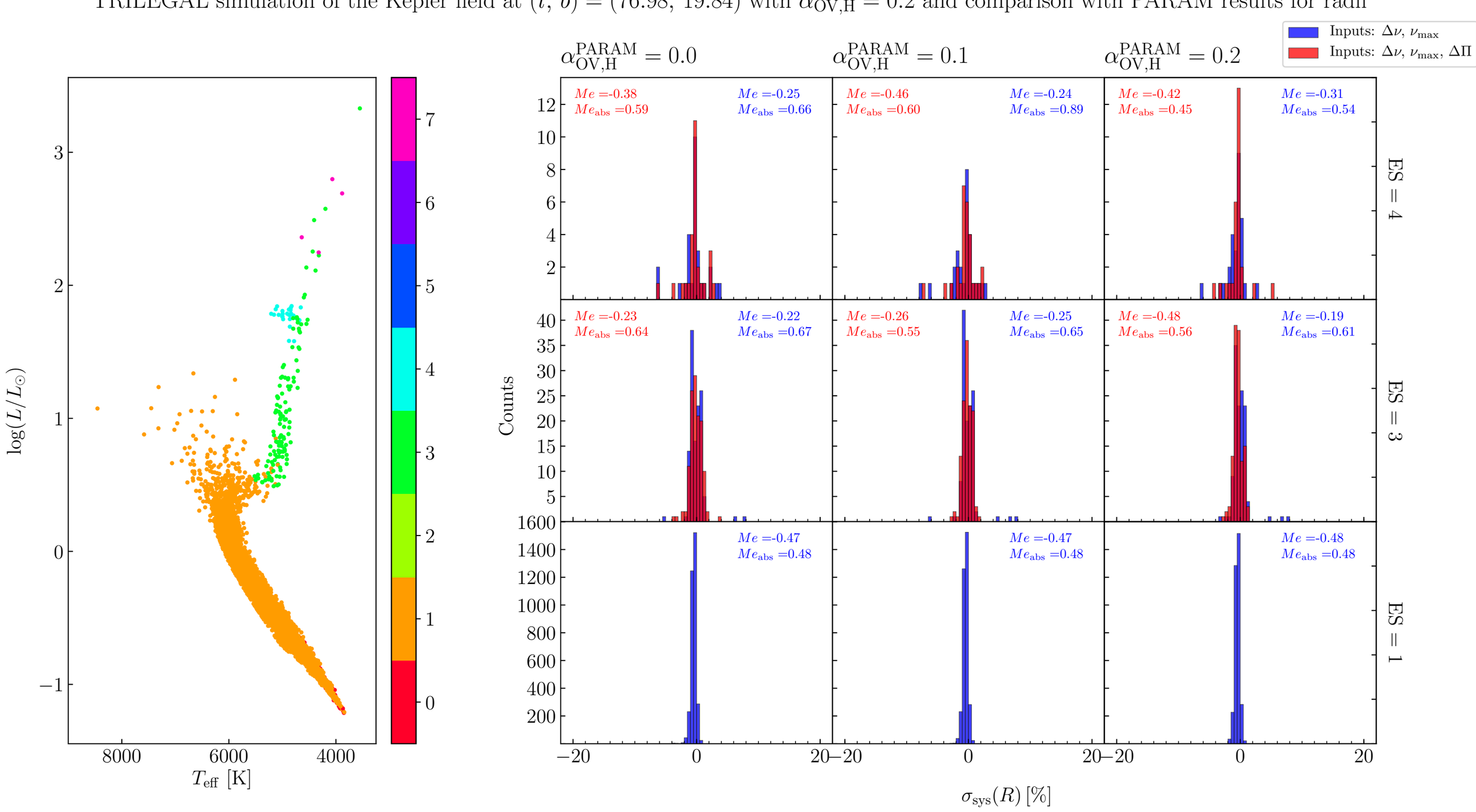
TRILEGAL simulation of the Kepler field at (l, b) = (76.98, 19.84) with $\alpha_{\rm OV,H} = 0.2$ and comparison with PARAM results for radii
Inputs: $\Delta\nu$, $\nu_{\rm max}$
Inputs: $\Delta\nu$, $\nu_{\rm max}$, $\Delta\Pi$
$\alpha_{\rm OV,H}^{\rm PARAM} = 0.0$
$\alpha_{\rm OV,H}^{\rm PARAM} = 0.1$
$\alpha_{\rm OV,H}^{\rm PARAM} = 0.2$
ES = 4
ES = 3
ES = 1
Counts
$\log(L/L_\odot)$
$T_{\rm eff}$ [K]
$\sigma_{\rm sys}(R)$ [%]
Me =-0.38
Me$_{\rm abs}$ =0.59
Me =-0.25
Me$_{\rm abs}$ =0.66
Me =-0.46
Me$_{\rm abs}$ =0.60
Me =-0.24
Me$_{\rm abs}$ =0.89
Me =-0.42
Me$_{\rm abs}$ =0.45
Me =-0.31
Me$_{\rm abs}$ =0.54
Me =-0.23
Me$_{\rm abs}$ =0.64
Me =-0.22
Me$_{\rm abs}$ =0.67
Me =-0.26
Me$_{\rm abs}$ =0.55
Me =-0.25
Me$_{\rm abs}$ =0.65
Me =-0.48
Me$_{\rm abs}$ =0.56
Me =-0.19
Me$_{\rm abs}$ =0.61
Me =-0.47
Me$_{\rm abs}$ =0.48
Me =-0.47
Me$_{\rm abs}$ =0.48
Me =-0.48
Me$_{\rm abs}$ =0.48

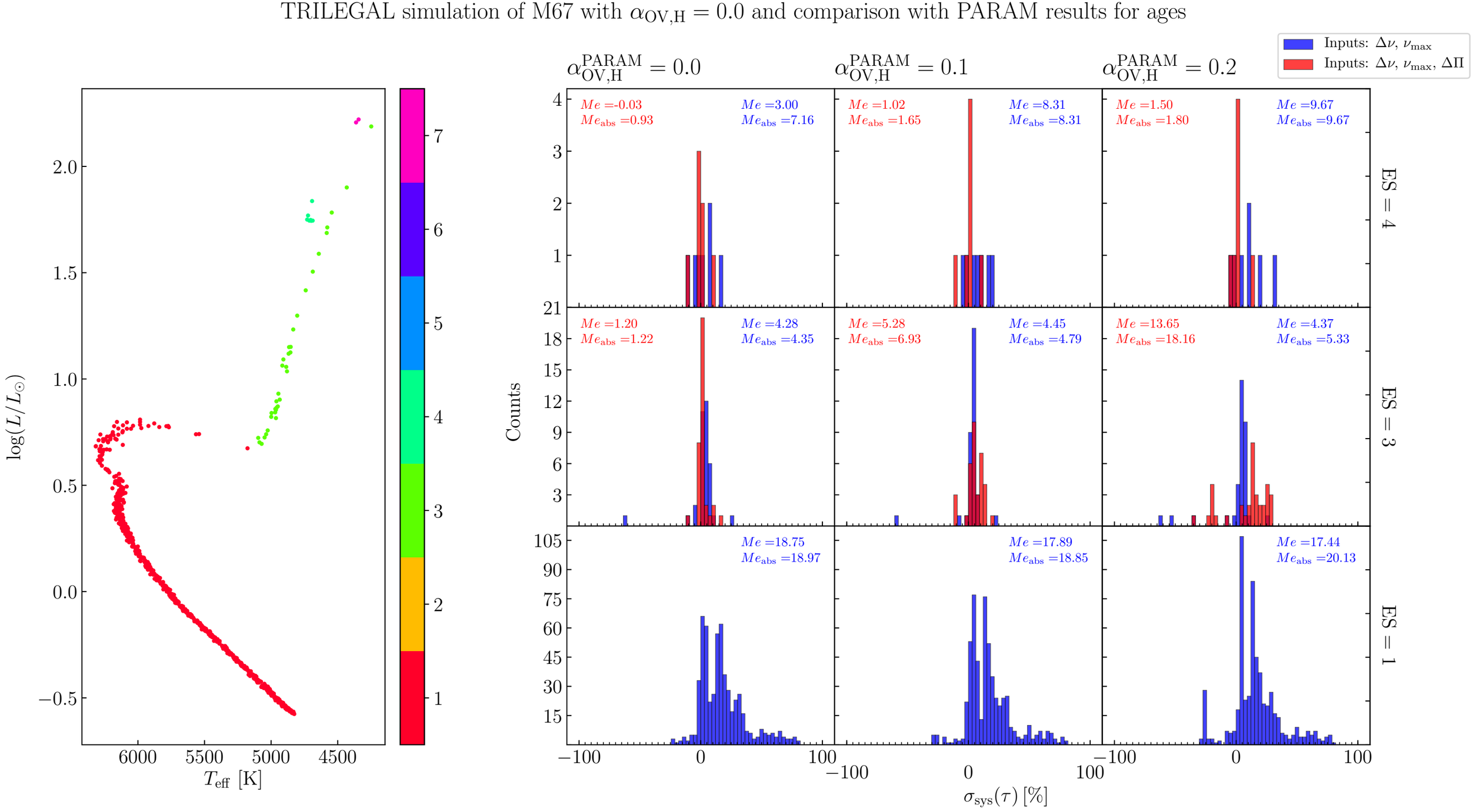
TRILEGAL simulation of M67 with $\alpha_{\rm OV,H} = 0.0$ and comparison with PARAM results for ages
Inputs: $\Delta\nu$, $\nu_{\rm max}$
Inputs: $\Delta\nu$, $\nu_{\rm max}$, $\Delta\Pi$
$\alpha_{\rm OV,H}^{\rm PARAM} = 0.0$
$\alpha_{\rm OV,H}^{\rm PARAM} = 0.1$
$\alpha_{\rm OV,H}^{\rm PARAM} = 0.2$
ES = 4
ES = 3
ES = 1
Counts
$\log(L/L_\odot)$
$T_{\rm eff}$ [K]
$\sigma_{\rm sys}(\tau)$ [%]
Me =-0.03
Me$_{\rm abs}$ =0.93
Me =3.00
Me$_{\rm abs}$ =7.16
Me =1.02
Me$_{\rm abs}$ =1.65
Me =8.31
Me$_{\rm abs}$ =8.31
Me =1.50
Me$_{\rm abs}$ =1.80
Me =9.67
Me$_{\rm abs}$ =9.67
Me =1.20
Me$_{\rm abs}$ =1.22
Me =4.28
Me$_{\rm abs}$ =4.35
Me =5.28
Me$_{\rm abs}$ =6.93
Me =4.45
Me$_{\rm abs}$ =4.79
Me =13.65
Me$_{\rm abs}$ =18.16
Me =4.37
Me$_{\rm abs}$ =5.33
Me =18.75
Me$_{\rm abs}$ =18.97
Me =17.89
Me$_{\rm abs}$ =18.85
Me =17.44
Me$_{\rm abs}$ =20.13

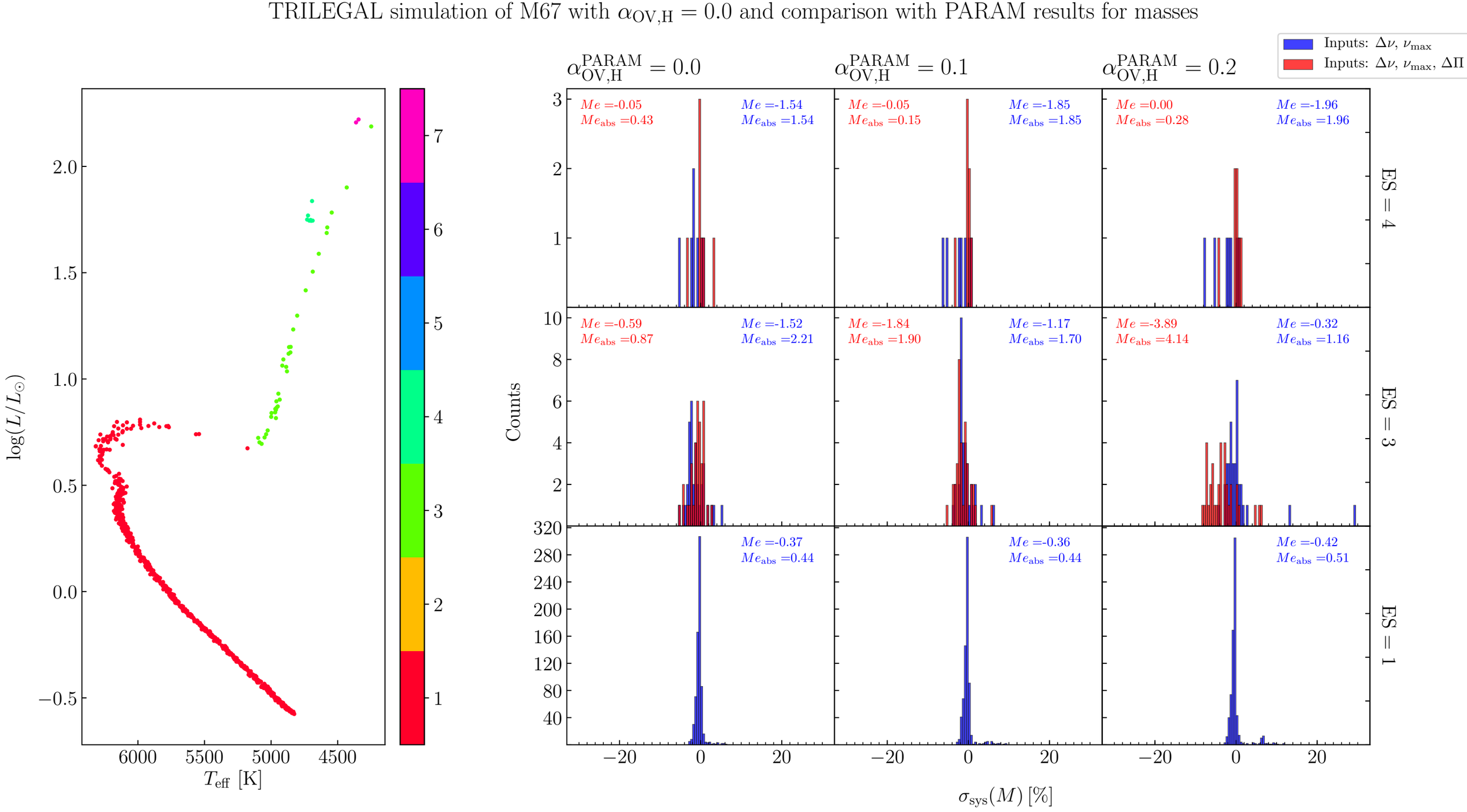
TRILEGAL simulation of M67 with $\alpha_{\rm OV,H} = 0.0$ and comparison with PARAM results for masses
Inputs: $\Delta\nu$, $\nu_{\rm max}$
Inputs: $\Delta\nu$, $\nu_{\rm max}$, $\Delta\Pi$
$\alpha_{\rm OV,H}^{\rm PARAM} = 0.0$
$\alpha_{\rm OV,H}^{\rm PARAM} = 0.1$
$\alpha_{\rm OV,H}^{\rm PARAM} = 0.2$
ES = 4
ES = 3
ES = 1
Counts
$\log(L/L_\odot)$
$T_{\rm eff}$ [K]
$\sigma_{\rm sys}(M)$ [%]
Me =-0.05
Me$_{\rm abs}$ =0.43
Me =-1.54
Me$_{\rm abs}$ =1.54
Me =-0.05
Me$_{\rm abs}$ =0.15
Me =-1.85
Me$_{\rm abs}$ =1.85
Me =0.00
Me$_{\rm abs}$ =0.28
Me =-1.96
Me$_{\rm abs}$ =1.96
Me =-0.59
Me$_{\rm abs}$ =0.87
Me =-1.52
Me$_{\rm abs}$ =2.21
Me =-1.84
Me$_{\rm abs}$ =1.90
Me =-1.17
Me$_{\rm abs}$ =1.70
Me =-3.89
Me$_{\rm abs}$ =4.14
Me =-0.32
Me$_{\rm abs}$ =1.16
Me =-0.37
Me$_{\rm abs}$ =0.44
Me =-0.36
Me$_{\rm abs}$ =0.44
Me =-0.42
Me$_{\rm abs}$ =0.51

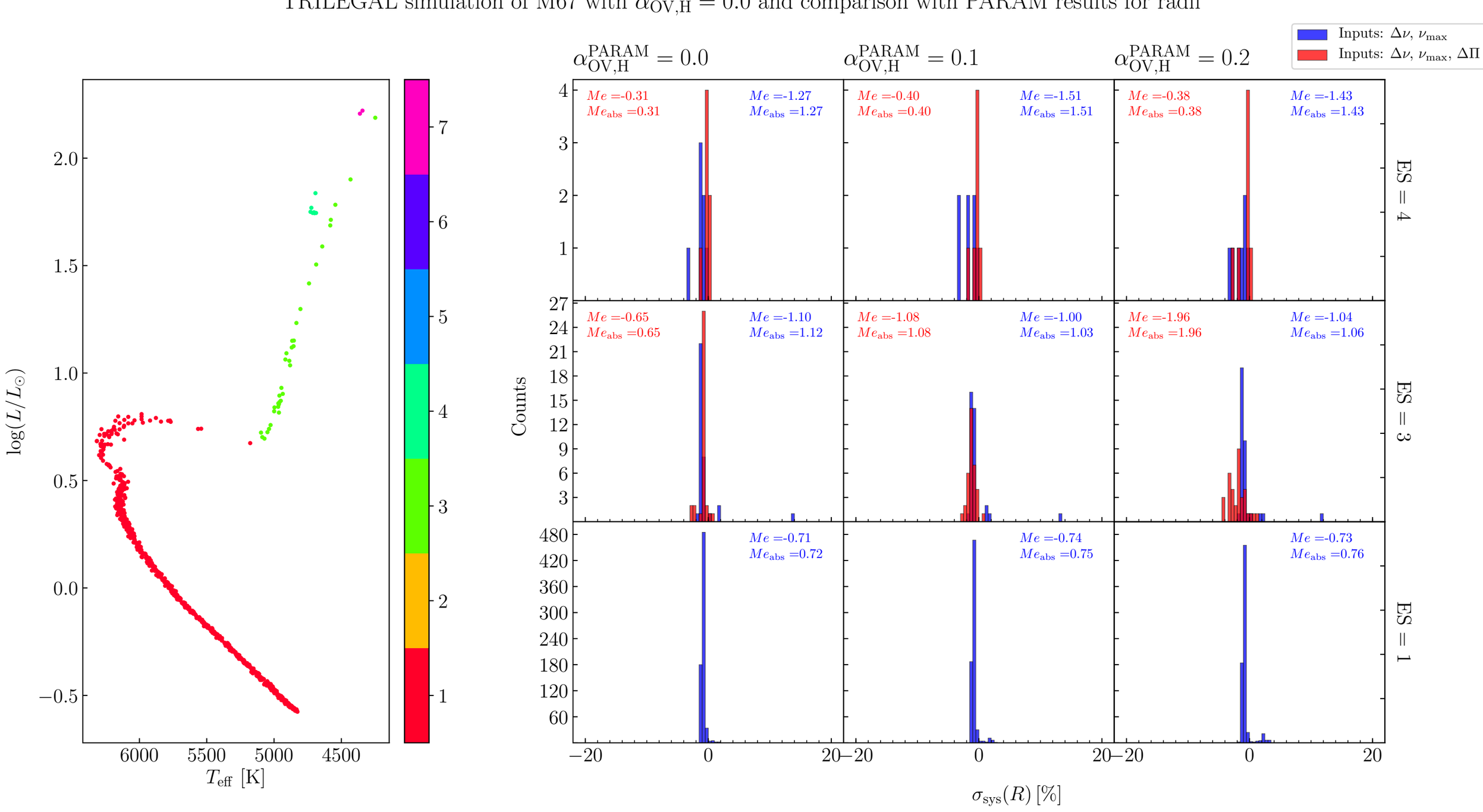
TRILEGAL simulation of M67 with $\alpha_{\rm OV,H} = 0.0$ and comparison with PARAM results for radii
Inputs: $\Delta\nu$, $\nu_{\rm max}$
Inputs: $\Delta\nu$, $\nu_{\rm max}$, $\Delta\Pi$
$\alpha_{\rm OV,H}^{\rm PARAM} = 0.0$
$\alpha_{\rm OV,H}^{\rm PARAM} = 0.1$
$\alpha_{\rm OV,H}^{\rm PARAM} = 0.2$
ES = 4
ES = 3
ES = 1
Counts
$\log(L/L_\odot)$
$T_{\rm eff}$ [K]
$\sigma_{\rm sys}(R)$ [%]
Me =-0.31
Me$_{\rm abs}$ =0.31
Me =-1.27
Me$_{\rm abs}$ =1.27
Me =-0.40
Me$_{\rm abs}$ =0.40
Me =-1.51
Me$_{\rm abs}$ =1.51
Me =-0.38
Me$_{\rm abs}$ =0.38
Me =-1.43
Me$_{\rm abs}$ =1.43
Me =-0.65
Me$_{\rm abs}$ =0.65
Me =-1.10
Me$_{\rm abs}$ =1.12
Me =-1.08
Me$_{\rm abs}$ =1.08
Me =-1.00
Me$_{\rm abs}$ =1.03
Me =-1.96
Me$_{\rm abs}$ =1.96
Me =-1.04
Me$_{\rm abs}$ =1.06
Me =-0.71
Me$_{\rm abs}$ =0.72
Me =-0.74
Me$_{\rm abs}$ =0.75
Me =-0.73
Me$_{\rm abs}$ =0.76

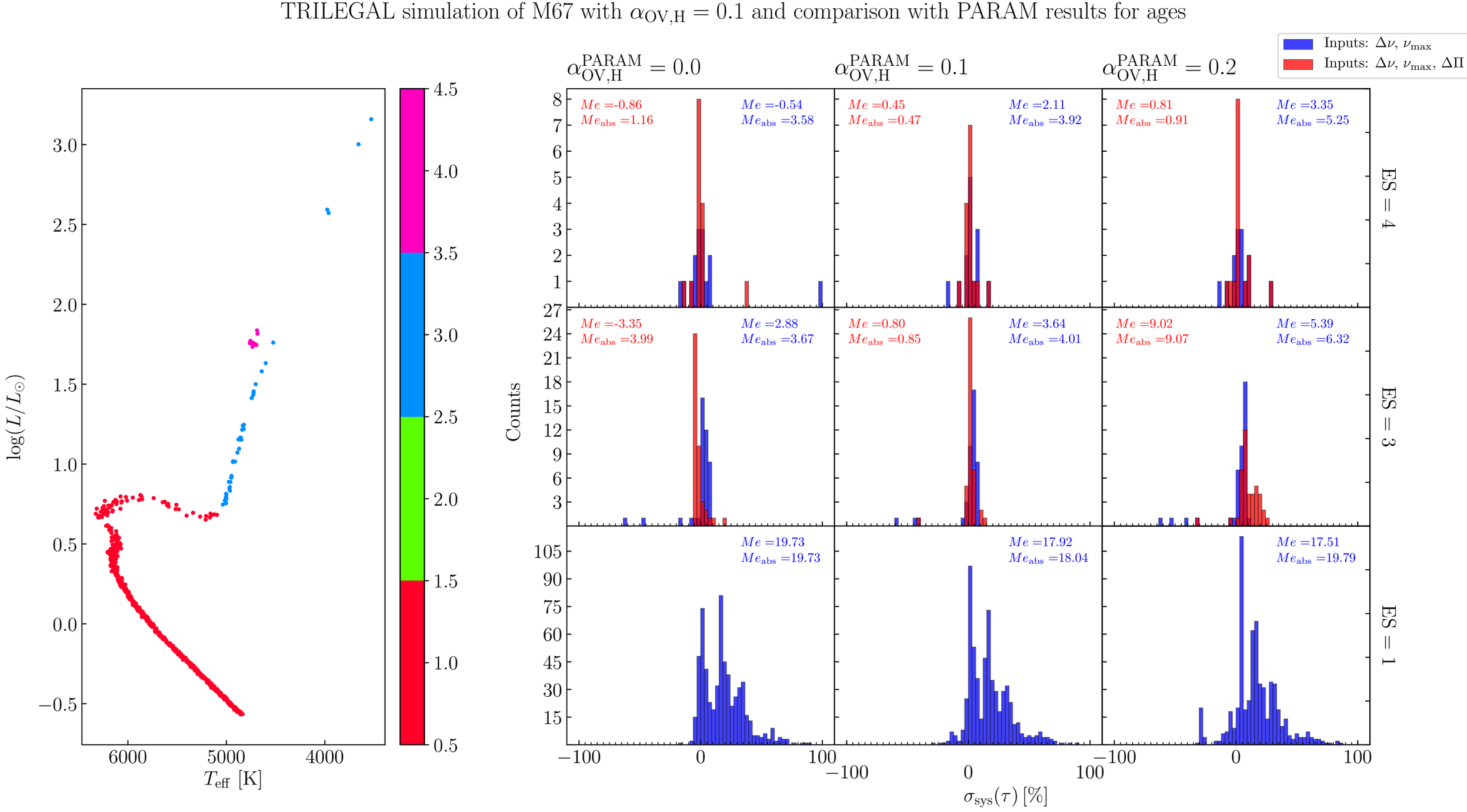
TRILEGAL simulation of M67 with $\alpha_{\rm OV,H} = 0.1$ and comparison with PARAM results for ages
Inputs: $\Delta\nu$, $\nu_{\rm max}$
Inputs: $\Delta\nu$, $\nu_{\rm max}$, $\Delta\Pi$
$\alpha_{\rm OV,H}^{\rm PARAM} = 0.0$
$\alpha_{\rm OV,H}^{\rm PARAM} = 0.1$
$\alpha_{\rm OV,H}^{\rm PARAM} = 0.2$
$\log(L/L_\odot)$
$T_{\rm eff}$ [K]
Counts
$\sigma_{\rm sys}(\tau)$ [%]
ES = 4
ES = 3
ES = 1
Me =-0.86
Me$_{\rm abs}$ =1.16
Me =-0.54
Me$_{\rm abs}$ =3.58
Me =0.45
Me$_{\rm abs}$ =0.47
Me =2.11
Me$_{\rm abs}$ =3.92
Me =0.81
Me$_{\rm abs}$ =0.91
Me =3.35
Me$_{\rm abs}$ =5.25
Me =-3.35
Me$_{\rm abs}$ =3.99
Me =2.88
Me$_{\rm abs}$ =3.67
Me =0.80
Me$_{\rm abs}$ =0.85
Me =3.64
Me$_{\rm abs}$ =4.01
Me =9.02
Me$_{\rm abs}$ =9.07
Me =5.39
Me$_{\rm abs}$ =6.32
Me =19.73
Me$_{\rm abs}$ =19.73
Me =17.92
Me$_{\rm abs}$ =18.04
Me =17.51
Me$_{\rm abs}$ =19.79

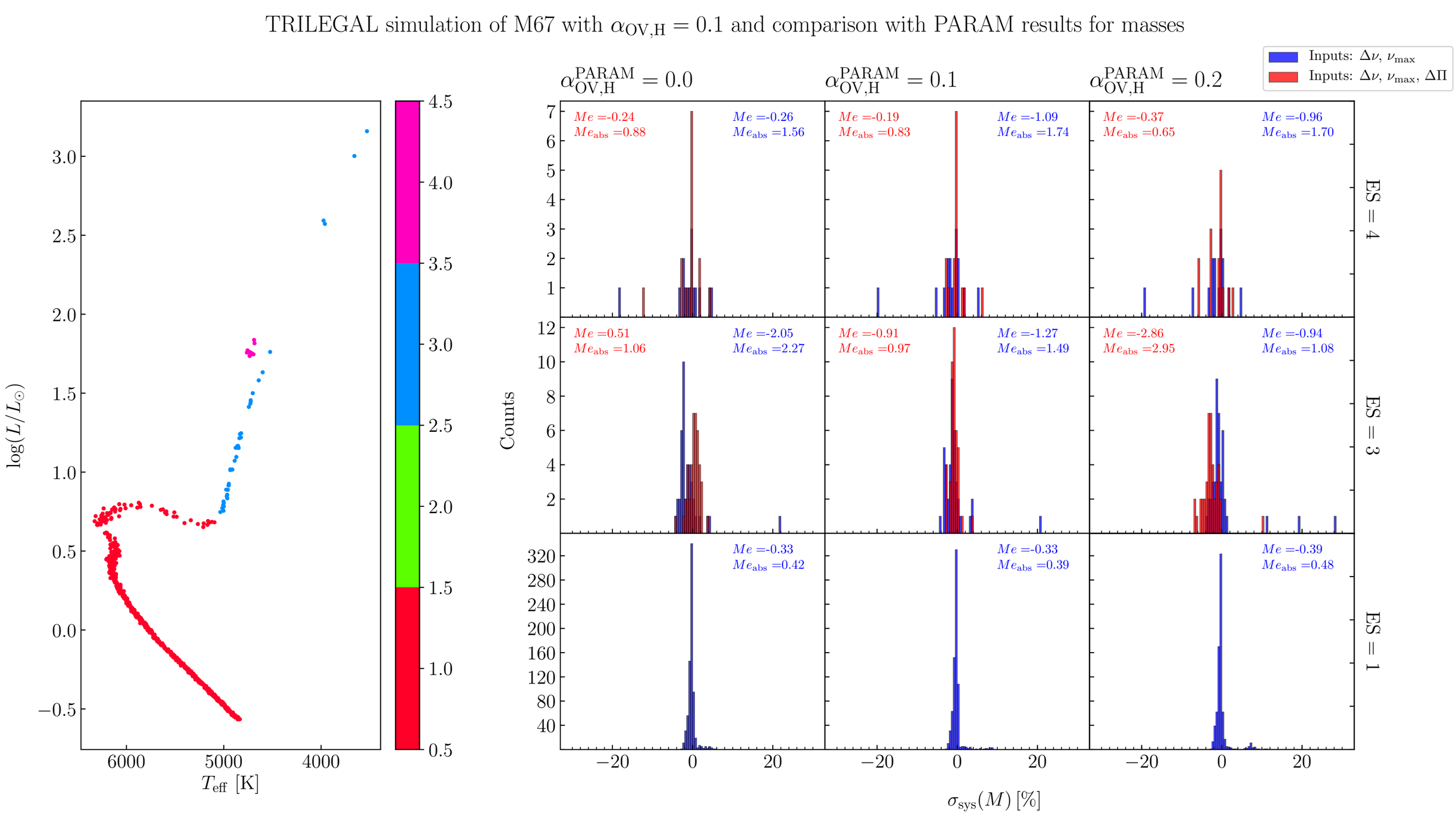
TRILEGAL simulation of M67 with $\alpha_{\rm OV,H} = 0.1$ and comparison with PARAM results for masses
Inputs: $\Delta\nu$, $\nu_{\rm max}$
Inputs: $\Delta\nu$, $\nu_{\rm max}$, $\Delta\Pi$
$\alpha_{\rm OV,H}^{\rm PARAM} = 0.0$
$\alpha_{\rm OV,H}^{\rm PARAM} = 0.1$
$\alpha_{\rm OV,H}^{\rm PARAM} = 0.2$
$\log(L/L_\odot)$
$T_{\rm eff}$ [K]
Counts
$\sigma_{\rm sys}(M)$ [%]
ES = 4
ES = 3
ES = 1
Me =-0.24
Me$_{\rm abs}$ =0.88
Me =-0.26
Me$_{\rm abs}$ =1.56
Me =-0.19
Me$_{\rm abs}$ =0.83
Me =-1.09
Me$_{\rm abs}$ =1.74
Me =-0.37
Me$_{\rm abs}$ =0.65
Me =-0.96
Me$_{\rm abs}$ =1.70
Me =0.51
Me$_{\rm abs}$ =1.06
Me =-2.05
Me$_{\rm abs}$ =2.27
Me =-0.91
Me$_{\rm abs}$ =0.97
Me =-1.27
Me$_{\rm abs}$ =1.49
Me =-2.86
Me$_{\rm abs}$ =2.95
Me =-0.94
Me$_{\rm abs}$ =1.08
Me =-0.33
Me$_{\rm abs}$ =0.42
Me =-0.33
Me$_{\rm abs}$ =0.39
Me =-0.39
Me$_{\rm abs}$ =0.48

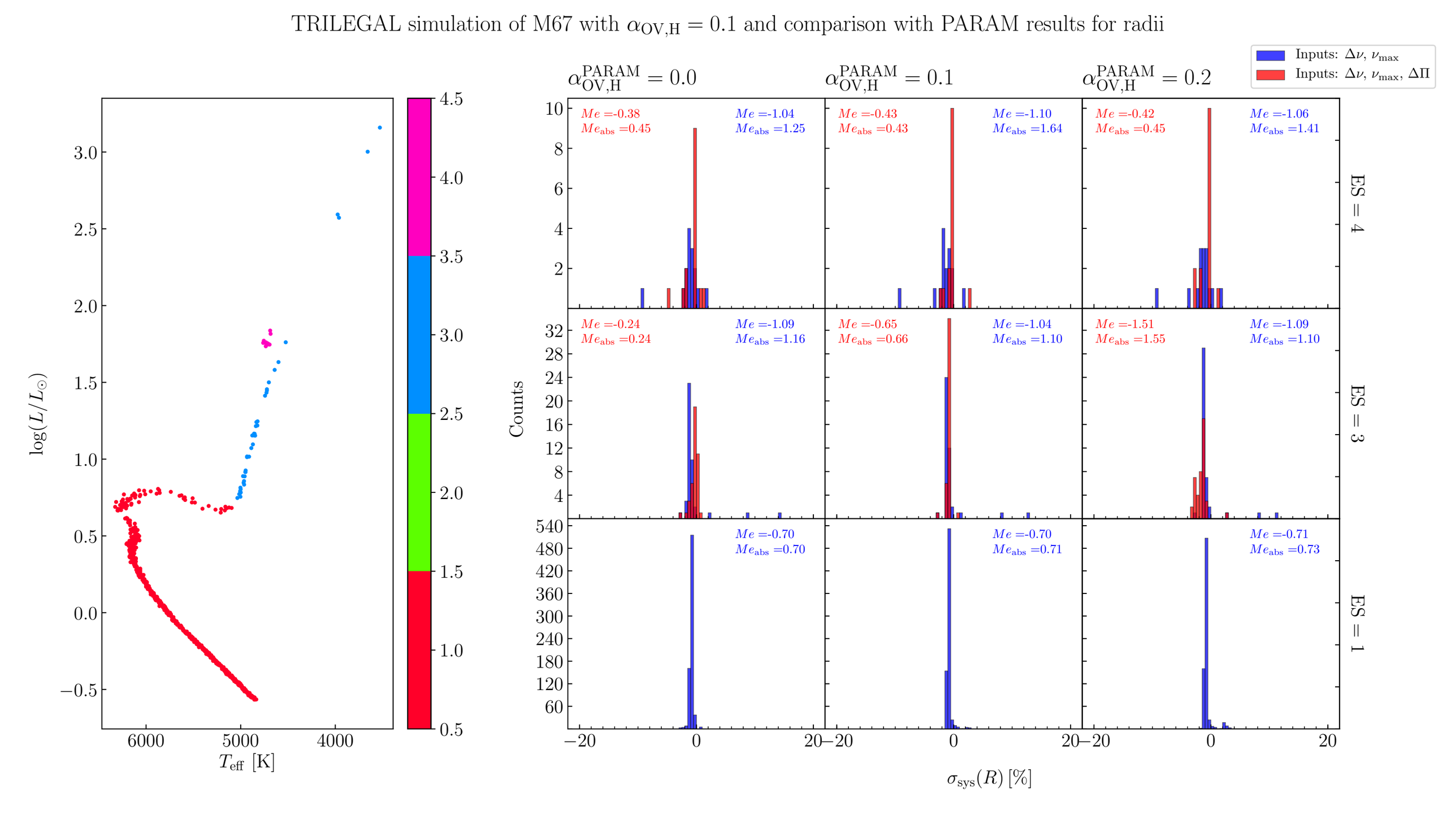
TRILEGAL simulation of M67 with $\alpha_{\rm OV,H} = 0.1$ and comparison with PARAM results for radii
$\log(L/L_\odot)$
$T_{\rm eff}$ [K]
$\alpha_{\rm OV,H}^{\rm PARAM} = 0.0$
$\alpha_{\rm OV,H}^{\rm PARAM} = 0.1$
$\alpha_{\rm OV,H}^{\rm PARAM} = 0.2$
Inputs: $\Delta\nu$, $\nu_{\rm max}$
Inputs: $\Delta\nu$, $\nu_{\rm max}$, $\Delta\Pi$
ES = 4
ES = 3
ES = 1
Counts
$\sigma_{\rm sys}(R)$ [%]
Me =-0.38
Me$_{\rm abs}$ =0.45
Me =-1.04
Me$_{\rm abs}$ =1.25
Me =-0.43
Me$_{\rm abs}$ =0.43
Me =-1.10
Me$_{\rm abs}$ =1.64
Me =-0.42
Me$_{\rm abs}$ =0.45
Me =-1.06
Me$_{\rm abs}$ =1.41
Me =-0.24
Me$_{\rm abs}$ =0.24
Me =-1.09
Me$_{\rm abs}$ =1.16
Me =-0.65
Me$_{\rm abs}$ =0.66
Me =-1.04
Me$_{\rm abs}$ =1.10
Me =-1.51
Me$_{\rm abs}$ =1.55
Me =-1.09
Me$_{\rm abs}$ =1.10
Me =-0.70
Me$_{\rm abs}$ =0.70
Me =-0.70
Me$_{\rm abs}$ =0.71
Me =-0.71
Me$_{\rm abs}$ =0.73

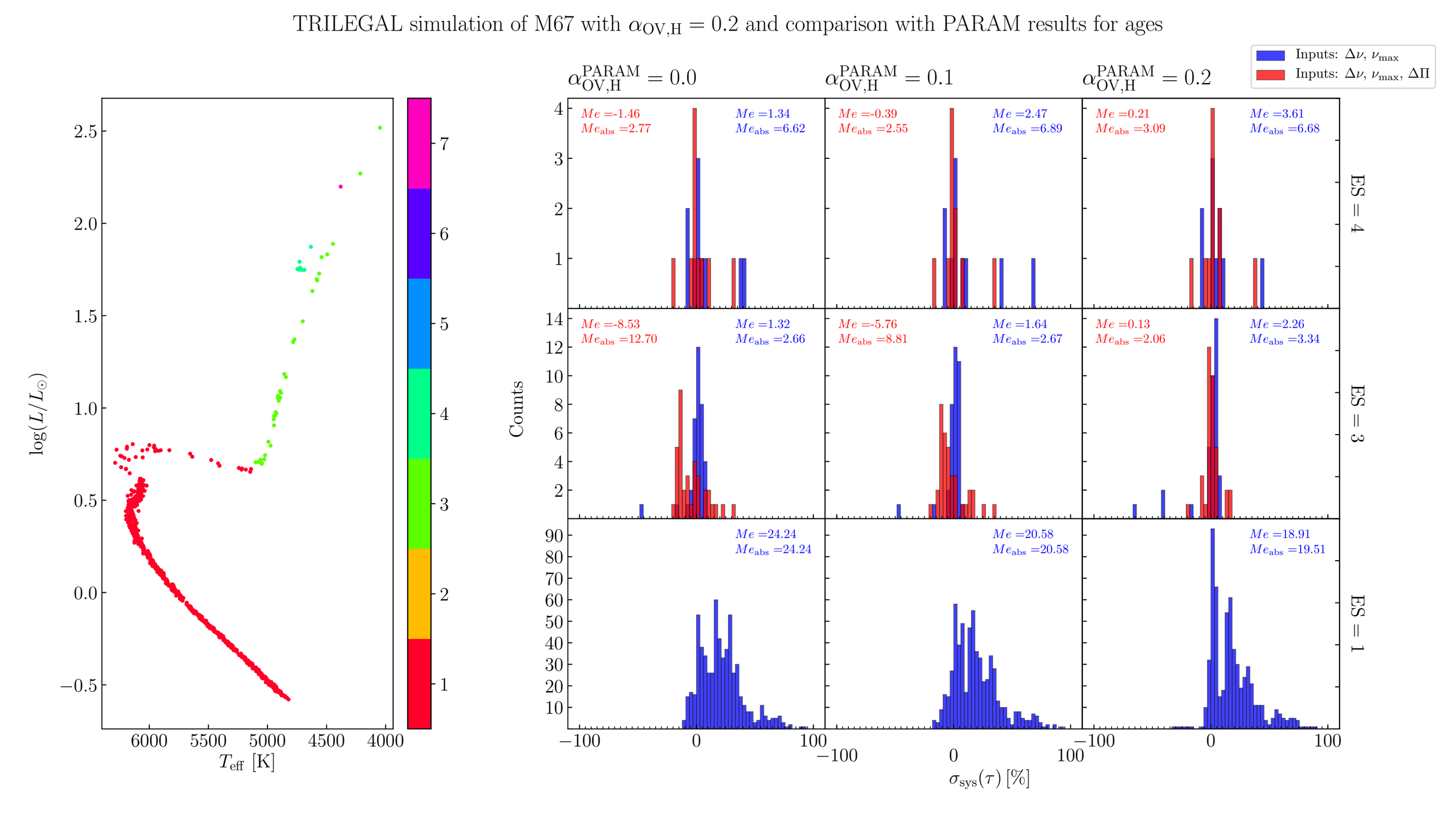
TRILEGAL simulation of M67 with $\alpha_{\rm OV,H} = 0.2$ and comparison with PARAM results for ages
Inputs: $\Delta\nu$, $\nu_{\rm max}$
Inputs: $\Delta\nu$, $\nu_{\rm max}$, $\Delta\Pi$
$\alpha_{\rm OV,H}^{\rm PARAM} = 0.0$
$\alpha_{\rm OV,H}^{\rm PARAM} = 0.1$
$\alpha_{\rm OV,H}^{\rm PARAM} = 0.2$
ES = 4
ES = 3
ES = 1
Counts
$\log(L/L_\odot)$
$T_{\rm eff}$ [K]
$\sigma_{\rm sys}(\tau)$ [%]
Me =-1.46
Me$_{\rm abs}$ =2.77
Me =1.34
Me$_{\rm abs}$ =6.62
Me =-0.39
Me$_{\rm abs}$ =2.55
Me =2.47
Me$_{\rm abs}$ =6.89
Me =0.21
Me$_{\rm abs}$ =3.09
Me =3.61
Me$_{\rm abs}$ =6.68
Me =-8.53
Me$_{\rm abs}$ =12.70
Me =1.32
Me$_{\rm abs}$ =2.66
Me =-5.76
Me$_{\rm abs}$ =8.81
Me =1.64
Me$_{\rm abs}$ =2.67
Me =0.13
Me$_{\rm abs}$ =2.06
Me =2.26
Me$_{\rm abs}$ =3.34
Me =24.24
Me$_{\rm abs}$ =24.24
Me =20.58
Me$_{\rm abs}$ =20.58
Me =18.91
Me$_{\rm abs}$ =19.51

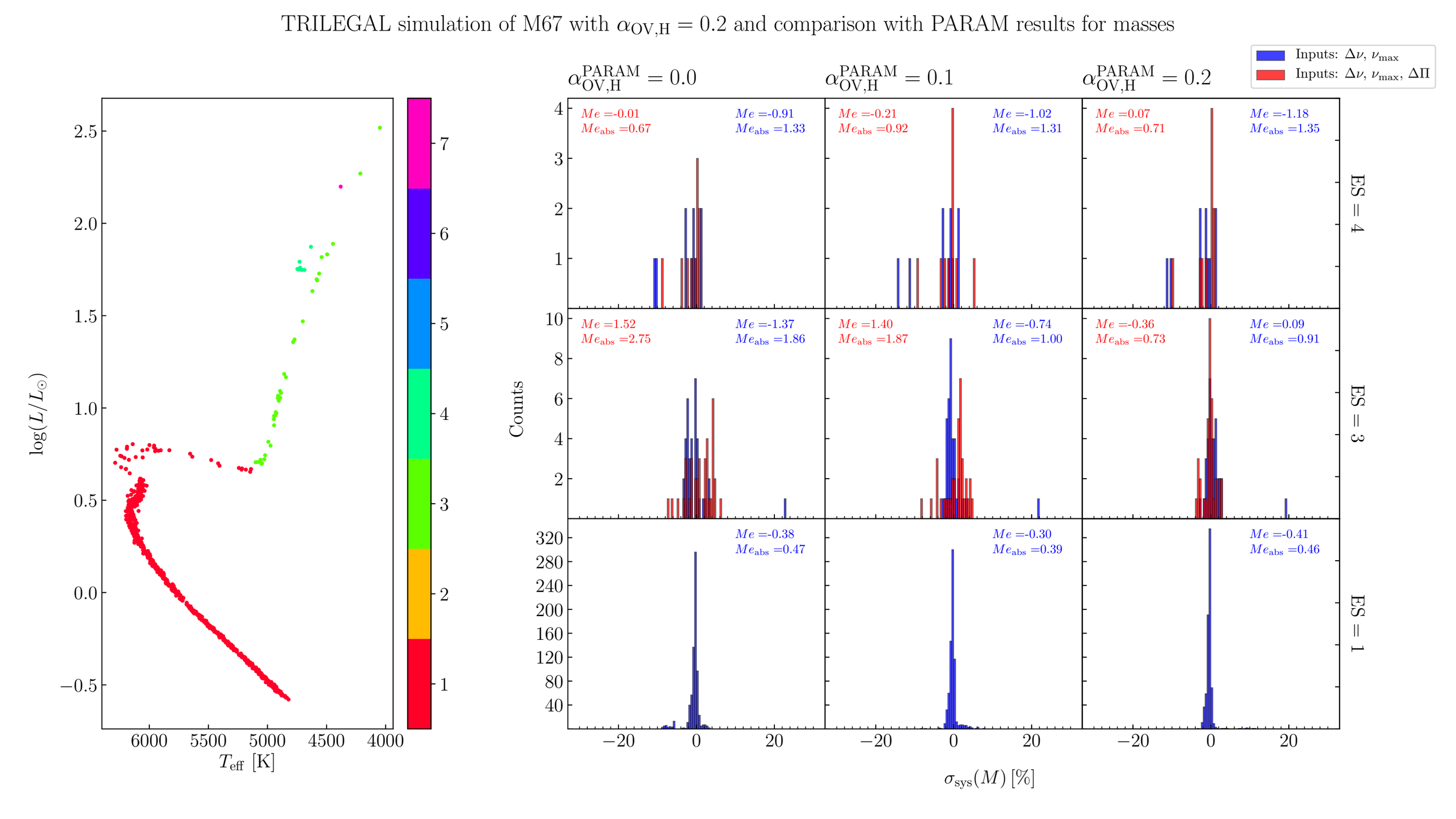
TRILEGAL simulation of M67 with $\alpha_{\rm OV,H} = 0.2$ and comparison with PARAM results for masses
Inputs: $\Delta\nu$, $\nu_{\rm max}$
Inputs: $\Delta\nu$, $\nu_{\rm max}$, $\Delta\Pi$
$\alpha_{\rm OV,H}^{\rm PARAM} = 0.0$
$\alpha_{\rm OV,H}^{\rm PARAM} = 0.1$
$\alpha_{\rm OV,H}^{\rm PARAM} = 0.2$
$\log(L/L_\odot)$
$T_{\rm eff}$ [K]
Counts
$\sigma_{\rm sys}(M)$ [%]
ES = 4
ES = 3
ES = 1
Me =-0.01
Me$_{\rm abs}$ =0.67
Me =-0.91
Me$_{\rm abs}$ =1.33
Me =-0.21
Me$_{\rm abs}$ =0.92
Me =-1.02
Me$_{\rm abs}$ =1.31
Me =0.07
Me$_{\rm abs}$ =0.71
Me =-1.18
Me$_{\rm abs}$ =1.35
Me =1.52
Me$_{\rm abs}$ =2.75
Me =-1.37
Me$_{\rm abs}$ =1.86
Me =1.40
Me$_{\rm abs}$ =1.87
Me =-0.74
Me$_{\rm abs}$ =1.00
Me =-0.36
Me$_{\rm abs}$ =0.73
Me =0.09
Me$_{\rm abs}$ =0.91
Me =-0.38
Me$_{\rm abs}$ =0.47
Me =-0.30
Me$_{\rm abs}$ =0.39
Me =-0.41
Me$_{\rm abs}$ =0.46

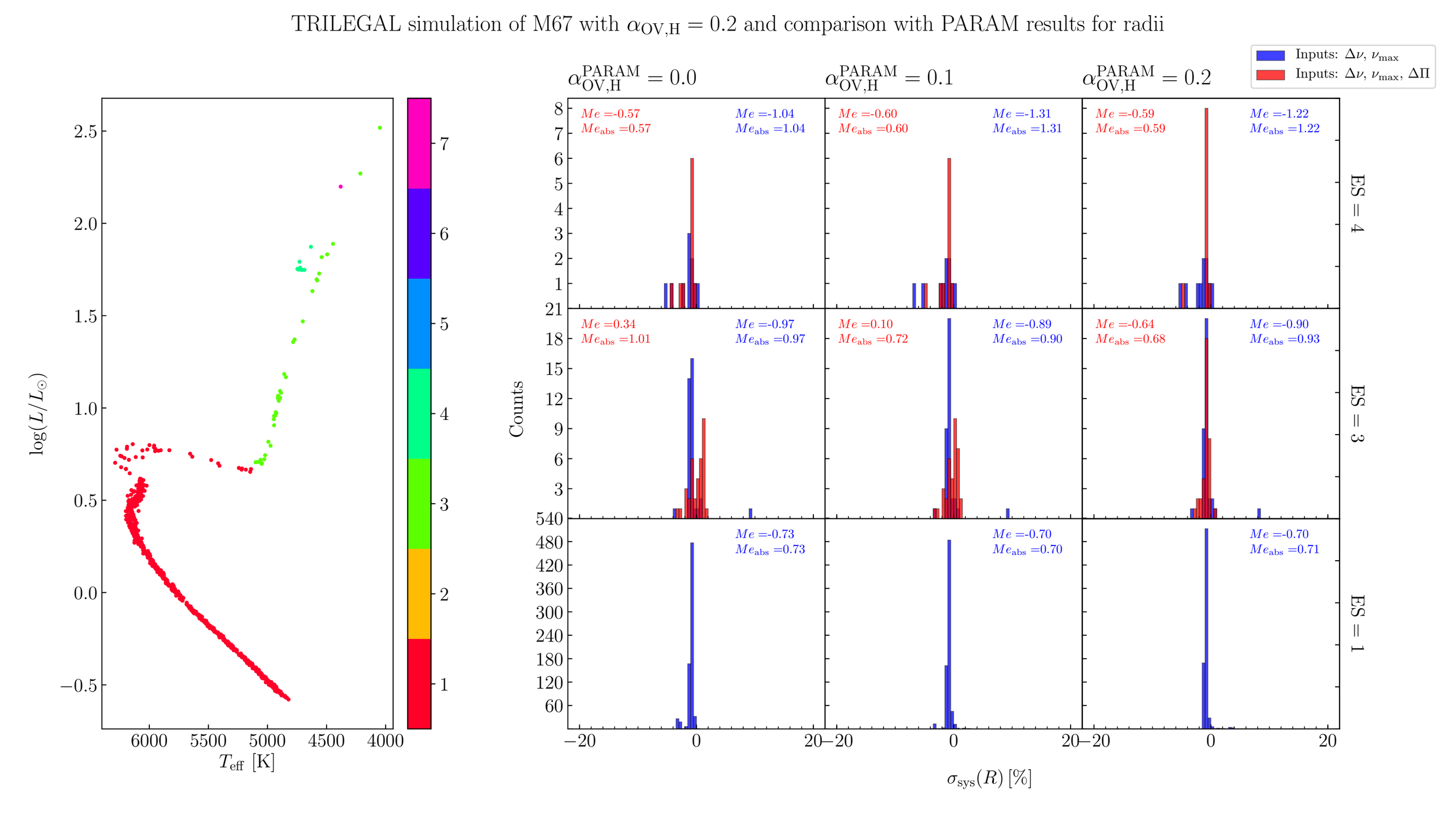
TRILEGAL simulation of M67 with $\alpha_{\rm OV,H} = 0.2$ and comparison with PARAM results for radii
Inputs: $\Delta\nu$, $\nu_{\rm max}$
Inputs: $\Delta\nu$, $\nu_{\rm max}$, $\Delta\Pi$
$\alpha_{\rm OV,H}^{\rm PARAM} = 0.0$
$\alpha_{\rm OV,H}^{\rm PARAM} = 0.1$
$\alpha_{\rm OV,H}^{\rm PARAM} = 0.2$
ES = 4
ES = 3
ES = 1
Counts
$\log(L/L_\odot)$
$T_{\rm eff}$ [K]
$\sigma_{\rm sys}(R)$ [%]
Me =-0.57
Me$_{\rm abs}$ =0.57
Me =-1.04
Me$_{\rm abs}$ =1.04
Me =-0.60
Me$_{\rm abs}$ =0.60
Me =-1.31
Me$_{\rm abs}$ =1.31
Me =-0.59
Me$_{\rm abs}$ =0.59
Me =-1.22
Me$_{\rm abs}$ =1.22
Me =0.34
Me$_{\rm abs}$ =1.01
Me =-0.97
Me$_{\rm abs}$ =0.97
Me =0.10
Me$_{\rm abs}$ =0.72
Me =-0.89
Me$_{\rm abs}$ =0.90
Me =-0.64
Me$_{\rm abs}$ =0.68
Me =-0.90
Me$_{\rm abs}$ =0.93
Me =-0.73
Me$_{\rm abs}$ =0.73
Me =-0.70
Me$_{\rm abs}$ =0.70
Me =-0.70
Me$_{\rm abs}$ =0.71

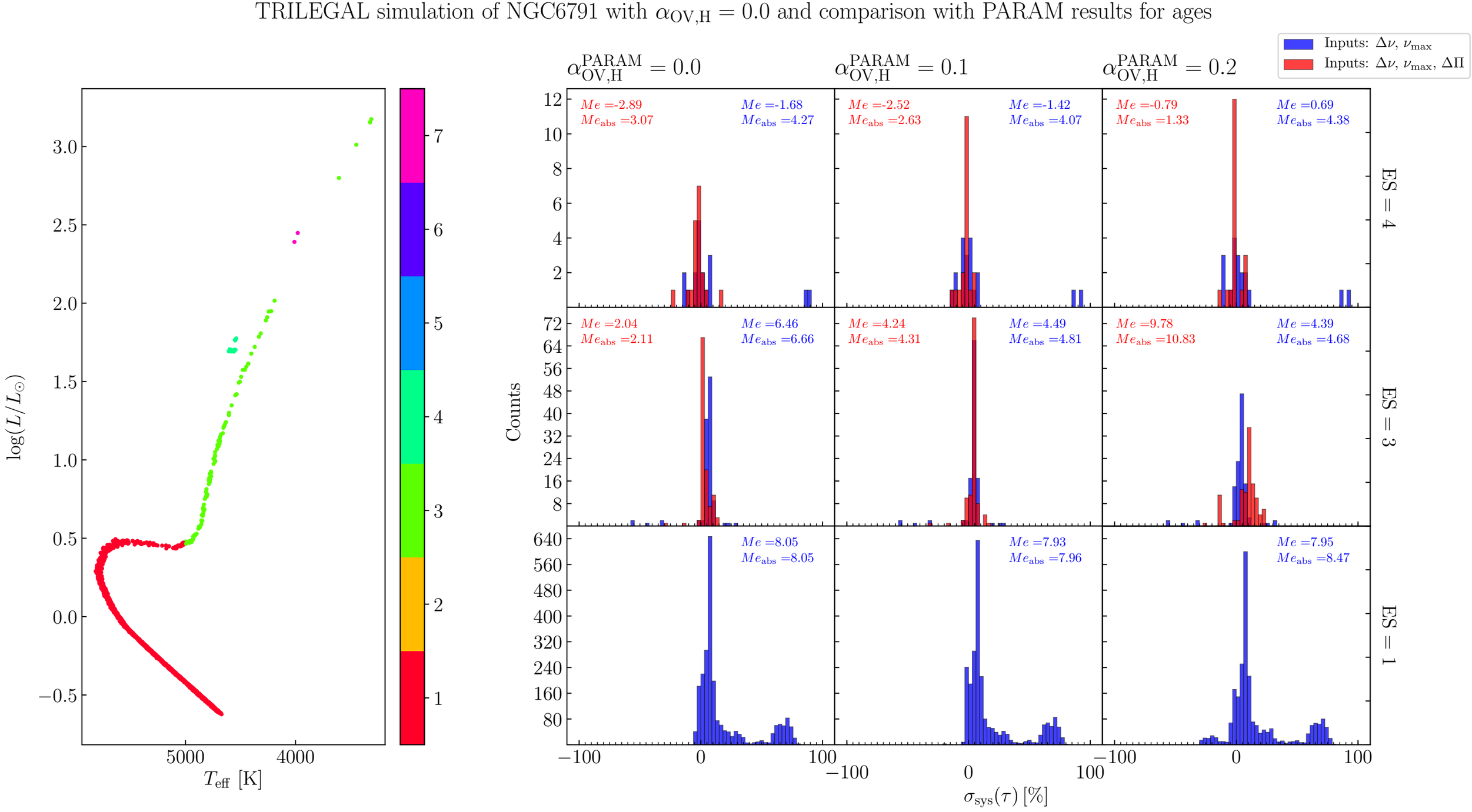
TRILEGAL simulation of NGC6791 with $\alpha_{\rm OV,H} = 0.0$ and comparison with PARAM results for ages
Inputs: $\Delta\nu$, $\nu_{\rm max}$
Inputs: $\Delta\nu$, $\nu_{\rm max}$, $\Delta\Pi$
$\alpha_{\rm OV,H}^{\rm PARAM} = 0.0$
$\alpha_{\rm OV,H}^{\rm PARAM} = 0.1$
$\alpha_{\rm OV,H}^{\rm PARAM} = 0.2$
ES = 4
ES = 3
ES = 1
Counts
$\sigma_{\rm sys}(\tau)$ [%]
$\log(L/L_\odot)$
$T_{\rm eff}$ [K]
Me =-2.89
Me$_{\rm abs}$ =3.07
Me =-1.68
Me$_{\rm abs}$ =4.27
Me =-2.52
Me$_{\rm abs}$ =2.63
Me =-1.42
Me$_{\rm abs}$ =4.07
Me =-0.79
Me$_{\rm abs}$ =1.33
Me =0.69
Me$_{\rm abs}$ =4.38
Me =2.04
Me$_{\rm abs}$ =2.11
Me =6.46
Me$_{\rm abs}$ =6.66
Me =4.24
Me$_{\rm abs}$ =4.31
Me =4.49
Me$_{\rm abs}$ =4.81
Me =9.78
Me$_{\rm abs}$ =10.83
Me =4.39
Me$_{\rm abs}$ =4.68
Me =8.05
Me$_{\rm abs}$ =8.05
Me =7.93
Me$_{\rm abs}$ =7.96
Me =7.95
Me$_{\rm abs}$ =8.47

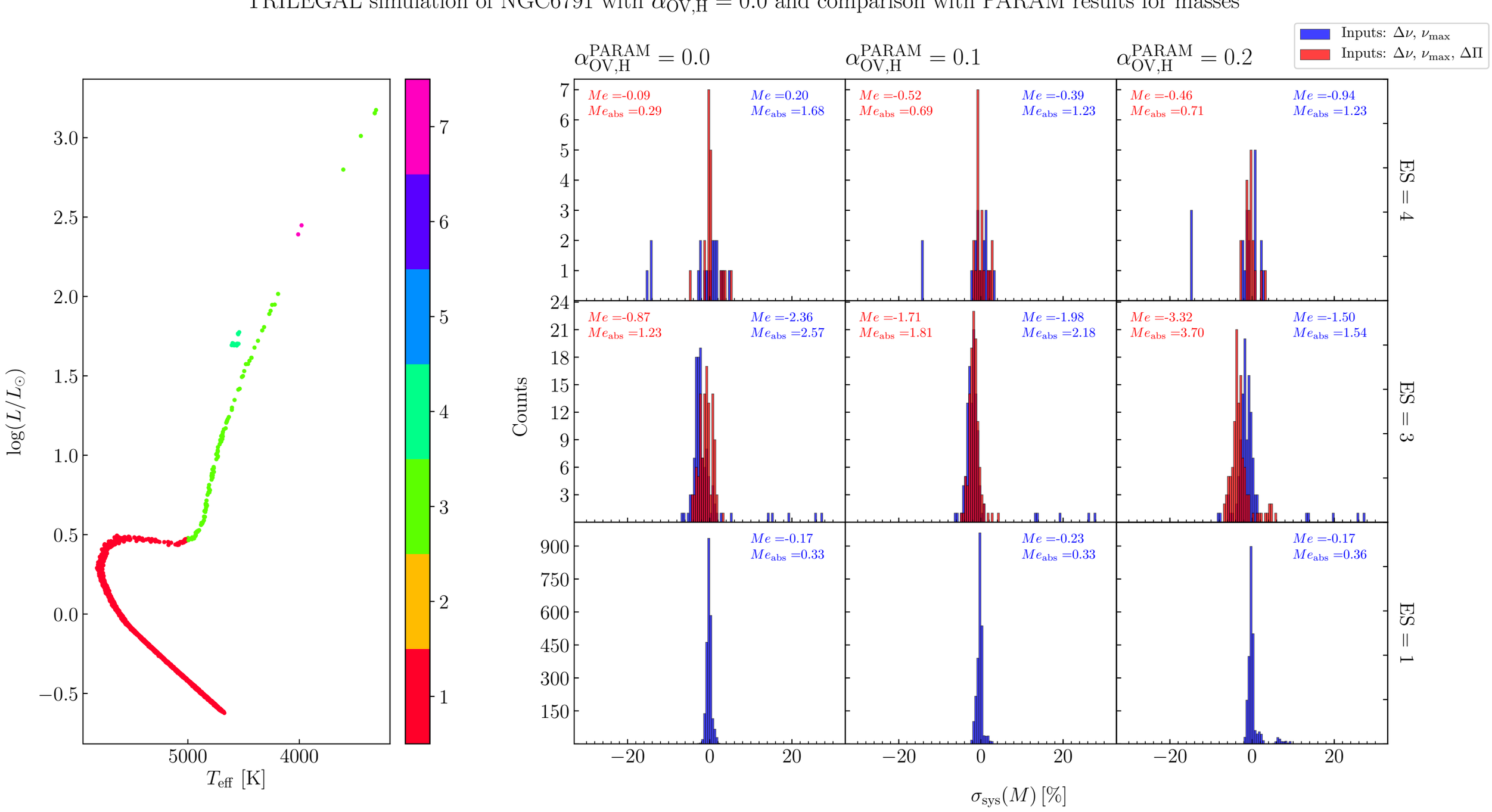
TRILEGAL simulation of NGC6791 with $\alpha_{\rm OV,H} = 0.0$ and comparison with PARAM results for masses
Inputs: $\Delta\nu$, $\nu_{\rm max}$
Inputs: $\Delta\nu$, $\nu_{\rm max}$, $\Delta\Pi$
$\alpha_{\rm OV,H}^{\rm PARAM} = 0.0$
$\alpha_{\rm OV,H}^{\rm PARAM} = 0.1$
$\alpha_{\rm OV,H}^{\rm PARAM} = 0.2$
$\log(L/L_\odot)$
$T_{\rm eff}$ [K]
Counts
$\sigma_{\rm sys}(M)$ [%]
ES = 4
ES = 3
ES = 1
Me =-0.09
Me$_{\rm abs}$ =0.29
Me =0.20
Me$_{\rm abs}$ =1.68
Me =-0.52
Me$_{\rm abs}$ =0.69
Me =-0.39
Me$_{\rm abs}$ =1.23
Me =-0.46
Me$_{\rm abs}$ =0.71
Me =-0.94
Me$_{\rm abs}$ =1.23
Me =-0.87
Me$_{\rm abs}$ =1.23
Me =-2.36
Me$_{\rm abs}$ =2.57
Me =-1.71
Me$_{\rm abs}$ =1.81
Me =-1.98
Me$_{\rm abs}$ =2.18
Me =-3.32
Me$_{\rm abs}$ =3.70
Me =-1.50
Me$_{\rm abs}$ =1.54
Me =-0.17
Me$_{\rm abs}$ =0.33
Me =-0.23
Me$_{\rm abs}$ =0.33
Me =-0.17
Me$_{\rm abs}$ =0.36

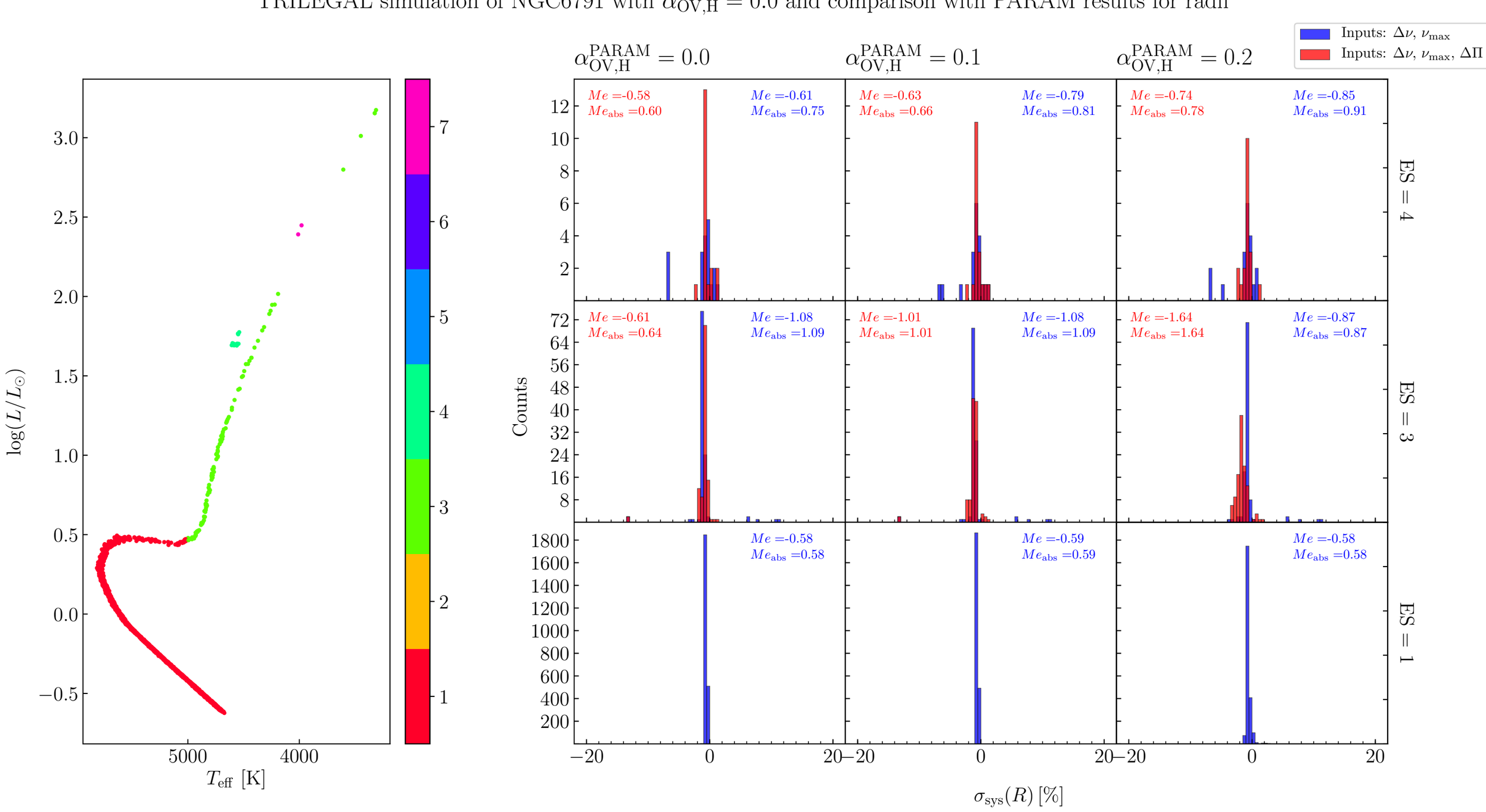
TRILEGAL simulation of NGC6791 with $\alpha_{\rm OV,H} = 0.0$ and comparison with PARAM results for radii
Inputs: $\Delta\nu$, $\nu_{\rm max}$
Inputs: $\Delta\nu$, $\nu_{\rm max}$, $\Delta\Pi$
$\alpha_{\rm OV,H}^{\rm PARAM} = 0.0$
$\alpha_{\rm OV,H}^{\rm PARAM} = 0.1$
$\alpha_{\rm OV,H}^{\rm PARAM} = 0.2$
ES = 4
ES = 3
ES = 1
Counts
$\log(L/L_\odot)$
$T_{\rm eff}$ [K]
$\sigma_{\rm sys}(R)$ [%]
Me =-0.58
Me$_{\rm abs}$ =0.60
Me =-0.61
Me$_{\rm abs}$ =0.75
Me =-0.63
Me$_{\rm abs}$ =0.66
Me =-0.79
Me$_{\rm abs}$ =0.81
Me =-0.74
Me$_{\rm abs}$ =0.78
Me =-0.85
Me$_{\rm abs}$ =0.91
Me =-0.61
Me$_{\rm abs}$ =0.64
Me =-1.08
Me$_{\rm abs}$ =1.09
Me =-1.01
Me$_{\rm abs}$ =1.01
Me =-1.08
Me$_{\rm abs}$ =1.09
Me =-1.64
Me$_{\rm abs}$ =1.64
Me =-0.87
Me$_{\rm abs}$ =0.87
Me =-0.58
Me$_{\rm abs}$ =0.58
Me =-0.59
Me$_{\rm abs}$ =0.59
Me =-0.58
Me$_{\rm abs}$ =0.58

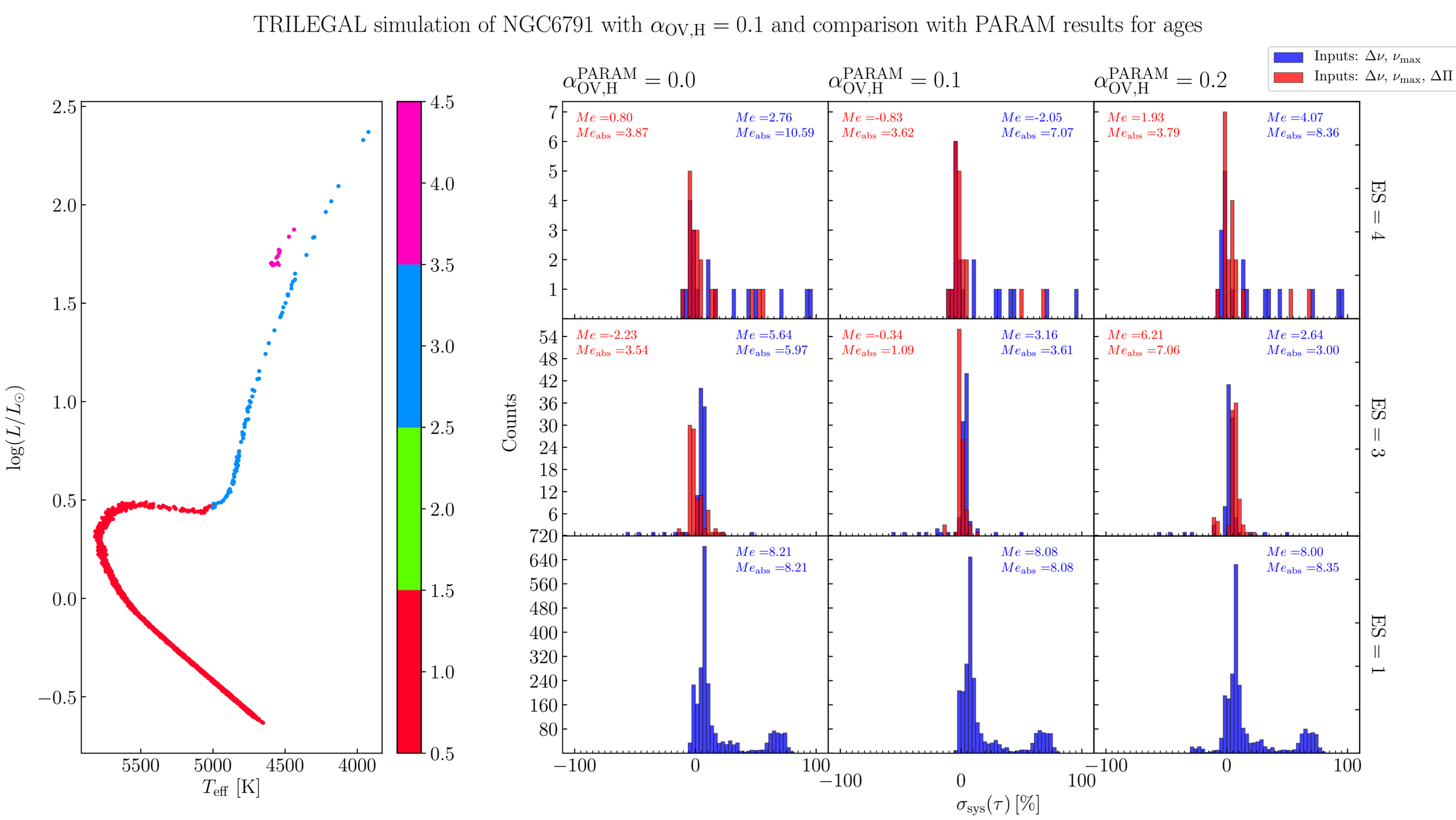
TRILEGAL simulation of NGC6791 with $\alpha_{\rm OV,H} = 0.1$ and comparison with PARAM results for ages
Inputs: $\Delta\nu$, $\nu_{\rm max}$
Inputs: $\Delta\nu$, $\nu_{\rm max}$, $\Delta\Pi$
$\alpha_{\rm OV,H}^{\rm PARAM} = 0.0$
$\alpha_{\rm OV,H}^{\rm PARAM} = 0.1$
$\alpha_{\rm OV,H}^{\rm PARAM} = 0.2$
ES = 4
ES = 3
ES = 1
Counts
$\log(L/L_\odot)$
$T_{\rm eff}$ [K]
$\sigma_{\rm sys}(\tau)$ [%]
Me =0.80
Me$_{\rm abs}$ =3.87
Me =2.76
Me$_{\rm abs}$ =10.59
Me =-0.83
Me$_{\rm abs}$ =3.62
Me =-2.05
Me$_{\rm abs}$ =7.07
Me =1.93
Me$_{\rm abs}$ =3.79
Me =4.07
Me$_{\rm abs}$ =8.36
Me =-2.23
Me$_{\rm abs}$ =3.54
Me =5.64
Me$_{\rm abs}$ =5.97
Me =-0.34
Me$_{\rm abs}$ =1.09
Me =3.16
Me$_{\rm abs}$ =3.61
Me =6.21
Me$_{\rm abs}$ =7.06
Me =2.64
Me$_{\rm abs}$ =3.00
Me =8.21
Me$_{\rm abs}$ =8.21
Me =8.08
Me$_{\rm abs}$ =8.08
Me =8.00
Me$_{\rm abs}$ =8.35

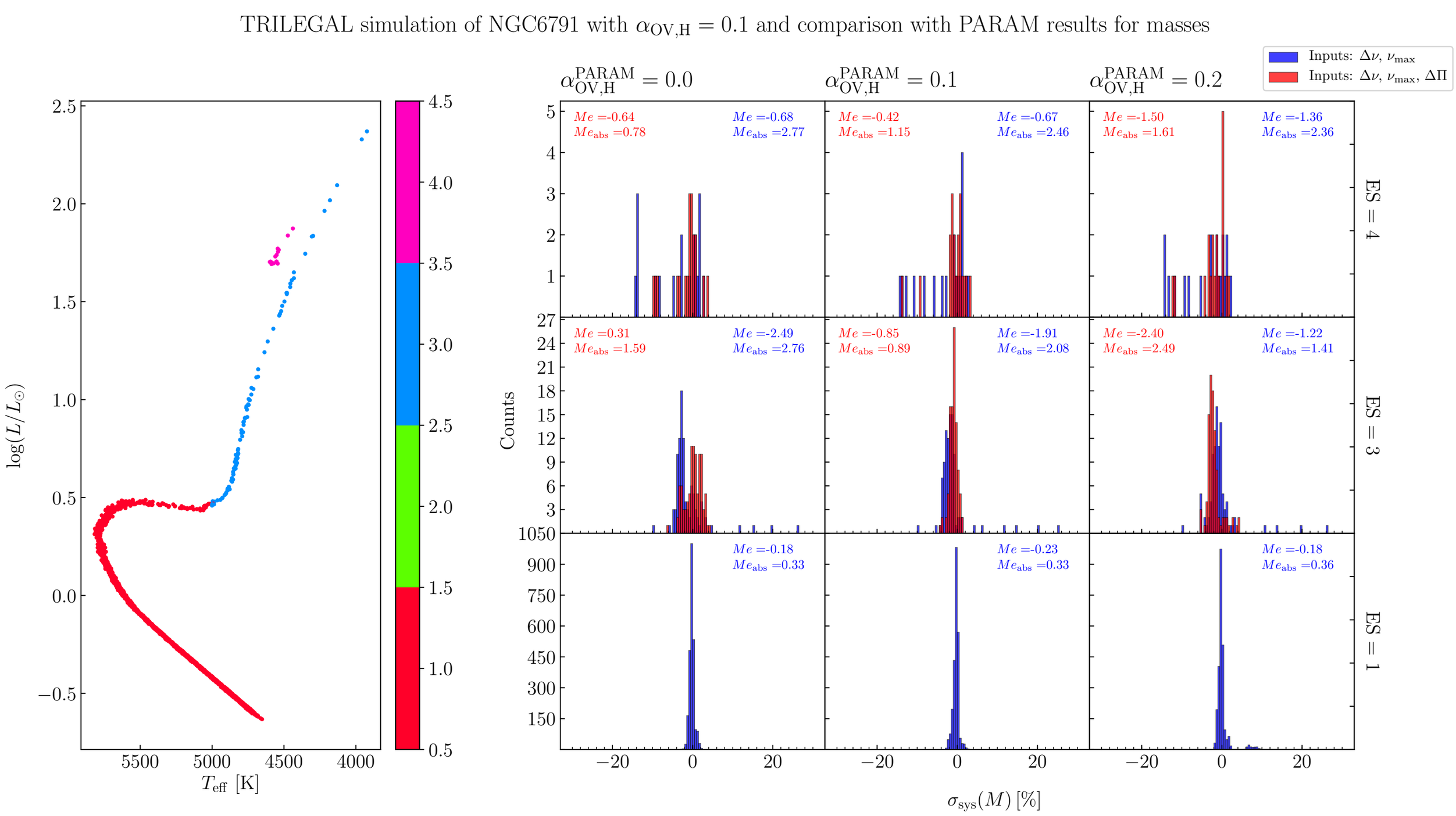
TRILEGAL simulation of NGC6791 with $\alpha_{\rm OV,H} = 0.1$ and comparison with PARAM results for masses
Inputs: $\Delta\nu$, $\nu_{\rm max}$
Inputs: $\Delta\nu$, $\nu_{\rm max}$, $\Delta\Pi$
$\alpha_{\rm OV,H}^{\rm PARAM} = 0.0$
$\alpha_{\rm OV,H}^{\rm PARAM} = 0.1$
$\alpha_{\rm OV,H}^{\rm PARAM} = 0.2$
ES = 4
ES = 3
ES = 1
Counts
$\sigma_{\rm sys}(M)$ [%]
$\log(L/L_\odot)$
$T_{\rm eff}$ [K]
Me =-0.64
Me$_{\rm abs}$ =0.78
Me =-0.68
Me$_{\rm abs}$ =2.77
Me =-0.42
Me$_{\rm abs}$ =1.15
Me =-0.67
Me$_{\rm abs}$ =2.46
Me =-1.50
Me$_{\rm abs}$ =1.61
Me =-1.36
Me$_{\rm abs}$ =2.36
Me =0.31
Me$_{\rm abs}$ =1.59
Me =-2.49
Me$_{\rm abs}$ =2.76
Me =-0.85
Me$_{\rm abs}$ =0.89
Me =-1.91
Me$_{\rm abs}$ =2.08
Me =-2.40
Me$_{\rm abs}$ =2.49
Me =-1.22
Me$_{\rm abs}$ =1.41
Me =-0.18
Me$_{\rm abs}$ =0.33
Me =-0.23
Me$_{\rm abs}$ =0.33
Me =-0.18
Me$_{\rm abs}$ =0.36

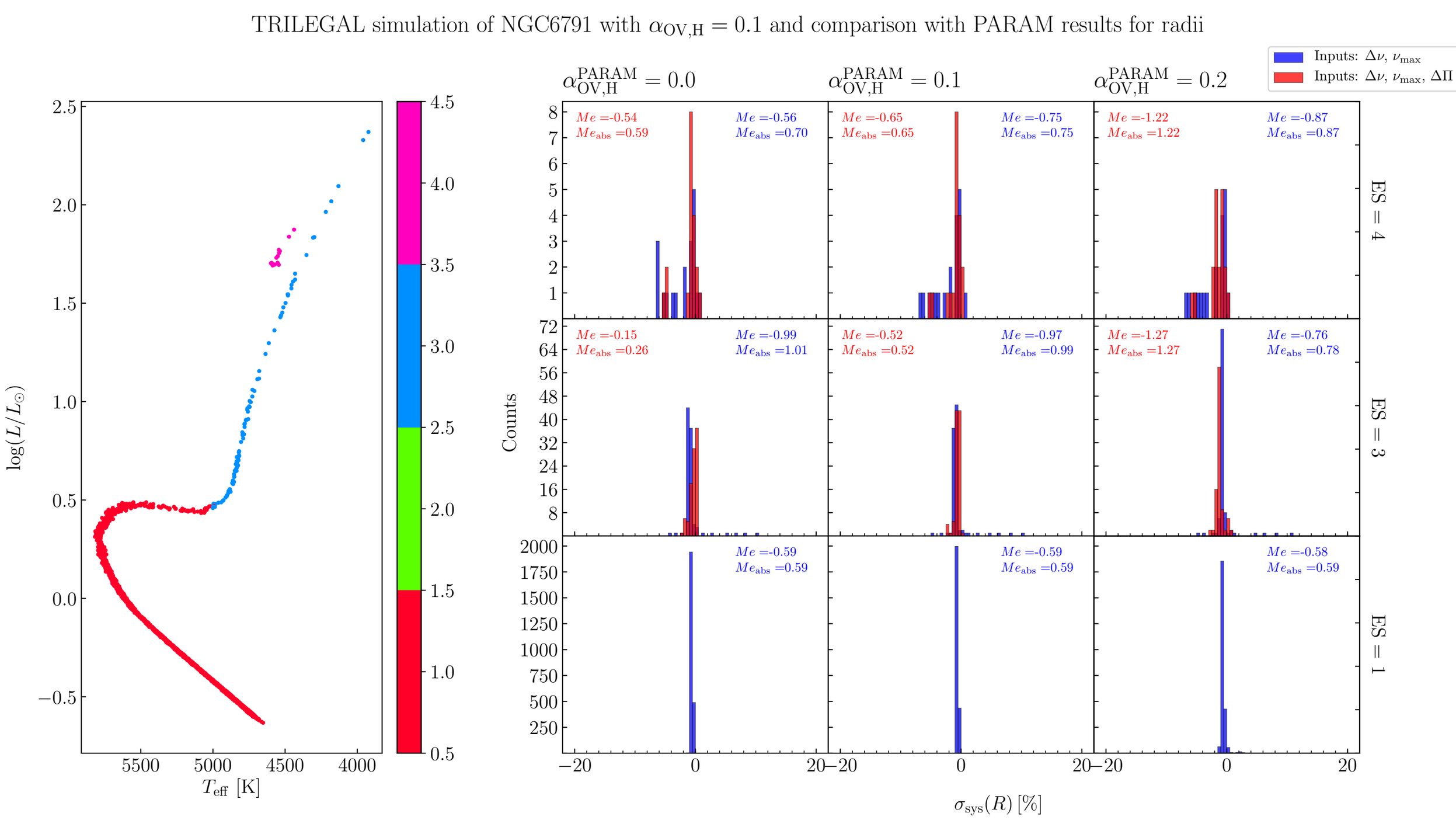
TRILEGAL simulation of NGC6791 with $\alpha_{\rm OV,H} = 0.1$ and comparison with PARAM results for radii
Inputs: $\Delta\nu$, $\nu_{\rm max}$
Inputs: $\Delta\nu$, $\nu_{\rm max}$, $\Delta\Pi$
$\alpha_{\rm OV,H}^{\rm PARAM} = 0.0$
$\alpha_{\rm OV,H}^{\rm PARAM} = 0.1$
$\alpha_{\rm OV,H}^{\rm PARAM} = 0.2$
ES = 4
ES = 3
ES = 1
Me =-0.54
Me$_{\rm abs}$ =0.59
Me =-0.56
Me$_{\rm abs}$ =0.70
Me =-0.65
Me$_{\rm abs}$ =0.65
Me =-0.75
Me$_{\rm abs}$ =0.75
Me =-1.22
Me$_{\rm abs}$ =1.22
Me =-0.87
Me$_{\rm abs}$ =0.87
Me =-0.15
Me$_{\rm abs}$ =0.26
Me =-0.99
Me$_{\rm abs}$ =1.01
Me =-0.52
Me$_{\rm abs}$ =0.52
Me =-0.97
Me$_{\rm abs}$ =0.99
Me =-1.27
Me$_{\rm abs}$ =1.27
Me =-0.76
Me$_{\rm abs}$ =0.78
Me =-0.59
Me$_{\rm abs}$ =0.59
Me =-0.59
Me$_{\rm abs}$ =0.59
Me =-0.58
Me$_{\rm abs}$ =0.59
Counts
$\sigma_{\rm sys}(R)$ [%]
$\log(L/L_\odot)$
$T_{\rm eff}$ [K]

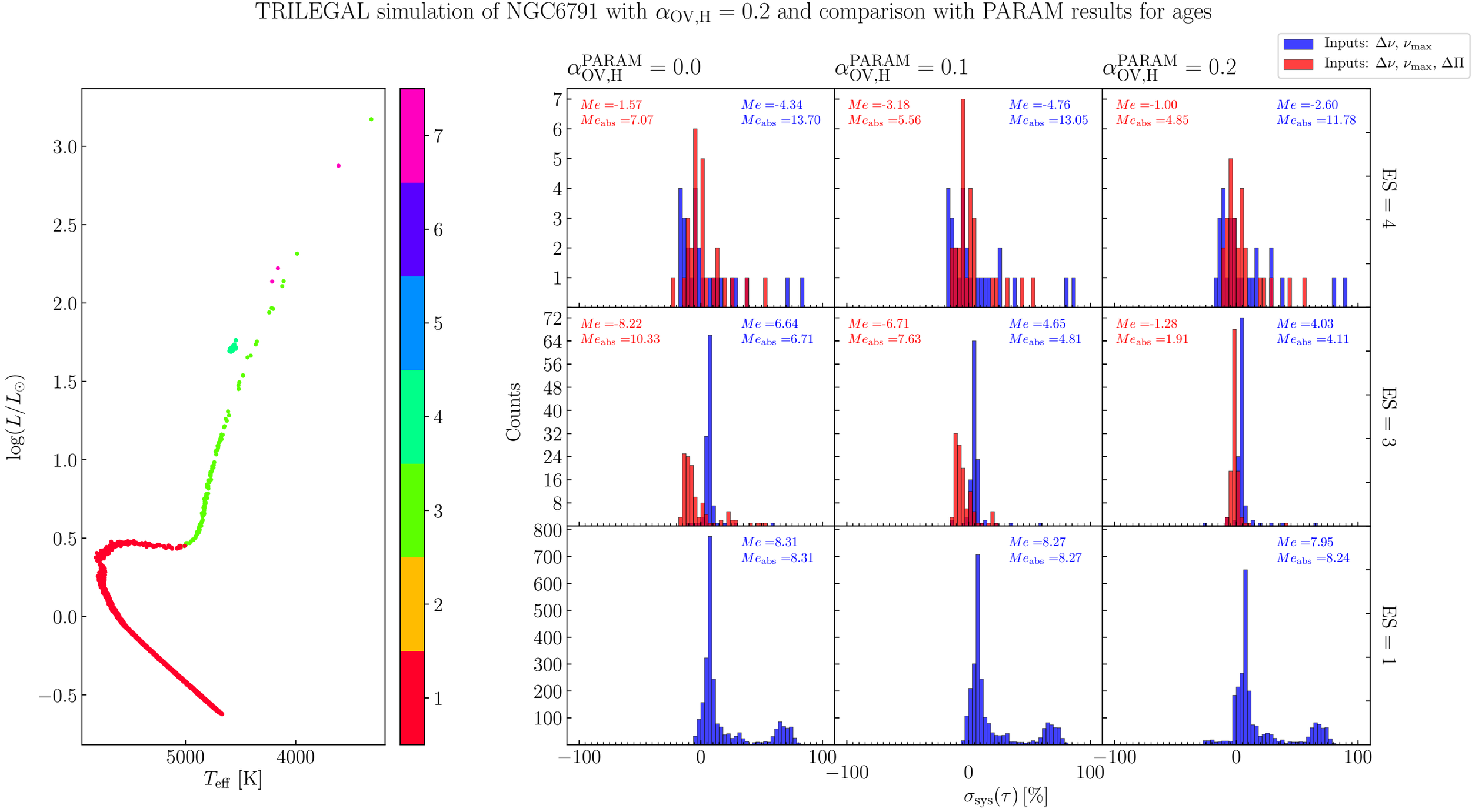
TRILEGAL simulation of NGC6791 with $\alpha_{\rm OV,H} = 0.2$ and comparison with PARAM results for ages
Inputs: $\Delta\nu$, $\nu_{\rm max}$
Inputs: $\Delta\nu$, $\nu_{\rm max}$, $\Delta\Pi$
$\alpha_{\rm OV,H}^{\rm PARAM} = 0.0$
$\alpha_{\rm OV,H}^{\rm PARAM} = 0.1$
$\alpha_{\rm OV,H}^{\rm PARAM} = 0.2$
ES = 4
ES = 3
ES = 1
Counts
$\log(L/L_\odot)$
$T_{\rm eff}$ [K]
$\sigma_{\rm sys}(\tau)$ [%]
Me =-1.57
Me$_{\rm abs}$ =7.07
Me =-4.34
Me$_{\rm abs}$ =13.70
Me =-3.18
Me$_{\rm abs}$ =5.56
Me =-4.76
Me$_{\rm abs}$ =13.05
Me =-1.00
Me$_{\rm abs}$ =4.85
Me =-2.60
Me$_{\rm abs}$ =11.78
Me =-8.22
Me$_{\rm abs}$ =10.33
Me =6.64
Me$_{\rm abs}$ =6.71
Me =-6.71
Me$_{\rm abs}$ =7.63
Me =4.65
Me$_{\rm abs}$ =4.81
Me =-1.28
Me$_{\rm abs}$ =1.91
Me =4.03
Me$_{\rm abs}$ =4.11
Me =8.31
Me$_{\rm abs}$ =8.31
Me =8.27
Me$_{\rm abs}$ =8.27
Me =7.95
Me$_{\rm abs}$ =8.24

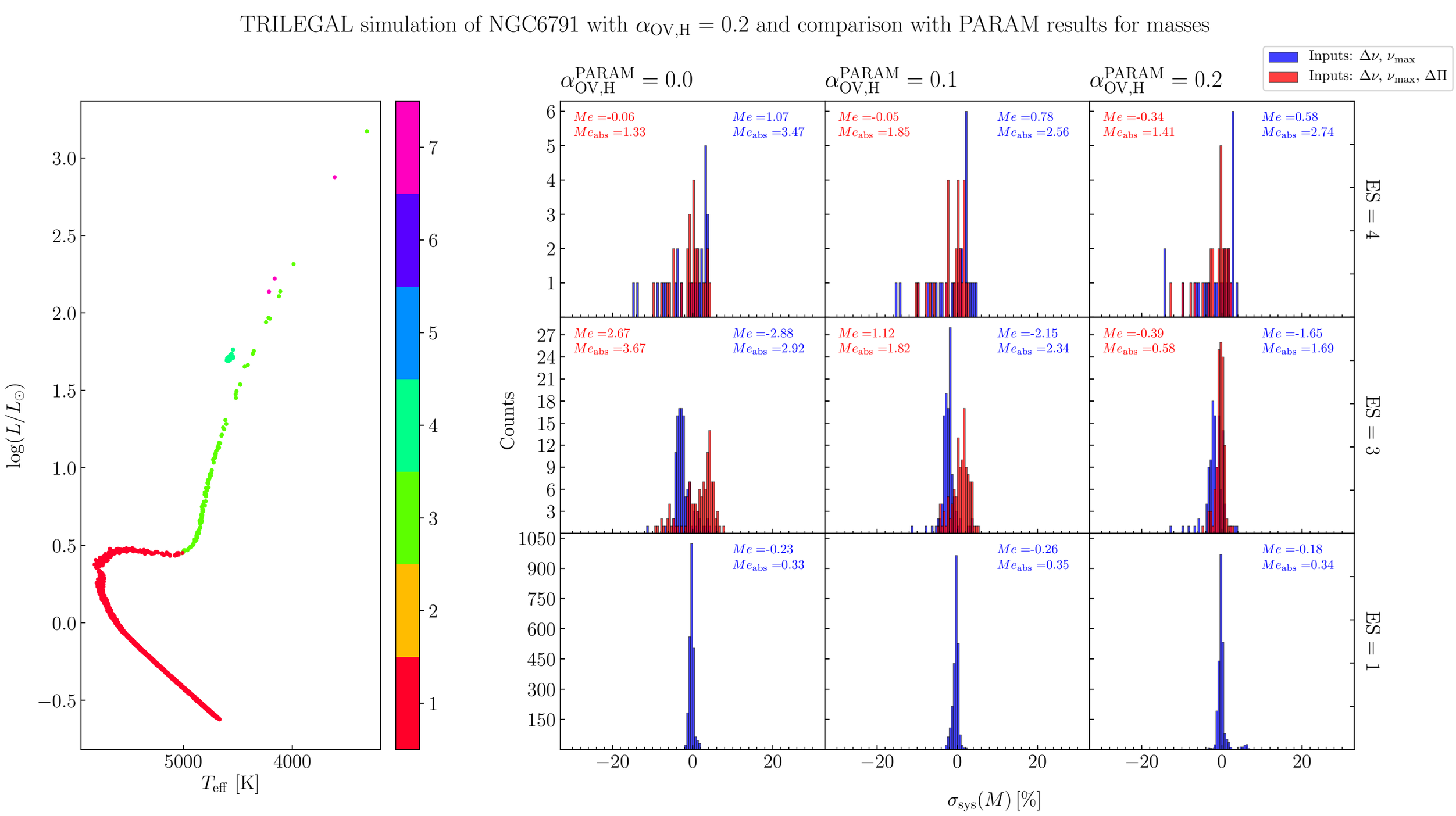
TRILEGAL simulation of NGC6791 with $\alpha_{\rm OV,H} = 0.2$ and comparison with PARAM results for masses
Inputs: $\Delta\nu$, $\nu_{\rm max}$
Inputs: $\Delta\nu$, $\nu_{\rm max}$, $\Delta\Pi$
$\alpha_{\rm OV,H}^{\rm PARAM} = 0.0$
$\alpha_{\rm OV,H}^{\rm PARAM} = 0.1$
$\alpha_{\rm OV,H}^{\rm PARAM} = 0.2$
ES = 4
ES = 3
ES = 1
Counts
$\log(L/L_\odot)$
$T_{\rm eff}$ [K]
$\sigma_{\rm sys}(M)$ [%]
Me =-0.06
Me$_{\rm abs}$ =1.33
Me =1.07
Me$_{\rm abs}$ =3.47
Me =-0.05
Me$_{\rm abs}$ =1.85
Me =0.78
Me$_{\rm abs}$ =2.56
Me =-0.34
Me$_{\rm abs}$ =1.41
Me =0.58
Me$_{\rm abs}$ =2.74
Me =2.67
Me$_{\rm abs}$ =3.67
Me =-2.88
Me$_{\rm abs}$ =2.92
Me =1.12
Me$_{\rm abs}$ =1.82
Me =-2.15
Me$_{\rm abs}$ =2.34
Me =-0.39
Me$_{\rm abs}$ =0.58
Me =-1.65
Me$_{\rm abs}$ =1.69
Me =-0.23
Me$_{\rm abs}$ =0.33
Me =-0.26
Me$_{\rm abs}$ =0.35
Me =-0.18
Me$_{\rm abs}$ =0.34

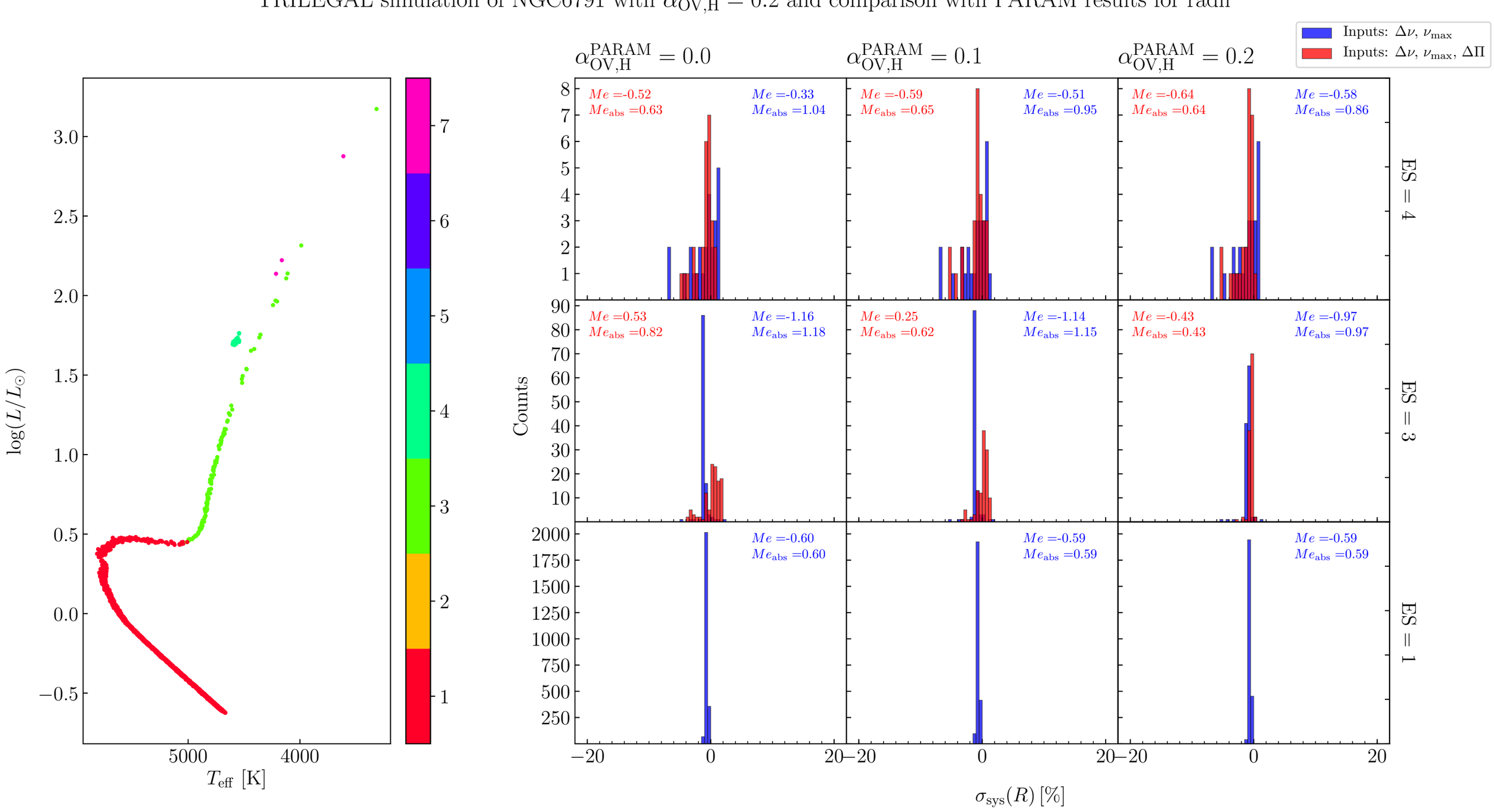
TRILEGAL simulation of NGC6791 with $\alpha_{\rm OV,H} = 0.2$ and comparison with PARAM results for radii
Inputs: $\Delta\nu$, $\nu_{\rm max}$
Inputs: $\Delta\nu$, $\nu_{\rm max}$, $\Delta\Pi$
$\alpha_{\rm OV,H}^{\rm PARAM} = 0.0$
$\alpha_{\rm OV,H}^{\rm PARAM} = 0.1$
$\alpha_{\rm OV,H}^{\rm PARAM} = 0.2$
ES = 4
ES = 3
ES = 1
Counts
$\log(L/L_\odot)$
$T_{\rm eff}$ [K]
$\sigma_{\rm sys}(R)$ [%]
Me =-0.52
Me$_{\rm abs}$ =0.63
Me =-0.33
Me$_{\rm abs}$ =1.04
Me =-0.59
Me$_{\rm abs}$ =0.65
Me =-0.51
Me$_{\rm abs}$ =0.95
Me =-0.64
Me$_{\rm abs}$ =0.64
Me =-0.58
Me$_{\rm abs}$ =0.86
Me =0.53
Me$_{\rm abs}$ =0.82
Me =-1.16
Me$_{\rm abs}$ =1.18
Me =0.25
Me$_{\rm abs}$ =0.62
Me =-1.14
Me$_{\rm abs}$ =1.15
Me =-0.43
Me$_{\rm abs}$ =0.43
Me =-0.97
Me$_{\rm abs}$ =0.97
Me =-0.60
Me$_{\rm abs}$ =0.60
Me =-0.59
Me$_{\rm abs}$ =0.59
Me =-0.59
Me$_{\rm abs}$ =0.59

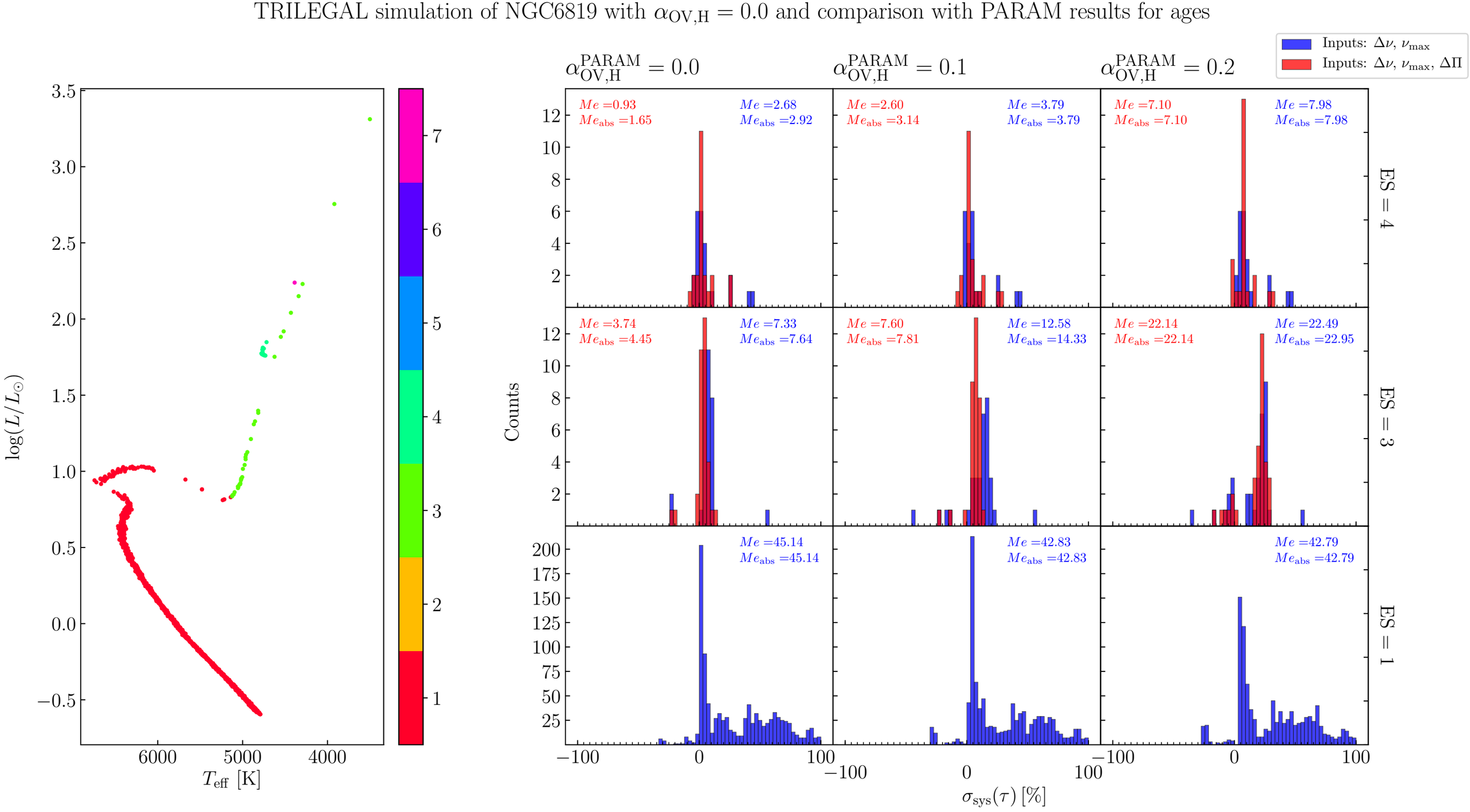
TRILEGAL simulation of NGC6819 with $\alpha_{\rm OV,H} = 0.0$ and comparison with PARAM results for ages
Inputs: $\Delta\nu$, $\nu_{\rm max}$
Inputs: $\Delta\nu$, $\nu_{\rm max}$, $\Delta\Pi$
$\alpha_{\rm OV,H}^{\rm PARAM} = 0.0$
$\alpha_{\rm OV,H}^{\rm PARAM} = 0.1$
$\alpha_{\rm OV,H}^{\rm PARAM} = 0.2$
ES = 4
ES = 3
ES = 1
Counts
$\log(L/L_\odot)$
$T_{\rm eff}$ [K]
$\sigma_{\rm sys}(\tau)$ [%]
Me =0.93
Me$_{\rm abs}$ =1.65
Me =2.68
Me$_{\rm abs}$ =2.92
Me =2.60
Me$_{\rm abs}$ =3.14
Me =3.79
Me$_{\rm abs}$ =3.79
Me =7.10
Me$_{\rm abs}$ =7.10
Me =7.98
Me$_{\rm abs}$ =7.98
Me =3.74
Me$_{\rm abs}$ =4.45
Me =7.33
Me$_{\rm abs}$ =7.64
Me =7.60
Me$_{\rm abs}$ =7.81
Me =12.58
Me$_{\rm abs}$ =14.33
Me =22.14
Me$_{\rm abs}$ =22.14
Me =22.49
Me$_{\rm abs}$ =22.95
Me =45.14
Me$_{\rm abs}$ =45.14
Me =42.83
Me$_{\rm abs}$ =42.83
Me =42.79
Me$_{\rm abs}$ =42.79

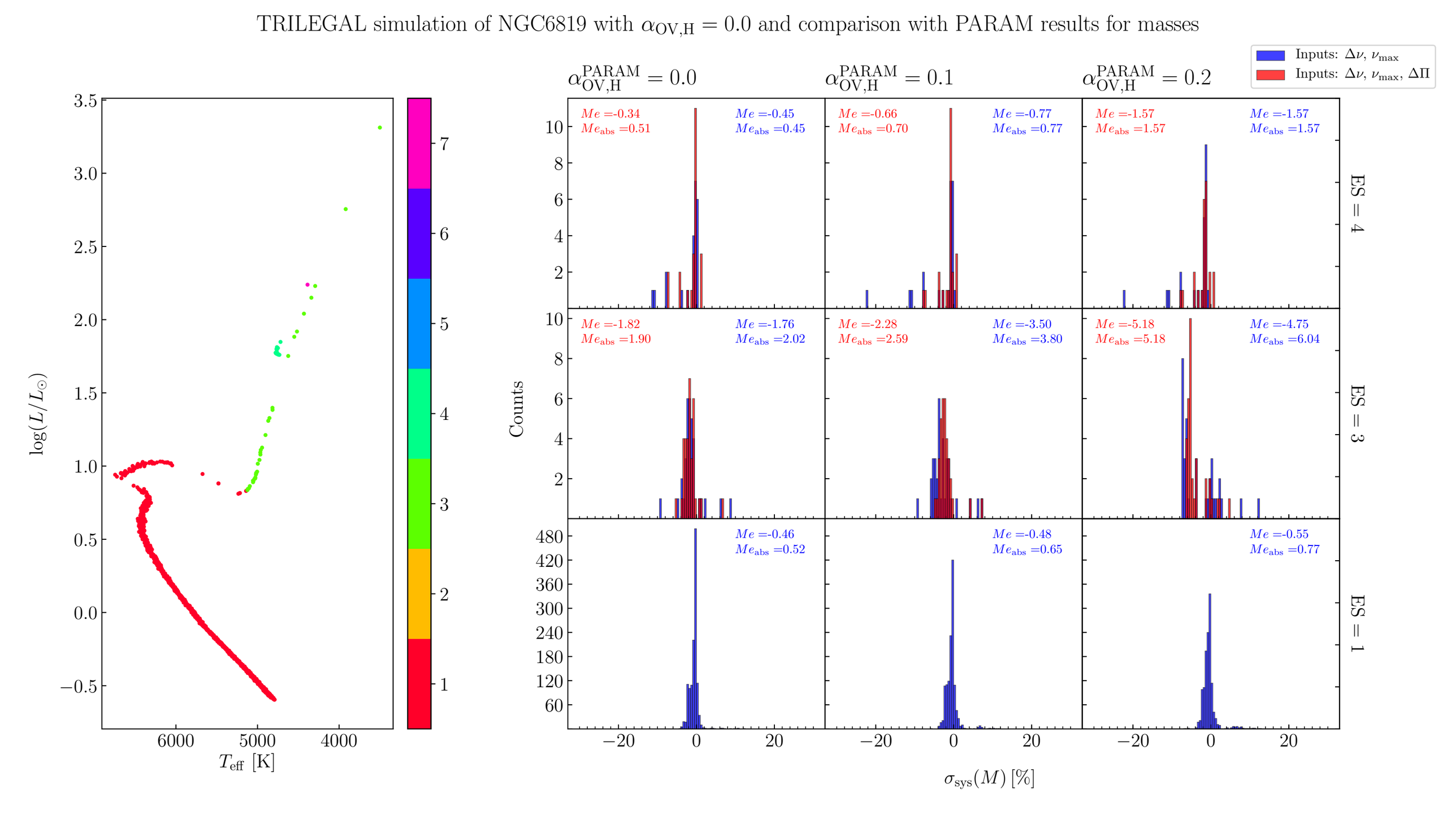
TRILEGAL simulation of NGC6819 with $\alpha_{\rm OV,H} = 0.0$ and comparison with PARAM results for masses
Inputs: $\Delta\nu$, $\nu_{\rm max}$
Inputs: $\Delta\nu$, $\nu_{\rm max}$, $\Delta\Pi$
$\alpha_{\rm OV,H}^{\rm PARAM} = 0.0$
$\alpha_{\rm OV,H}^{\rm PARAM} = 0.1$
$\alpha_{\rm OV,H}^{\rm PARAM} = 0.2$
ES = 4
ES = 3
ES = 1
Counts
$\log(L/L_\odot)$
$T_{\rm eff}$ [K]
$\sigma_{\rm sys}(M)$ [%]
Me =-0.34
Me$_{\rm abs}$ =0.51
Me =-0.45
Me$_{\rm abs}$ =0.45
Me =-0.66
Me$_{\rm abs}$ =0.70
Me =-0.77
Me$_{\rm abs}$ =0.77
Me =-1.57
Me$_{\rm abs}$ =1.57
Me =-1.57
Me$_{\rm abs}$ =1.57
Me =-1.82
Me$_{\rm abs}$ =1.90
Me =-1.76
Me$_{\rm abs}$ =2.02
Me =-2.28
Me$_{\rm abs}$ =2.59
Me =-3.50
Me$_{\rm abs}$ =3.80
Me =-5.18
Me$_{\rm abs}$ =5.18
Me =-4.75
Me$_{\rm abs}$ =6.04
Me =-0.46
Me$_{\rm abs}$ =0.52
Me =-0.48
Me$_{\rm abs}$ =0.65
Me =-0.55
Me$_{\rm abs}$ =0.77

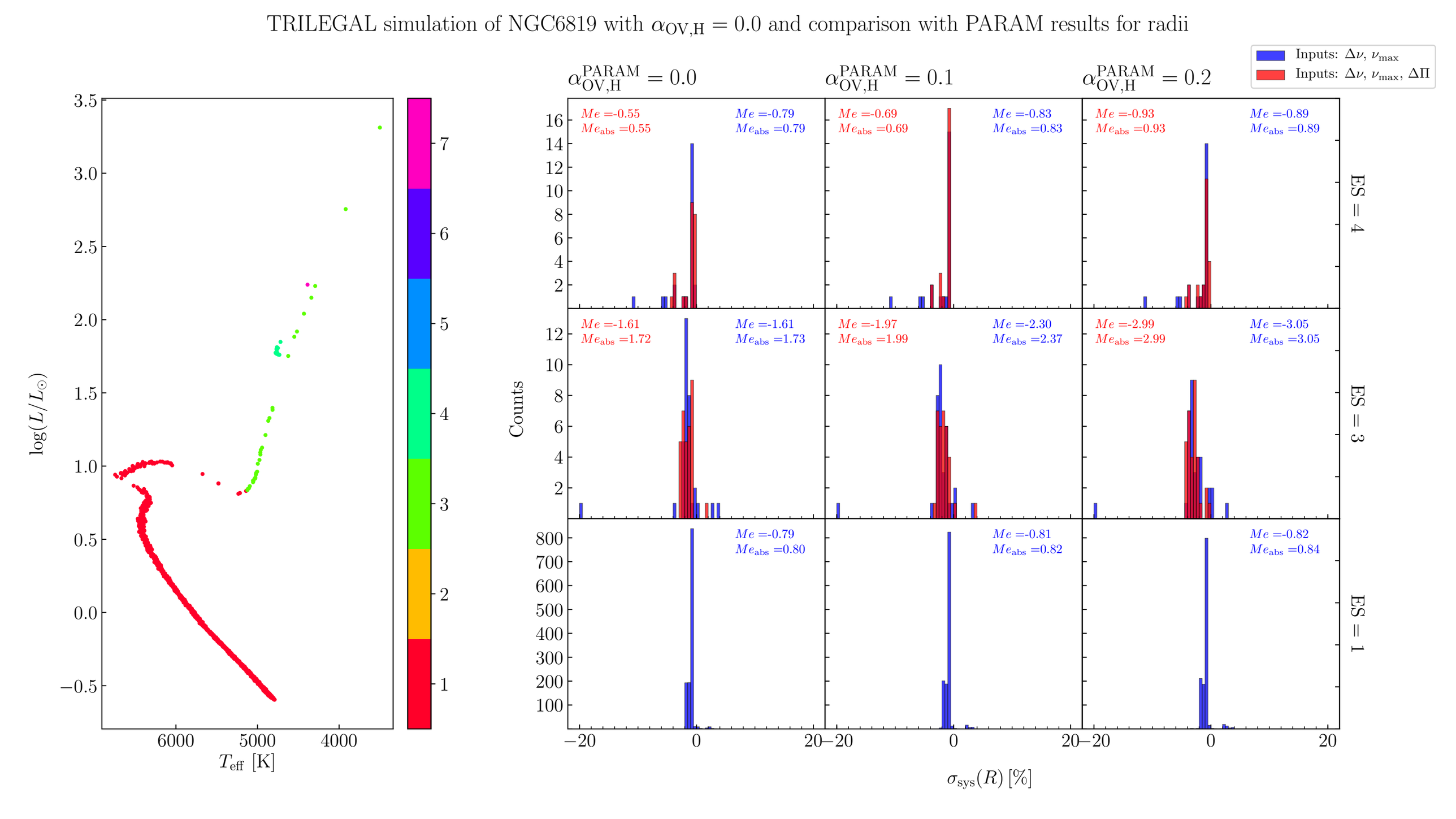
TRILEGAL simulation of NGC6819 with $\alpha_{\rm OV,H} = 0.0$ and comparison with PARAM results for radii
Inputs: $\Delta\nu$, $\nu_{\rm max}$
Inputs: $\Delta\nu$, $\nu_{\rm max}$, $\Delta\Pi$
$\alpha_{\rm OV,H}^{\rm PARAM} = 0.0$
$\alpha_{\rm OV,H}^{\rm PARAM} = 0.1$
$\alpha_{\rm OV,H}^{\rm PARAM} = 0.2$
ES = 4
ES = 3
ES = 1
Counts
$\log(L/L_\odot)$
$T_{\rm eff}$ [K]
$\sigma_{\rm sys}(R)$ [%]
Me =-0.55
Me$_{\rm abs}$ =0.55
Me =-0.79
Me$_{\rm abs}$ =0.79
Me =-0.69
Me$_{\rm abs}$ =0.69
Me =-0.83
Me$_{\rm abs}$ =0.83
Me =-0.93
Me$_{\rm abs}$ =0.93
Me =-0.89
Me$_{\rm abs}$ =0.89
Me =-1.61
Me$_{\rm abs}$ =1.72
Me =-1.61
Me$_{\rm abs}$ =1.73
Me =-1.97
Me$_{\rm abs}$ =1.99
Me =-2.30
Me$_{\rm abs}$ =2.37
Me =-2.99
Me$_{\rm abs}$ =2.99
Me =-3.05
Me$_{\rm abs}$ =3.05
Me =-0.79
Me$_{\rm abs}$ =0.80
Me =-0.81
Me$_{\rm abs}$ =0.82
Me =-0.82
Me$_{\rm abs}$ =0.84

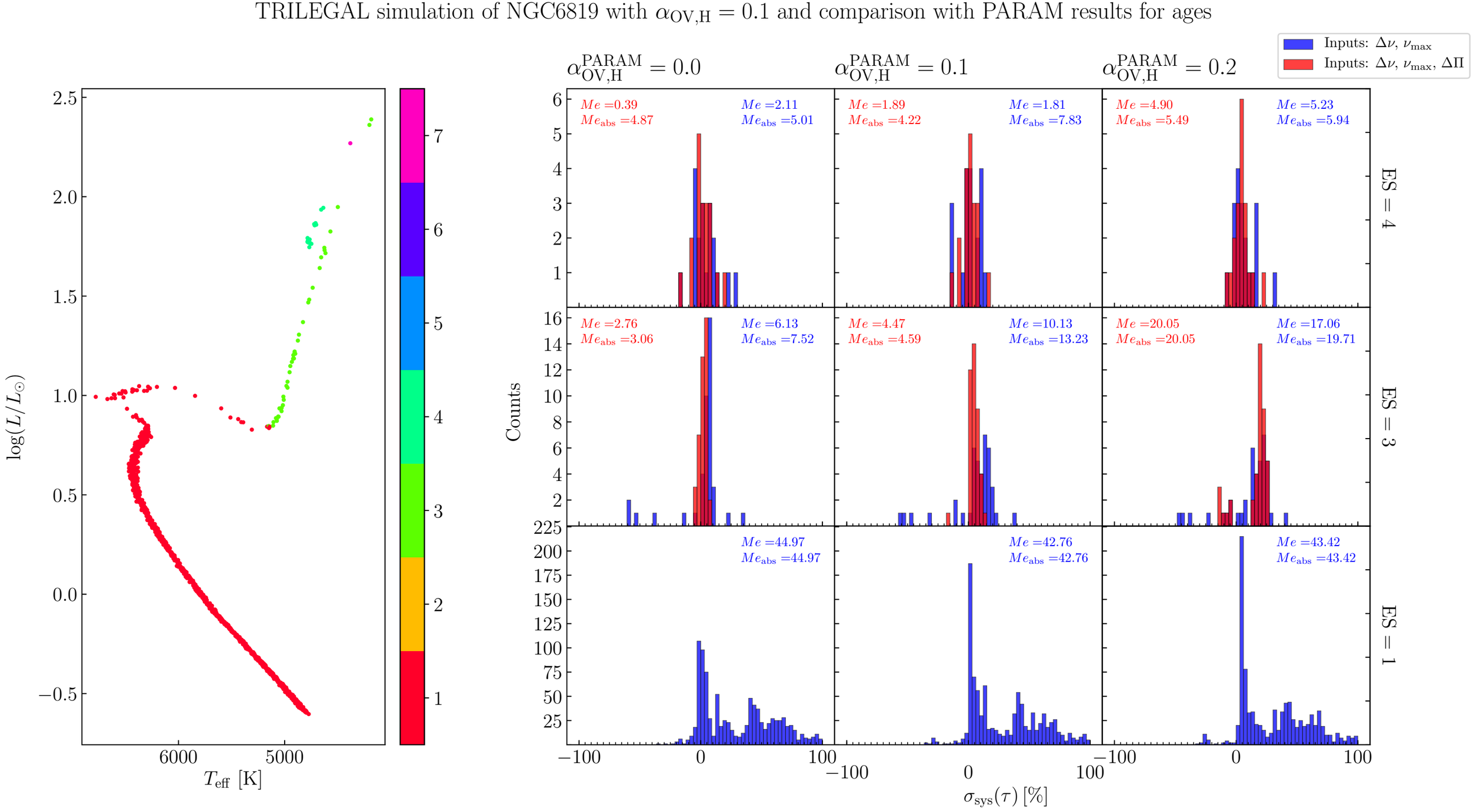
TRILEGAL simulation of NGC6819 with $\alpha_{\rm OV,H} = 0.1$ and comparison with PARAM results for ages
$\log(L/L_\odot)$
$T_{\rm eff}$ [K]
Inputs: $\Delta\nu$, $\nu_{\rm max}$
Inputs: $\Delta\nu$, $\nu_{\rm max}$, $\Delta\Pi$
$\alpha_{\rm OV,H}^{\rm PARAM} = 0.0$
$\alpha_{\rm OV,H}^{\rm PARAM} = 0.1$
$\alpha_{\rm OV,H}^{\rm PARAM} = 0.2$
ES = 4
ES = 3
ES = 1
Counts
$\sigma_{\rm sys}(\tau)$ [%]
Me =0.39
Me$_{\rm abs}$ =4.87
Me =2.11
Me$_{\rm abs}$ =5.01
Me =1.89
Me$_{\rm abs}$ =4.22
Me =1.81
Me$_{\rm abs}$ =7.83
Me =4.90
Me$_{\rm abs}$ =5.49
Me =5.23
Me$_{\rm abs}$ =5.94
Me =2.76
Me$_{\rm abs}$ =3.06
Me =6.13
Me$_{\rm abs}$ =7.52
Me =4.47
Me$_{\rm abs}$ =4.59
Me =10.13
Me$_{\rm abs}$ =13.23
Me =20.05
Me$_{\rm abs}$ =20.05
Me =17.06
Me$_{\rm abs}$ =19.71
Me =44.97
Me$_{\rm abs}$ =44.97
Me =42.76
Me$_{\rm abs}$ =42.76
Me =43.42
Me$_{\rm abs}$ =43.42

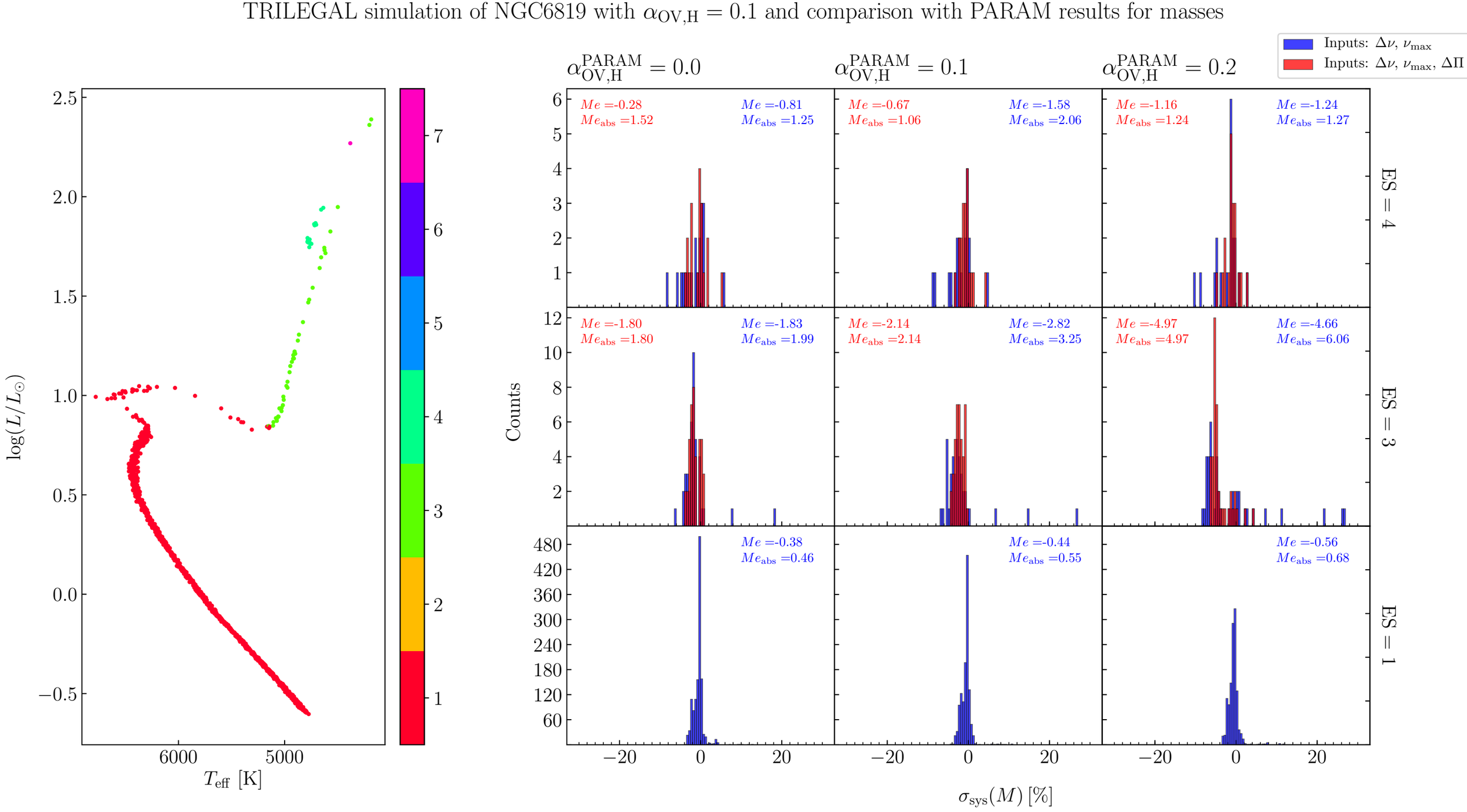
TRILEGAL simulation of NGC6819 with $\alpha_{\rm OV,H} = 0.1$ and comparison with PARAM results for masses
Inputs: $\Delta\nu$, $\nu_{\rm max}$
Inputs: $\Delta\nu$, $\nu_{\rm max}$, $\Delta\Pi$
$\alpha_{\rm OV,H}^{\rm PARAM} = 0.0$
$\alpha_{\rm OV,H}^{\rm PARAM} = 0.1$
$\alpha_{\rm OV,H}^{\rm PARAM} = 0.2$
ES = 4
ES = 3
ES = 1
Counts
$\log(L/L_\odot)$
$T_{\rm eff}$ [K]
$\sigma_{\rm sys}(M)$ [%]
Me =-0.28
Me$_{\rm abs}$ =1.52
Me =-0.81
Me$_{\rm abs}$ =1.25
Me =-0.67
Me$_{\rm abs}$ =1.06
Me =-1.58
Me$_{\rm abs}$ =2.06
Me =-1.16
Me$_{\rm abs}$ =1.24
Me =-1.24
Me$_{\rm abs}$ =1.27
Me =-1.80
Me$_{\rm abs}$ =1.80
Me =-1.83
Me$_{\rm abs}$ =1.99
Me =-2.14
Me$_{\rm abs}$ =2.14
Me =-2.82
Me$_{\rm abs}$ =3.25
Me =-4.97
Me$_{\rm abs}$ =4.97
Me =-4.66
Me$_{\rm abs}$ =6.06
Me =-0.38
Me$_{\rm abs}$ =0.46
Me =-0.44
Me$_{\rm abs}$ =0.55
Me =-0.56
Me$_{\rm abs}$ =0.68

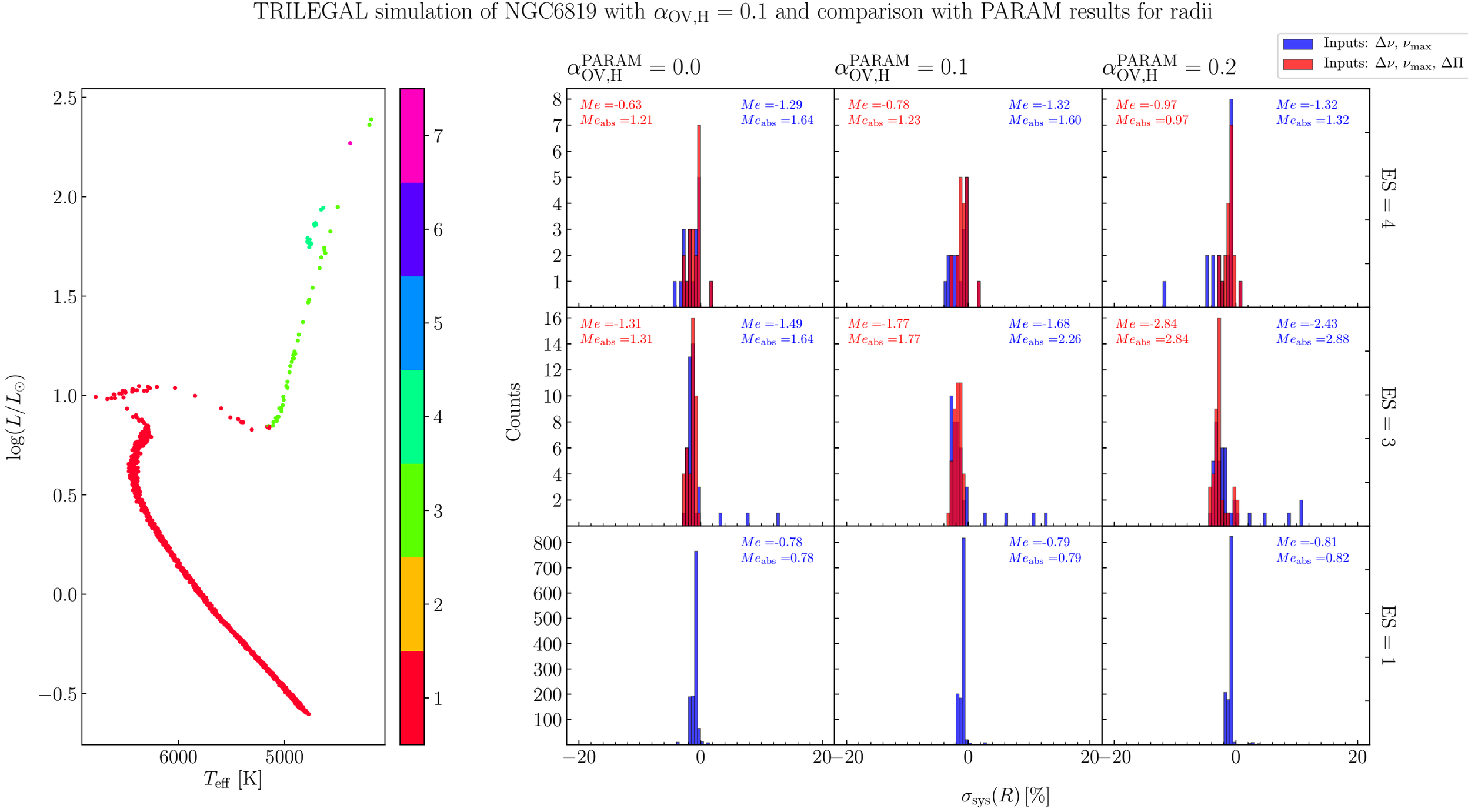
TRILEGAL simulation of NGC6819 with $\alpha_{\rm OV,H} = 0.1$ and comparison with PARAM results for radii
$\log(L/L_\odot)$
$T_{\rm eff}$ [K]
$\alpha_{\rm OV,H}^{\rm PARAM} = 0.0$
$\alpha_{\rm OV,H}^{\rm PARAM} = 0.1$
$\alpha_{\rm OV,H}^{\rm PARAM} = 0.2$
Inputs: $\Delta\nu$, $\nu_{\rm max}$
Inputs: $\Delta\nu$, $\nu_{\rm max}$, $\Delta\Pi$
ES = 4
ES = 3
ES = 1
Counts
$\sigma_{\rm sys}(R)$ [%]
Me =-0.63
Me$_{\rm abs}$ =1.21
Me =-1.29
Me$_{\rm abs}$ =1.64
Me =-0.78
Me$_{\rm abs}$ =1.23
Me =-1.32
Me$_{\rm abs}$ =1.60
Me =-0.97
Me$_{\rm abs}$ =0.97
Me =-1.32
Me$_{\rm abs}$ =1.32
Me =-1.31
Me$_{\rm abs}$ =1.31
Me =-1.49
Me$_{\rm abs}$ =1.64
Me =-1.77
Me$_{\rm abs}$ =1.77
Me =-1.68
Me$_{\rm abs}$ =2.26
Me =-2.84
Me$_{\rm abs}$ =2.84
Me =-2.43
Me$_{\rm abs}$ =2.88
Me =-0.78
Me$_{\rm abs}$ =0.78
Me =-0.79
Me$_{\rm abs}$ =0.79
Me =-0.81
Me$_{\rm abs}$ =0.82

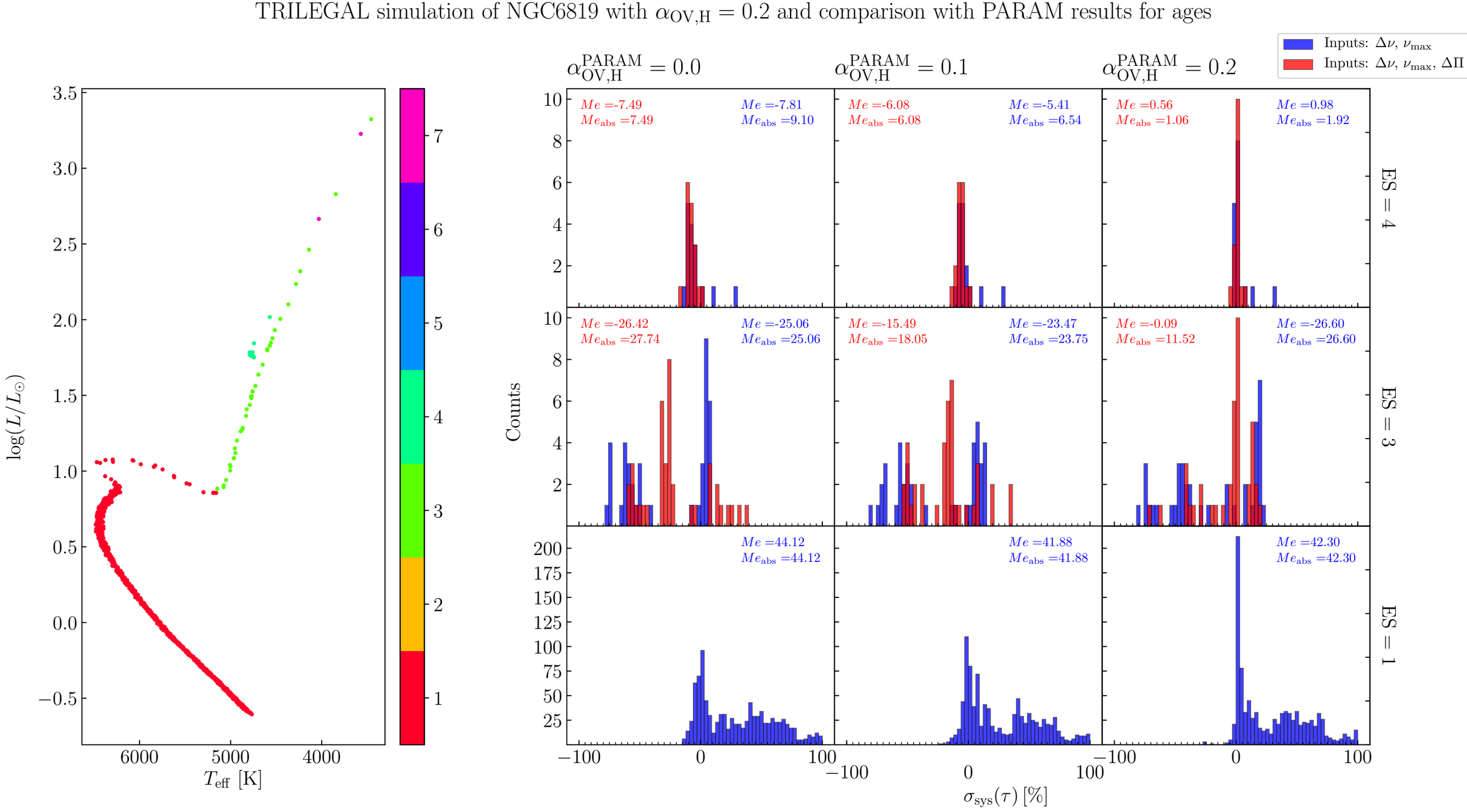
TRILEGAL simulation of NGC6819 with $\alpha_{\rm OV,H} = 0.2$ and comparison with PARAM results for ages
$\log(L/L_\odot)$
$T_{\rm eff}$ [K]
Inputs: $\Delta\nu$, $\nu_{\rm max}$
Inputs: $\Delta\nu$, $\nu_{\rm max}$, $\Delta\Pi$
$\alpha_{\rm OV,H}^{\rm PARAM} = 0.0$
$\alpha_{\rm OV,H}^{\rm PARAM} = 0.1$
$\alpha_{\rm OV,H}^{\rm PARAM} = 0.2$
ES = 4
ES = 3
ES = 1
Counts
$\sigma_{\rm sys}(\tau)$ [%]
Me =-7.49
Me$_{\rm abs}$ =7.49
Me =-7.81
Me$_{\rm abs}$ =9.10
Me =-6.08
Me$_{\rm abs}$ =6.08
Me =-5.41
Me$_{\rm abs}$ =6.54
Me =0.56
Me$_{\rm abs}$ =1.06
Me =0.98
Me$_{\rm abs}$ =1.92
Me =-26.42
Me$_{\rm abs}$ =27.74
Me =-25.06
Me$_{\rm abs}$ =25.06
Me =-15.49
Me$_{\rm abs}$ =18.05
Me =-23.47
Me$_{\rm abs}$ =23.75
Me =-0.09
Me$_{\rm abs}$ =11.52
Me =-26.60
Me$_{\rm abs}$ =26.60
Me =44.12
Me$_{\rm abs}$ =44.12
Me =41.88
Me$_{\rm abs}$ =41.88
Me =42.30
Me$_{\rm abs}$ =42.30

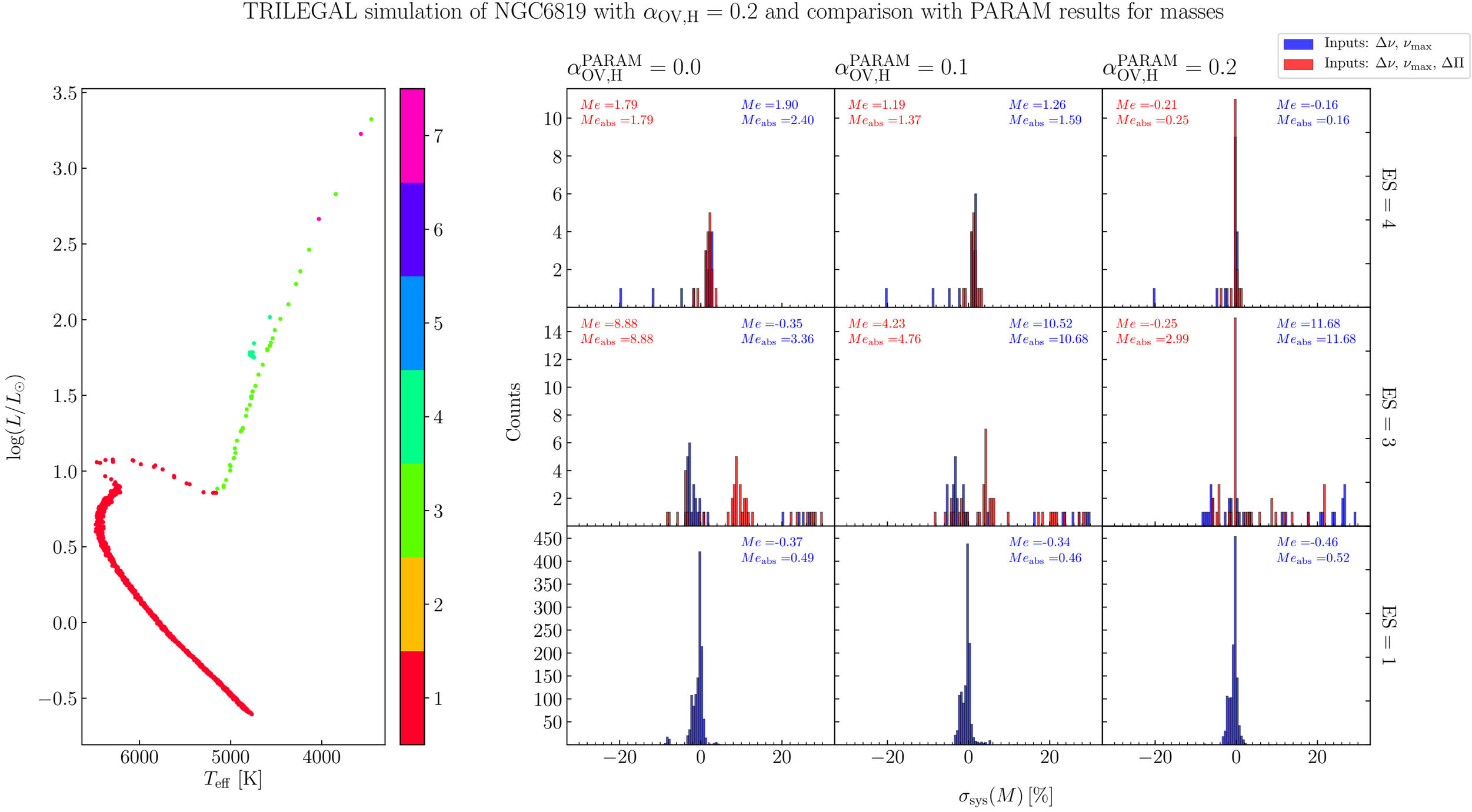
TRILEGAL simulation of NGC6819 with $\alpha_{\rm OV,H} = 0.2$ and comparison with PARAM results for masses
$\log(L/L_\odot)$
$T_{\rm eff}$ [K]
$\alpha_{\rm OV,H}^{\rm PARAM} = 0.0$
$\alpha_{\rm OV,H}^{\rm PARAM} = 0.1$
$\alpha_{\rm OV,H}^{\rm PARAM} = 0.2$
Inputs: $\Delta\nu$, $\nu_{\rm max}$
Inputs: $\Delta\nu$, $\nu_{\rm max}$, $\Delta\Pi$
ES = 4
ES = 3
ES = 1
Counts
$\sigma_{\rm sys}(M)$ [%]
Me =1.79
Me$_{\rm abs}$ =1.79
Me =1.90
Me$_{\rm abs}$ =2.40
Me =1.19
Me$_{\rm abs}$ =1.37
Me =1.26
Me$_{\rm abs}$ =1.59
Me =-0.21
Me$_{\rm abs}$ =0.25
Me =-0.16
Me$_{\rm abs}$ =0.16
Me =8.88
Me$_{\rm abs}$ =8.88
Me =-0.35
Me$_{\rm abs}$ =3.36
Me =4.23
Me$_{\rm abs}$ =4.76
Me =10.52
Me$_{\rm abs}$ =10.68
Me =-0.25
Me$_{\rm abs}$ =2.99
Me =11.68
Me$_{\rm abs}$ =11.68
Me =-0.37
Me$_{\rm abs}$ =0.49
Me =-0.34
Me$_{\rm abs}$ =0.46
Me =-0.46
Me$_{\rm abs}$ =0.52

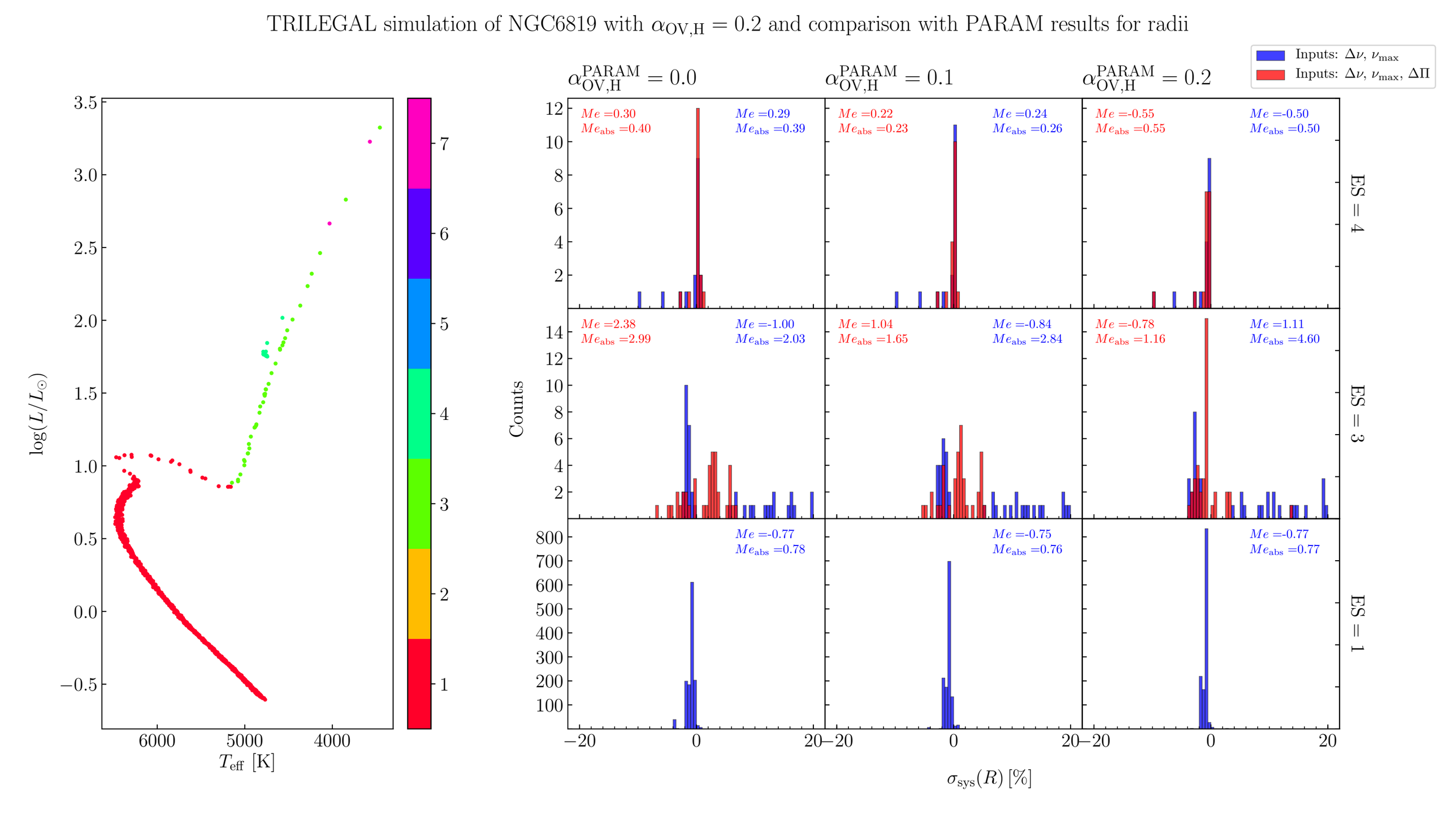
TRILEGAL simulation of NGC6819 with $\alpha_{\rm OV,H} = 0.2$ and comparison with PARAM results for radii
$\log(L/L_\odot)$
$T_{\rm eff}$ [K]
$\alpha_{\rm OV,H}^{\rm PARAM} = 0.0$
$\alpha_{\rm OV,H}^{\rm PARAM} = 0.1$
$\alpha_{\rm OV,H}^{\rm PARAM} = 0.2$
Inputs: $\Delta\nu$, $\nu_{\rm max}$
Inputs: $\Delta\nu$, $\nu_{\rm max}$, $\Delta\Pi$
ES = 4
ES = 3
ES = 1
Counts
$\sigma_{\rm sys}(R)$ [%]
Me =0.30
Me$_{\rm abs}$ =0.40
Me =0.29
Me$_{\rm abs}$ =0.39
Me =0.22
Me$_{\rm abs}$ =0.23
Me =0.24
Me$_{\rm abs}$ =0.26
Me =-0.55
Me$_{\rm abs}$ =0.55
Me =-0.50
Me$_{\rm abs}$ =0.50
Me =2.38
Me$_{\rm abs}$ =2.99
Me =-1.00
Me$_{\rm abs}$ =2.03
Me =1.04
Me$_{\rm abs}$ =1.65
Me =-0.84
Me$_{\rm abs}$ =2.84
Me =-0.78
Me$_{\rm abs}$ =1.16
Me =1.11
Me$_{\rm abs}$ =4.60
Me =-0.77
Me$_{\rm abs}$ =0.78
Me =-0.75
Me$_{\rm abs}$ =0.76
Me =-0.77
Me$_{\rm abs}$ =0.77